UNIVERSITAT ROVIRA I VIRGILI

Crystal growth and characterization of ytterbium or neodymium doped type III-KGd$(PO_3)_4$. A new bifunctional nonlinear and laser crystal

Isabel Parreu i Alberich

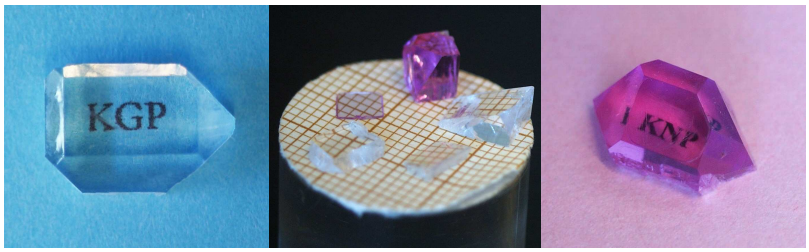

Supervised by:
Prof. Dr. Francesc Díaz and
Prof. Dr. Magdalena Aguiló

Física i Cristal.lografia de Materials
FiCMA

Tarragona, 2006

Crystal growth and characterization of ytterbium or neodymium doped type III-$KGd(PO_3)_4$. A new bifunctional nonlinear and laser crystal

Isabel Parreu i Alberich

Doctoral thesis
supervised by
Prof. Francesc Díaz and
Prof. Magdalena Aguiló

Física i Cristal·lografia de Materials (FiCMA)
Department of Physical and Inorganic Chemistry
Rovira i Virgili University
Tarragona, 2006

UNIVERSITAT ROVIRA I VIRGILI

Crystal growth and characterization of ytterbium or neodymium doped type III-$KGd(PO_3)_4$. A new bifunctional nonlinear and laser crystal

Isabel Parreu i Alberich

Física i Cristal·lografia de Materials (FiCMA)
Department of Physical and Inorganic Chemistry
Rovira i Virgili University
Marcel·lí Domingo
E-43007, Tarragona, Spain

Crystal growth and characterization of ytterbium or neodymium doped type III-$KGd(PO_3)_4$. A new bifunctional nonlinear and laser crystal.

Isabel Parreu i Alberich

Abstract

Bifunctional nonlinear and laser crystals are nonlinear optical crystals with sites that are suitable for laser active ions such as neodymium or ytterbium, which can combine the 1μm infrared laser emission with the second harmonic generation properties of the host to generate blue or green laser radiation by self-frequency doubling.

The aim of this doctoral thesis is to investigate how to synthesize a new nonlinear crystal, type III-$KGd(PO_3)_4$ alternatively doped with ytterbium or neodymium, and to evaluate its potentiality as a self-frequency doubling laser crystal. The thesis focuses on the growth, the optical and spectroscopic properties, and the laser generation of Yb:$KGd(PO_3)_4$ and Nd:$KGd(PO_3)_4$ crystals, which are very promising candidates for self-frequency doubling. The interest and originality of the investigations lie in different areas of Physics, Crystallography, Chemistry and Materials Science.

The chapters describe the crystal growth process of macrodefect-free single crystals of a size and doping level that are suitable for laser action and, thus, make self-frequency doubling possible. Both the linear and nonlinear optical properties of type-III $KGd(PO_3)_4$ indicate that it can be used as a nonlinear host. The spectroscopic properties of both ions suggest that efficient laser generation can be achieved and has been in Yb:$KGd(PO_3)_4$.

Keywords: Top seeded solution growth, X-ray diffraction, Laser crystals, Nonlinear optics, Second harmonic generation, Self-frequency doubling.

"Who can no longer pause to wonder and stand rapt in awe, is as good as dead; his eyes are closed"

Albert Einstein

Preface

The Ph.D. investigation contained in this thesis has been carried out at the group of Física i Cristal·lografia de Materials (FiCMA) in the Departament de Química Física i Inorgànica de la Universitat Rovira i Virgili de Tarragona and was advised by the Professors Francesc Díaz González and Magdalena Aguiló Díaz.

Within the development of this investigation, we have collaborated actively with the following groups: Prof. Xavier Solans at the University of Barcelona (Barcelona, Spain); Prof. Benoît Boulanger and Ass. Prof. Patricia Segonds at the Joseph Fourier University (Grenoble, France); Dr. Valentin Petrov at the Max-Born Institute for Non-linear Optics and Ultrafast Spectroscopy (Berlin, Germany), and Dr. Santiago Surinyach at the Autonoma University (Barcelona Spain).

This project was possible thanks to financial support from Departament d'Universitats, Recerca i Societat de la Informació de la Generalitat de Catalunya under projects 2005SGR-00658 and 2001SGR-317 and from Ministerio de Educación y Ciencia (MEC) of the Spanish Government under projects MAT2005-06354-C03-02, MAT2004-20471-E, MAT2002-04603-C05-03 and CIT-020400-2005-14. I would like to thank also personal financial support from Fons Social Europeu i Departament d'Universitats, Recerca i Societat de la Informació de la Generalitat de Catalunya under grants 2003FI00770-2006FIC00469.

Isabel Parreu i Alberich

Tarragona, 2006

Acknowledgements

First, I would like to thank my advisors, Professor Francesc Díaz and Professor Magdalena Aguiló, for giving me the opportunity to joint the FiCMA group and for their support, guidance and encouragement over the development of my PhD. investigation here. I would like to thank Francesc Díaz for his never-ending enthusiasm and for entering in innumerable scientific discussions with me, usually at the end of the working day, from which I have learnt a great deal. I will never be able to thank enough Magdalena Aguiló for sharing her huge knowledge of crystallography with me and for having always her office door open for me. I am grateful for everything I have learnt from them.

As any investigation work, this thesis involves comments and contributions of a team. I would like therefore to thank all the members of the FiCMA team for doing their bit in this thesis, which has been possible thanks to them to a large extend.

I would like to thank Dr. Jaume Massons for his helpful solutions in the everyday life at the optical laboratory, to Dra. Josefina Gavaldà for teaching me how to use the scanning electron microscope and for the fun time spent together, and to Dra. Mª Rosa Solé for guiding me in my first crystal growth experiments at the very beginning of my thesis.

I would like specially to acknowledge the technicians Agustí Montero, Nicol kker and Pere Fibla for their invaluable contribution to this thesis. I thank Agustí Montero for his helpful solutions in the everyday work not only at laboratory but also outside, especially with my old car, Nicole Bakker for cutting and polishing almost impossible samples from my delicate and usually small crystals and for her sense of humour, and Pere Fibla for helping me with everything related to electronics.

It has been a pleasure to work with all the pre- or post-doctoral members of FiCMA, who are no longer workmates but friends. I thank Dra. Cinta Pujol for

entering into innumerable discussions with me, especially about optics and spectroscopy but also about any matter, from which I have learnt a great deal, Dr. Joan Carvajal for infecting me with his enthusiasm and optimism and Dr. Xavier Mateos for helping me in the laser operation investigations. I thank Alexandra Peña for being always ready to help and listen to me, Oscar Silvestre for making me laugh and lighten stress on me many times and Montse Galceran for her practical sense of life and her red faces. I would also like to remember here Anna Aznar with who I have spent many fun times not only at FiCMA but also at the gym and Arantxa Vilalta for her positive sense of life.

I would like to express my appreciation to all the research groups that have collaborate with me during the PhD. investigations. I am much indebted to Professor Benoît Boulanger and Associated Professor Patricia Segonds for sharing with me their knowledge on nonlinear optics at the *Laboratoire de Spectrométrie Physique* in the Joseph Fourier University of Grenoble and everybody there for making my stay more enjoyable, especially Yannick Petit for helping me with the second harmonic generation measurements. I would particularly thank Patricia Segonds for helping me not only to analyse but also to understand the nonlinear properties of my crystals and for revising the nonlinear characterization section included in this thesis. Also, I greatly appreciate the refinement of the single crystal structures made by Professor Xavier Solans at the University of Barcelona. Finally, I would thank Dr. Valentin Petrov for helping me in the laser operation measurements at the *Max-Born Institute of Nonlinear Optics and Ultrafast Spectroscopy*, for being always ready to give me advice on related topics and for revising the sections of the thesis related to them.

I would acknowledge John Bates, who has read this entire thesis except this part, for the effort to correct the language in a record time.

I thank to my wonderful best friends Sandra, Gerard and Franc for their never-ending support and for listening to me even though they were not sure of what I

was doing. Also, I thank to my best friends from the university course, Maria and Patri, for understanding and encouraging me to follow in research.

Most of all, I am deeply grateful to my parents, Francesc Parreu and Mª Pilar Alberich, for showing me to struggle for what I want and being humble enough to have always the need to learn more. To my sisters, Ariadna and Pili, simply for being like they are, to their partners, David and Ferran, for bearing and loving them, and to my dogs, Plató and Bita, for always relaxing me. In addition, I want to thank Helena for helping me on any matter if possible at all and Nuria for showing always great love for me and revising the language of this part of the thesis. Finally, I sincerely thank my husband Lluis Blasco who is also my best friend and my best fan and who has given me the best possible support during the thesis, especially this last year, listening to me, encouraging me and sharing his life with me. I would like to dedicate this thesis especially to him.

To Lluis and to my close family
with great love

List of publications

This doctoral thesis is partially based on the work contained in the following papers, referred to by roman numerals in the text:

Paper I: I. Parreu, R. Solé, Jna. Gavaldà, J. Massons, F. Díaz, M. Aguiló, "Crystal growth, structural characterization, and linear thermal evolution of $KGd(PO_3)_4$", *Chem. Mater.* **2005**, *17(4)*, 822

Paper II: I. Parreu, R. Solé, J. Massons, F. Díaz, M. Aguiló, "Crystal growth and characterization of type III ytterbium-doped $KGd(PO_3)_4$: a new nonlinear laser host", *submitted to Chem. Mater.*

Paper III: I. Parreu, J. J. Carvajal, X. Solans, F. Díaz, M. Aguiló, "Crystal structure and optical characterization of pure and Nd-substituted type III $KGd(PO_3)_4$", *Chem. Mater.* **2006**, *18(1)*, 221

Paper IV: I. Parreu, R. Solé, Jna. Gavaldà, J. Massons, F. Díaz, M. Aguiló, "Crystallization region, crystal growth, and phase transitions of $KNd(PO_3)_4$", *Chem. Mater.* **2003**, *15(26)*, 5059

Paper V: I. Parreu, R. Solé, J. Massons, F. Díaz, M. Aguiló, "Crystal growth, crystal morphology and surface micromorphology of type III $KGd(PO_3)_4$ and $KNd(PO_3)_4$", *Cryst. Growth and Design (in press)*

Paper VI: I. Parreu, M .C. Pujol, F. Díaz, M. Aguiló, X. Mateos, V. Petrov, "Growth, spectroscopy and laser operation of Yb:$KGd(PO_3)_4$ single crystals", *Opt. Express (in press)*

Table of contents

Chapter 1: Introduction

In 1917, Albert Einstein[1] first theorized about the quantum basis of laser physics, the stimulation emission effect. In 1954, Charles Townes and Arthur Schalow created the first maser (microwave amplification by stimulated emission of radiation)[2]. In December 1958, the same authors reported the possibility of maser action in the infrared and visible spectrum, which Gordon Gould was later to refer to as laser (light amplification by stimulated emission of radiation)[3]. In 1960, Theodore Maiman created the first successful solid-state laser[4]. Pulsed laser emission was obtained by using high energy flashes to stimulate a synthetic ruby crystal ($Cr:Al_2O_3$). In the same year, Ali Javan created the first gas laser (He-Ne) which emitted a continuous beam after initiating the laser action by an electric discharge. The next 20 years were dominated by gas lasers even though first dye lasers and semi-conductor lasers were created in 1962 and 1963. In the mid-80s, cheap semi-conductor or diode lasers took over. Advances in diode lasers made a decisive contribution to the development of solid-state lasers (SSL).

1.1. Solid state lasers

A solid-state laser (SSL) is generally made up of three components: a solid active medium, a pump source to excite the gain medium, and a laser cavity or laser resonator in which the laser radiation circulates and pass through the gain medium to amplify the power of the emitted light.

Active medium

The active medium is composed by the host and the active ions, which are able to generate and amplify light. The host should be thermically and mechanically stable and transparent in both the absorption and emission wavelength ranges of the active ions. These active ions substitute some of the constitutive ions of the solid host, e.g. a crystal or a glass, either partially or totally. So, the host carry the active ions as impurities or dopants or even as stoichiometric elements. Lanthanide or transition-metal ions are the most used as laser-active ions whose light amplification have been proved in more than 500 active media.

Optical amplification takes place in an active medium as a result of the stimulated emission of additional photons. Electronic transitions of laser-active ions from an excited level to a lower level are induced by an input light with the appropriate frequency verifying the Bohr's relation, E_2-E_1=$h\nu$. Therefore, electrons must be previously transferred to the excited level by external pumping in order to invert the electronic population between the energy levels. The generation of this inverted population is highly dependent on the energy-level scheme of the active ion. Here, there is a distinction between the four-level and three-level active media.

In a four-level active medium, the lower laser level is quickly depopulated by non-radiative transitions e.g. multiphonon transitions, to lower lying levels. Thus, there can be no appreciable population in this level and reabsorption of the laser radiation is avoided. In a quasi-three-level active medium, the lower laser level is the ground level so the population can be appreciable in thermal equilibrium at

the operating temperature. Consequently, amplification is only possible above a particular threshold pump power, when the laser threshold has just been reached. Below the laser threshold, the excited ions return to the ground state by spontaneous emission. High-intensity sources are needed therefore to pump quasi-three-level active media and longer radiative lifetime of the fluorescent level to reach the population inversion. However, quasi-three-level active media present a small quantum defect because this scheme just enforces a small energy difference between the lower laser level and the ground state. The most prominent examples of such media are ytterbium-doped active media, neodymium-doped media, on the other hand, are four-level active media. The optical, spectroscopic, and laser properties of both ions in the $KGd(PO_3)_4$ host have been investigated in this thesis.

Pump source

Generally, solid-state lasers are optically pumped. From the mid-80s, the most efficient pump source is the diode laser. These lasers emit radiation at wavelengths that are close to the strong absorption bands of several active laser ions, so the diode pump output can lead to an efficient population inversion. This good spectral match improves the pumping efficiency and thus reduces the operating temperature of the laser, which alleviates the thermo-optical effects and leads to better beam quality. The fact that the pumping efficiency of diodes is higher than that of lamps led to the design of more efficient, simple, and compact SSL. Some very useful active media such as $Nd:Y_3Al_5O_{12}$ (YAG), $Nd:YVO_4$, or $Nd:LiYF_4$ (YLF) can be both lamp- and diode- pumped but they only rose to prominence with diode pumps. In spite of this, they continued to be lamp-pumped for a long time because the price per watt of generated pump power was cheaper than that of diode lasers. Both active ions studied in this thesis, ytterbium and neodymium, can be directly pumped with high-power diode lasers such as

InGaAs or AlGaAs, respectively. The InGaAs diodes are more robust than the AlGaAs ones.

However, diode lasers have a narrow tuning range. Broad band tunable laser operation can be reached using the Ti:sapphire laser as a continuous-wave (cw) pump source. Wavelengths can be tuned because the strong coupling between titanium and the sapphire host causes broad and widely separated absorption and fluorescence bands, which in turn means that titanium has a very large gain bandwidth. A very important application of this laser is the generation and amplification of femtosecond mode-locked pulses. Ti:sapphire was introduced[5] in 1986 and it quickly replaced most dye lasers which had dominated the ultrashort pulse generation field. Ti:sapphire is also suitable for pumping test setups of new SSL because it can be easily tuned to the required pump wavelength with a high pump brightness. This pump source has been used for the laser operation of ytterbium-doped $KGd(PO_3)_4$ in this thesis.

Laser cavity

The efficiency of the laser system heavily depends on the pumping efficiency. A laser resonator efficiently transfers radiation between the pump source and the active media. It also controls the pump density distribution in the active media and thus the uniformity, divergence, and optical distortions of the output laser beam. The design of the pump geometry plays an important role in the laser system to optimize the mode matching, that is the overlap between the pumped volume and the volume occupied by a low-order resonator mode. For low-power SSL pumped by a diode laser, the end-pumping geometry has become more common than face- or side-pumping geometries. In the end-pumping technique, pump radiation is introduced longitudinally to the active medium i.e. co-linear with the resonator axis, whereas in the side-pumping technique, it enters transverse to the resonator axis. However, there is an increasingly large number of cavity designs that has been employed in lasers such as Z-, X- or V-shaped

resonators in which the sample is placed under Brewster angle to avoid pump reflections. In this thesis, a Z-shaped cavity has been used for laser experiments.
The laser resonator requires mirrors in both sides: a high-reflective mirror (HR) in one of them and a partially transmissive output-coupler (OC) in the other. Output intensity will be maximum for a unique output-coupler reflectivity. The design of the laser cavity - basically comprising optical elements, angles of incidence, and the distance between components - determines the cavity modes, which can be longitudinal or transverse at resonance frequencies.
The gain in a laser is basically determined by the active medium and the optical pump source. As far as the active medium is concerned, the laser gain is directly related to the absorption and emission cross-sections and to the population inversion, thus to the inversion dependent gain cross section. The spectral match with the pump source determines the population inversion besides the fluorescent level lifetime.

1.2. Bifunctional nonlinear and laser materials. The self-frequency doubling (SFD)

Since 1960, when Maiman[4] demonstrated the first SSL, the importance of lasers has increased dramatically and they are now used not only in science but also in society. Lasers emitting at wavelengths ranging from the ultraviolet to the infrared are needed for the huge variety of new applications that have emerged since then. By the late 70s and early 80s the interest was mainly focused on developing powerful and compact sources of blue and green light.
The development of SSL together with the improvement in nonlinear optical materials opened up the possibility of applying the second-harmonic generation to the infrared outputs of the diode-pumped SSL. In 1988, the interest in this type of configuration increased after demonstrations[6] of compact green-sources based on intracavity frequency doubling of diode-pumped neodymium lasers.

One alternative to this are upconversion lasers in which the pump wavelength can be longer than the lasing wavelength (i.e. infrared light can be used to directly pump a green laser). Upconversion was first demonstrated[7] in 1971 but was not focused on until 1986, by which time efficient diode-pumping was reached. Bulk crystals were the first to be developed followed by optical fibres [8,9].

Solid-state laser sources in the visible spectral region play an important role in laser technology because they are potentially interesting for numerous applications such as high-density optical data storage[10,11], reprographics[12], colour displays[13], medicine, biotechnology[14,15], submarine communications[16], transparent atmosphere applications, etc.[17]

As stated above, such laser sources can be managed from either upconversion or frequency conversion by nonlinear optical processes such as frequency doubling and sum-frequency mixing. Promising investigations into second-harmonic generation by phase-matching in nonlinear crystals have increased the interest in this latter kind of design[18]. Harmonic generation is one of the main nonlinear optical effects, first observed by Franklen in 1961[19]. Nonlinear optical interactions can be only generated when the intensity of the applied electric field is high enough (i.e. a laser beam). Hence, nonlinear optics and laser spectroscopy are necessarily related. Why not combine them?

Bifunctional optical and laser materials, in which the nonlinear optical process and the laser effect occur simultaneously, are very promising for such compact laser designs because solid-state lasers operate mainly in the infrared. Such self-frequency doubling (SFD) lasers involve fewer losses (absorption, refection and scattering) than the intracavity frequency doubling lasers, which means that resonator designs are simpler and more compact[20].

The first SFD lasers were Tm:$LiNbO_3$[21] and Nd:$LiNbO_3$:MgO[22] and today these systems are efficient and can be diode pumped. As a rule, if a nonlinear optical crystal is to be used as a SFD laser it must (i) accept fluorescent ion doping

(usually neodymium or ytterbium) and (ii) be phase-matchable for its laser emission. The potentiality of these crystals relies on a strong and wide pump absorption bandwidth as well as on a relative gain cross-section. The crystal should also be transparent in the infrared and second harmonic generated wavelength ranges, to prevent re-absorption losses. So far, only a few noncentrosymmetric crystals satisfy all these requirements and they are mainly doped with neodymium[23]. Nonlinear optical crystals with suitable sites for Nd^{3+} ions can combine the 1μm infrared laser emission ($^4F_{3/2} \rightarrow {}^4I_{11/2}$) with the second-harmonic generation properties of the host to produce green laser radiation by self-frequency doubling. The main results of Nd-doped SFD lasers that have been described recently by Brenier in ref. 23 and they are reprinted below in Table 1.1.

Table 1.1. Main results of Nd-doped SFD lasers (*reprinted from Brenier, ref. 23*)

Crystal	Input (mW)	Output (mW)	Pumping	Reference
$LiNbO_3$:MgO	215	1	Dye	Fan,1986[24]
$YAl_3(BO_3)_4$	870	10	D/CW	Schütz,1990[25]
$YAl_3(BO_3)_4$	280	3	D/CW	Wang,1991[26]
$YAl_3(BO_3)_4$	400	69	D/CW	Amano,1991[27]
$YAl_3(BO_3)_4$	1380	51	D/CW	Hemmati,1992[28]
$YAl_3(BO_3)_4$	369	35	D/CW	Qui,1993[29]
$LiNbO_3$:MgO	850	18	Dye	Li,1993[30]
$LiNbO_3$:Sc_2O_3	65	0.14	TS/QCW	Yamamoto,1994[31]
$LiNbO_3$:MgO	100	0.2	D/QCW	Ishibashi,1996[32]
$YAl_3(BO_3)_4$	1600	225	D/CW	Bartschke,1997[33]
$YAl_3(BO_3)_4$	2200	450	TS/CW	Bartschke,1997[33]
$LaBGeO_5$	600	0.09	TS/CW	Capmany,1999[34]
Nd,Lu:YAB	880	24	D/CW	Dekker,1998[35]
$LiNbO_3$:Zn	430	0.65	TS/CW	Capmany,1999[36]
$Ba_2NaNb_5O_{15}$	270	46	TS/CW	Kaminskii,1999[37]
$YCa_4O(BO_3)_3$	900	62	D/CW	Einchenholtz,1999[38]
$GdCa_4O(BO_3)_3$	1600	192	TS/CW	Zhang,1999[39]
$GdCa_4O(BO_3)_3$	1250	115	D/CW	Augé,1999[40]

Results are best with $YAl_3(BO_3)_4$ (YAB) and those of $GdCa_4O(BO_3)_3$ (GdCOB) and $YCa_4O(BO_3)_3$ (YCOB) remain below. $Ba_2NaNb_5O_{15}$ (BNN) remains in a good position. The SFD power extracted from $LiNbO_3$ (LNB) and $LaBGeO_5$ (LBG) is much weaker.

The ytterbium ion is an interesting alternative to neodymium in the same wavelength range near 1 μm ($^2F_{5/2} \rightarrow {}^2F_{7/2}$) while the second harmonic is also in the green region. It has several important advantages[41,42,43,44].

The simple two-manifold energy level scheme of ytterbium excludes a number of competitive processes such as excited-state absorption (ESA), upconversion and cross relaxation, which can depopulate the upper laser level and hence reduce the laser efficiency. The small Stokes shift between absorption and emission (i.e. the small quantum defect) reduces the thermal load and leads to efficient operation at high powers. The ytterbium ion possesses higher energy-storage capability because the radiative lifetime of the upper laser manifold is substantially longer than that of the neodymium ion. Moreover, the pump band of ytterbium is well matched for diode pumping near 980 nm such as with high-power InGaAs diode lasers. Finally, ytterbium has no bands in the green region, so the inevitable reabsorption losses of neodymium in the wavelength range of the second harmonic can be avoided. The introduction of ytterbium into the nonlinear host is favoured by the fact that the ionic radius of ytterbium is smaller than that of neodymium and other rare-earth ions, so doping levels can be high. The ytterbium ion also has also some disadvantages as a result of the quasi-three level scheme: higher threshold, reabsorption loses and temperature related defects[45]. However, the advantages of ytterbium outweigh the disadvantages[46,47].

Recently, highly efficient laser operation in some nonlinear crystals doped with ytterbium has been reported[48,49,50,51,52,53,54] and even a better laser efficiency than ever reported for a Nd-doped SFD laser[45]. In all cases, the intensity of the

generated green light is quadratically dependent on the incident infrared pumping light. Table 1.2 shows the main results of Yb-doped SFD lasers.

The very low green output power of Yb:GdCOB may be caused by its broad emission spectra[54,55]. The results are best with YYAB, which can produce record CW green powers of 1.1 W.

Table 1.2. Main results of Yb-doped SFD lasers

Crystal	Input (mW)	Output (mW)	Pumping	Reference
$LiNbO_3$:MgO	101	30	TS/CW	Montoya,1999[45]
$GdCa_4O(BO_3)_3$	600	180	D/CW	Augue,1999[56]
$YCa_4O(BO_3)_3$	3800	245	HBMLS*	Richardson,2000[20]
$YAl_3(BO_3)_4$	220	1	D/CW	Wang,2000[57]
$YAl_3(BO_3)_4$	160	1.4	D/CW	Wang,2000[58]
$LiNbO_3$:MgO	421	58	TS/CW	Montoya,2000[59]
$YAl_3(BO_3)_4$	11000	1100	D/CW	Jiang,2001[60]
$YAl_3(BO_3)_4$	11000	1100	D/CW	Dekker,2001[61]
$YCa_4O(BO_3)_3$	---	1	TS/CW	Aron,2001[62]
$GdCa_4O(BO_3)_3$	1200	0.15	DCW	Zhang,2001[63]
$YAl_3(BO_3)_4$	---	1	D/CW	Burns,2002[64]
$YAl_3(BO_3)_4$	---	270	D/CW	Lederer,2002[65]
$YAl_3(BO_3)_4$	11100	65	TS/CW	Dekker,2003[66]
$LiNbO_3$:MgO	900	58	TS/CW	Bausá,2004[67]

(*) HBMLS: high-brightness multi-laser source

1.3. Structural framework of $KGd(PO_3)_4$

$KGd(PO_3)_4$ (KGP) belongs to the wide and versatile family of condensed phosphates[68].Though this class of phosphates has been widely studied because of its range of applications, even today it is relatively poorly understood. Corbridge wrote that the word phosphates must apply to any compound in which the phosphorus atoms are surrounded by a tetrahedron of four oxygen atoms[69]. Hence, condensed phosphates are various phosphoric anions built from corner-sharing PO_4 tetrahedra in which the O/P ratio is from 5/2 to 4. The simplest

process by which condensed phosphates can be obtained is the reorganization of monohydrogenmonophosphate (HPO_4) molecules after water elimination. The condensation phenomenon can generate numerous phosphoric anions with three very different types of geometries. A linear linkage of PO_4 tetrahedra that shares two of their oxygen atoms leading to long-chains; a cyclic linkage that also shares two of their oxygen atoms and leading to rings; and some PO_4 tetrahedra that share three of their oxygen atoms leading to various possible geometries such as infinite ribbons or layers or three-dimensional networks. These are called long-chain polyphosphates, cyclophosphates, and ultraphosphates, respectively. Surprising though it may seem, it is now well recognized that any classification of condensed phosphates must be based on the geometry of the ions rather than on chemistry. Therefore, the nomenclature used for condensed phosphates over the years has often been very confusing.

$KGd(PO_3)_4$ belongs to the wide family of condensed phosphates, more specifically to the class of double phosphates of alkali and lanthanide ions with the general formula $M^{I}Ln^{III}(PO_3)_4$. Compounds of this type can be either double polyphosphates, the phosphoric anions of which have a long-chain geometry, $M^{I}Ln^{III}(PO_3)_4$, or cyclotetraphosphates, the phosphoric anions of which have a cycling geometry, $M^{I}Ln^{III}P_4O_{12}$.

Most of the literature dealing with double phosphates was rather confusing for a long time but it is currently well established that they can be classified into ten structural types.

Palkina et al. first proposed the classification in 1981[70]. The six structural types of polyphosphates were denoted by roman numerals (I-VI) and the three cyclophosphates by Latin letters (A-C). Palkina noted that the nine structural types probably did not exhaust the whole diversity of double phosphates of alkali and lanthanide ions and, as new compounds were synthesized and studied, the

list would be extended. However, up to now, only one more type has been added: the seventh structural type of polyphosphates (VII)[71,78].

Table 1.3 shows the main structural features of each of these ten structural types. Soviet and Tunisian researchers discovered most of these double phosphates during investigations into numerous M_2O-Ln_2O_3-P_2O_5 systems. Whereas the Soviets used flux methods, the Tunisians systematically produced the MPO_3-$Ln(PO_3)_3$ phase-equilibrium diagrams.

Table 1.3. Main structural features of double polyphosphates and cyclophosphates

Type	Space group	Z	Geometry	c.n.(M^I)	c.n.(Ln^{III})	Ref.
I	$I2/c$	4	$(PO_3)_4$	4	8	[72]
II	$P2_1/n$	4	$(PO_3)_4$	7	8	[73]
III	$P2_1$	2	$(PO_3)_4$	8	8	[74]
IV	$P2_1/n$	4	$(PO_3)_4$	10	8	[75]
V	$P2_1/n$	4	$(PO_3)_4$	8	7	[76]
VI	$P2_1$	4	$(PO_3)_4$	8	8	[77]
VII	$C222_1$	8	$(PO_3)_4$	8	9	[78]
A	$B2/b$	4	(P_4O_{12})	8	8	[79]
B	$C2/c$	4	(P_4O_{12})	8	8	[80]
C	$I\bar{4}\,3d$	12	(P_4O_{12})	9	8	[81]

Table 1.4 shows how the structural types are distributed among the series of double phosphates of lanthanide and the alkali ions Li, Na, K, Rb, and Cs. This table includes the classification first made by Palkina in ref. 70, which was later updated by Durif in ref. 68 and by us in our exhaustive review of the literature.

Some of these compounds are polymorphic because of the versatility of the condensation process. The number of polymorphs seems to increase as the ionic radius of the alkali ion also increases. Moreover, the structure is highly dependent not only on the size of this ion, but also on the size of the lanthanide. When the alkali ion remains constant, there are two groups throughout the lanthanide series, one of ions belonging to the first part and another of ions belonging to the

second part. Since the gadolinium ion is placed just in the middle of the series, it can have structural types that have characteristics of both parts. Palkina[70] has already suggested two structural types for the double phosphate of potassium and gadolinium: type III-$KGd(PO_3)_4$ and type A-$KGdP_4O_{12}$. The crystal structures of type III (see *paper III*) and type A[82] have recently been solved by single-crystal diffraction analysis. Both structural types are characteristic of the first part of the lanthanide series. Structural type IV, typical of the second part of the series, has been reported recently and its crystal structure solved[83].

During the synthesis and subsequent structural characterization of the double phosphate of potassium and gadolinium, the first two polymorphs will often appear.

Table 1.4. Distribution of structural types of double phosphates among lanthanide series and alkali metals

	La	Ce	Pr	Nd	Sm	Eu	Gd	Tb	Dy	Ho	Er	Tm	Yb	Lu
Li	I	I	I	I	I	I	I	I	I	I	I	I	I	I
Na	II	II	II	II	II	II	II	II	II	II	II			
K	III	III	III	III	III	III	III	III	III	III	III			
							IV			IV	IV	IV	IV	IV
										V		V	V	V
											VII			
	A	A	A	A	A	A	A	A	A	A	A			
Rb		IV		IV	IV	IV	IV	IV	IV	IV	IV	IV	IV	IV
	VI		VI	VI	VI	VI	VI	VI	VI	VI	VI			
	C		A	A	A	A	A							
			B	B	B	B	B							
Cs	IV		IV	IV	IV	IV	IV	IV	IV	IV	IV	IV	IV	IV
	VI	VI	VI	VI	VI	VI	VI	VI	VI	VI	VI			
	C	C	C	C	C									

The aim of the doctoral thesis

As stated above, solid-state lasers are part of everyday life. New SSL are continually being developed to be used in new applications and to improve existing ones. Therefore, the design and development of new promising materials does not stop.

In the mid 70s, the miniaturization of neodymium laser sources for optical fiber communications was of considerable interest because of the lower dispersion of silica at the neodymium emissions of 1.05 and 1.32 μm[84]. Stoichiometric laser materials of neodymium are very attractive for this purpose. Several of them were developed and were largely shown to have LED-pumped cw laser action. The most prominent were NdP_5O_{14}[85,86,87], and $LiNd(PO_3)_4$[88,89,90,91] but also $NaNd(PO_3)_4$[92], and $KNd(PO_3)_4$[93] were also reported to be promising. $KNd(PO_3)_4$ (KNP) has the advantage that it is noncentrosymmetric (Table 1.3 and 1.4) so it can be regarded as a highly Nd-doped self-frequency doubling crystal. In fact, the nonlinear optical properties of $KNd(PO_3)_4$, theoretically predicted from its structural data, showed that it is a promising SFD crystal[94]. However, the spectroscopic related problems of the neodymium ion could be aggravated by its high concentration in the structure. We attempt, therefore, to reduce the doping level in the host to reduce concentration-quenching effects. A good alternative should be to replace neodymium with ytterbium, the benefits of which are extensively explained in Section 1.2 of this introduction. It should also be pointed out that the stoichiometric $KYb(PO_3)_4$ does not crystallize as type III but as type IV and V, which are both centrosymmetric (Tables 1.3 and 1.4).

Taking all these aspects into account, we propose the isostructural $KGd(PO_3)_4$ (KGP) as a solid-state laser host to be doped with either ytterbium or neodymium. $KGd(PO_3)_4$ should maintain all the good properties of $KNd(PO_3)_4$ and because of the high capacity of the gadolinium ion to be substituted by any

other lanthanide ion, it should easily doped with ytterbium and neodymium or even by any other lanthanide ion.

Thus, the aim of the doctoral thesis is to synthesize and characterize undoped type III $KGd(PO_3)_4$ crystals and ytterbium- and neodymium-doped type III $KGd(PO_3)_4$ crystals.

The method chosen to grow the crystals was the top seeded solution growth (TSSG)–slow cooling because of the incongruent melting of $KGd(PO_3)_4$. Despite of the high viscosity of the growth solution, we decided not to introduce a solvent to avoid impurities and crystals were grown in their self-flux. The crystallization region was determined for type III $KGd(PO_3)_4$, $Yb:KGd(PO_3)_4$, $Nd:KGd(PO_3)_4$ and $KNd(PO_3)_4$ in the ternary system of the corresponding oxides $(Ln_2O_3+Gd_2O_3)$-K_2O-P_2O_5, with $Ln=Yb^{3+}$ and Nd^{3+}.

To our knowledge, $KGd(PO_3)_4$ has never been previously reported, so we made structural characterizations of pure $KGd(PO_3)_4$ and Yb- and Nd-doped $KGd(PO_3)_4$. The literature dealing with the synthesis and structural characterization of the stoichiometric $KNd(PO_3)_4$ is rather poor and often confusing, as with other condensed phosphates, so we also included this crystal in our investigations.

If it is to be a potential SSL or a SFD laser, the crystal must fulfil some requirements, some of which have been mentioned above. Hence, it is necessary to characterize physically the crystals, maybe especially to determine the optical properties of the host. The spectroscopic properties of the lanthanide ion in the host must be also studied since the potentiality of the new laser directly depends on them. All these studies have been made here for the following isostructurals: $KGd(PO_3)_4$, $Yb:KGd(PO_3)_4$, $Nd: KGd(PO_3)_4$, and $KNd(PO_3)_4$.

Finally, we made a more in-depth study of ytterbium-doped $KGd(PO_3)_4$. Lasing experiments have been done and laser action has been achieved in this material for the first time.

Chapter 2: Experimental techniques and methodologies

In this chapter, we summarise the main experimental techniques used in the thesis. We give a brief description of the theoretical fundamentals and the procedure related to each technique. The experimental equipment is described in detail and schematic views and illustrations of some of the systems we used are included.

The experimental techniques described are available at the Universitat Rovira i Virgili, the Universitat de Barcelona, the Universitat Autonoma de, the Université Joseph Fourier (Laboratoire de Spectrométrie Physique) and the CNRS (Laboratoire de Crystallographie) in Grenoble, and the Max-Born Institute for Non-linear Optics and Ultrafast Spectroscopy in Berlin.

2.1. Ternary phase diagram. Determination of the crystallization region

The first step for growing a new crystal is to choose the suitable growth method to use. As $KGd(PO_3)_4$ melts incongruently, a flux method has to be used. Flux methods enable to grow crystals that cannot grow from their stoichiometric melts because they melt incongruently or undergo a phase transition before melting. From the flux, which contains the components of the final desired material dissolved in a solvent, crystals can grow below the melting temperature.

The flux compositions solute/solvent from which the material crystallizes as the desired single phase has to be determined. The process consists in growing small crystals at different flux compositions and determining later their crystalline phase. So, as we decided to grow $KGd(PO_3)_4$ crystals from its self-flux, the crystallization region of type III $KGd(PO_3)_4$ in the ternary system of the corresponding oxides Gd_2O_3-K_2O-P_2O_5 was determined. Variations of this region introduced by doping were also analyzed. We determined therefore the type III $KGd(PO_3)_4$ crystallization of Yb:$KGd(PO_3)_4$, Nd:$KGd(PO_3)_4$ and $KNd(PO_3)_4$ in the ternary system of the corresponding oxides Ln_2O_3-K_2O-P_2O_5, with Ln=Yb^{3+} and Nd^{3+}.

To perform the experiments, a vertical tubular furnace heated by a Kantal AF resistance heating wire was used. The whole system was thermically insulated using thermal wool and an external steel cover. The temperature in the furnace was measured with an S-type thermocouple Pt/Pt-Rh 10% placed near the resistances in the central zone to guarantee a reliable and stable measurement. We controlled the temperature using a Eurotherm 818 P controller/programmer depending on the cooling program used. It was connected to a thyristor that controls the power of the furnace.

Around 20 g of solution were prepared mixing the desired ratios of the corresponding oxides, Ln_2O_3, K_2O, and P_2O_5, with Ln=Gd^{3+}, Yb^{3+}, or Nd^{3+}, using an excess of phosphorous and potassium oxides as a solvent. The solution

was homogenised at 50-100 K above the crystallization temperature, which was accurately determined by observing the growth or dissolution of small crystals freely nucleated on the solution surface or on an immersed platinum wire. From the crystallization temperature, a typical slow cooling program of 1 or 0.5 K/h, depending on the material, was applied to a final temperature of around 25 K below. The crystals were grown on a platinum disk with a constant rotation of 45 rpm, which was kept in contact with the solution surface. The axial gradient in the crucible was rather high, 10 K/mm, to enhance the mass transport in the solution and to the disk by free convection because the flux was very viscous.

The small crystals obtained were cleaned with water and identified by direct observation of their shape by optical microscopy. To determine the phase crystallized, the crystals were analysed by X-ray powder diffraction technique.

2.2. Characterization of the growth solution

High-temperature growth techniques are related with the thermofluodynamics of the liquid phase. The quality of the single crystals heavily depends on whether the flow mechanisms coexisting in solution are free or forced convection and thermocapillarity[95]. Thus, the thermal dependence of some physical properties of the solution such as density, viscosity, and surface tension needs to be determined if the thermohydrodynamical conditions of the crystal growth process are to be optimized[96].

To measure the density, viscosity, and surface tension of the growth solution under controlled and reproducible conditions, we developed a polyvalent device and specific experimental methodologies, which allow us to work in a wide range of temperatures. The reliability of the measurements and the calibration of the equipment were determined using as a standard some liquids whose physical properties were known. Figure 2.1 shows the experimental equipment used in the thesis and which is available from the FiCMA (*Física i Cristal·lografia de Materials*)

group of the Universitat Rovira i Virgili. It consists of a thermal subsystem and a mechanical subsystem.

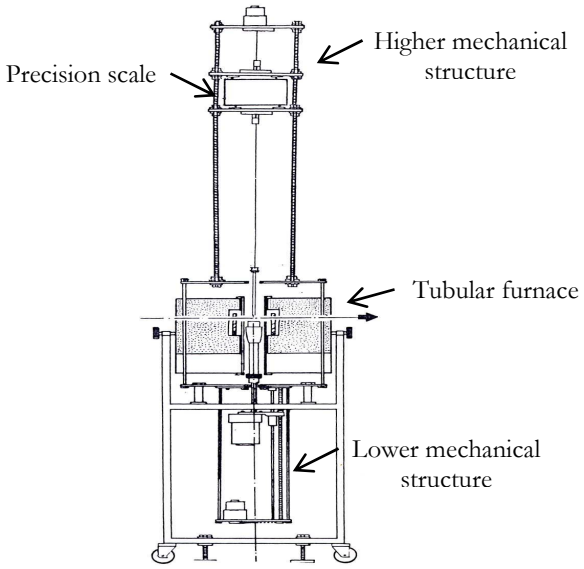

Figure 2.1. Schematic of the experimental device used in viscosity, density, and surface tension measurements

The thermal subsystem includes a tubular furnace heated by Kantal AF resistance heating wire of 1 mm in diameter rolled on an alumina tube. The temperature is measured with an S-type thermocouple (Pt/Pt - Rh 10%) and controlled by a Eurotherm 818 P (± 0.1 ºC) controller/programmer connected to a thyristor.

The mechanical subsystem has two structures placed under and above the furnace. They allow the crucible to move axially and the various immersors used as sensors for the measurements (Figure 2.2) to move axially and rotationally.

To measure the density and the viscosity we used the spherical immersors that are made of Pt/Pt-Rh 10%. They are 10 mm and 12 mm in diameter, and weigh 11.3192 and 18.1110 g, respectively. The open cylindrical immersor was used to measure the surface tension. It is 15 mm long and 16 mm in diameter, weighs 4.8802 g, and is made of 0.25 mm-thick walls of Pt/Pt-Rh 10%.

Figure 2.2. Pt/Pt-Rh 10% immersors used as sensors for density, viscosity, and surface tension measurements

The main part of the lower mechanical structure is a platform, which contains the held axis of the crucible. The platform can be automatically raised or lowered with an asynchronous-reduction combined engine attached to the base of the structure. The upper mechanical structure works in the same way as the lower one but, in this case, on the platform there are either a Mettler PM 200 precision scales with 1 mg of sensitivity, used to determine the density or the surface tension, or a torsion wire to determine the viscosity. Specific software was designed to digitalize the acquisition of the output scales data. The frequency of the digital lecture in all experimental determinations was fixed at 1 Hz.

The symmetry axes of the lower and upper mechanical structures and the axis of the useful thermal area inside the furnace are aligned to coincide with the vertical axis of the whole device.

Before making any measurements, the useful thermal area of the furnace must be thermally characterized using previously calibrated thermocouples. The axial gradient must be low around the centre of the thermal area. The solution contained in the crucible and placed in this region will be thermally stable during the measurements, which were made in a temperature range that was always above the crystallization temperature to prevent the nucleation of small crystals on the solution surface. For the same reason, the immersor was kept above the solution surface for about two hours before the measurements to reach the thermal equilibrium between the immersor and the solution surface.

2.2.1. Density

To determine the density of the solution from which $KGd(PO_3)_4$ single crystals were grown, we used the Archimedean method, which determines the apparent weight of an immersor submerged in a solution. We digitally recorded the apparent weight of a spherical immersor submerged in the solution and suspended from the scales on the platform of the upper mechanical system. The difference between the immersor weight in air and in solution is due to the Archimedean buoyancy. However, the wire where the immersor is suspended undergoes some residual effects because of the surface tension, air friction and the buoyancy on the part that is submerged.

Consequently, the apparent weight of the suspended wire-spherical immersor system can be calculated with the expression:

$$W_{ap} = W - V_0\delta(T)g(\rho_{sol} - \rho_{air}) + \tau + F - l_b \qquad \text{eq. 2.1}$$

where, W_{ap} and W are the immersor weights in the solution and in air, respectively; V_0 is the immersor volume at room temperature (T_0); $\delta(T)$ is a correction factor of the immersor dilation at the working temperature (T); ρ_{sol} and ρ_{sair} are the solution and air densities, respectively; τ is the vertical component of the surface tension in the meniscus of the suspended wire; F is the vertical component of the friction between the suspended wire and the ascending hot air; and l_b is the buoyancy exerted on the submerged part of the suspended wire.

Using two spherical immersors of different diameters, 10 and 12 mm (Figure 2.2), suspended on an identical wire, the correction factors τ, F, and l_b, can be eliminated because they are the same for both of them.

Thus, using the previous expression for the bigger immersor (2) and the smaller one (1), the analytical expression of the density is finally:

$$\rho_{sol} = \rho_{air} + \rho_{sol} = \rho_{air} + \frac{(W_2 - W_1) - (W_{ap2} - W_{ap1})}{(V_2 - V_1)\delta(T)g} \qquad \text{eq. 2.2}$$

The correction factor of the immersor dilation at the working temperature $\delta(T)$ is defined as:

$$\delta(\Gamma) = e^{\int_{T_0}^{T} 3\alpha(T)dt} \qquad \text{eq. 2.3}$$

taking into account that the volumical thermal expansion coefficient (α_v) is three times the lineal one (α), which in the case of platinum corresponds to

$$\alpha(T) = 8.88 \cdot 10^{-6} + 1.28 \cdot 10^{-9} T + 4 \cdot 10^{-14} T^2 \qquad \text{eq. 2.4}$$

where T is the working temperature (K).

To control the submersion depth, the position of the free surface of the solution was accurately determined by measuring the immersor weight. Because of surface tension effects, the immersor weight undergoes a drastic discontinuity just at the moment of contact between the immersor and the solution surface.

2.2.2. Viscosity

Accurately measuring the viscosity of solutions at high temperatures with sufficient accuracy is a difficult challenge. Of the various methods for measuring the viscosity of high-temperature solutions, we chose the torsion pendulum method[97,98], which is based on the logarithmic decrement of damping caused by the friction in the melt.

Thus, the viscosity of the growth solution was measured by determining the oscillatory motion of the pendulum, made up of the small spherical immersor (10 mm) hung from a tungsten wire. To make more precise measurements, the pendulum oscillations were transported to a graduate pattern with the aid of a laser beam and a reflector system placed on the axial plane of the pendulum. The immersor was totally submerged in the solution to a depth that fulfilled the geometrical condition that the distance between the crucible base and the lower part of the sphere and between the free surface and the upper part of the sphere was the same. Then, a torque was applied to excite the torsion of the pendulum

system. When the torque of the torsion wire compensates the viscous pair, the pendulum system oscillates.

The dynamic viscosity *(μ)* can be obtained from the expression of the cinematic viscosity *(ν)*:

$$\nu = \frac{\mu}{\rho} = Cd^k \qquad \text{eq. 2.5}$$

where ρ is the solution density; *C* and *k* are apparatus constants; and *d* is the logarithmic decrement, which is calculated from the logarithmic slope of the angular amplitude of oscillation versus the number of oscillations.

Note that the solution density needs to be known. To evaluate the apparatus constants, *C* and *k*, the whole system was calibrated by measuring the logarithmic decrement of at least two several Newtonian liquids of dynamic viscosities of 0.0992, 0.928 and 1.7596 Pa·s (or 99.2, 925 and 1759.6 Cp) at room temperature.

2.2.3. Surface tension

The surface tension is measures by determining the maximum traction applied on the open cylindrical immersor (Figure 2.2) just at the moment when the surface film of the solution is going to break. This method can be called as the open cylinder method[99,100,101]. The analytical expression for the surface tension *(σ)* is:

$$\sigma = \beta \frac{W_{\max}}{4\pi R\lambda(T)} \qquad \text{eq. 2.6}$$

where W_{max} is the maximum traction applied; *R* is the average cylinder radius; $\lambda(T)$ is a correction factor of the immersor dilation at the working temperature; and β is a correction factor of the effects of the cylinder walls (Verschaffelt correction)[101], which is expressed as:

$$\beta = 1 - \frac{2.8284\delta}{\sqrt{h}R} - \frac{0.6095\delta}{R} - \frac{3\delta^2}{R\sqrt{h}R} - \frac{0.371\delta^2}{R^2} \qquad \text{eq. 2.7}$$

where 2δ is the thickness of the cylinder walls and $h = \frac{W_{\max}}{\pi R^2 \rho_{sol} g}$ eq. 2.8

Note that the solution density also needs to be known.

The correction factor $\lambda(T)$ for the linear thermal expansion of the cylinder walls is calculated using the expression

$$\lambda(T) = e^{\int_{T_0}^{T} \alpha(T)dt} \quad \text{eq. 2.9}$$

To determine accurately the value of W_{max}, the free solution surface is determined by the discontinuity of the immersor weight, as in the case of density measurements. We measured the cylinder weight while it was being extracted from the solution. The extraction velocity was set at 1 cm per minute to ensure that the geometrical shape of the solution film adhered to the cylinder base. During a typical extraction, the cylinder weight initially increases to a maximum value because the adhered film increased to a maximum length. Then, when the film breaks, it drops sharply to a stable value when the immersor is totally separated from the solution surface. The W_{max} value was then determined from the maximum weight recorded just before the separation.

2.3. Crystal growth: the top-seeded solution growth-slow cooling method

The top seeded solution growth (TSSG) technique is a flux growth technique commonly used to growth crystals from high temperature solutions. In TSSG, crystals are completely submerged in the flux, which allows the crystal facets to grow freely. The crystal begins to grow on a crystalline seed in contact with the solution surface, which should be placed at the coldest point of the solution to avoid secondary nucleation. The growth starts when the solution becomes supersaturated. To reach this situation, we slowly cool the solution from its crystallization temperature, which is previously accurately determined by observing the growth or dissolution of the crystalline seed in contact with the

solution surface. While the solution temperature decreases steadily, the crystal continues to grow. The top seeded solution growth-slow cooling (TSSG-SC) technique enables bulk single crystals of a few millimetres to be grown free of macroscopic defects. The convection flow in the solution must be good in order to obtain macrodefect-free crystals since this is what determines the shape and stability of the crystal-solution interface[95,102]. The free convection flow caused by the axial temperature gradient in the solution is compensated by the forced convection flow generated by the seed/crystal rotation. To avoid flux inhomogeneities or asymmetrical flow rates, the direction of rotation should be periodically reversed[103].

Figure 2.3 schematically shows the vertical tubular furnace that we use at the FiCMA to grow single crystals of $KGd(PO_3)_4$ (see *paper I*), $Yb:KGd(PO_3)_4$ (see *paper II*), $Nd:KGd(PO_3)_4$ (see *paper III*), and $KNd(PO_3)_4$ (see *paper IV*).

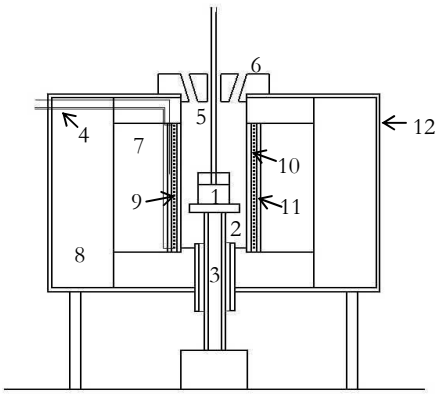

Figure 2.3. Scheme of the lateral section of a vertical tubular furnace

The furnace is heated using Kantal AF resistance-heating wire (1 mm in diameter) rolled into an alumina tube. The whole system is thermically insulated using thermal wool and an external steel cover. The temperature in the furnace is measured with an S-type thermocouple Pt/Pt-Rh 10% placed near the resistances in the central zone to guarantee a reliable and stable measurement. The

temperature is controlled by a Eurotherm 902 controller/programmer. It is connected to a thyristor that controls the power of the furnace.

To identify the best location of the crucible inside the furnace, both the axial and radial thermal gradients of the furnace must be determined. An alumina column, which supports the crucible, can be manually moved to place the crucible in the right position. The axial gradient inside the solution is also important and it is different from that of the empty furnace because of the crucible and the solution. Because the growth solution is very viscous, we used a rather high axial gradient inside the growth solution (see *papers I-IV*) to guarantee the convection flow.

The mechanical part of the growth device, placed above the furnace, supports, vertically displaces and rotates the crystalline seed. It compromises a vertical metal structure that is extremely rigid and stable from which an alumina rod is hung. The seed is attached to a platinum holder, which is also attached to the rod, both of which are laced with platinum wire. We used a holder equipped with a platinum turbine to increase the mass transport in the solution (see Figure 2 in *paper V*). To measure the position of the seed we used a Mitutoyo comparer to determine the crystallization temperature to an accuracy of 0.01 mm.

A platinum conical crucible of 125 cm^3 is used to hold the solution in the crystal growth experiments. The platinum melts at a temperature (2041.4 K) much higher than the crystallization temperature of our crystals and, in addition, it does not react with the oxides used as starting materials. In the experiments on preliminary crystal growth, 25 cm^3 conical or cylindrical crucibles were used. Consequently, a smaller furnace was used.

Around 200 or 20 g of solution, depending on the size of the crucible, was prepared by mixing the desired ratios of the corresponding oxides: Ln_2O_3, K_2O, and P_2O_5, with Ln=Gd^{3+}, Yb^{3+}, or Nd^{3+}. The crystals were grown from their self-flux using an excess of phosphorous and potassium oxides as a solvent. The solution was homogenised at 50-100 K above the crystallization temperature.

From the crystallization temperature, a slow cooling program from 1 to 0.02 K/h, depending on the material, was applied to a final temperature of around 20 K below. The crystal was then slowly extracted from the solution and slowly cooled to room temperature. The growth methodologies are extensively explained in *papers I-IV*.

2.4. Sample preparation: orientation, cutting and polishing

When anisotropic materials are being characterized, the samples must be appropriately prepared in order to evaluate each property as a function of their directions. The first step is to orientate the sample either along the crystallographic directions **a***, **b** and **c*** for structural, chemical, or mechanical studies; or along the principal optical axes $\boldsymbol{N}_p$, $\boldsymbol{N}_m$ and $\boldsymbol{N}_g$ for optical and spectroscopic studies.

The as-grown faces that appeared on the crystals are used as a reference to prepare the samples perpendicular to the **a***, **b** and **c*** directions. **a***- and **c***-oriented plates are prepared by cutting a slice of the desired thickness parallel to the (100) and (001) faces, respectively. To prepare **b**-oriented plates the crystal must be put on an aluminium holder cut at the right angle between the (011) and $(01\bar{1})$ faces (87º) and a plane normal to the [010] direction must be cut. The **b**-oriented slice is then cut parallel to this plane.

We verify the orientation of the **b**-oriented plates by texture analysis. These were made using a D5000 Siemens diffractometer with a Bragg-Brentano parafocusing geometry and a horizontal θ-2θ goniometer with an open Eulerian cradle, which is available at the *Servei de Recursos Científics i Tècnics* of the Universitat Rovira i Virgili. The samples are supported on a goniometric head in case disorientations are detected and need to be corrected by polishing.

We measure the pole figure of the (020) plane. A pole figure is a stereographic projection, with a specified orientation relative to the crystalline sample that

shows the variation of pole density with pole orientation for a selected set of crystal planes, which in our case are {020} . The orientation of the crystal plane of the sample is defined by three angles with respect to the diffraction plane: the Bragg diffraction angle *(θ)*, the rotation angle around the axis of the intersection between the sample and diffraction plane *(χ)*, and the rotation angle around the normal axis to the sample plane *(φ)*. In the measurements, the χ angle was increased from 0 to 5º with $\Delta\chi$ a of 0.5º and the φ angle was increased from 0 to 360º with a $\Delta\varphi$ of 3º and 3s of counting time for the 2θ angle corresponding to the diffraction of the (020) reflection (21.119º). Figure 2.4 plots the intensities recorded in a stereographic projection with level lines (pole figure) and the corresponding 2θ-scan at fixed χ and φ angles obtained from the pole figure.

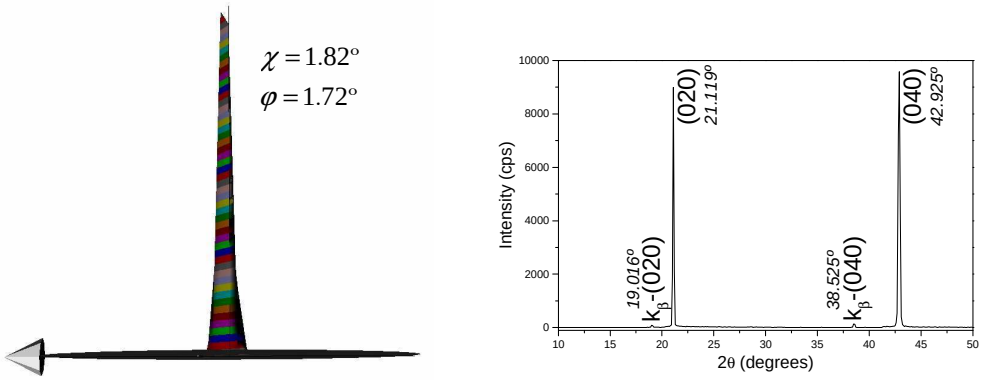

Figure 2.4. Pole figure corresponding to the (020) reflection with a 2θ=21.119º and 2θ-scan for (χ,φ)=1.82º, 1.72º

The procedure for preparing the samples oriented along the principal optical axes, $\boldsymbol{N}_p$, $\boldsymbol{N}_m$ and $\boldsymbol{N}_g$ is rather similar to the one for preparing **b**-oriented plates. Typical samples are plate- or cube-shaped. Cutting crystals as cubes saves crystals since the three axes are contained in a single sample. Therefore, we prepared

optically oriented cubes whether the crystal size and quality made it possible for us to do so.

The first step is to cut sample with planes normal to the $[010]$ and $[0\bar{1}0]$ directions and transform the crystal into a cube oriented along the crystallographic axes. The first plane is prepared exactly as a **b**-oriented plate though, in this case, no slices are cut. Its orientation is also verified by texture analysis and corrected, if necessary. The second plane is cut planoparallel to the first one. The parallelism between the opposite planes is measured with an autocollimator. The following step is to build a cube with planes normal to the principal optical axes instead of the crystallographic ones. As the $[010]$ direction coincides with one of the optical axes, $\boldsymbol{N}_p$, the (010) and $(0\bar{1}0)$ planes are not modified. A new plane normal to $\boldsymbol{N}_g$ is cut at a particular angle from the (001) face. This angle is 39.0º for $KGd(PO_3)_4$ and 37.6º for KNP (see *paper III*). Then, because the $\boldsymbol{N}_p$, $\boldsymbol{N}_m$ and $\boldsymbol{N}_g$ are orthogonal by definition, the plane normal to $\boldsymbol{N}_m$ is cut at 90º to the plane normal to $\boldsymbol{N}_g$. Finally, planoparallel planes to $\boldsymbol{N}_m$ and $\boldsymbol{N}_g$ are cut and their parallelism checked.

We used a diamond wire Logytech model 15 saw to cut the samples in order to avoid cleaving and fractures. We chose this technique because it induces less mechanical stress than other techniques such as the diamond disk saw. In spite of their considerable hardness (around 7 in the Mohs hardness scale) (see *paper V)*, this family of materials easily spilt up parallel to the (100) and (001) faces because of cleavage planes. For the same reason, the load applied to the sample during the cut was as minimal as it could be for the sample weight and the wire rotation velocity is kept rather high.

The samples were polished in a Logytech PM5 polisher with an oscillatory arm that enabled the samples to be rotated and pressurised according to their hardness. Depending on the quality that was required of the samples, alumina or diamond abrasive powders were used. The final quality of the polish was

measured with such parameters as roughness, flatness and parallelism. An average roughness value was obtained by a confocal microscope (see section 2.6.3). The flatness and parallelism were measured with the autocollimator.

All the samples were completely prepared at the FiCMA where the diamond wire and disk saws, the polisher, the confocal microscope and the autocollimator are available. Figure 2.5 shows some of the $KGd(PO_3)_4$ and $KNd(PO_3)_4$ prepared at the FiCMA such as plates, cubes or prisms oriented along the optical principal axes.

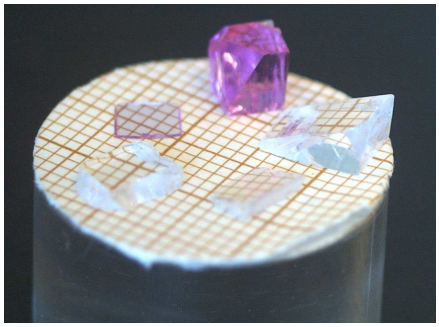

Figure 2.5. Typical $KGd(PO_3)_4$ and $KNd(PO_3)_4$ samples plate-, cube- and prism-shaped.

2.5. Concentration analysis of the dopant elements: electron probe microanalysis (EPMA)

The dopant concentration in the crystals was measured by electron probe microanalysis (EPMA) in a Cameca SX-50 microprobe analyzer available at the *Servei de Recursos Científico-Tècnics* of the Universitat de Barcelona.

This technique measures the characteristic X-rays emitted by the sample after they have been excited with a focused electron beam generated at an intensity of 30 nA at an accelerating voltage of 20kV. A wavelength-dispersive spectrometer (WDS) detects and characterizes these X-rays.

The most commonly used spectrometer crystals are: lithium fluoride 200 (LIF), pentaerythritol 002 (PET), thallium acid phthalate 1011 (TAP), and

PC1:W/simultilayered pseudo-crystal. These crystals cover the wavelength range from 1 to 24 Å. The chemical composition is determined by comparing the X-ray intensity of the sample with that of standard samples of known concentration. Table 2.1 summarizes the measurement conditions and the standards used, which are detailed in *papers II* and *III* and in Table 2.1.

Quantitative analysis requires the absorption, fluorescence and atomic number effects to be corrected, which we did with PAP[104].

Table 2.1. Measurement conditions used in EMPA analysis

Element	Line	Spectrometer crystals	Standard	Detection limit (%wt)	Experimental error (%)
P	K_α	PET	$KGd(PO_3)_4$	0.08	1
K	K_α	PET	$KGd(PO_3)_4$	0.05	1
Gd	L_α	LIF	$KGd(PO_3)_4$	0.03	1
Nd	L_α	LIF	ree4	0.04	2
Yb	L_α	LIF	$KYb(WO_4)_2$	0.03	3
O	K_α	PC1	$KGd(PO_3)_4$	0.24	1

*The integration time of the measurements is 10 s

To prepare the sample, a small piece of macrodefect-free crystal is put in a plastic cylindrical container and included in a polyester resin with its corresponding catalyst. After around 12 hours, the mixture is completely solidified. The solid sample is initially planed with a SiC disk and with distilled water as coolant. It is then polished with 3μm- and 1μm-diamond disks cooled with lubricant MGS. This preparation is made at the FiCMA using a Struers DAP-7 polisher, which allows the simultaneous and inverse rotation of the disk and the sample. The sample is finally cleaned with alcohol. Before the analysis, the sample must be coated with a fine layer of a conductor metal such as carbon or gold because of the low electric conduction of the crystals.

The experimental error *(ε)* of the measurements for all the elements analysed was determined using equation 2.12, particularly for those with low concentration:

$$\varepsilon = \sqrt{\frac{I_p/t_p + I_b/t_b}{(I_p - I_b)^2} + \frac{I_p^s/t_p^s + I_b^s/t_b^s}{(I_p^s - I_b^s)}} x100 \qquad \text{eq. 2.10}$$

where I_p and I_b are the intensities of the peak of the sample and the background of the sample (c/s), respectively; t_p and t_b are the is the integration times of the peak of the sample and the background of the sample (s); I_p^s and I_b^s are the intensities of the peak of the standard and the background of the standard (c/s); and t_p^s and t_b^s are the integration times of the peak of the standard and the background of the standard (s).

We also determined the detection limit of each analysed element with the expression:

$$DL = \left[\frac{C^s}{(I_p^s - I_b^s)}\right] 3\sqrt{2}\left(\frac{I_f}{t_b}\right)^2 \qquad \text{eq. 2.11}$$

where C^s is the concentration of the element in the standard (wt %).

2.6. X-ray diffraction techniques

In 1913, W. L. Bragg was the first to use the diffraction of X-rays by crystals to explore matter. He and his father earned the Nobel Prize for Physics in 1915 for their work published in an abridged form in *X-rays and Crystal Structure*[105]. Since then, X-ray diffraction has been used to go deeper into the molecular structure of all kinds of species in their monocrystalline or powder forms.

W. L. Bragg showed that the diffracted beam from a crystal behaves as if the radiation is scattered by individual atoms periodically aligned on planes acting as reflecting mirrors. The waves "reflected" by these lattice planes interfere constructively in accordance with Bragg's law:

$$n\lambda = 2d_{hkl}\sin(\theta) \qquad \text{eq. 2.12}$$

where $n\lambda$ is the path difference between waves scattered by adjacent lattice planes with equivalent indices; d_{hkl} is the spacing distance between to consecutive lattice planes, and θ is the incident angle of the X-ray beam[106].

2.6.1. X-ray powder diffraction

When the sample is a powdered crystalline specimen, many different tiny crystals are present simultaneously. Bragg's law will be fulfilled in some of crystallites, so the complete diffraction pattern will be observed for any orientation of the crystalline powder with respect to the X-ray beam[106].

Powder diffraction is an extremely powerful technique for identifying crystalline phases and analysing mixtures. It compares the recorded diffraction patterns with those compiled by the Joint committee for powder diffraction standards (JCPDS) [106]. This technique is also used to analyse how the cell parameters evolve as a function of the temperature, the pressure, or the dopant concentration, and to determine phase diagrams and phase transitions.

We used a Siemens D-5000 powder diffractometer with Bragg-Brentano parafocusing geometry and θ-θ configuration using a Cu source ($\lambda_{K\alpha}$=1.540560 Å) available at the *Servei de Recursos Científics i Tècnics* of the Universitat Rovira i Virgili. In this system, the source, the sample and the detector occupy three consecutive positions on a circumference. The source and the detector vary synchronously, always symmetrically and the sample is kept fixed. By varying the 2θ angle of the source and the detector, we can obtain a discrete pattern of the reflection for the families of planes parallel to the sample surface.

For thermal characterizations, the diffractometer is equipped with an Anton-Paar HTK10 camera with a platinum ribbon-heating holder. This is connected to a thermocouple and to a controller, which allows different heating/cooling programs (temperature ranges and velocities). We used a scintillation counter and a Braun position-sensitive detector (PSD) as detectors for the measurements.

Powder diffraction does not allow three-dimensional crystallographic information and solving structures is therefore very hard work. However, some methods give the possibility to precise cell-parameters, atomic coordinates, and temperature factors by adjusting parameters with an experimental powder diffraction pattern. We used the FULLPROF program[107] to refine the parameters with the Rietveld method[108].

2.6.2. X-ray texture diffraction

The orientation of a monocrystalline sample can be determined using X-ray texture diffraction[109]. To determine a *(hkl)* pole figure, the counter is fixed at the proper 2θ angle to receive the *hkl* reflection from the X-ray source and the sample is rotated on its own plane about an axis normal to its surface *(φ)* and about a horizontal axis *(χ)*. We used the Schulz reflection method[110], which enables to explore the central region of the pole figure. The horizontal axis lies in the sample surface and it is initially adjusted, by rotation about the diffractometer axis, to make equal angles with the incident and diffracted beams. Once it is done, no further rotation of the diffractometer axis is made. Since the horizontal axis remains in a fixed position during the other rotations of the sample, the irradiated sample surface is always tangent to a focusing circle passing through the X-ray source and the counter slit and the diffracted beam will converge to a focus at the counter.

The D5000 Siemens diffractometer available at the *Servei de Recursos Científics i Tècnics* of the Universitat Rovira i Virgili enables this kind of analysis since it has a Bragg-Brentano parafocusing geometry and a horizontal θ-2θ goniometer with an open Eulerian cradle. The diffractometer is fitted with an aperture slit close to the sample (70 mm long) and 0.03º receiving slit. The Ni-filtered Cu K_α radiation (30 mA, 40 kV) generated in a point focus Cu tube is detected by a scintillation counter.

2.6.3. X-ray single crystal diffraction

X-ray single crystal diffraction is still the method of choice for determining crystal structures. It is used to determine the basic geometry (the space group and the cell parameters) of the crystal, its structure and the position of the atoms in the lattice. The X-ray diffraction pattern of a single crystal is the sampling at the reciprocal lattice points of the contents of a single unit cell. Analysis of the diffraction angles produces an electron density map since the X-rays are diffracted by the electrons of the atoms. Whereas the spatial arrangement of the diffracted beams is determined by the geometry of the crystal lattice, the intensities are determined by the arrangement of atoms within one unit cell. The entire crystal structure is given by repeating the unit cell according to the direct lattice.

To collect all the intensities, the single crystal is rotated with respect to the X-ray beam. The result of the data collection is a complete list of reflections (*hkl* indices) with their corresponding peak positions and intensities. The electron density map is calculated from these results; this map, in turn, enables the atomic positions to be obtained by Fourier synthesis and they are improved with mathematical refinement techniques. Finally, the coordinates and anisotropic displacement parameters for each atomic position are obtained. From the atomic coordinates, the atomic bond lengths and torsion angles can be calculated.

We made the single crystal X-ray diffraction analysis at the *Servei de Recursos Científico-Tècnics* of the Universitat de Barcelona in a CAD4 Enraf-nonius diffractometer with Mo monochromatic radiation.

2.7. Microscopy techniques

Reflection optical microscopy was the first technique we used to get an immediate and detailed view of the crystals. We used scanning electron microscopy (SEM) to visualize the forms appeared on etched and indented

planes and confocal microscopy to study the micromorphologies on as-grown crystal faces. The cleavage planes of the crystals were analyzed using both confocal microscopy and atomic force microscopy (AFM).

2.7.1. Reflection optical microscopy

Reflection optical microscopy is based on the simultaneous normal incidence of visible light on the sample surface and normal visualization through the objective. This specific configuration of the incident and reflected light paths gives a reflected unobscured image that is highly illuminated. The high contrast enhances the observation of details on the sample surface. This technique is immediate since no sample preparation is needed. We used Olympus BH-2 and Olympus TL-2 microscopes available at the FiCMA.

2.7.2. Scanning electron microscopy (SEM)

The scanning electron microscopy (SEM) is one of the most commonly used techniques in a wide number of research areas today. This is because its magnification, depth of focus, and resolution are all greater than those of other microscopic techniques. SEM can focus on a large amount of the sample simultaneously because of its large depth of field. High-resolution images can be produced, so closely spaced features can be examined at a high magnification. In addition, the samples are relatively easy to prepare since the only requirement is that they be conductive. Crystals are therefore coated with a fine layer of a conductor metal such as carbon or gold.

With this technique, the surface of the crystal is scanned with a fine electron beam. When the electron beam impinges on the sample, it is scattered by the atomic layers near the surface, which leads to energy loss. Among other types of quanta generated, the most commonly used are the secondary electrons and the backscattered electrons, which carry information about the topography and

atomic number of the sample, respectively. Whereas the secondary electron detector produces a clear and focused topographical image of the sample, the backscatter electron detector produces an image that is useful for determining the composition of the sample. This information is converted into a video signal that is displayed on a screen where each topographical feature or element in the sample appears as a different shade, from almost white to black. This technique can provide between 20 and 30000 magnifications.

We used a Jeol JSM 6400 electron microscope to do the SEM studies. The crystalline samples were coated with gold using a Bal-Tec SCD004 sputter coating. Both apparatus are available at the *Servei de Recursos Científics i Tècnics* of the Universitat Rovira i Virgili.

2.7.3. Confocal microscopy

Confocal microscopy has several advantages over conventional optical microscopy, for example, controllable depth of field and elimination of out-of-focus information that degrades the image. It also enables serial optical sections from thick specimens to be collected. In recent years, this technique has become popular in many areas of current research interest, partly because of the relative ease with which high-quality images can be obtained from specimens prepared for conventional optical microscopy.

Confocal microscopy illuminates the sample with a laser beam at a selected wavelength, normally in the blue spectral region. When the laser beam impinges on the sample, it fluoresces at a higher wavelength. The image is constructed from this emitted electromagnetic radiation. In fact, this is the basis of fluorescence microscopy. Confocal microscopy, however, illuminates only one point in the sample. It is the focal point of the lens, where the excitation light is the most intense. So, only the fluorescence of this individual point instead of that of the whole sample is measured and this drastically reduces the background haze

in the resulting image. A complete image of the sample is never given: at any given instant, only one point of the sample is observed. The detector is attached to a computer, which builds up the image, one pixel at a time by scanning the volume of the sample layer by layer.

This restricted illumination of the sample can be managed by adding a pinhole at the point where the focal point of the objective lens of the microscope forms the image. These two points are known as "conjugate points". So, the pinhole is conjugate to the focal point of the lens, and is thus a confocal pinhole.

In these studies, we used a Sensofar Plμ 2300 confocal microscope illuminated with blue laser light at λ=470 nm available at the FiCMA.

2.7.4. Atomic force microscopy (AFM)

Atomic force microscopy (AFM) is a scanned-proximity probe microscopy, which measures the local attractive/repulsive forces with a probe or tip placed very close to the sample. The small probe-sample separation enables measurements to be made in a very small area.

The resolution of a scanned-probe system is determined by the size of the probe rather than by the diffraction effects of traditional microscopes. AFM can achieve a resolution of 10 pm.

To acquire the image, the microscope moves an atomically sharp probe over the sample surface while measuring the local attractive/repulsive forces, which consist of many rows or lines of information, one on top of the other.

In the repulsive or contact mode, the probe at the end of a cantilever lightly touches the sample. The piezo-electric scanners maintain the probe at a constant force and the microscope measures the vertical deflection of the cantilever that indicates the local height from the sample.

In the attractive or tapping mode, the probe is kept at a fixed height from the sample surface and the microscope derives topographic images from

measurements of attractive forces. This mode allows high-resolution topographic imaging, which overcomes problems caused by friction, adhesion, electrostatic forces among others of conventional AFM scanning. As the sample does not need to be coated, AFM provides extraordinary topographic contrast and direct height measurements.

We used atomic force microscopes available at the *Servei de Recursos Científics i Tècnics* of the Universitat Rovira i Virgili and at the *Servei de Recursos Científico-Tècnics* of the Universitat de Barcelona.

2.8. Differential thermal analysis (DTA)

The thermal analysis of a specimen involves studying the evolution of several physical properties as a function of the temperature. When the material is subjected to heating or cooling, its chemical composition and crystal structure undergo such changes as reaction, oxidation, decomposition, fusion, expansion, contraction, crystallization, or phase transition. All these changes can be detected using differential thermal analysis.

Differential thermal analysis (DTA) measures the temperature, the direction and the magnitude of thermal transitions induced by heating or cooling a material in a controlled way. DTA measures these properties by comparing the temperature of the sample and that of a reference material, which is inert under similar conditions.

This temperature difference is measured as a function of time or temperature under a controlled atmosphere and it provides useful information about the transition temperature but also about its thermodynamics and kinetics.

Thermogravimetric analysis (TGA) determines the weight gain or loss of a phase due to gas absorption or release as a function of temperature under a controlled atmosphere. This technique provides information about the purity of the sample,

as well as its water, carbonate and organic content. It is also useful for studying decomposition reactions.

In the combined DAT-TGA system, both thermal and mass transfers of the sample are measured simultaneously. We made these analyses at the FiCMA using a SDT 2960 analysis instrument from TA Instruments. These measurements make it possible to differentiate between endothermic/exothermic transitions with (e.g. degradation) and without weight change (e.g. fusion or crystallization).

2.9. Mechanical studies: microhardness measurements

Hardness is the property of a material that enables it to resist plastic deformation, usually by penetration. However, the term hardness may also refer to resistance to bending, scratching, abrasion or cutting.

The usual way of finding the hardness value is to measure the depth or area of an indentation left by an indenter of a specific shape, applied with a specific force for a specific time. There are three principal standard test methods for expressing the relationship between hardness and the size of the impression: Brinell, Vickers, and Rockwell. Microhardness tests usually use static indentations made with loads not exceeding 1 N[111]. The procedure for testing is very similar to that of the standard Vickers hardness test, except that it is done on a microscopic scale with higher precision instruments. The indenter is either the Vickers diamond pyramid or the Knoop elongated diamond pyramid.

We used the Vickers diamond pyramid as the indenter to measure the microhardness of $KGd(PO_3)_4$ and $KNd(PO_3)_4$. The measurements were made at the *Physics Department* of the Universitat Autonoma de Barcelona.

The Vickers microhardness method consists of indenting the test material with a diamond indenter, in the form of a right pyramid with a square base and an angle of 136º between opposite faces, subjected to a load of 0.1 to 100 N. In our measurements, we used loads from 0.1 to 1 N, which were normally applied for 2

seconds. The two diagonals of the indentation in the surface of the material after the load was removed were measured using the scanning electron microscope described above and their average calculated. The area of the sloping surface of the indentation was calculated. The Vickers hardness is the quotient obtained by dividing the load by the square area of indentation with the expression:

$$H_V = \frac{2Lg\,sin(136^o/2)}{d^2} \approx 1.8544\,g\,\frac{L}{d^2} \qquad \text{eq. 2.13}$$

where L is the standard load applied (N) and d is the arithmetic mean of the two diagonals of the pyramid (mm).

The experimental methodology consists of measuring the H_v by applying various indenter forces for during different exposure times. To evaluate the microhardness anisotropy, measurements were taken on about 1mm-thick plates cut normal to the **a***, **b**, and **c*** directions (see *paper V*).

2.10. Linear and non-linear optical characterization

It is essential to optically characterize the crystal to evaluate its potentialities as a good candidate for solid state or self-frequency doubling laser. In this section, we describe the methodology used to determine the main optical properties of the crystals.

2.10.1. Orientation of the optical frame

Type III $KGd(PO_3)_4$ and isostructurals crystallize in the monoclinic system and belong to the $P2_1$ space group (Tables 1.2 and 1.3). So, the optical frame $\boldsymbol{N_p}$, $\boldsymbol{N_m}$, $\boldsymbol{N_g}$ does not correspond to the main directions of the crystallographic coordinate system **a**, **b**, **c**. However, for monoclinic crystals, one of the principal optical axes is always parallel to the *2*-fold axis along the **b** crystallographic direction. The other two principal axes lie on the **a-c** plane because it is normal to the **b** direction. The orientation of the optical frame is determined by the angle

between one of the principal axes and one of the crystallographic axes on this plane.

To localize the principal axes, we used two crossed polarizers. Two ideal polarizers would eliminate all light if their transmission directions were placed at 90º. In a general case, when anisotropic material is placed between the crossed polarizers, light is transmitted because the crystal splits the light into two orthogonal components (Figure 2.6). However, if the incident beam is polarized parallel to one of these directions, only this component will be transmitted, the polarisation state will remain unchanged and the analyser will block the beam. This is an extinction position. There will be another extinction position when the crystal is rotated 90º so that the polarization of incident light is parallel to the other component.

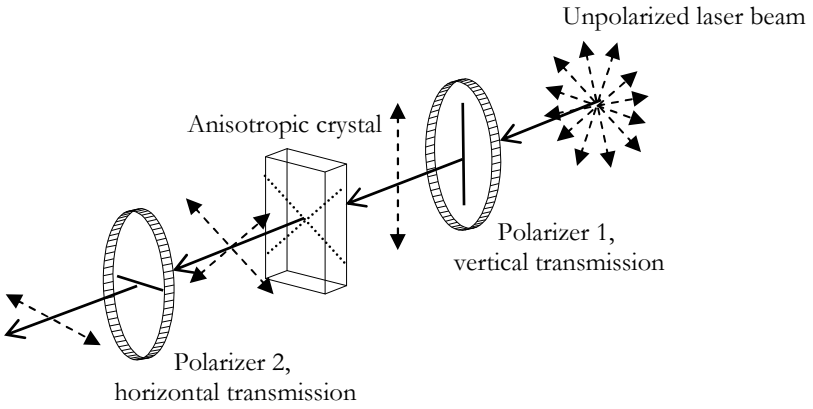

Figure 2.6. General situation when an anisotropic crystal is placed between two crossed polarizers.

If the anisotropic crystal is an **a-c** plane, the incident light propagates along **b** so that the two orthogonal components are the principal optical axes. Therefore, we used a polished plate oriented normal to the **b** direction and determined the position of one of the principal axes with respect to the **c** direction by rotating the crystal until an extinction position was reached. The experimental set-up used

to determine the orientation of the optical frame of $KGd(PO_3)_4$ and $KNd(PO_3)_4$ is available at the FiCMA and it comprises an oscillator arm where the sample can be placed between two fixed Glan-Taylor polarizers under normal illumination of a diode laser (λ=632.8 nm). The uncertainty associated to the angle measurement is $3x10^{-1}$.

The orientation of the optical frame can vary as a function of the wavelength. This is critical if nonlinear materials are to reach phase matching. Therefore, we check this effect by using the conoscopy technique at the *Laboratoire de Crystallographie* of CNRS under illumination by a He-Ne laser (λ=632.8 nm) and a Zn-Cd-Hg lamp (λ=546 nm). This technique observes interference figures of polarized convergent light. The interference effects at each point in the interference field are the result of all the individual emergent waves that enter the objective in a particular direction converging on a focus above the objective lens. For a monoclinic crystal, a complete figure of interference consists of isogyres, which can be geometrically related to the principal optical axes, superimposed on isochromatic curves (isochromes). The isogyres are black areas produced by the extinction of light that appear in the form of crosses, bars, or hyperbolic segments. The figure of interference of a plate oriented normal to a principal axis, so a principal plane, consist of a black cross that is superimposed on colour curves (Figure 2.7). Two black points indicate the two optic axes in the $\boldsymbol{N_p}$-$\boldsymbol{N_g}$ plane because a monoclinic crystal belongs to the optical biaxial class.

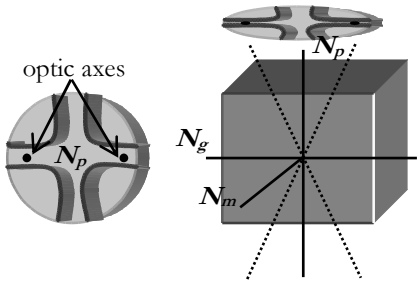

Figure 2.7. Interference figure for a biaxial crystal section normal to a principal optical axis

2.10.2. Determination of the refractive indices

The refractive indices must be accurately determined for nonlinear optical materials since they determine the phase matching directions and the spectral bandwidth acceptances.

An electric field (E) induces dipoles in a dielectric medium, so it generates a polarisation field (P). They are related by χ, an adimensional constant of proportionality called optical susceptibility:

$$P(\omega) = \varepsilon_0 \chi E(\omega) \qquad \text{eq. 2.14}$$

In an anisotropic medium, the optical susceptibility is not a unique value because the polarization field is not parallel to the electric field. It cannot be written as a scalar quantity, only as a second rank tensor (χ_{ij}).

Hence, we can also represent the refractive index as a second rank tensor (n_{ij}):

$$n_{ij} \equiv \sqrt{1+\chi_{ij}} \equiv \begin{pmatrix} \sqrt{1+\chi_{11}} & \sqrt{1+\chi_{12}} & \sqrt{1+\chi_{13}} \\ \sqrt{1+\chi_{21}} & \sqrt{1+\chi_{22}} & \sqrt{1+\chi_{23}} \\ \sqrt{1+\chi_{31}} & \sqrt{1+\chi_{32}} & \sqrt{1+\chi_{33}} \end{pmatrix} \equiv \begin{pmatrix} n_{11} & n_{12} & n_{13} \\ n_{21} & n_{22} & n_{23} \\ n_{31} & n_{32} & n_{33} \end{pmatrix} \qquad \text{eq. 2.15}$$

The Onsager theorem[112] demonstrates the symmetric nature of this tensor. So, we need only six values to fully determine the index tensor. A symmetric matrix can always be diagonalised by calculating the eigenvalues using the orthogonal system of the principal axes as eigenvectors. The refractive index tensor is described, therefore, as a diagonal matrix, in which each value represents a principal direction:

$$n_{ij} = \begin{pmatrix} n_{11} & 0 & 0 \\ 0 & n_{22} & 0 \\ 0 & 0 & n_{33} \end{pmatrix} \qquad \text{eq. 2.16}$$

This diagonalised tensor can be assimilated to the Fresnel ellipsoid, which can be expressed as:

$$\frac{x^2}{n_{11}^2} + \frac{y^2}{n_{22}^2} + \frac{z^2}{n_{33}^2} = 1 \qquad \text{eq. 2.17}$$

This ellipsoid represents the refractive index value for any spatial direction and it is called the optical ellipsoid. It intercepts the principal axes $\boldsymbol{N}_p$, $\boldsymbol{N}_m$ and $\boldsymbol{N}_g$ at $\pm n_p$, $\pm n_m$ and $\pm n_g$.

The crystal symmetry gives additional conditions over the symmetry type of the second order tensor by the Neumann principle. For the monoclinic $P2_1$ symmetry of $KGd(PO_3)_4$ and isostructurals, the three diagonal elements of the tensor n_{ij} are different. Thus, the refractive indices along the principal directions are different so that $\boldsymbol{N}_p$, $\boldsymbol{N}_m$ and $\boldsymbol{N}_g$ correspond to the directions with minimum, medium, and maximum values of refractive indices: n_p, n_m and n_g.

We measure the refractive indices using the minimum deviation angle method[113,114] with a slight modification. A monochromatic light beam passing through a prism of angular directrix α and refractive index n is deviated from its incident path a certain angle δ. For a particular incident angle, the deviation angle is minimal (δ_{min}). The refractive index is then:

$$n = \frac{\sin(\alpha + \delta_{\min} / 2)}{\sin(\alpha / 2)} \qquad \text{eq. 2.18}$$

This configuration is fulfilled when the beam symmetrically propagates throughout the prism in a direction normal to the bisecting plane of the prism.

The slight modification we made to this method consists of using a semi-prism with an angular directrix $\alpha/2$ and the partial reflection on the second face of the semi-prism, which would correspond to the bisecting plane of a prism[115]. If this second face is a principal plane and the light beam propagates parallel to a principal axis, and so normal to a principal plane, we can measure the refractive indices corresponding to the principal axes on the plane. This is because the anisotropic behaviour of the crystal allows two beams with orthogonal polarizations to propagate throughout it and so the refractive indices in these directions can be measured. Therefore, we cut and polished two semi-prisms with an angle of about 22.5º between faces, one of which was a principal plane:

N_p-N_g and N_p-N_m. We measured n_p and n_g with one prism and n_p and n_m with the other Note that as n_p was measured twice, we were able to estimate the error in the measurements. This error is limited by the encoder accuracy, which is of 10^{-4}. We prepared semi-prisms for both $KGd(PO_3)_4$ (Figure 2.8) and $KNd(PO_3)_4$.

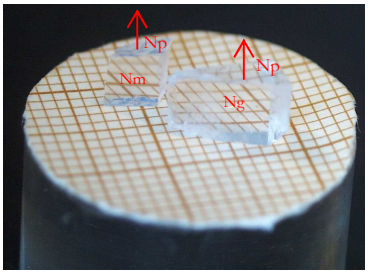

Figure 2.8. $KGd(PO_3)_4$ semiprisms ***Np-Ng*** and ***Np-Nm***

The first face of the semi-prism was illuminated by an unpolarized laser beam under normal incidence. The prism was then rotated until incidence on the second face (the principal plane) was normal. The minimum deviation angle (δ_{min}) was then measured. Figure 2.9 shows the experimental set-up used to determine the refractive indices at the FiCMA. We used a BMI VEGA optical parametric oscillator (OPO) pumped by a BMI SAGA seeded Nd:YAG laser to determine the refractive indices as a function of the wavelength.

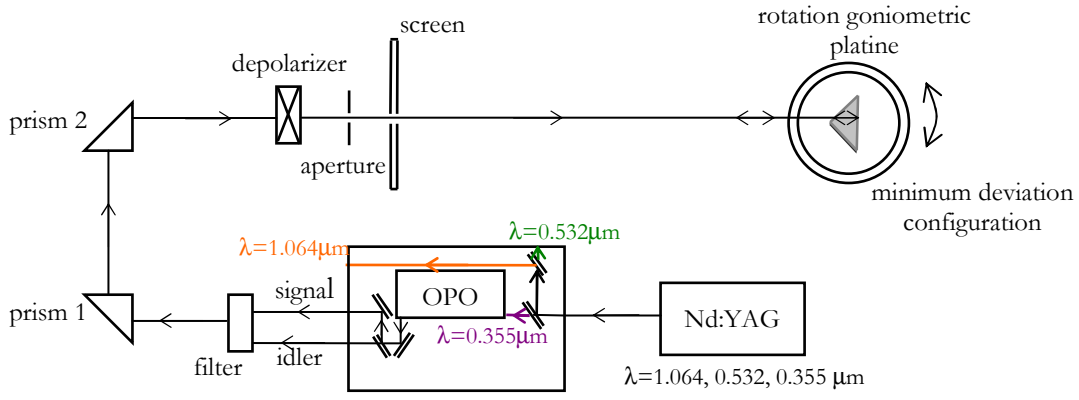

Figure 2.9. Experimental set-up for measuring the refraction indices

The prisms were placed on a rotating goniometric palatine connected to an encoder to accurately measure the minimum deviation angle (δ_{min}). Reflected spots corresponding to the beams propagating parallel to the two principal directions were visualized (with the aid of an infrared viewing in the IR range) on a screen that functions as a 1 mm-thick aperture at the same time.

The thermal dependence of the principal refractive indices of $KGd(PO_3)_4$ was analyzed using a prism coupler (Metricon model 2010), which scans the incident angle to determine the critical angle for total internal reflection (TIR). The refractive indices were measured at λ=632.8 nm and between room temperature and 293 K, which cover the range of temperature that suffers the crystal during laser operation. We used very thin (around 200 μm) sample in order to assure its good coupling with the prism. We prepared $KGd(PO_3)_4$ plate-shaped samples of around 6 mm^2 cut and polished normal to $\boldsymbol{N}_p$ and $\boldsymbol{N}_g$. Note that the thermal evolution along $\boldsymbol{N}_m$ was measured twice, which provided an accuracy estimation of the measurements of 10^{-4}.

2.10.3. Second harmonic generation (SHG) efficiency in powder

Kurtz and Perry[116] demonstrated that it was possible to perform second harmonic generation (SHG) studies on microcrystalline powders to predict the phase matching direction in crystals and determine their averaged nonlinear efficiency. The SHG intensity generated by a powder in a solid angle of 360º depends on the averaged nonlinear efficiency of the material but also on the particle size and the total number of small crystals irradiated by the incident beam. Only if we consider that all the crystallographic orientations are equally represented in the powder, will an averaged nonlinear intensity of the material be measured. Obviously, several simple assumptions are needed to reduce a theoretical analysis of SHG in powders to manageable portions. The basic assumptions made by Kurtz and Perry were that the powder particles were small crystals of almost

identical size, randomly orientated and densely packed. These assumptions mean that form factors, polycrystallinity, and voids are avoided. Taking these assumptions into account the small crystals of undoped and Yb- and Nd-doped $KGd(PO_3)_4$ and $KNd(PO_3)_4$ were powdered and graded with standard sieves to obtain a uniform particle size between 5 and 20 μm. Then, they were uniformly packed in a 2 mm-thick quartz cell. Figure 2.10 shows the experimental set-up used to make the measurements, which is available at the FiCMA.

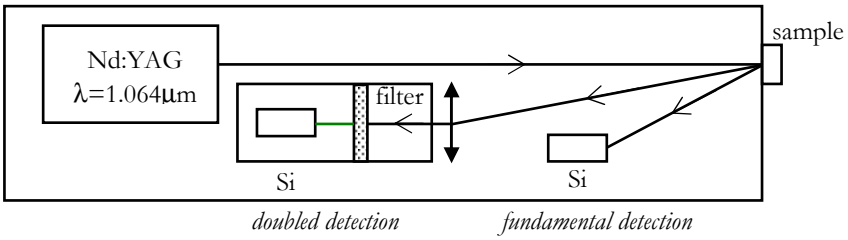

Figure 2.10. Experimental set-up used to measure SHG efficiency in powder

To irradiate the sample, we used a Nd:YAG laser emitting at 1.064 μm. The fundamental power at 1.064 μm reflected by the sample was measured using a silicon photodiode. The doubled beam generated by the sample was focalized with a lens to a silicon photodiode and an interferometric filter to eliminate the non-doubled portion of the incident power. We used the ratio between the fundamental and the doubled powers, calculated as the average of about 100 laser shots, to estimate the SHG efficiency of the sample. Signals were collected and analysed using a digital oscilloscope. We also measured the SHG efficiency of KH_2PO_4 (KDP)[117] and used it as a standard.

2.10.4. Second harmonic generation (SHG) efficiency in crystal

Preliminary attempts of second harmonic generation (SHG) from a single crystal of $KNd(PO_3)_4$ were performed by propagating a laser beam successively along

the three principal optical axes $\boldsymbol{N}_p$, $\boldsymbol{N}_m$ and $\boldsymbol{N}_g$ of a parallelepipedic sample accurately oriented along them. Figure 2.11 shows the experimental set-up used for the SHG experiments. This equipment is available at the *Laboratoire de Spectrométrie Physique* of the Université Joseph Fourier.

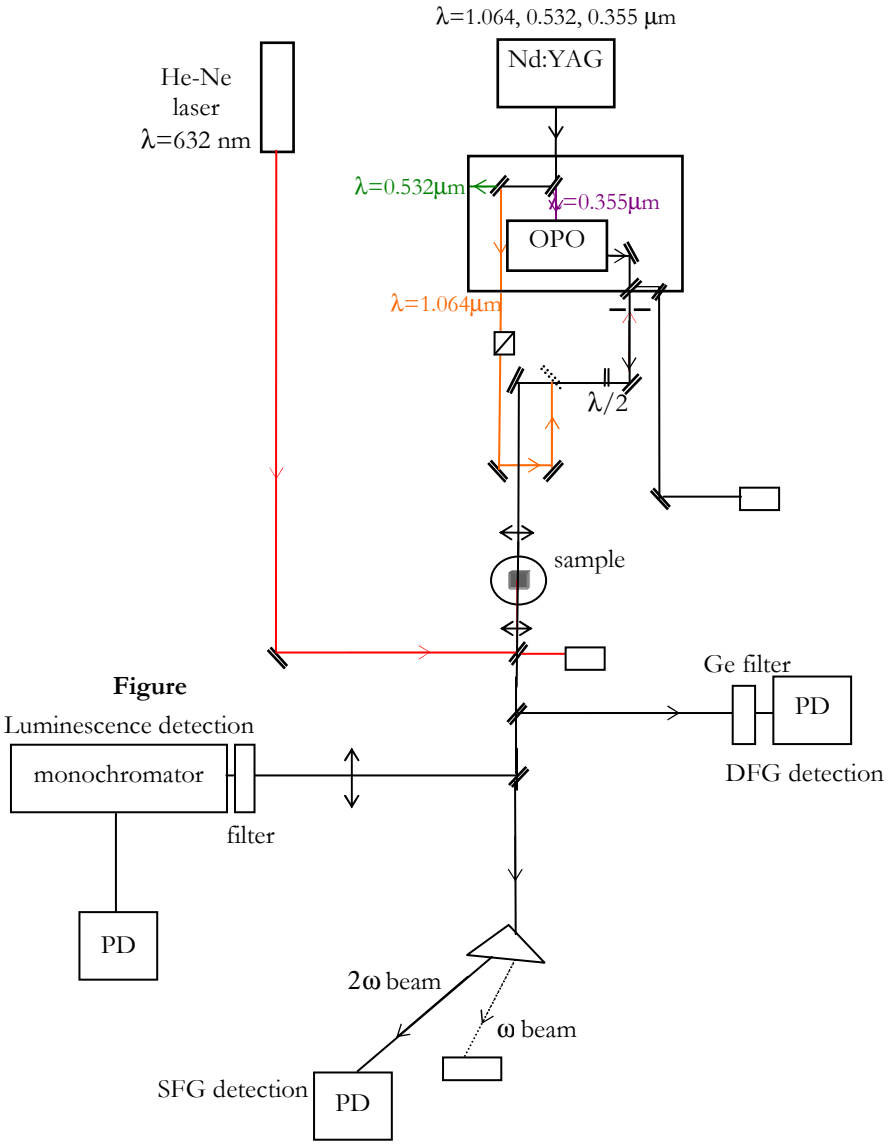

2.11. Experimental set-up used for second harmonic generation experiments on $KNd(PO_3)_4$. SFG: sum frequency generation, DFG: difference frequency generation

To pump the sample, we used an optical parametric oscillator (OPO) Continuum Panther, pumped with a Nd:YAG laser Continuum SLI-10. The exit laser wavelength of the OPO was measured in order to avoid calibration problems. It ranges between 0.4 and 2.4 μm.

2.10.5. Determination of the phase-matching directions

For collinear waves, the power of the doubled wave $P(\theta,\phi,\omega_3,L)$ generated by a sum-frequency generation (SFG) process is highly dependent on the phase mismatch (Δk) according to the equation:

$$P(\theta,\phi,\omega_3,L) \propto P(\theta,\phi,\omega_1,0)P(\theta,\phi,\omega_2,0)\chi_{eff}^{(2)}(\theta,\phi,\omega_3)L^2 \, sinc^2(L\cdot\Delta k/2)$$

eq.2.19

Δk is the phase-mismatch between the nonlinear polarisation $P^{NL}(\omega_3,\theta,\phi)$ and the electromagnetic field $E(\omega_3,\theta,\phi)$ inside a crystal:

$$\Delta k = \frac{n^{\pm}(\omega_3,\theta,\phi)\omega_3}{c} - \left(\frac{n^{\pm}(\omega_1,\theta,\phi)\omega_1}{c} + \frac{n^{\pm}(\omega_2,\theta,\phi)\omega_2}{c} \right) \qquad \text{eq. 2.20}$$

In the case of collinear waves depending on (θ,ϕ), the phase-matching condition ($\Delta k=0$) for a SFG process is given by:

$$n^{\pm}(\omega_3,\theta,\phi)\omega_3 = n^{\pm}(\omega_1,\theta,\phi)\omega_1 + n^{\pm}(\omega_2,\theta,\phi)\omega_2 \qquad \text{eq. 2.21}$$

with $\omega_3=\omega_1+\omega_2$.

In the particular case of second harmonic generation, $\omega_3=2\omega$ and $\omega_1=\omega_2=\omega$, the phase-matching condition in given by:

$$n^{\pm}(2\omega,\theta,\phi)2\omega = n^{\pm}(\omega,\theta,\phi)\omega + n^{\pm}(\omega,\theta,\phi)\omega \qquad \text{eq. 2.22}$$

Under normal dispersion, the refractive index increases with the frequency and therefore $n_{2\omega}^{\pm} > n_{\omega}^{\pm}$. The phase-matching interactions must fulfil this condition.

For type I collinear phase-matching, the fundamental waves have the same polarization:

$$n^{-}(2\omega,\theta,\phi)2\omega = n^{+}(\omega,\theta,\phi)\omega + n^{+}(\omega,\theta,\phi)\omega = 2n^{+}(\omega,\theta,\phi)\omega \qquad \text{eq. 2.23}$$

For type II collinear phase-matching, the fundamental waves have orthogonal polarizations:

$$n^{-}(2\omega,\theta,\phi)2\omega = n^{+}(\omega,\theta,\phi)\omega + n^{-}(\omega,\theta,\phi)\omega \qquad \text{eq. 2.24}$$

The phase-matching directions for type I and II SHG can be determined by measuring the refractive indices of the fundamental and doubled waves as a function of the propagation direction (θ,ϕ) using the Fresnel equation:

$$\frac{\sin^2(\theta)\cos^2(\phi)}{1/n_{\omega}^2 - 1/n_{p,\omega}^2} + \frac{\sin^2(\theta)\sin^2(\phi)}{1/n_{\omega}^2 - 1/n_{m,\omega}^2} + \frac{\cos^2(\theta)}{1/n_{\omega}^2 - 1/n_{g,\omega}^2} = 0 \qquad \text{eq. 2.25}$$

where n_{ω} corresponds to the refractive index for the propagation direction and $n_{p,\omega}$, $n_{m,\omega}$ and $n_{g,\omega}$ are the principal refractive indices. This set of solutions of this equation leads to the index surface with two sheets (+) and (-) corresponding to n^{+} and n^{-} shown in Figure 2.12[118] for both positive and negative biaxial crystals. For a positive biaxial crystal $n_x < n_y < n_z$, thus $\boldsymbol{N_p}//\boldsymbol{x}$, $\boldsymbol{N_m}//\boldsymbol{y}$ and $\boldsymbol{N_g}//\boldsymbol{z}$; for a negative biaxial crystal $n_x > n_y > n_z$, thus $\boldsymbol{N_p}//\boldsymbol{z}$, $\boldsymbol{N_m}//\boldsymbol{y}$ and $\boldsymbol{N_g}//\boldsymbol{x}$.

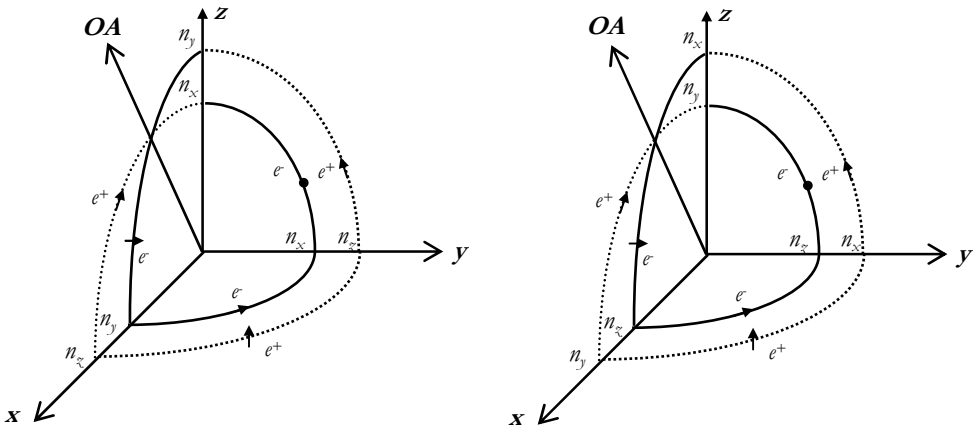

Figure 2.12. Index surfaces of the positive and negative biaxial classes. e^{+} and e^{-} are the electric field vectors relative to the external (+) or internal (-) sheets for a propagation in the principal planes. OA is the optic axis.

2.11. Spectroscopic techniques

In this section, we analyse the fundamentals of the spectroscopic techniques we used in this thesis.

2.11.1. Absorption and transmission

Most materials absorb some light to a degree that depends on the wavelength. In the near ultraviolet (UV), visible, and infrared (IR) spectral ranges of light, radiation is mainly absorbed by electrons in atoms, ions, or molecules. Thus, the absorption is due to electronic transitions. The Beer-Lambert law, also known as Beer's law, is an empirical relationship that relates the absorption of light to the properties of the material through which it is travelling:

$$I = I_0 e^{-\alpha d} \qquad \text{eq. 2.26}$$

where I_o is the incident light intensity; α is the absorption coefficient; and d is the thickness of the sample.

The absorption is reflected in the variation of the intensity of the electromagnetic radiation (I) as a function of the wavelength. To measure this absorption, we experimentally measure the optical density (OD) using a double ray spectrophotometer:

$$OD = -\log(I / I_0) \qquad \text{eq. 2.27}$$

Combining the equations 2.26 and 2.27, we can correlate the absorption coefficient with the optical density:

$$\alpha = OD\left(\frac{1}{d \log e}\right) \qquad \text{eq. 2.28}$$

We can also correlate α with the absorption cross-section of every absorbing atom or ion as:

$$\sigma = \frac{\alpha}{N} \qquad \text{eq. 2.29}$$

where N is the density of absorbent centres. In this expression α is given in cm^{-1} and N in atoms cm^{-3}; thus, the units of σ are atoms cm^{-2} or simply cm^{-2}.

The absorption was measured at the FiCMA using a Varian Cary 500 Scan spectrophotometer. It is a double ray spectrophotometer with an effective spectra range from 0.175 to 3.3 μm and it measures optical densities up to 10. This spectrophotometer has two monochromators that can separate 1200 lines/mm in the UV-visible region and 300 lines/mm in the IR region. The UV light source is a deuterium lamp and the visible-IR one a quartz halogen lamp. The UV-visible light is detected by a photomultiplier and the IR light by a lead sulphide detector.

When we expected absorption dichroism, we used a Glan-Thompson polarizer located before the sample. The light emitted by the lamps is partially polarized when it passes through the optical components of the spectrophotometer. Therefore, we used a polarizer to ensure a unique polarization component of the incident light in the sample. In all experiments, we set an aperture diameter appropriate for the sample size to avoid crystal-edge obscurations.

To measure absorption at low temperatures (6K), we used a Leybold helium close circuit cryostat with a temperature controller that stabilises the temperature to a precision of ±3 and ±5 K in the 6-100 and 100-300 K ranges, respectively.

The same spectrophotometer also enables the transmission to be measured. We determined the transparency window of the crystals in the 0.175-3.3 μm range. To determine their transmission in the IR region, we use a FTIR Midac Prospect spectrophotometer in the 3.0-10.0 μm range. This is available at the *Servei de Recursos Científics i Tècnics* of the Universitat Rovira i Virgili. The UV and IR cut-off were calculated as the maximum transmission value divided by the *e* number.

2.11.2. Luminescence and lifetime measurements

Optical emission, or luminescence, is the result of a radiative transition of an electron from an excited or higher energy level to a lower energy level. The

luminescence spectra are determined by fixing the excitation wavelength and changing the detection wavelength. It is also interesting to determine the temporal evolution of the luminescence after excitation. Usually, the luminescence intensity declines exponentially. The time at which the intensity has decreased to $1/e$ of its initial value is called the radiative lifetime (τ). The radiative lifetime is an important parameter since it characterises how an electronic level is depopulated and what the thermalisation mechanisms of this excitation are. To determine the lifetime, a pulsed excitation source is needed. Moreover, the pulses must be shorter than the mean lifetime of the electronic level of the ion we are studying in a certain material.

The luminescence studies were made at the FiCMA with the experimental set-up shown in Figure 2.13.

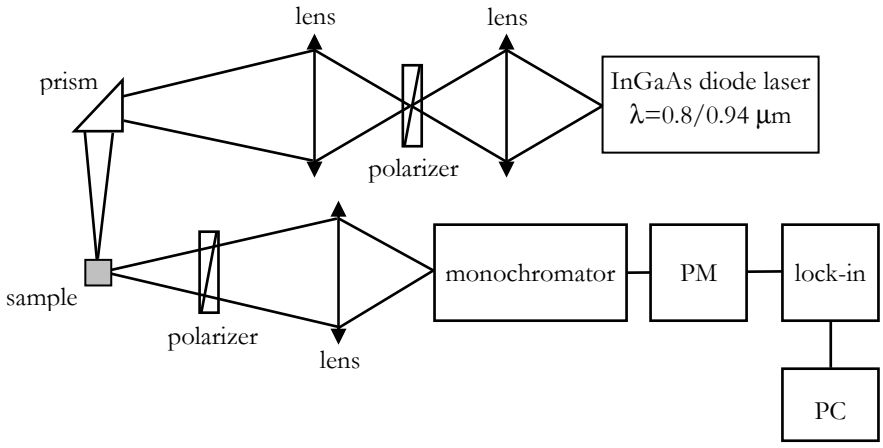

Figure 2.13. Experimental set-up used to measure luminescence of Yb- and Nd-doped $KGd(PO_3)_4$

Excitation was provided by a 200 mW InGaAs diode laser emitting in the wavelength range between 0.94 and 0.8 μm, which was modulated at 1 kHz. The luminescence was recorded in a 90º geometry to minimize the influence of the laser pump and it was dispersed by a Jobin Yvon-Spex HR 460 double

monochromator, which has a focal length of 460 mm and a spectral resolution of 0.05 nm. The detector used was a cooled Hamamatsu NIR R5509-72 photomultiplier. The signals were processed by a EG&G 7265 DSP lock-in amplifier. The signals for the lifetime measurements were treated with a computer –controlled Tektronik TDS-714 digital oscilloscope.

To cool the sample for the low temperature measurements (10 K), an Oxford CCC1104 closed-cycle helium cryostat was used.

2.12. Raman spectroscopy

Raman scattering provides useful information about the vibrational energy levels of molecules (that is of the structure of a material). It allows therefore identifying immediately solid, liquid, or gaseous substances. In addition, it is non-contact and non-destructive, and requires minimal sample preparation. Together with infrared absorption, which provides complimentary information, it completely characterises the vibrational, rotational, and other low-frequency modes of molecules, such as the lattice vibrations of the crystals.

When light impinges on a molecular system, it scatters. Most of the photons are elastically scattered (Rayleigh scattering) and have the same wavelength as the absorbing photon. But Raman scattering relies on inelastic scattering of monochromatic light resulting in the energy of the scattered photons being shifted down or up for the Stokes or anti-Stokes lines, respectively. The shift in energy gives information about the phonon modes in the system because it is related to the vibrational energy spacing at the ground level. The Stokes and anti-Stokes lines are equally displaced from the Rayleigh line because in each case one vibrational quantum energy is lost or gained. However, the anti-Stokes line is much less intese than the Stokes line because only molecules that are vibrationally excited prior to radiation can lead to the anti-Stokes line.

Spontaneous Raman scattering is typically very weak and, as a result, the main difficulty of Raman spectroscopy is separating the weak inelastically scattered light from the intense Rayleigh scattered light. We need, therefore, a high power monochromatic excitation source. Typically, a sample is illuminated with a laser beam in the visible, near infrared, or near ultraviolet range. Light from the illuminated spot is collected with a lens and sent through a monochromator. Wavelengths close to the laser line (due to elastic Rayleigh scattering) are filtered out and those in a particular spectral window away from the laser line are dispersed onto a detector.

Raman scattering combined with an optical microscope make Raman microstructural investigations possible. The experimental set-up we used for these measurements consisted of Jobin-Yvon T64000 spectrometer with excitation in the visible by a cw argon laser (Coherent INNOVA 300, λ=514 nm). Behind the triple-monochromator (1800 g.mm^{-1}), the light was detected by a two-dimensional CCD matrix cooled with liquid N_2. A pre-monochromator eliminated the plasma discharge lines of the laser. A microscope (Olympus BH2) with high resolution was used to locate the laser spot in the sample. The laser power incident on the sample was about 60 mW. We chose a backward scattering scheme to increase the signal-to-noise ratio. This equipment is available at the *Servei de Recursos Científico-Tècnics* of the Universitat de Barcelona.

2.13. Laser set-up

The laser experiments with ytterbium-doped $KGd(PO_3)_4$ crystals were made in a standard astigmatically compensated Z-shaped cavity 129 cm long (Figure 2.14) available at the *Max-Born Institute for Non-linear Optics and Ultrafast Spectroscopy.*

The sample was positioned in the focal region between the folding mirrors (M1 and M2). M2 was highly transmitting at the pump wavelength, λ=977.1 nm and M1 highly reflective at both the laser (λ_l) and the pump (λ_p) wavelengths. There

were two plane reflectors at the ends of the cavity, a rear mirror (M3) and an output coupler (M4) whose transmission (T_{OC}) ranged from 1 to 5%.

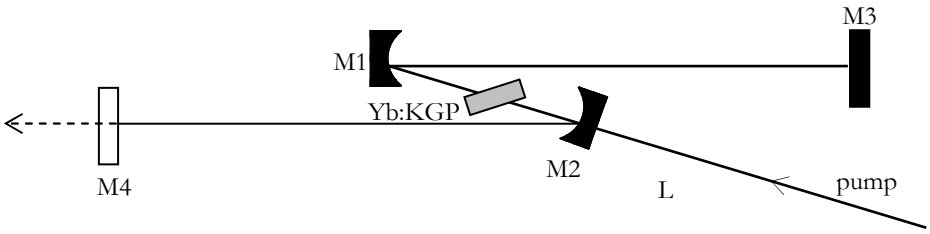

Figure 2.14. Laser set-up for the CW experiments in ytterbium doped $KGd(PO_3)_4$ crystals

The pump source was a home-made Ti:sapphire laser optimized for operation at relatively long wavelengths. This laser was tunable between 0.96-1.025 μm, FWHM<1 nm, and had a maximal output power of 3 W. The pump radiation was focused by an anti-reflection coated lens of f=6.28 cm (L), the focus of which had a waist of around 30 μm. The pumping was done in a single-pass.
The uncoated Yb:$KGd(PO_3)_4$ sample was attached to a Cu-holder without active cooling and positioned under Brewster angle between the two folding mirrors.

Chapter 3: Crystal growth and structural and morphological characterization

Single crystals, once valued only for their beauty, are now found in many electronic, optoelectronic and optical devices in one form or another. These devices have entered almost every home throughout the world. In fact, it is hard to imagine what our electronics or optical industry would have been like if large, defect-free crystals could not be produced. The crystallographic characterization of crystals is essential if they are to be fully understood. The structure and symmetry of a crystal play an important role in determining its mechanical, optical, and spectroscopic properties.

3.1. Crystallization region of type III $KGd(PO_3)_4$ in its self-flux

The double phosphate of potassium and gadolinium, $KGd(PO_3)_4$ (KGP), decomposes at 1142 K into other gadolinium phosphates before melting (see *Paper I*). For this reason, KGP cannot be grown from its stoichiometric melt. The literature reports that hydrothermal growth methods[119,120] or crystallization from high-temperature solutions[74,121] have been used to synthesize the isostructural $KNd(PO_3)_4$ (KNP), which incongruently melts at 1165 K (see *Paper IV*). During hydrothermal growth, OH^- groups are incorporated into the crystal lattice resulting in detrimental changes to the optical properties, e.g. the optical transmission or the nonlinear polarisability are reduced. Therefore, we grew KGP single crystals and isostructurals from a high-temperature solution or flux.

The first important step when using high-temperature growth techniques is to choose the appropriate solvent and to understand the properties of the solutions obtained. If these factors are known, the best growth regimes can be chosen[122]. The solubility curves and the physical properties of the growth solution are determined in the following sections of this chapter.

In order to avoid impurities in the single crystals, we grew KGP from its self-flux using solution compositions in the ternary crystallization region of the corresponding oxides, Gd_2O_3-K_2O-P_2O_5. An excess of phosphorous and potassium oxides was used as a solvent. These solutions are very viscous (see section 3.4) so it is recommended that a component such as tungstate, molibdate or lead fluoride be added in order to reduce it. Unfortunately, this means that impurities may find their way into the crystals. As long as growth is possible, it is recommended that self-flux be used. In fact, we successfully grew KGP single crystals free of macroscopic defects and of suitable sizes from their self-flux.

Before our study on the crystallization region of KGP (see *paper I*), there was no data available about the solution composition regions and temperatures of type III KGP crystallization. Several solution compositions, around 50, in the ternary

system of the corresponding oxides, Gd_2O_3-K_2O-P_2O_5, were investigated. The phase crystallized from each composition was determined by X-ray powder diffraction analysis and the shape of the small crystals was observed using reflection optical microscopy and scanning electron microscopy (SEM).

Figure 1 in *paper I* shows the crystallization region of KGP in self-flux and the crystallization temperature isotherms. These were roughly parallel to the isoconcentrational lines of P_2O_5 and increased from 825 to 963 K when the Gd_2O_3/K_2O molar ratio also increased. In the same figure, we added SEM pictures of the $P2_1$-phase (type III) and its neighbouring phases. Up to five neighbouring phases were identified: GdP_5O_{14}, in the richest P_2O_5 region, above the KGP crystallization region; $Gd(PO_3)_3$, $KGdP_4O_{12}$ (type A), and $GdPO_4$, in the same P_2O_5 concentration range as the crystallization region but richer in Gd_2O_3; and KPO_3 below the crystallization region. The KGP crystallization region was rather irregular and therefore its limits are show in Table 2 of the same paper. The gadolinium ion (Table 1.4) is in the middle of the lanthanide series (see 1.3 section) and it is therefore highly versatile. This is probably the reason for the irregular crystallization region and the numerous neighbouring phases, one of which is type A-$KGdP_4O_{12}$ (cycling geometry, S. G. $C2/c$).

Although varied the viscosity of the solutions is quite high throughout the crystallization region. We qualitatively studied how the viscosity evolved with the solution composition by comparing the growth rates, which are directly influenced by the viscosity. We found that it increased when the P_2O_5 molar concentration was increased by keeping the Gd_2O_3/K_2O molar ratio fixed. It also increased when this ratio was decreased, probably because the crystallization temperature also decreased. The KGP crystallization region was limited to a K_2O concentration of 98 mol %. Above this concentration, the solution was so viscous that any crystal was able to grow at any P_2O_5 concentration.

Taking these results into account, we defined an optimal zone of the crystallization region to grow KGP single crystals, where the P_2O_5 concentration was limited to 60 mol % and the Gd_2O_3/K_2O molar ratio went from 15/85 to 10/90.

3.2. Changes in the crystallization region of $KGd(PO_3)_4$ when the ytterbium and neodymium ions are added to the solution

As the main objective is to grow KGP single crystals doped with ytterbium or neodymium, we studied how the KGP crystallization region evolved when these lanthanide ions were added to the solution.

We studied how the crystallization region changed when ytterbium was added to the optimal concentration zone of the solution, which had been previously determined. In the solution compositions investigated, the P_2O_5 concentration was kept fixed at 60 mol % and the $(Yb_2O_3+Gd_2O_3)/K_2O$ molar ratio was varied among 15/85, 10/90 and 5/95. The ytterbium concentration for each solution composition ranged from 0.5 to 50 atomic %.

Table 2 in *paper II* lists the crystalline phase identified for each composition. In this zone, Yb:KGP crystallizes into two different polymorphs: type III and type A. Both phases appeared in the crystallization region of KGP. The border between them was at a Gd_2O_3/K_2O molar ratio of 20/80 at 60 mol % P_2O_5. However, in this case, the border between these two phases depended on the ytterbium concentration in solution. If the ytterbium content in solution was between 3 and 10 atomic %, the border was similar to that of undoped KGP but if it was either reduced or increased from this concentration, the border shifted to a lower $(Yb_2O_3+Gd_2O_3)/K_2O$ ratio, so the type III crystallization region was slightly narrowed. In the crystallization region of Yb:KGP, the temperature isotherms were also roughly parallel to the isoconcentrational lines of P_2O_5 and increased around the same temperature range when the Gd_2O_3/K_2O molar ratio

also increased. The morphological shape of both polymorphs was observed and studied. In the same paper, 1 shows a SEM picture and a morphological scheme for both of them.

The evolution of the KGP crystallization region when neodymium was added to the solution was determined between the two stoichiometric extremes, KGP and KNP, because they are isostructural. Figure 1 in *paper III* shows the type III crystallization regions of the intermediate $KNd_{0.53}Gd_{0.47}(PO_3)_4$ in relation to those of $KGd(PO_3)_4$ and $KNd(PO_3)_4$ and Figure 1 in *paper IV* shows the crystallization region of KNP.

The type III crystallization region got wider when the neodymium content of the solution was increased. So, the type III crystallization region of KNP was the widest and that of KGP was the narrowest. The crystallization region of KGP was also much more irregular because gadolinium is much more versatile than neodymium. The crystallization region of the intermediate $KNd_{0.53}Gd_{0.47}(PO_3)_4$ was more similar to that of KNP than that of KGP. The number of neighbouring phases identified was also reduced from five to four. They were: LnP_5O_{14}, $Ln(PO_3)_3$, $LnPO_4$, and KPO_3. The type A polymorph in the cycling geometry $KGdP_4O_{12}$ disappeared. The common crystalline phases were in the same regions and their morphological shapes were also comparable. The crystallization temperature isotherms were also roughly parallel to the isoconcentrational lines of P_2O_5 and increased from 973 to 1123 K for KNP when the Gd_2O_3/K_2O molar ratio also increased.

3.3. Solubility curve of $KGd(PO_3)_4$ in its self-flux

The solubility of KGP in its self-flux was studied over a range of solution compositions within the type III crystallization region. Thus, the solubility curve of KGP was determined in a solute concentration range between 1.5 and 14 mol %. The methodology used to determine the solubility curve was similar to that

used to determine the crystallization region. First, the crystallization temperature was determined with a platinum wire and then small crystals were grown on a platinum disk by slowly cooling the solution from this temperature. The phase crystallized was identified by X-ray powder analysis.

To evaluate the effect of doping on the solubility of KGP, the solubility curve of KNP was determined in a solute concentration region from 4 to 20 solute mol %. Figure 1 in *paper V* shows the solubility curves of both KGP and KNP. They were almost parallel in the solution composition range between 8 and 12 solute mol %, which was the optimal zone that had been determined for growing the single crystals. The crystallization temperature depended on the lanthanide constitutional element since it is slightly lower for KGP. So, KGP is more soluble than KNP in self-flux. The crystallization temperature rose sharply as the solute concentration increased for both materials.

3.4. Physical properties of the growth solution

During the growth process, the composition of the solution continuously changes from the very moment that crystallization begins. Therefore, the physical properties must be studied at various temperatures if it is to be determined how they evolve thermically.

We determined the density, viscosity, and surface tension of the optimal solution composition for growing KGP single crystals: Gd_2O_3:K_2O:P_2O_5=6:34:60 mol %. These properties were measured from 950 K, which is 25 K above the crystallization temperature of KGP in this solution composition. Figure 3.1 shows the thermal evolution of the solution density. When the temperature increased, the density slightly decreased from a maximum value of about 2.32×10^3 $Kg \cdot cm^{-3}$, which was constant in the temperature range near to the crystallization temperature. The dynamic viscosity linearly increased when the temperature decreased (Figure 3.2) even in the temperature range near the crystallization

temperature, for which was around 16 Pa·s. The surface tension behaves the same as the viscosity (Figure 3.3).

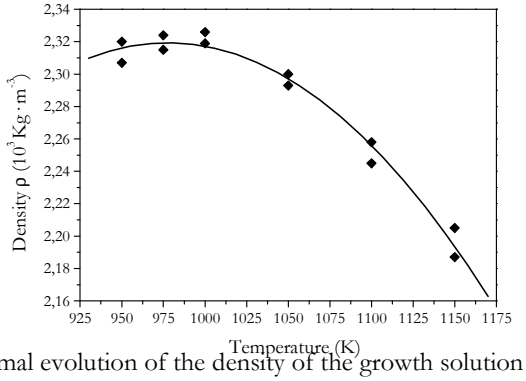

Figure 3.1. Thermal evolution of the density of the growth solution of composition Gd_2O_3:K_2O:P_2O_5=6:34:60 mol %

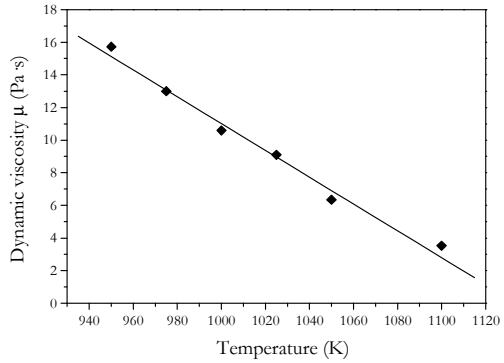

Figure 3.2. Thermal behaviour of the dynamic viscosity versus the temperature of the solution of composition Gd_2O_3:K_2O:P_2O_5=6:34:60 mol

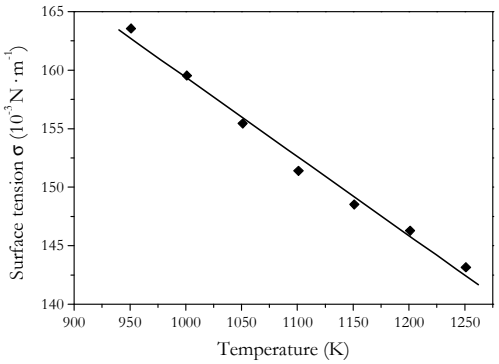

Figure 3.3. Thermal behaviour of the surface tension versus the temperature of the solution of composition Gd_2O_3:K_2O:P_2O_5=6:34:60 mol %

3.5. The crystal structure of $KGd(PO_3)_4$

At room temperature, the crystal structure of KGP is monoclinic and belongs to the noncentrosymmetric space group $P2_1$. We solved the structure of KGP for the first time and compared it to that of KNP, whose structure we also solved (see *paper III*). In fact, the KNP structure was first solved by Hong[74] but we noted some inconsistencies so we solved it again. However, both KNP structures were in rather good agreement. The cell parameters of KGP are: a=7.255(4) Å, b=8.356(5) Å, c=7.934(5) Å, β=91.68(5)°, and Z=2; those of KNP are: a=7.2860(10) Å, b=8.4420(10) Å, c=8.0340(10) Å, β=92.170(10)°, and Z=2. The KGP cell parameters are in good agreement with those previously calculated from the X-ray diffraction data using the FULLPROF program[107] and the Rietveld method[108], using the KNP structure solved earlier by single crystal X-ray diffraction as the starting model (see *paper I*).

Type III double polyphosphates of potassium and gadolinium belong to the family of long chain polyphosphates. Thus, their PO_4 tetrahedra are self-linked by sharing two vertexes to form chains. The basic unit of these chains consists of four PO_4 tetrahedra, which repeats by periodicity to generate the zigzag chains along the **a** crystallographic direction (Figure 3.4).

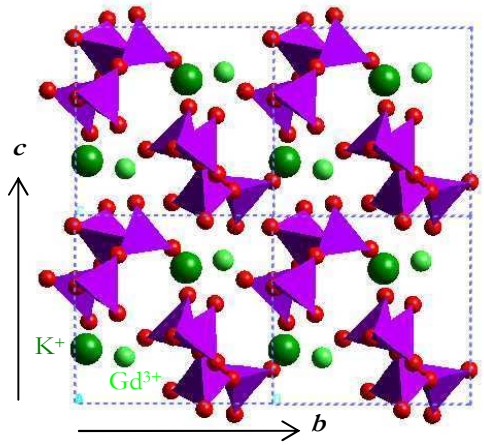

Figure 3.4. Zigzag arrangement of the PO_4 long chains along [100] in a projection parallel to[100]

The chains are joined through the Gd^{3+} and K^{+} ions because they share the two other vertexes. These ions are also in a zigzag arrangement parallel to the PO_4 chains. The PO_4 tetrahedra are slightly distorted because the intrachain bond distances O-P-O are larger than those of the interchain O-P-Gd or O-P-K. The distortion parameter <*d*>, defined in *paper III*, is relatively high. The <*d*> values for P_1, P_2, P_3, and P_4 (Figure 3.5) are $1.79x10^{-3}$, $4.58x10^{-3}$, $4.48x10^{-3}$ and $3.71x10^{-3}$, respectively.

The gadolinium ions are eight-coordinated with oxygen atoms to form a distorted dodecahedron. These GdO_8 dodecahedra are isolated from each other since they only share oxygen atoms with the PO_4 tetrahedra to join the chains. Each GdO_8 dodecahedron is surrounded by four other dodecahedra at long distances of about 7 Å (Figure 3.5).

The potassium ions are also eight-coordinated with oxygen atoms and have the largest bond distances in the structure. The potassium ions are placed close to the holes in the $[Gd(PO_3)_4]^-$ three-dimensional framework.

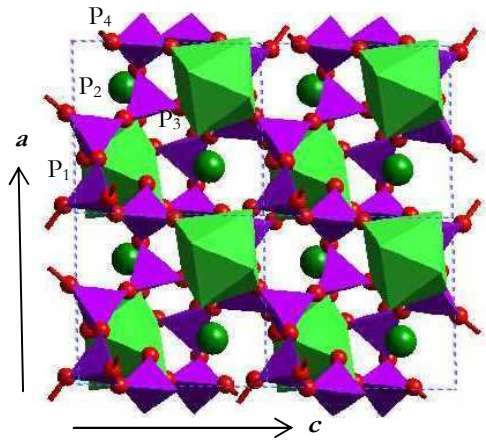

Figure 3.5. GdO_8 dodecahedra and potassium ions close to the $[Gd(PO_3)_4]^-$ framework holes in projection parallel to [010]

3.6. Effect of temperature on $KGd(PO_3)_4$ and isostructurals

Before crystals are used as laser emitters, it is essential to study how the structure is affected by temperature. The evolution of anisotropy must also be evaluated.

3.6.1. Thermal expansion ellipsoid

We analyzed how the cell parameters *a*, *b*, *c* and β and cell volume (*V*) evolved with the increase in temperature by applying the FULLPROF program[107] and the Rietveld method[108] the X-ray powder patterns recorded between room temperature and 773 K.

Figure 3 in *paper I* shows the linear relationship between the average change in each parameter and the temperature for KGP, and Figure 3 in *paper IV* shows the same for KNP. Both materials behaved in almost the same way: both of them slightly dilated as the temperature increased. Whereas the β angle remained almost constant, the cell parameters *a*, *b*, and *c* increased in a similar way though *c* slightly less so.

This almost isotropic dilation prevents crystals from deforming during laser operation and is advantageous for crystal growth and the processing of active elements.

The linear thermal expansion tensor of KGP and KNP (*paper I* and *IV*, respectively) reflected this low thermal anisotropy. The linear thermal coefficients (α_{ij}) were calculated from the slope of the linear relationship of each parameter ($\Delta L/L$) with the temperature. The axis with minimal thermal expansion of KGP was found to be 2.69º anticlockwise from the **c** direction.

3.6.2. Phase transitions

The phase transitions were studied between room temperature and 1273 K using differential thermal analysis (DTA) and X-ray powder diffraction analysis. Figure 5 in *paper I* shows the KGP thermogram where only one endothermic peak appeared at 1142 K. The sample weight was almost constant throughout the temperature range.

The X-ray powder diffraction patterns recorded in this range (Figure 6 in the same paper) show that at this temperature KGP decomposed into three

crystalline phases: $GdPO_4$, $Gd(PO_3)_3$, and $Gd_2P_4O_{13}$. There was some amorphous phase since there was no weight loss during the process. However, these phases behaved differently because at room temperature $GdPO_4$ was the only phase. $Gd(PO_3)_3$ completely transformed into $GdPO_4$ at 1273 K in the heating process and $Gd_2P_4O_{13}$ at 1223 K in the cooling process. Note that $GdPO_4$ and $Gd(PO_3)_3$ coincide with some of the neighbouring phases of the KGP crystallization region (see section 3.1).

We studied whether introducing ytterbium into the KGP structure affected its thermal transformations (see *paper II*). The decomposition temperature was slightly lower than that of KGP (1130 K) though it was not affected by the ytterbium content in the KGP structure (Figure 3 in the paper).

Yb:KGP decomposed without weight loss into four crystalline phases: $GdPO_4$, $Gd(PO_3)_3$, $Gd_2P_4O_{13}$, and GdP_5O_{14}. Three of them are common with KGP but the last one, which coincided with the remaining neighbouring phase of the crystallization region, is not. Between 1273 K in the heating process and room temperature only $GdPO_4$ and $Gd_2P_4O_{13}$ remained after the steady transformation of $Gd(PO_3)_3$ and GdP_5O_{14}.

KNP decomposed at 1165 K into two of the three previous phases: $NdPO_4$ and $Nd(PO_3)_3$ (see *paper IV*). $NdPO_4$ then became the only phase at room temperature because $Nd(PO_3)_3$ steadily transformed into it from 1173 to 1223 K, when it disappeared completely. Neither was any weight loss observed during the process, so another of the decomposition products of KNP was an amorphous phase. Both phases were also neighbouring on the KNP crystallization region.

In conclusion, we can say that the greater structural versatility of the gadolinium ion is reflected in the thermal decomposition of KGP and that the introduction of ytterbium in the KGP structure seems to strength this versatility. KNP has the simplest decomposition process.

3.7. Effect of Yb- and Nd-doping on $KGd(PO_3)_4$: variation of the lattice parameters

Figure 2 in *paper II* and Figure 4 in *paper III*, show the evolution of the lattice parameters *a*, *b*, *c*, and β, and volume as a function of the ytterbium and neodymium content in the KGP structure, respectively.

The crystal cell parameters *a*, *b*, and *c* and the volume slightly decreased as the concentration of ytterbium increased in crystals because it progressively substituted gadolinium in its structural position. The β angle remained roughly constant. The evolution was just the inverse when gadolinium was substituted by neodymium. However, all cell parameters evolved linearly with the concentration for both ions. Table 3 in *paper II* and Table 5 in *paper III* list the values of the cell parameters and the volume for each dopant concentration tested.

3.8. Crystal morphology of $KGd(PO_3)_4$

It is extremely important to know the morphology of any anisotropic material since all properties are highly dependent on the sample orientation and the crystals must therefore be well orientated when cutting and polishing (see section 2.3).

In the first steps of KGP crystal growth, when the seed orientation could still not be controlled, texture analyses were needed to correctly determine the morphology of the crystals grown, which seemed to be more symmetrical than they really were because of the unique 2-fold axis along the **b** direction. This was because the KGP structure is rather isometric. The cell parameters *a*, *b*, and *c* are similar and the β angle is very close to 90º. It was therefore necessary to use texture analysis to identify and orientate the crystalline forms that comprised the morphological habit of KGP.

Table 2 in *paper V* lists the crystalline forms {*hkl*}, equivalent faces, and d_{hkl} values for KGP. The values for KNP were included so that any changes caused by the

Nd^{3+} ion could be detected. Figure 6 in the paper shows the morphological scheme and the corresponding stereographic projections parallel to the **b** and **c*** directions. The projection parallel to **a*** direction is shown in *paper I*. Those projections parallel to directions **a*** and **c*** are very similar. In fact, crystals grown on **a***- or **c***-oriented seeds were not only comparable but were also easily confused. Therefore, the pole figures for faces (200) and (002) were recorded and analysed. The **b** orientation was also determined by comparing the theoretical and experimental angles between the faces (200) and (220) or (002) and (022). All these texture analysis and their results are described in *paper V*. Figure 3.6 shows the morphological scheme of KGP and isostructurals in projection parallel to the **a***, **b**, and **c*** directions drawn with the Software Shape utility[123]. Another morphological aspect complicated by the β angle being so close to 90º is that it is difficult to determine whether the **b** direction is positive or negative. This distinction is essential if the optical frame is to be correctly orientated with respect to the crystallographic frame in monoclinic crystals. *Paper V* also deals with this aspect.

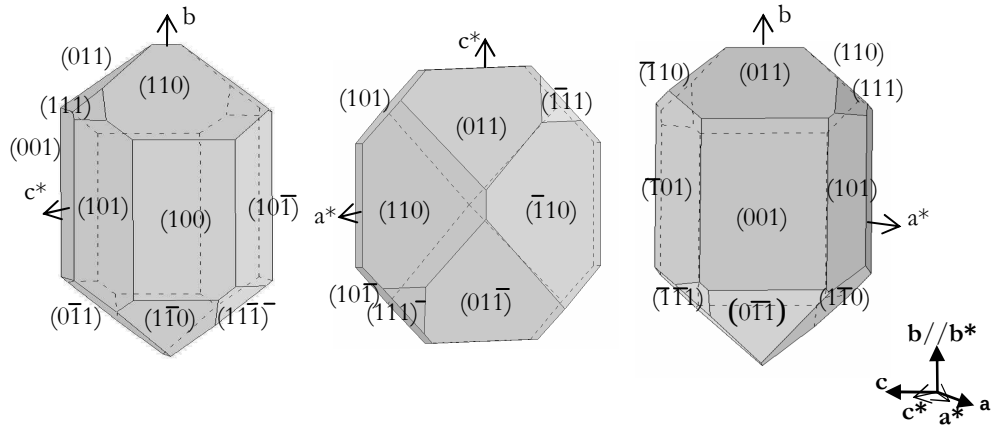

Figure 3.6. Morphological scheme of KGP and isostructurals in projection parallel to **a***, **b**, and **c*** directions. Direct (**a, b, c**) and reciprocal (**a*, b*, c***) lattices are indicated.

There were no important morphological changes in KGP crystals when doping with either ytterbium or neodymium. A slight tendency to twinning was observed

when the ytterbium concentration in solution was increased (see figure 1 in *paper II*). The morphological habit of KNP is equivalent to that of KGP (see *paper IV* and *V*). The (020) face was observed only very occasionally in KGP crystals but never in doped KGP or KNP.

3.9. Crystal growth of single crystals of $KGd(PO_3)_4$ and isostructurals

The conditions and results of the crystal growth experiments can be found in all the papers in this Thesis (see *papers I-IV*). In this section, therefore, we make a general analysis of the results of growing KGP, Yb:KGP, Nd:KGP, and KNP.

Preliminary growth experiments of undoped and doped KGP were made in a small crucible (25 cm^3) using a flux consisting of the corresponding lanthanide (i.e. gadolinium, ytterbium, and neodymium), potassium, and phosphorous oxides. The growth of KNP crystals from their self-flux had already been reported[74] though the information was not very extensive. In the paper, tiny platelet-shaped KNP crystals were obtained from a flux composition of Nd_2O_3:K_2O:P_2O_5=10:30:60 mol %. We successfully grew bulk single crystals of KNP using this solution composition although their quality left something to be desired. However, this composition could not be used to grow KGP crystals since it was outside of the type III crystallization region. From this composition, the isomorph type A $KGdP_4O_{12}$ crystallizes (Figure 1 in *paper I*). To grow KGP crystals, we chose a solution composition inside its crystallization region close to that for KNP, it was Gd_2O_3:K_2O:P_2O_5=6:34:60 mol %. As the crystallization region of KGP was contained within that of KNP, this composition was also suitable for growing KNP.

In order to evaluate the effect of the solution composition on the crystal growth process, we chose two other solution compositions in the area common to both crystallization regions. These were Ln_2O_3:K_2O:P_2O_5=7:31:62, and 4:31:65 mol %, with Ln=Gd and Nd. The main effect of the solution composition was on its

viscosity. The relationship between the two compositions was qualitatively predicted during crystallization region studies and confirmed by the results of the crystal growth experiments. The viscosity increased when either the phosphorous or the potassium oxide concentrations increased, though the increase in P_2O_5 had a more dramatic effect than of the increase in K_2O. The increase in viscosity not only decreased the growth rate but also increased the number of macrodefects in the crystals (e.g. polycrystallization, inclusions, and cracks). Therefore, the P_2O_5 concentration was not raised from 60 mol % to grow both undoped and doped KGP crystals. The optimal solution composition was therefore Gd_2O_3:K_2O:P_2O_5=6:34:60 mol %. This corresponded to a Gd_2O_3/K_2O molar ratio of 15/85, which ensured the stability of the type III phase since it was placed far enough from the crystallization region border with type A $KGdP_4O_{12}$. This composition also led to low viscosity because it was in the zone that was poorest in K_2O. Although the viscosity of the composition Gd_2O_3:K_2O:P_2O_5=6:34:60 mol % was slightly higher than that of 10:30:60 mol %, we decided that the optimal solution composition for growing KNP was 6:34:60 mol % to assure the type III phase stability, as in the case of KGP.

After the preliminary experiments, we could ensure that KGP and Nd-doped KGP, and even the stoichiometric KNP, would grow under almost the same conditions. On the other hand, we encountered many more difficulties when growing Yb-doped KGP. This was probably because the corresponding stoichiometric crystals, KGP and KYbP, are not isostructural to each other (see Table 1.4). Moreover, the crystallization region of Yb:KGP was narrower than that of KGP for an ytterbium content higher than the 10 mol % in solution. The flux composition was therefore determined not only by the viscosity of the solution but also by the stability of the type III phase. However, the P_2O_5 concentration was kept at 60 mol % and the solution composition was chosen to be as near as possible to the optimal one (Yb_2O_3+Gd_2O_3):K_2O:P_2O_5=6:34:60 mol

%. Therefore, we used the composition (Yb_2O_3+Gd_2O_3):K_2O:P_2O_5=4:36:60 mol % to grow those Yb:KGP crystals with an ytterbium content in solution higher than 10 mol %. Adding either ytterbium or neodymium to the solution did not cause a substantial change in its viscosity.

In these experiments, no additional stirring was used apart from the rotation of the seed/crystal pair. The first seeds were obtained from crystals grown by spontaneous nucleation on the solution surface. The crystals were then oriented using texture analysis and the seeds were prepared (i.e. cut and polished) as parallelepipedic seeds oriented parallel to the **a***-, **b**-, and **c***- crystallographic directions. These were typically 10 mm long in the axial direction and 2 mm thick in the radial directions of rotation. As long as possible, crystals were grown with seeds of the same composition in order to avoid cracks caused by the slight lattice mismatch between the seed and the crystal. KGP single crystals were able to grow on **a***-, **b**-, and **c***-oriented seeds. The quality of the crystals was not affected by seed orientation but it was the growth rate. Crystals grew fastest on **c***-oriented seeds and slowest on **b**-oriented seeds. However, crystals grown on **c***-oriented seeds were sometimes lost because of the cleavage plane normal to this direction. Although there is another cleavage plane normal to the **b** direction, crystals grown on seeds oriented parallel to the **b** direction were never lost. This effect was usual for KNP crystals but was hardly observed for KGP and Yb- or Nd-doped KGP. Therefore, we generally used **a***-oriented seeds to grow the crystals but depending on the desired shape and orientation of the sample to be prepared from the crystal, we sometimes used **b**- and **c***-oriented seeds.

KGP single crystals were grown by cooling the solution at a rate of 0.1 $K \cdot h^{-1}$ so that the growth system seed/solution had enough time to reach conditions near to the thermal equilibrium. It seems that crystallization units can be incorporated onto the seed/crystal surface more efficiently at slow cooling programs. This led to higher growth rates and crystal quality. KNP crystals were successfully grown

using the same cooling rate. Although we expected the same for Nd:KGP, the incorporation of a foreign ion into the KGP structure led to more macroscopic defects (basically inclusions). Inclusion-free single crystals of Nd:KGP were only obtained when the cooling rate was reduced by half (0.05 K/h). This effect was even more dramatic when ytterbium was added since the difference between the ionic radii is higher. Moreover, the crystals were usually polycrystalline because those with an ytterbium content in solution higher than 10 mol % were grown from a flux that was slightly more viscous. So, to obtain macrodefect-free crystals, the cooling rate had to be reduced to 0.02 K/h, which doubled the time of the growth process to obtain around the same size of crystals. The higher the viscosity, the more difficult the mass transport in the solution. To induce a convection flow high enough to enhance the mass transport in solution and to the seed/crystal surface rotation velocities needed to be high not only to grow Yb:KGP crystals but also undoped KGP and Nd:KGP because the viscosity is comparable. We rotated the seed/crystal pair at velocities of 45, 60, 75, and 100 rpm. Up to 75 rpm, both the quality of the crystals and the growth rate increased as the velocity also increased. But when the pair was rotated at a rate higher than 75 rmp, it produced a negative effect on the crystal morphology. Figure 3.7 shows the shape of the crystals that were grown at a rotation rate of 100 rpm. Therefore, we used a rotation velocity of 75 rpm to grow all the crystals.

Figure 3.7. Crystal shape produced in KNP crystals when the rotation velocity is too high

The greatest difficulties encountered in growing of these crystals were created by the high viscosity of the solution. This viscosity also caused the lower part of the crystal to redissolve because a solution drop adhered to it during extraction and cooling. This led to many surface defects on the as-grown faces besides of their rounding (Figure 3.8 (b) and (c)). To prevent this from occurring, the crucible was placed in just the right position inside the furnace so that the axial gradient above the solution was greater than inside it. To cool the crystal, it was placed near the solution surface (around 2 cm from it) where the temperature was slightly lower than on the solution surface. The axial gradient in the solution was rather high, around 1 K/mm, to enhance natural convection (i.e. the mass transport).

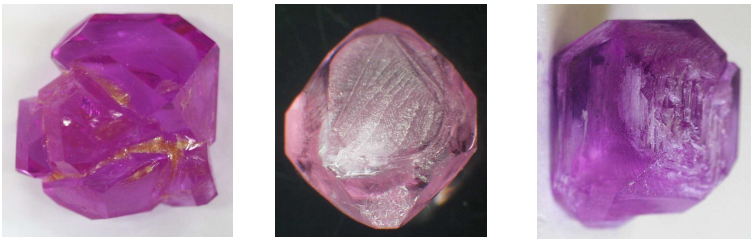

(a) (b) (c)

Figure 3.8. Defects related to the high viscosity of the growth solution. (a) polycrystallization, (b) rounding, (c) surface defects

To counter to the difficulties caused by the high viscosity, we replaced the single seed holder with one that could support two seeds and equipped with a platinum turbine to enhance the mass transport. The stirrer rotation was reversed every 60 seconds. Then, a bigger crucible was used (125 cm^3). Both the acentric position of the seed and the additional stirring of the turbine helped to increase the transport of the crystallization units to the seed/crystal surface. When this additional stirrer was used not only was the growth process accelerated because of the faster homogenization and growth rate but the quality of the crystals was

also enhanced. To obtain bigger crystals, we placed only one acentered seed in the stirrer.

Table 3.1 and 3.2 summarize the main growth data of with KGP and KNP single crystals, respectively. Crystals grown using the small crucible (20 g) were always centered and had no additional stirring. Crystals were always grown using the stirrer in the big crucible (200 g). The main growth data of Yb:KGP are summarized in Table 1 in *paper II*. To conclude, Table 3.3 summarizes the growth conditions optimized to grow the KGP, Yb:KGP, Nd:KGP, and KNP single crystals. Figure 3.9 shows some of the crystals obtained.

Table 3.1. Growth data associated for KGP single crystals

A	B	C	D	E	F	G	H	I
4:31:65	20	918	**a***	15K/0.1	75	1.4x2.4x1.8	0.01	inclusions
6:34:60	20	959	**a***	16K/0.1	60	2.7x8.8x6.0	0.28	good
6:34:60	20	951	**a***	14K/0.1	75	3.4x7.1x5.5	0.30	very good
6:34:60	200	942	**a***	19K/0.1	75	5.9x15.6x10.3	1.77	very good
6:34:60	200	956	**b**	20K/0.1	75	8.1x4.2x9.3	1.52	very good
6:34:60	200	950	**c***	20K/0.1	75	11.0x16.2x5.6	1.94	some cracks

A: solution composition Gd_2O_3:K_2O:P_2O_5 (mol %), **B**: solution weight (g), **C**: T_s (K), **D**: seed orientation, **E**: cooling program (Kh^{-1}), **F**: rotation velocity (rpm), **G**: crystal dimensions *a* x *b* x *c* (mm^3), **H**: crystal weight, **I**: crystal quality

Table 3.2. Growth data associated for KNP single crystals

A	B	C	D	E	F	G	H	I
10:30:60	20	1140	**a***	17K/0.1[1]	45	2.7x8.8x6.7	0.32	some cracks
10:30:60	20	1136	**b**	15K/0.1	45	7.1x2.6x9.0	0.33	good
10:30:60	20	1138	**c***	12K/0.1	45	---	---	---
10:30:60	20	1146	**a***	16K/0.1	60	3.0x9.1x6.8	0.36	good
10:30:60	20	1152	**a***	12K/0.1	75	2.8x8.9x6.5	0.38	good
6:34:60	20	1078	**a***	16K/0.1	75	3.5x9.3x6.9	0.47	very good
7:31:62	20	1138	**a***	17K/0.1	60	3.1x7.8x8.5	0.34	cracks
4:31:65	20	1025	**a***	24K/0.1	60	2.6x8.7x7.5	0.26	inclusions /cracks
6:34:60	200	1066	**a***	17K/0.1	75	7.0x16.3x11.7	2.16	very good
6:34:60	200	1045	**b**	19K/0.1	75	16.0x6.2x6.2	1.98	very good

Table 3.3. Optimal growth conditions to grow KGP, Yb:KGP, Nd:KGP, KNP

	A	B	C	D
KGP	0:6:34:60	0.1	75	**a*, c***
Yb:KGP	X:6-X:34:60 (X=0.18-0.6)	0.05	75	**a*, c***
	X:4-X:36:60 (X<0.12 or X>0.4)	0.02	75	**a*, c***
Nd:KGP	X:6-X:34:60	0.05	75	**a*, c***
KNP	6:0:34:60	0.1	75	**a***

A: Solution composition Ln_2O_3:Gd_2O_3:K_2O:P_2O_5 (mol %), where Ln_2O_3 = Yb_2O_3, Nd_2O_3, **B**: cooling rate (Kh^{-1}), **C**: rotation velocity (rpm), **D**: seed orientation

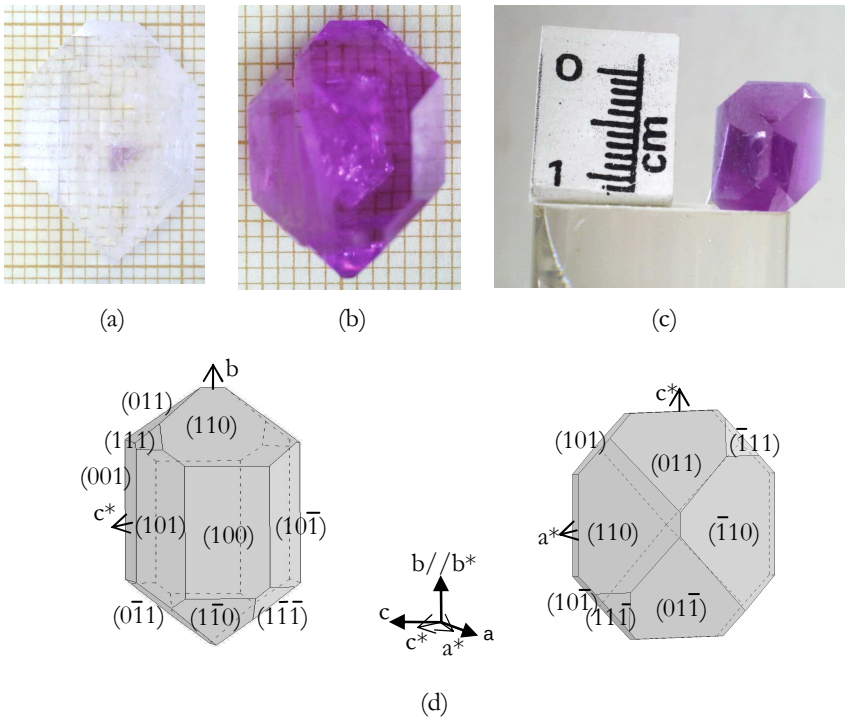

Figure 3.9. (a) **a***-oriented KGP crystal, (b) **a***-oriented KNP crystal gd, (c) **b**-oriented KGP crystal , (d) morphological schemes in projection parallel to **a*** and **b**, (e) **b**-oriented KNP crystal on the stirrer, (f) KNP single crystal, (g) **c***-oriented Yb:KGP crystal

3.10. Dopant concentration analysis

The results of EPMA enable the concentration and distribution coefficients for each doping in *papers II and III* to be calculated. The results are summarized in Table 3.4.

Table 3.4. Distribution coefficients of Yb, Nd, and Gd in KGP crystals

Solution composition *Ln_2O_3:Gd_2O_3:K_2O:P_2O_5 (mol %)	K_{Yb}	K_{Nd}	K_{Gd}	Ln concentration (cm^{-3})	Chemical formula
0.04:3.96:36:60	0.50		1.01	$2.081x10^{19}$	$KYb_{0.005}Gd_{0.995}(PO_3)_4$
0.18:5.82:34:60	0.53		1.01	$6.656x10^{19}$	$KYb_{0.016}Gd_{0.981}(PO_3)_4$
0.3:5.7:34:60	0.48		1.03	$1.007x10^{20}$	$KYb_{0.024}Gd_{0.976}(PO_3)_4$
0.6:5.4:34:60	0.40		1.07	$1.653x10^{20}$	$KYb_{0.040}Gd_{0.960}(PO_3)_4$
0.6:3.4:36:60	0.51		1.02	$3.203x10^{20}$	$KYb_{0.077}Gd_{0.923}(PO_3)_4$
0.8:3.2:36:60	0.58		1.10	$4.831x10^{20}$	$KYb_{0.116}Gd_{0.884}(PO_3)_4$
1.2:2.8:36:60	0.66		1.14	$8.271\ x10^{20}$	$KYb_{0.198}Gd_{0.802}(PO_3)_4$
2:2:36:60	0.60		1.40	$1.241\ x10^{21}$	$KYb_{0.300}Gd_{0.700}(PO_3)_4$
0.03:5.97:34:60		1.33	0.99	$4.549x10^{19}$	$KNd_{0.010}Gd_{0.990}(PO_3)_4$
0.06:5.94:34:60		1.09	1.00	$5.026x10^{19}$	$KNd_{0.012}Gd_{0.988}(PO_3)_4$
0.3:5.7:34:60		1.06	0.99	$2.195\ x10^{20}$	$KNd_{0.056}Gd_{0.944}(PO_3)_4$
0.6:5.4:34:60		0.95	0.98	$4.916x10^{20}$	$KNd_{0.090}Gd_{0.910}(PO_3)_4$
1.5:4.5:34:60		0.99	0.99	$1.235x10^{21}$	$KNd_{0.247}Gd_{0.753}(PO_3)_4$
3:3:34:60		1.06	1.00	$2.186\ x10^{21}$	$KNd_{0.562}Gd_{0.438}(PO_3)_4$
4.5:1.5:34:60		1.01	1.02	$3.125\ x10^{21}$	$KNd_{0.765}Gd_{0.235}(PO_3)_4$

*Ln_2O_3 = Yb_2O_3, Nd_2O_3

There are some differences between the doping with ytterbium and with neodymium. Inserting Yb^{3+} into the KGP structure is much more difficult than inserting Nd^{3+} probably for structural reasons. On the one hand, the ionic radius of Nd^{3+} is much closer to that of Gd than that of Yb and, on the other, whereas KNP is isostructural to KGP, KYbP is not. These differences are reflected in the distribution coefficients. The coefficients for Nd^{3+} were approximately constant whatever the solution composition was and close to the unit. The coefficients for Yb^{3+} varied among the solution compositions and were close to half the unit.

3.11. Micromorphology of the as-grown faces

The micromorphology of the as-grown faces is the result of the solidification process occurring at the crystal-medium interface. Well-known theories[124,125] of crystal growth state that surface structures consist of growth steps of unit height emitted from dislocations on the face. In fact, the micromorphologies usually observed on faces are thicker and much more variable. On the as-grown faces of KGP crystals, growth macrolayers 100-350 times the unit height (around 80-300 nm) were commonly observed.

The usual surface structures generally consisted of highly polygonized macrohillocks made up of these growth macrolayers. Their perimeter shapes were always parallel to those of the external morphology of the face on which they appeared (Figure 3.10). These macrohillocks were attributed to unstable growth conditions similar to those of hopper morphology, when both the stability of the surfaces and the instability of the edges participate[126].

We observed also isolated macrohillocks on internal planes attributed, in this case, to growth dislocations. These macrohillocks were distributed rather parallel to the macrolayers, which were orientated parallel to the [100] direction.

In *paper V*, the micromorphologies observed on as-grown faces of KGP and KNP are extensively analyzed. Figures 3-5 in the same paper show the commonly observed figures.

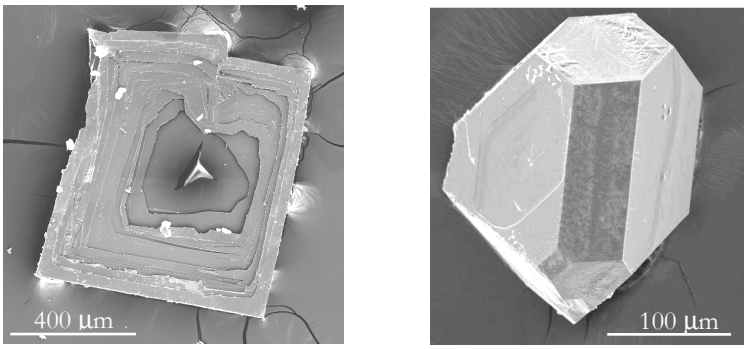

Figure 3.10. SEM image of polygonized growth layers on the (100) or (001) face of a KGP crystal

3.12. Chemical stability and micromorphology of the etched surfaces

To ensure that a laser device has a long useful life, it is essential to prove the inalterability of the laser crystal, which must be both non hygroscopic and stable in the presence of low acid and basic media.

To check the stability of KGP against various acid and basic etchants, a piece of crystal of each material was kept submerged in solution for different periods, from 1 minute to 100 hours. The samples were periodically weighted and observed using an optical microscope to localize possible etch pits. Etch pits are the most frequently observed figures on etched crystal surfaces and are often formed at the emergence points of dislocations. Their geometry depend on (i) external factors such as the composition and temperature of the etching solution and (ii) internal factors related to crystallographic aspects, the structure and type of the surface to be etched and the character and nature of defects. They are therefore manifestation of the anisotropy and chemical interactions of the crystal structure[127,128]. However, there is no universal theory that can predict all the observed etching pits, their location, their growth rate and, specially, their shape. Once localized the etch pits, they were ore accurately analyzed using a confocal microscope and a scanning electron microscope. The experimental methodology used and results of the chemical etching on crystal surfaces are described in detail in *paper V*.

KGP is nonhygroscopic and highly stable in normal room conditions. No weight loss was observed in low acid or basic media but in the stronger acid media, etch pits of various shapes were observed on several faces of the crystals. When we analyzed the etched (100), (001) and hand-made (010) faces of KGP, we found highly polygonal etch pits either at isolated positions or in rows. These etch pits appeared always well orientated on the faces and their contour walls corresponded to families of low-index planes[128]. This agreed with the polygonal macrohillocks of growth that have been observed. Probably, the crystal structure

mainly dominates the dissolution process. We observed hexagonal, rhombohedral, triangular and rectangular etch pits on different faces. Figure 8 in *paper V* shows a selection of these etch pits. Figure 3.11 shows some others. The sidewalls of these polygonal etch pits mostly corresponded to high- and low-index planes[129,130]. As well as these large deep etch pits, rows of smoother etch pits with a more spherical outline appeared on most faces (Figure 3.11. (a)). These rows seemed not to be dominated by the structure since they were distributed along different directions on the surface. Exactly the same effects were observed on as-grown faces of KNP crystals.

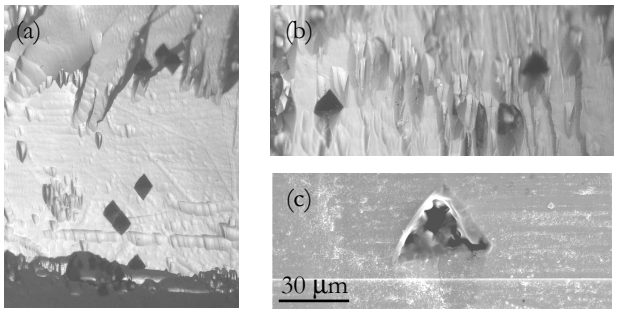

Figure 3.11. (a) Rhombohedral etch pits on the (100) plane, (b) triangular etch pits on the (001) planes, (c) SEM image of the triangular etch pits

3.13. Mechanical stability: microhardness and cleavage

The Vickers microhardness of KGP measured on the planes {100}, {010}, and {001} were H_v=668, 586, 648. These values were calculated with a reference load of 0.1 N because the impressions on the {010} plane were accompanied by radial cracks when the load values exceeded form 0.3 N. Figure 3.12 shows the indentations observed on these planes for various loads. The low anisotropy of microhardness may be due to the almost isometric structure of KGP. An average KGP microhardness can therefore be defined as H_v=634, which would correspond to hardness about 7 in the Mohs hardness scale. So type III KGP is as hard as quartz.

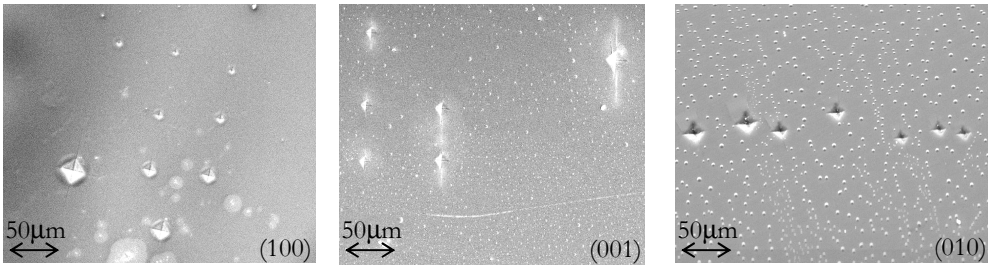

Figure 3.12. SEM images of indentations on {100}, {010} and {001} planes of KGP

We also tested KNP and obtained H_v=705, 633, 702 for KNP, so an average microhardness of H_v=680. KNP is slightly harder than KGP. However, its microhardness corresponds also to a hardness about 7 in the Mohs hardness scale. Hence, KGP, KNP, and Yb- or Nd-doped KGP are as hard as quartz. This high microhardness means that the polishing of the optical and laser surfaces can be of high quality.

Although these crystals are rather hard, they are also fragile. This is because they cleaved along the {010} and {001} planes. The cleavage behaviour is determined by the structural framework (see section 3.5). Because the P-O bonds generating the long chains ran along the [100] direction, this is the strongest bond direction. [010] and [001] directions are weaker and similar to each other. Therefore, the crystal framework agreed with the cleavage behaviour not only because of the bond strength but also in a more geometrical sense, since cleavage occurred between chains that were on each of the cleavage planes. *Paper V* deals with this subject.

On both cleavage planes usually appeared monolayer steps of height about the unit height *b* or *c* placed between much more thicker steps (multilayer steps). Both mono and multilayer steps were straight and always parallel to the [100] direction. Figure 3.13 shows a typical multilayer step distribution on a (010) cleavage plane of KGP. Figure 9 in *paper V* shows a selection of mono and multilayer steps on both cleavage planes and the related cross sections.

The density of both mono and multilayer steps was quite regular and higher on the {010} plane than on the {001} plane. The steps were also thicker on {010}.

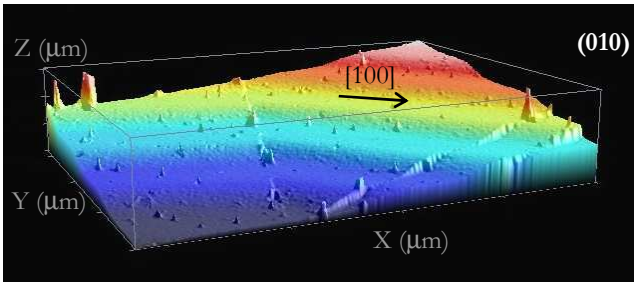

Figure 3.13. Confocal image of the multilayer steps observed on {010}

Chapter 4: Optical characterization of the host

For later applications, it is essential to fully characterize the host in which the active ions will be hosted. The potentialities of a new crystal such as solid-state laser or self-frequency doubling laser will be mostly determined not only by the spectroscopic properties of the active ions but also by the optical properties of the host.

4.1. Dielectric frame orientation

Using the crossed polarizers method (see section 2.10.1) we located the two principal axes on the **a-c** plane of a $KGd(PO_3)_4$ plate sample 1030 μm thick. Special care was taken to position the sample and ensure that the positive direction of **b** was toward us. We took the **c** direction as a reference. A minimum of light transmission (extinction position) was encountered when the sample was clockwise-rotated 37.3º from **c**. Another minimum was observed when the sample was anticlockwise rotated 90º from this first position. Figure 6 in *paper III* shows the $KGd(PO_3)_4$ optical ellipsoid at λ=632.8 nm and room temperature.

The same operation was carried out with $KNd(PO_3)_4$. We observed the first minimum of transmission when the sample was rotated 35.4º from **c** (Figure 6 in *paper III*).

The difference in the optical frame orientation between the stoichiometric crystals is of about 2º, so lower concentrations of Yb^{3+} or Nd^{3+} in the $KGd(PO_3)_4$ structure are not expected to disorient the optical frame.

Figure 4.1 shows the relative orientation between the optical and crystallographic frames and the optical axes of $KGd(PO_3)_4$ at λ=632.8 nm and room temperature. The angle V_g between the optic axis (***OA***) and the principal optical axis $\boldsymbol{N_g}$ in the $\boldsymbol{N_p}$-$\boldsymbol{N_g}$ plane.

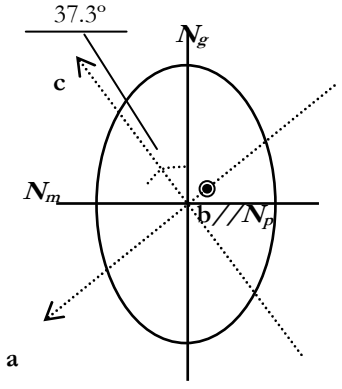

Figure 4.1. Relative orientation between the crystallographic frame (**a**, **b**, **c**) and the optical frame ($\boldsymbol{N_p}$, $\boldsymbol{N_m}$, $\boldsymbol{N_g}$) at λ=632.8 nm and room temperature. V_g is the angle between the $\boldsymbol{N_g}$ axis and the optic axis (***OA***).

4.2. Chromatic dispersion and thermal evolution of the refractive indices

Figure 1 in *paper VI* shows the chromatic dispersion of the principal refractive indices n_p,n_m and n_g of $KGd(PO_3)_4$ in the wavelength range between 0.45 and 1.2 μm. They were nearly equidistant, so the birefringence was similar between all polarizations over the visible and near-IR spectral regions. The same behaviour was observed when measuring the chromatic dispersion of $KNd(PO_3)_4$. Figure 4.2 shows the dispersion curves of $KGd(PO_3)_4$ and $KNd(PO_3)_4$. The points in the figure were fitted using one UV pole and an IR correction term with the Sellmeier equation:

$$n^2 = A + \frac{B}{1-\left(\frac{C}{\lambda}\right)^2} - D\lambda^2 \qquad \text{eq. 4.1}$$

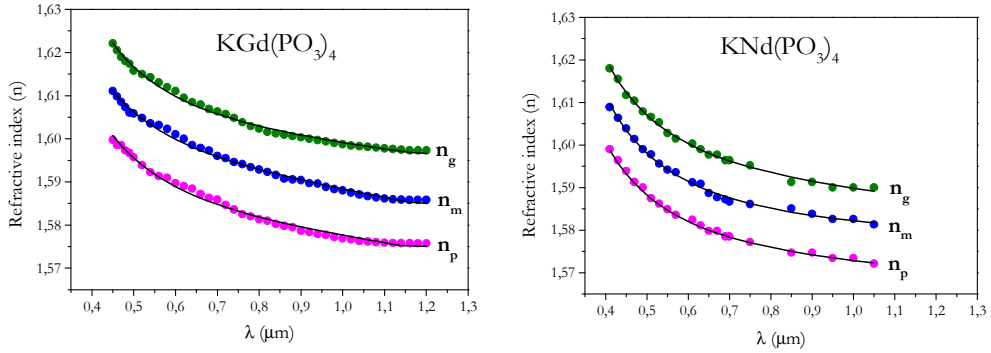

Figure 4.2. Chromatic dispersion of the principal refractive indices of $KGd(PO_3)_4$ and $KNd(PO_3)_4$ at room temperature

Figure 4.2 shows that the birefringence of both materials is quite similar but that the dispersion in $KNd(PO_3)_4$ is slightly higher than in $KGd(PO_3)_4$. The lack of data points in the IR region for $KNd(PO_3)_4$ is due to the strong absorption bands of neodymium in this region, which makes it impossible to visualize the reflected spots corresponding to the beams propagating parallel to the two principal directions measured in each case.

Table 4.1 summarizes the Sellmeier coefficients obtained for $KGd(PO_3)_4$ and $KNd(PO_3)_4$ at room temperature.

Table 4.1. Sellmeier coefficients of KGP and KNP

Principal refractive indices	*A*	*B*	*C*(μm)	*D*(μm^{-2})
KGP				
n_p	1.7404	0.7479	0.1374	0.0138
n_m	1.7624	0.7667	0.1304	0.0193
n_g	1.7728	0.7782	0.1391	0.0091
KNP				
n_p	1.7753	0.6888	0.1425	0.0048
n_m	1.7878	0.7003	0.1468	0.0001
n_g	1.8044	0.7151	0.1441	0.0069

Figure 4.3 shows how the principal refractive indices n_p,n_m and n_g of $KGd(PO_3)_4$ evolves with the temperature. They slightly decrease with temperature in the range between 298 and 383 K at λ=632.8 nm.

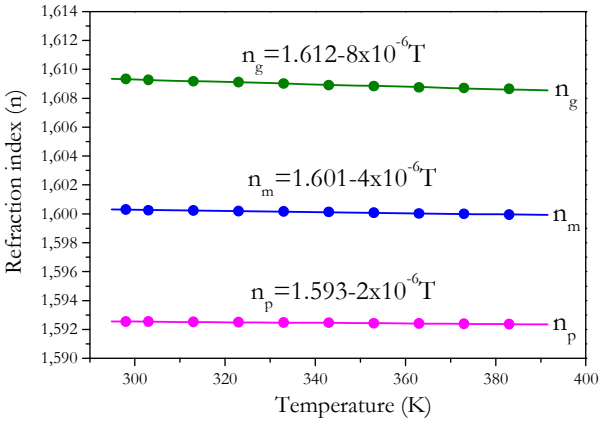

Figure 4.3. Temperature variation of the principal refractive indices of $KGd(PO_3)_4$ at λ=632.8 nm

The refractive index change induced by temperature gradient inside the active laser medium together with its thermal expansion cause thermal lensing. The

thermally induced refractive index change is called the thermooptic effect and is quantified by the coefficient dn/dT. For each principal refraction index of $KGd(PO_3)_4$, this coefficient is: dn_p/dT=-2.15x10^{-6}, dn_m/dT=-3.86x10^{-6} and dn_g/dT=-8.27x10^{-6} (K)$^{-1}$., which are lower than those of other nonlinear phosphate crystals such as KH_2PO_4 (KDP)[131] or $KTiOPO_4$ (KTP)[132]. The ratio of $dn/dT/k$, with k being the thermal conductivity, should be as small as possible to prevent thermal lensing effects. The focusing power (inverse focal length) of the thermal lens is proportional to this ratio by:

$$f^{-1} = \frac{dn/dT}{2kA} P_{heat} \qquad \text{eq. 4.2}$$

with A the pump area and the P_{heat} the dissipate power.

To avoid temperature gradient inside the crystal it is interesting to determine the athermal direction, along which the change in the optical path length is negligible as the material is uniformly heated. Along this direction, the refractive index change is compensated by the optical path length change[133]:

$$\frac{dn}{dT} = n\alpha \qquad \text{eq. 4.3}$$

where α is the thermal dilation.

4.3. Transparency window of the KGP host and variations introduced by doping

If a crystal is to be a good laser host it must be transparent in the wavelength range in which the active ions both absorb and fluoresce. From this point of view, $KGd(PO_3)_4$ is an excellent candidate to be a laser host since it has a very broad transmission window extending from about 180 nm to 4 μm. This covers the wavelength ranges of absorption, emission, and lasing of both active ions, Yb^{3+} and Nd^{3+}, as well as the second harmonic range. Its rather large band-gap not only leads to high damage resistivity but also enables this host to be used in the UV range either as a nonlinear crystal or as a host for cerium.

Figure 5 in *paper II* shows the transmission window of $KGd(PO_3)_4$ at room temperature. The UV and IR cut-offs are defined as the wavelength at which the transparency is decreased by an *e*-factor of its maximum value. The transmission window of $KNd(PO_3)_4$ was also measured and included in the same paper. It extended over the same wavelength range as that of $KGd(PO_3)_4$ but it had numerous strong absorption bands because the neodymium ions constantly interrupted the transparency.

Figure 6 in *paper II* shows the transparency window of $KYb_{0.0024}Gd_{0.976}(PO_3)_4$. The transmission range was also similar to that of $KGd(PO_3)_4$ (from 200 nm to 5.5 μm). There was a strong absorption band close to 1 μm corresponding to the ytterbium absorption $^2F_{7/2} \rightarrow {}^2F_{5/2}$.

The ultraviolet absorption bands close to the UV cut-off can affect the optical transparency of the crystal because they are related in many cases to the increase in susceptibility to optical damage, which is enhanced by the presence of dopant ions in the crystal. It can shift the UV edge to longer wavelengths. We checked therefore whether introducing Yb^{3+} or Nd^{3+} ions into the $KGd(PO_3)_4$ host produced this effect. As this shift was clearer when the absorption coefficient (α) being measured rather than the transmission, we measured the optical absorption of 1mm-thick plate samples of Yb:$KGd(PO_3)_4$ and Nd:$KGd(PO_3)_4$ between 175 and 500 nm. The cut-off wavelength in the UV region gradually shifted to longer wavelengths as the ytterbium concentration increased, for example to 208 and 205 nm for $KYb_{0.029}Gd_{0.971}(PO_3)_4$ and $KYb_{0.045}Gd_{0.955}(PO_3)_4$, respectively (see *paper II*). This shift was not observed when neodymium was introduced into $KGd(PO_3)_4$ whatever the concentration was.

The cut-off of the transmission window in the IR region is common to undoped and doped $KGd(PO_3)_4$ and, generally, to phosphate compounds in bulk crystals. The IR absorption edge is caused by the first and second overtones of the ν_3 and ν_1 fundamental vibrations of the phosphate ion in the PO_4 tetrahedra. The

thicker the sample is, the higher the intensity of the ν_3 band. So, depending on the sample thickness, the IR limit can be shifted from around 4 μm to higher wavelengths (figure 4.4).

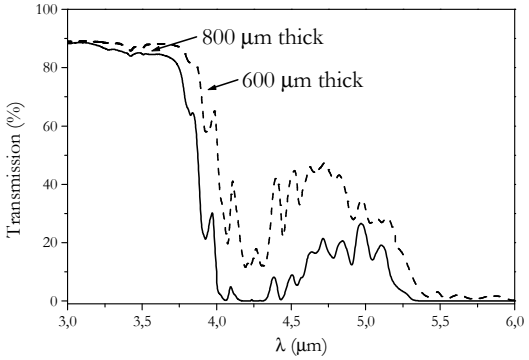

Figure 4.4. IR transmission limit of KGP as a function of the sample thickness

4.4. Non linear optical properties

The Kurtz and Perry analysis of powdered $KGd(PO_3)_4$ showed that its second harmonic generation efficiency (η) was comparable to that of standard KH_2PO_4 (KDP), η_{KGP}/η_{KDP} of the order of 1. This efficiency was not substantially different when gadolinium in $KGd(PO_3)_4$ was partially substituted by ytterbium or neodymium. Therefore, both undoped $KGd(PO_3)_4$ and Yb- or Nd-doped $KGd(PO_3)_4$ are equally efficient at doubling the fundamental radiation of λ=1064 nm.

We found that a crystalline sample of $KNd(PO_3)_4$ generated green light, which was detectable with the naked eye, by propagating along the principal optical axis $\boldsymbol{N_m}$. In the experiment, the fundamental laser beam (Nd:YAG, λ=1050 nm) was polarized parallel to $\boldsymbol{N_g}$ ($\boldsymbol{E_\omega // N_g}$) and the doubled beam was polarized parallel to $\boldsymbol{N_p}$ ($\boldsymbol{E_{2\omega} // N_p}$). No second harmonic generation was found by propagating the laser beam along $\boldsymbol{N_p}$, or $\boldsymbol{N_g}$..

In a phase-matching direction, the polarization configuration of the fundamental and doubled beams is fixed according to the type of the frequency mixing process and the power of the doubled wave ($P(\theta,\phi,\omega_3,L)$) highly depends on slight variations of the propagation direction and the fundamental wavelength. Therefore, we determined the angular and spectral acceptance to check if the principal optical axis $\boldsymbol{N}_m$ was a noncritical phase-matching direction.

The power of the doubled wave ($P(\theta,\phi,\omega_3,L)$) is highly dependent on the phase mismatch (Δk) (equation 2.9). If it is null, $\Delta k=0$, the light propagates along a phase matching direction and the power of the doubled wave increases as a quadratic function of L, which is the interaction length of the three waves ω_1, ω_2 and ω_3 involved in the frequency mixing process inside the crystal. In the particular case of SHG: $\omega_3= 2\omega$ and $\omega_1=\omega_2=\omega$. Contrary, if the light propagates along a phase mismatch direction, $\Delta k=k_{2\omega}-k_{\omega}-k_{\omega}\neq 0$, the power of the doubled wave is a periodical function of L with a spatial periodicity: $L_c = \pi/2\Delta k$, where L_c is the coherence length. During propagation inside the crystal, the sign of the power of the fundamental and doubled waves vary, thus the interference among the three waves is alternatively constructive and destructive with a period $2L_c$.

To determine the spectral acceptance along $\boldsymbol{N}_m$ we determined the power of the doubled wave by varying the wavelength of the fundamental wave from 980 to 1100 nm. A maximum doubled wave power was obtained at λ=1014 nm (Figure 4.5). The power of the doubled wave generated is critical with the wavelength of the fundamental wave, which would indicate that $\boldsymbol{N}_m$ is a phase matching direction.

The results of the spectral acceptance suggest that $\boldsymbol{N}_m$ could be close to a phase-matching direction. The power of the doubled wave generated propagating along $\boldsymbol{N}_m$ seemed to evolve critically with the wavelength of the fundamental wave.

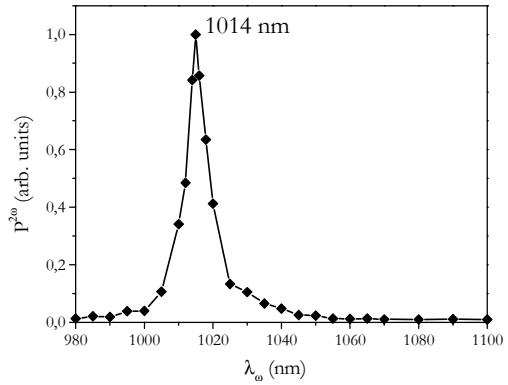

Figure 4.5. Evolution of the doubled wave power as a function of the fundamental wavelength

From the Sellemier equations of $KNd(PO_3)_4$ (Table 4.1) we calculated the phase-matching directions of this crystal. The optical sign of this family of crystals was not provided by the value of the V_g angle because it was too close to 45º. Neither the measurement of the refractive indices on the prisms using polarized light discriminated between the positive and negative optical sign. Therefore, we took into account both possibilities to make the calculations of the phase-matching directions.

The simulations on second harmonic generation (SHG) showed that $KLn(PO_3)_4$ crystals, with Ln=Nd, Gd, can be phase-matchable for type I SHG in the ***xy*** and ***yz*** planes. Phase-matching of type II SHG was found not to be possible in any plane. Finally, the calculated effective coefficients χ_{eff} were completely different between optical signs because they were close to zero for the positive sign and showed much more important values for the negative sign. Thus, we suggest that $KGd(PO_3)_4$, Yb- and Nd-doped $KGd(PO_3)$ and $KNd(PO_3)_4$ are negative biaxial crystals.

Figure 4.6 shows that in the wavelength region near to 1000 nm phase-matching for type I SHG on the ***xy*** plane is possible around $\phi \approx 55º$ for KGP and $\phi \approx 70º$ for KNP very close to the ***y*** or $\boldsymbol{N_m}$ principal optical axis and on the ***yz*** plane it is possible around $\theta \approx 55º$ for KGP and $\theta \approx 60º$ for KNP around 30-35º displaced

from ***y*** or $\boldsymbol{N_m}$. This situation equals simultaneously to a e-oo interaction in the ***xy*** plane and a o-ee interaction in the ***yz*** plane and it agrees with the indications of the spectral acceptance found for beam propagation along ***y*** or $\boldsymbol{N_m}$.

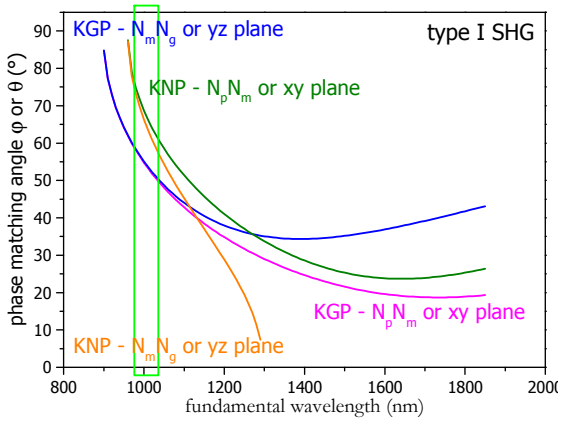

Figure 4.6. Type I second harmonic generation of $KGd(PO_3)_4$ and $KNd(PO_3)_4$ on the ***xy*** and ***yz*** planes

The wavelength range for which the crystal can be phase-matchable for type I SHG on the ***xy*** and ***yz*** planes perfectly covers the luminescence wavelength range of the Nd^{3+} ion in $KGd(PO_3)_4$ (see section 5.2.2), which has the maximum at λ=1.054 μm. It also covers the luminescence wavelength range of the Yb^{3+} ion (see section 5.1.2), which has the maximum at λ=0.977 μm and the oscillation wavelengths (see chapter 6) of $KYb_{0.024}Gd_{0.976}(PO_3)_4$ around λ=1.015 μm. Therefore, both Yb:$KGd(PO_3)_4$ and Nd:$KGd(PO_3)_4$ are very promising a candidates to be applied as self-frequency doubling crystals.

4.5. Raman spectroscopy

As the intermanifold electronic transitions of ytterbium are strongly coupled with lattice vibrations, knowledge of the phonon frequencies can be useful for interpreting the substructure in absorption and emission spectra.

Raman spectroscopic properties of phosphate crystals and glasses have been extensively studied. The properties of condensed polyphosphates are qualitatively the same for each O/P ratio. In $KGd(PO_3)_4$ this ratio is equal to three, which corresponds to metaphosphates. So, the Raman spectra of all polyphosphates have the same characteristic peaks independently of the geometry of the PO_4 units is as long-chains of as cycles. The spectra are affected neither by the number of repetitive units $(PO_3)_x$ which generate the chains or cycles and even neither by the lanthanide nor alkali ions in the structure. They therefore have the same characteristic peaks for all double polyphosphates or cyclopolyphosphates of lanthanide and alkali ions with general formulas $M^{I}Ln^{III}(PO_3)_4$ and $M^{I}Ln^{III}P_4O_{12}$, respectively.

All the Raman spectra have two characteristic strong peaks at around 1185 and 700 cm^{-1}. The strong peak at around 1185 cm^{-1}, which is accompanied by other weaker peaks in the region between 1000 and 1300 cm^{-1}, is a common feature of materials constructed from linked PO_4 tetrahedra. This peak is generally attributed to the symmetric stretching vibration ν_s of the PO_2 group, which corresponds to the motion of the nonbridging oxygen. The weaker peaks around it are assigned to symmetric ν_s and antisymmetric ν_a vibrations of the same group. The strong peak around 700 cm^{-1} is attributed to the symmetric stretching vibration ν_s of the P-O-P chain linkage. Very weak peaks attributed to symmetric ν_s and antisymmetric ν_a vibrations of the same group are often observed in the region between 650 and 1000 cm^{-1}. Peaks around this region are a useful indicator of the structure of metaphosphate.

We cut and polished about 1mm-thick plate samples of $KGd(PO_3)_4$, $KYb_{0.029}Gd_{0.971}(PO_3)_4$, and $KNd(PO_3)_4$ to make the Raman measurements. For all the samples, the laser propagation was parallel to the $\boldsymbol{N}_p$ principal optical axis, so the measurement involved the phonons propagating in this direction (i.e. the **b** direction). Unpolarized Raman spectra were recorded at room temperature

between 17 and 1700 cm^{-1}. Figure 5 *in paper II* shows the Raman spectra for $KGd(PO_3)_4$ and Yb:$KGd(PO_3)_4$.

To make it easy to compare the three crystals, the corresponding Raman spectra are shown in Figure 4.7.

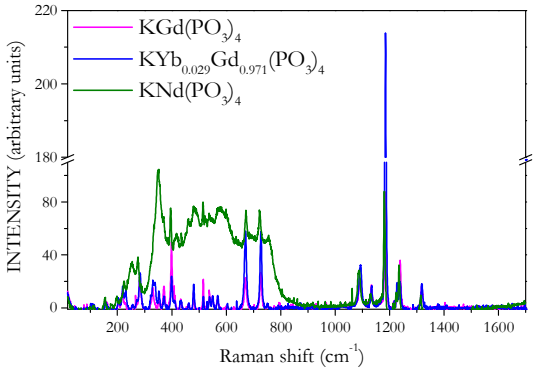

Figure 4.7. Raman spectra of $KGd(PO_3)_4$, $KYb_{0.029}Gd_{0.971}(PO_3)_4$, and $KNd(PO_3)_4$ at room temperature

As we expected, all the characteristic peaks for metaphosphate described above were present in the spectra. The strong peak of the symmetric stretching vibration ν_s of the PO_2 group at 1185 cm^{-1} was accompanied with some weaker peaks corresponding to symmetric ν_s and antisymmetric ν_a vibrations of the same group at 1318, 1239, 1227, 1134, and 1093 cm^{-1}. Two peaks were observed for the symmetric stretching vibration ν_s of the P-O-P chain linkage caused by the different positions of the lanthanide and alkali ions in the structure.[134]

Chapter 5: Spectroscopic characterization of the active ions in the KGP host

The spectroscopic properties of lanthanide ions are determined by their special electronic configuration[135]. All lanthanides are *f*-block elements, corresponding to the filling of the 4*f* electron shell. The 4*f* shell is efficiently shielded by the filled 5s and 5p outer shells and this means that the ligand environment has little influence on its electronic cloud. As a result, the absorption and emission spectra are characterized by very sharp lines and the energy level scheme varies slightly from one host to another. So, lanthanide ions largely behave like free ions. The effect of the crystal field is normally treated therefore as a perturbation of the energy level scheme of the free ions. Though it is weak, the crystal filed splits each of the free-ion energy levels (manifolds) into many closely spaced levels, which is called the Stark splitting. From the spectra of lanthanide ions, we can extract different information. The position of the peaks describes the electronic structure of the 4*f* shell; the splitting caused by the crystal field describes the symmetry of the lanthanide structural position and the shape of the coordination polyhedron; and the intensity of the spectral lines describes the interaction between the lanthanide and its environment[136]. Hence, a detailed spectroscopic study of the crystal must be made if its spectroscopic behaviour and the energy level scheme of the lanthanide ion are to be determined.

5.1. Spectroscopic properties of Yb^{3+} in $KGd(PO_3)_4$ crystals

The advantages of using ytterbium over neodymium as the laser-active ion in the 1 μm range have been extensively explained in section 1.2 and are largely the result of the simple energy level scheme of ytterbium made up of only two manifolds: the $^4F_{7/2}$ ground state and the $^4F_{5/2}$ excited state. Ytterbium can also be used to dope nonlinear crystals since it has no absorption bands in the green region. So, the inevitable reabsorption losses of neodymium in the wavelength range of the second harmonic can be avoided.

All the results found for Yb:$KGd(PO_3)_4$ reported in this section are based on a sample of composition $KYb_{0.024}Gd_{0.976}(PO_3)_4$ corresponding to an ytterbium concentration of 1.007×10^{20} cm^{-3}. The single crystal was cut and polished as a cube, accurately oriented along the $\boldsymbol{N_p}$, $\boldsymbol{N_m}$ and $\boldsymbol{N_g}$ principal optical axes, with dimensions of 2.34, 2.68, and 2.47 mm along these axes, respectively.

5.1.1. Optical absorption

As ytterbium has an odd number of electrons in the 4*f* shell (Yb^{3+}: $[Xe]4f^{13}$) polarization dependent selection rules are not expected but the intensity of the individual peaks may still vary. Therefore, we studied the polarized optical absorption of Yb^{3+} in $KGd(PO_3)_4$ along the three principal optical axes $\boldsymbol{N_p}$, $\boldsymbol{N_m}$ and $\boldsymbol{N_g}$. The absorption band associated with the ytterbium transition $^2F_{7/2}\rightarrow{}^2F_{5/2}$ in $KGd(PO_3)_4$ extends from 925 to 1025 nm (10800-9750 cm^{-1}) at room temperature (Figure 5.1). It is characterized by three main peaks centered at 977.5, 970.4, and 944.6 nm (10230, 10305 and 10586 cm^{-1}, respectively) for all three polarizations. As its rather isometric structure led us to expect, the anisotropy of the optical absorption was rather low though the absorption cross section was maximized for $\boldsymbol{E//N_m}$. The maximum cross section at 977.5 nm (zero line), calculated with the exact Yb^{3+} concentration of 1.007×10^{20} cm^{-3},

amounts to 1.17×10^{-20} cm^2. The corresponding maximum absorption cross sections at the same wavelength amount to 0.72×10^{-20} and 0.80×10^{-20} cm^2 for $\boldsymbol{E//N_p}$ and $\mathbf{E//}\boldsymbol{N_g}$, respectively. These values are similar to those reported for other nonlinear crystals such as $Yb:CaY_4O(BO_3)_4$[62], $Yb:CaGd_4O(BO_3)_4$[63] and $Yb:YAl_3(BO_3)_4$[66] and also to the well known $Yb:Y_3AlO_{12}$[41].

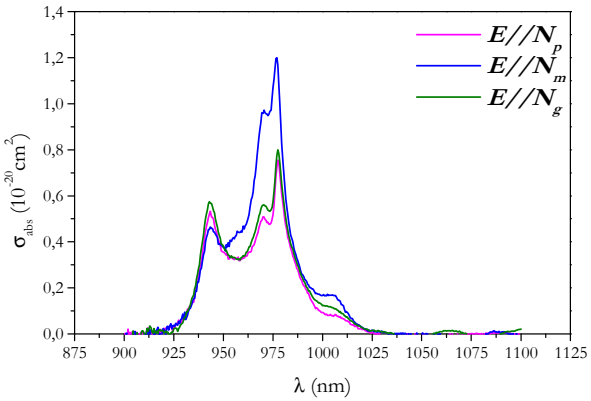

Figure 5.1. Absorption cross sections of $KYb_{0.024}Gd_{0.976}(PO_3)_4$ at room temperature for the three orthogonal polarizations

To accurately determine the energies of the three Stark sublevels of the excited state multiplet $^2F_{5/2}$, the polarised absorption spectra were measured at 6 K (Figure 5.2). The peaks in the spectrum are associated with the transitions from the ground sublevel $^2F_{7/2}(0)$, the most populated at low temperature, to the three excited sublevels $^2F_{5/2}(0')$ (zero line), (1'), and (2').

The absorption spectra at 6 K shows a substructure that may be related to phonon-electron coupled transitions, which are more pronounced for lanthanides at the beginning and the end of the series[137]. The polarized absorption with $\boldsymbol{E//N_m}$ was therefore studied between 6 K and room temperature. Figure 2 in paper VI shows the evolution of the absorption coefficient for $\boldsymbol{E//N_m}$ with the temperature between 6 and 300 K. The maximum absorption of the (0)→(0') transition decreased when the temperature increased because of the population

redistribution among the other sublevels of the ground state. When the temperature increased, an additional peak appeared at 10140 cm^{-1} though it anomalously disappeared at room temperature. This peak is probably related to the thermal population of the $^2F_{7/2}(1)$ sublevel with transition to $^2F_{5/2}(0')$.

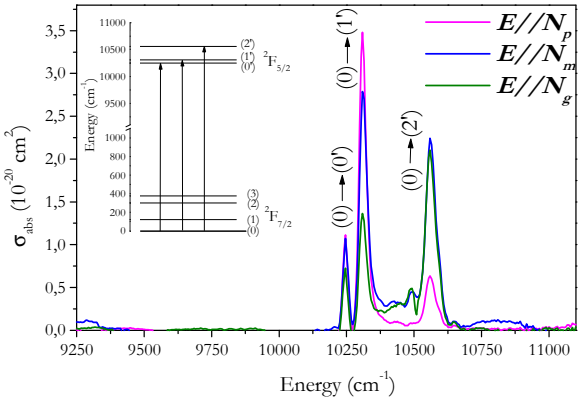

Figure 5.2. Absorption cross sections of $KYb_{0.024}Gd_{0.976}(PO_3)_4$ at 6K for the three orthogonal polarizations

5.1.2. Optical emission

The emission spectra of $Yb:KGd(PO_3)_4$ were studied at room and low temperatures to determine the emission channels and the Stark sublevels of the ground state multiplet $^2F_{7/2}$. The sample was pump at λ=0.94 μm. Figure 7 in paper II shows the polarized emission spectra for the three orthogonal polarizations both at 300 and 10 K. As expected, the anisotropy of the optical emission was rather low and even less than that of the optical absorption.

Figure 5.3 shows the emission spectra for $\boldsymbol{E//N_m}$ at both temperatures. The four main lines correspond to the transitions from the lowest excited sublevel $^2F_{5/2}(0')$ to the four ground sublevels $^2F_{7/2}(0)$, $^2F_{7/2}(1)$, $^2F_{7/2}(2)$, and $^2F_{7/2}(3)$. These are accompanied by phonon added peaks. A dim peak corresponding to the transition from the thermally populated $^2F_{5/2}(1')$ sublevel to $^2F_{7/2}(0)$ is also observed. The reduced intensity of the emission associated with the

$^2F_{5/2}(0') \rightarrow {}^2F_{7/2}(0)$ transition is a consequence of the reabsorption at this wavelength though this effect is lower than in other crystals. Reabsorption in this crystal is probably lower because the concentration of ytterbium is low and its absorption in this host is lower than for example in $KRE(WO_4)_2$ (RE=Y, Gd, Lu) (ten times higher) [138,139].

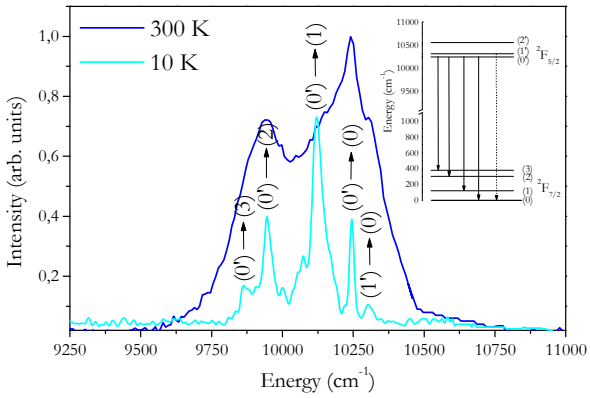

Figure 5.3. Emission spectra of $KYb_{0.024}Gd_{0.976}(PO_3)_4$ at 300 and 10 K for ***E//N$_m$***

Figure 5.4 shows a schematic diagram of the Stark sublevels and the absorption and emission transitions among them of Yb^{3+} in $KGd(PO_3)_4$ crystals obtained from the low temperature absorption and emission spectra.

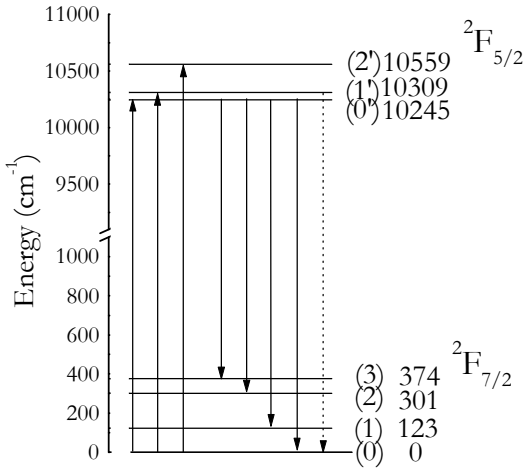

Figure 5.4. Schematic diagram of the Stark sublevels and transitions of Yb^{3+} in $KGd(PO_3)_4$

The crystal field splitting of $KGd(PO_3)_4$ is much lower than that of other well known materials such as $Yb:KRE(WO_4)_2$ [138,139], $Yb:RbTiOPO_4$[140] or $Yb:Y_3Al_5O_{12}$[141]. The crystal field of the $KGd(PO_3)_4$ host is much weaker probably because the gadolinium ions in the structure are isolated from each other since in all these structures, the lanthanide ion has the same distorted dodecahedron of coordination. The Ln-O distances are also comparable: 2.292-2.477 Å for $KGd(PO_3)_4$, 2.271-2.371 Å for $KGdWO_4$, and 2.303-2.432 Å for $Y_3Al_5O_{12}$ but the Ln-Ln distances are much larger for $KGd(PO_3)_4$ than for $KGdWO_4$ or $Y_3Al_5O_{12}$.

The reciprocity method[141] was used to compute the emission cross sections from the absorption cross sections at room temperature and the sublevel positions. The calculation is based on the equation:

$$\sigma_e(\nu) = \sigma_{abs}(\nu)\frac{Z_l}{Z_u}e\left[\frac{(E_{zl} - h\nu)}{kT}\right] \qquad \text{eq. 5.1}$$

where Z_u and Z_l are the partition functions of the ground and excited manifolds, respectively, and E_{zl} is the temperature-dependent excitation potential, which almost coincides with zero line energy[141].

Figure 4 in paper VI shows the calculated emission cross sections σ_e together with the corresponding absorption cross sections σ_{abs} for the three orthogonal polarizations. In the zero line (977.5 nm), the spectra are completely overlapped, so reabsorption is expected to be high even though the emission spectra show that it should be low because of the low doping level.

5.1.3. Lifetime measurements

The lifetime of the excited-state of Yb^{3+} needs to be measured in order to further characterize $Yb:KGd(PO_3)_4$ as a laser crystal. One of the most important parameters for a solid-state laser is the quantum efficiency (η_q) of its laser active

ions. This parameter is defined as the ratio of the radiative transition rate to the sum of the radiative and nonradiative transition rates:

$$\eta_q = \frac{W_{rad}}{W_{rad} + W_{nonrad}} = \frac{\tau}{\tau_{rad}} \qquad \text{eq. 5.2}$$

So, by measuring the fluorescence decay time (τ) and comparing it to the radiative lifetime (τ_{rad}), the quantum efficiency can be easily calculated.

In order to obtain accurate values for the fluorescence decay time in Yb-doped crystals, radiation trapping must be taken into account. This effect is due to the large degree of overlap between the absorption and the emission bands of the ytterbium ion. The measured decay time of a bulk sample is generally not an indicator of the true fluorescence lifetime because much of the radiation emitted from an Yb^{3+} ion can also be reabsorbed by a neighbouring Yb^{3+} ion. This effect increases the measured decay time and can combine with the total internal reflection (TIR) of all the radiation that impinges on the sample-air interface above a certain angle. The average refractive index of $KGd(PO_3)_4$ is around 1.6 (see Figure 4.2) and leads to an angle of 38.7°. TIR increases the emission path length in the crystal and artificially lengthens also the measured decay time.

To eliminate both effects, very thin samples or low ytterbium-doped or diluted samples should be used to measure decay times. The measurement of accurate decay times has been discussed in the literature and several solutions have been proposed[142,143,144].

We used the pinhole method to minimise the radiation trapping when measuring the decay time of $KYb_{0.024}Gd_{0.976}(PO_3)_4$. This method consists of exciting the sample, a thin crystal plate is better than a bulk crystal, through an aperture with various pinhole diameters and measuring the fluorescent decay from the same side. The extrapolation of the measured decay time data to zero diameter yields an accurate lifetime that is not effected by radiation trapping.

Figure 5.5 shows that the radiation trapping in $KYb_{0.024}Gd_{0.976}(PO_3)_4$ was very low, probably because of the low Yb^{3+} doping level in the sample. This agrees with the small discrepancy between the decay time measured from the bulk sample, which was 1486 μs and the radiative lifetime obtained from the pinhole measurements, which was 1223 μs.

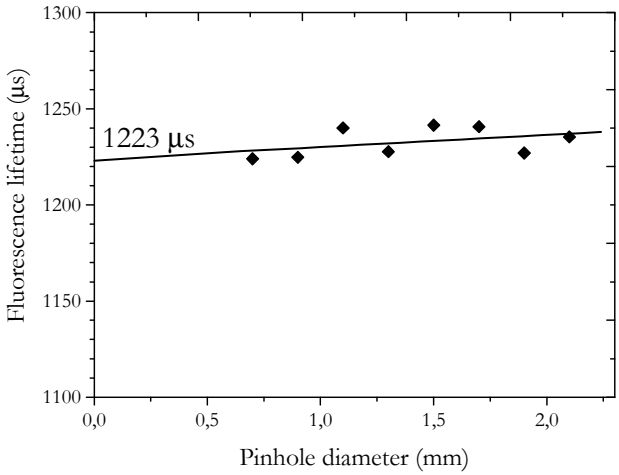

Figure 5.5. Fluorescence lifetime of $KYb_{0.024}Gd_{0.976}(PO_3)_4$ versus the pinhole diameter

When the $\sigma_e(\nu)$ calculated by the reciprocity method was averaged over the three polarizations, a radiative lifetime of τ_{rad}=1570 μs is obtained at room temperature using the Füchtbauer-Ladenburg equation[141]. The discrepancy originating from the thermal distribution in the ground state manifold at room temperature when calculating $\sigma_{abs}(\nu)$ can be suppressed by integrating the corresponding equation over the frequency.

$$\frac{1}{\tau_{rad}} = 8\pi n^2 \int \frac{\langle \sigma_e(\nu) \rangle}{\lambda^2} d\nu \qquad \text{eq. 5.3}$$

The ration between the measured fluorescence radiative lifetime and the calculated radiative lifetime leads to a quantum efficiency of 80% for $KYb_{0.024}Gd_{0.976}(PO_3)_4$.

5.1.4. Laser parameters

The absorption and emission cross sections and the measured lifetime are useful for estimating of some important laser parameters. The pump ($I_{p,sat}$) and the laser ($I_{l,sat}$) saturation intensities are defined as intensity values at which the absorption at the pump wavelength and the gain at the laser wavelength, for infinitesimally thin samples, are reduced to 50% of their small signal values.

For pump and laser transitions that are decoupled, these intensities are simply given by:

$$I_{p,sat} = \frac{h\nu_{pump}}{\sigma_{abs}\tau} \qquad \text{eq. 5.4}$$

$$I_{l,sat} = \frac{h\nu_{laser}}{\sigma_{e}\tau} \qquad \text{eq. 5.5}$$

However, in active media with overlapped absorption and emission spectra, like he quasi-three-level system of Yb^{3+}, the expressions are more complex. The pump saturation intensity increases with the intracavity laser intensity I_l and the laser saturation intensity increases with the pump intensity I_p.

$$I_{p,sat}(I_l) = I_{p,sat}(I_l = 0)\left(1 + \frac{I_l}{I_{l,sat}(I_p = 0)}\right) \qquad \text{eq. 5.6}$$

$$I_{l,sat}(I_p) = I_{l,sat}(I_p = 0)\left(1 + \frac{I_p}{I_{p,sat}(I_l = 0)}\right) \qquad \text{eq. 5.7}$$

In the case of zero laser intensity (laser threshold), the pump saturation intensity in eq. 5.6 is given by:

$$I_{p,sat}(I_l = 0) = \frac{h\nu_p}{[\sigma_{abs}(\lambda_p) + \sigma_e(\lambda_p)]\tau} \qquad \text{eq. 5.8}$$

Similarly, for the laser saturation intensity at zero pump intensity in eq. 5.7 one has:

$$I_{l,sat}(I_p = 0) = \frac{h\nu_l}{[\sigma_{abs}(\lambda_l) + \sigma_e(\lambda_l)]\tau} \qquad \text{eq. 5.9}$$

Thus the bleaching of the absorption and the depletion of the gain in the quasi-three-level system are stronger because the corresponding saturation intensities from eq. 5.8 and 5.9 are lower in comparison to eq. 5.4 and 5.5, but both these effects can be compensated by the actual pump and laser intensities which increase the pump and laser saturation intensities, respectively, in accordance with eq. 5.6 and 5.7.

In the presence of reabsorption at the laser wavelength, it is useful to define a gain cross section (σ_g) as:

$$\sigma_g = \beta\sigma_e - (1-\beta)\sigma_{abs} \qquad \text{eq. 5.10}$$

where the inversion parameter is defined by $\beta = N_1/N$ with N_1 as the population of the upper laser level and N the total number of active centres (ions).

The wavelength dependence of σ_g for a given inversion value, which depends on the cavity loses, gives information on the expected oscillation wavelength in the continuous wave regime.

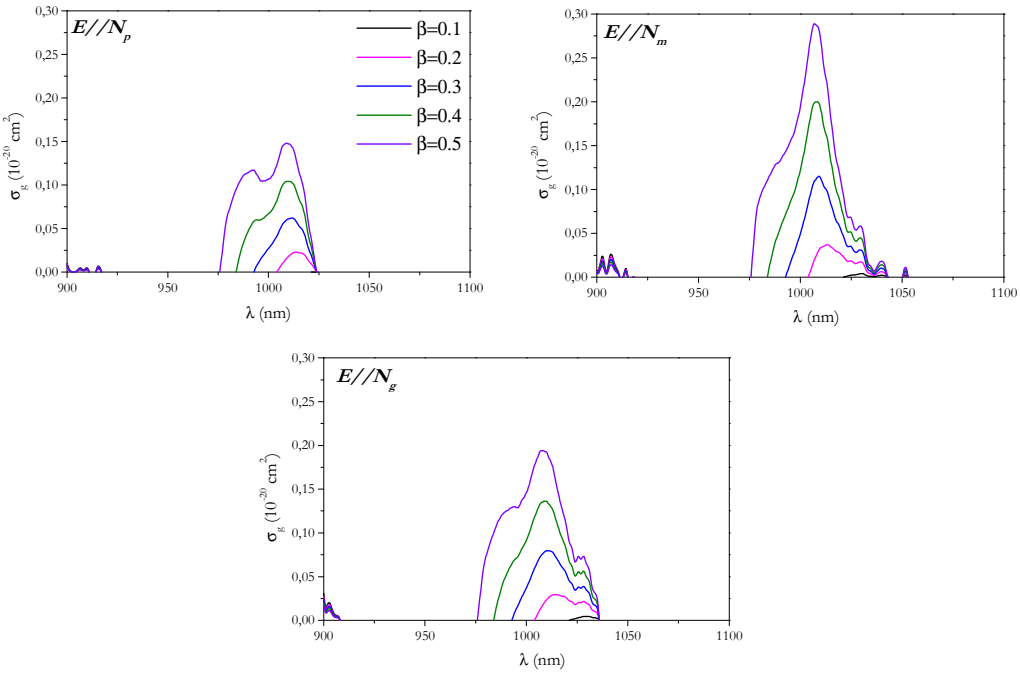

Figure 5.6. Inversion dependent gain cross sections of $KYb_{0.024}Gd_{0.976}(PO_3)_4$

Figure 5.6 shows the inversion dependent gain cross section of $KYb_{0.024}Gd_{0.976}(PO_3)_4$ for the three polarizations for an inversion parameter (β) varying from 10% to 50%.

From this figure, lasing in $KYb_{0.024}Gd_{0.976}(PO_3)_4$ can be expected to have a lower threshold for $\boldsymbol{E//N_m}$ and between 1030 nm (β=0.1) and 1010 nm (β=0.5), which corresponded to the $^2F_{5/2}(0') \rightarrow {}^2F_{7/2}$ (2) transition.

This relative short oscillation wavelength is a feature that distinguishes Yb:KGP with respect other Yb-doped acentric hosts such as Yb:YCOB (1090 nm)[62], Yb:GdCOB (1082 nm)[63] and Yb:YAB (1090 nm)[66].

The minimum pump intensity ($I_{p,min}$) to reach laser threshold can be calculated from the minimum inversion necessary (β_{min}):

$$I_{p,\min} = \frac{\beta_{\min}}{\sigma_{abs}(\lambda_p) - \beta_{\min}[\sigma_{abs}(\lambda_p) + \sigma_e(\lambda_p)]} \frac{h\nu_p}{\tau} \qquad \text{eq. 5.11}$$

If we consider the ideal case of zero cavity loses, i.e. no output coupling, we can estimate the pump threshold from the inversion value for which the gain cross section reaches zero at some wavelength. The wavelength for which the gain cross section reaches zero at minimum inversion parameter (β_{min}) is the expected laser wavelength (λ_l).

Table 5.1 shows these estimated laser parameters of $KYb_{0.024}Gd_{0.976}(PO_3)_4$ for the three orthogonal polarizations for zero cavity loses. $I_{p,min}$ was calculated using eq. 5.8 (Ti:sapphire wavelength used in laser experiments) and $I_{p,min}$ using eq. 5.11 with λ_{pump}=977.1 nm.

Table 5.1. Estimated laser parameters of $KYb_{0.024}Gd_{0.976}(PO_3)_4$ for the three orthogonal polarizations for zero cavity loses

	λ_l(nm)	β_{min} (%)	$I_{p,sat}$ (KW cm^{-2})	$I_{p,min}$ (KW cm^{-2})
$\boldsymbol{E//N_p}$	1020	9.5	11.43	2.80
$\boldsymbol{E//N_m}$	1035	5.5	6.90	0.88
$\boldsymbol{E//N_g}$	1034.5	4.3	10.58	1.04

If we consider cavity loses, i.e. output couplers of 1, 3 and 5 % that have been used in lasing experiments (see paper VI), we can estimate the pump threshold from the inversion value (β_{min}) for which the gain cross section reaches the calculated value considering the loses at some wavelength (λ_l). We calculated σ_g assuming cavity loses T_{OC}%=1, 3, 5, using the equation:

$$2NL\sigma_g = 0.01, 0.03, 0.05 \qquad \text{eq. 5.12}$$

where N is the total number of active centres, 1.007×10^{20} cm^{-3} in $KYb_{0.024}Gd_{0.976}(PO_3)_4$, and L is the length of the sample, which is 2.5 mm is average for the cubic sample used. The factor 2 comes from the fact that there is twice gain per round-trip.

The calculated σ_g values from eq. 5.12 are 0.0199, 0.0596, and 0.0993×10^{-20} cm^2 for 0.01, 0.03, and 0.05 cavity loses, respectively. Table 5.2 shows these estimated laser parameters of $KYb_{0.024}Gd_{0.976}(PO_3)_4$ for the three orthogonal polarizations assuming 1, 3, and 5% cavity loses. As the σ_g values are higher, the β_{min} values to reach them are necessary higher and consequently, the λ_l are shorter.

Table 5.2. Estimated laser parameters of $KYb_{0.024}Gd_{0.976}(PO_3)_4$ for the three orthogonal polarizations for 1, 3, and 5% cavity loses

	loses	λ_l (nm)	β_{min} (%)	$I_{p,min}$ (KW cm^{-2})
	0.01	1016.5	18.5	7.11
$E//N_p$	0.03	1012	28.7	7.23
	0.05	1010	37.9	42.0
	0.01	1015	17.0	3.72
$E//N_m$	0.03	1010	23.3	6.37
	0.05	1009.5	28.1	9.48
	0.01	1018.5	16.8	5.66
$E//N_g$	0.03	1012.5	25.5	11.88
	0.05	1010	32.7	22.32

5.2. Spectroscopic properties of Nd^{3+} in $KGd(PO_3)_4$ crystals

The spectroscopic advantages of ytterbium over neodymium have been extensively described above. These advantages, however, are offset by a

significant disadvantage, which is the quasi-three-level laser operation at room temperature compared with the four-level operation in Nd^{3+} lasers. The quasi-three-level operation for Yb^{3+} involves higher power laser thresholds. However, once they are above threshold, Yb^{3+} lasers tend to have greater slope efficiency than Nd^{3+} lasers. If operation is to be well above the laser threshold, pump intensities must be high. Hence, though Yb^{3+} lasers can compete with Nd^{3+} lasers, the laser architectures operating above laser threshold involve additional costs because they are more complex than Nd^{3+} lasers. Much of the research efforts have focused on the design of laser architectures for operating in the above threshold regime[145]. However, the advantages of Yb^{3+} overcome the disadvantages and in recent years, Yb^{3+} has progressively been replacing Nd^{3+}.

The stoichiometric $KNd(PO_3)_4$ (KNP) crystal was extensively studied in the mid 70's as a potential neodymium minilaser source for optical fiber communications. Hence, preliminary spectroscopic and laser studies were performed and the Judd-Ofelt[146,147] parameters calculated.

Various papers have calculated the laser emission cross section of Nd-stoichiometric crystals[148,149], determined the fluorescence quantum efficiency[149] and accurately measured the lifetime. Many spectroscopic studies have been made of the energy levels involved with laser action (^4I_j and $^4F_{3/2}$) and the Judd-Ofelt calculations were reported[150,151]. However, a completely spectroscopic characterization of Nd^{3+} in $KNd(PO_3)_4$ has never been done.

In this section, therefore we include all the spectroscopic characterization of Nd^{3+} in the $KGd(PO_3)_4$ host, review the studies that have been made and add our own to complete the characterization.

All the results on Nd:$KGd(PO_3)_4$ reported in this section are based on single crystals of compositions $KNd_{0.006}Gd_{0.994}(PO_3)_4$ and $KNd(PO_3)_4$ corresponding to a neodymium concentrations of 1.560×10^{19} and $4.050\text{x}10^{21}$ cm^{-3}, respectively. The crystals were cut and polished as platelets and accurately oriented along the $\boldsymbol{N}_p$,

$\boldsymbol{N}_m$ and $\boldsymbol{N}_g$ principal optical axes. $KNd_{0.006}Gd_{0.994}(PO_3)_4$ was around 1550 μm thick and $KNd(PO_3)_4$ around 800 μm.

Polarized spectroscopic experiments are necessary even though polarization-dependent selection rules are not expected because of the fact that the Nd^{3+} ion has an odd number of electrons in the 4*f* shell (Nd^{3+}:[Xe]$4f^3$) but the intensity of the individual peaks may still vary.

5.2.1. Optical absorption

Neodymium absorbs light throughout the UV-visible and near-IR spectral regions, from around 250 to 2500 nm (2857-4000cm^{-1}) because its energy level scheme is complex.

Figure 5.7 shows the polarized absorption spectra of $KNd(PO_3)_4$ at room temperature and at 6K. A total of 24 multiplets were resolved. These were: $^4D_{1/2}$, $^4D_{3/2}$, $^4D_{5/2}$, $^2P_{3/2}$, $^2D_{5/2}$, $^2P_{1/2}$, $^2G_{9/2}$, $^2D_{3/2}$, $^4G_{11/2}$, $^2K_{15/2}$, $^2K_{13/2}$, $^4G_{9/2}$, $^4G_{7/2}$, $^4G_{5/2}$, $^2G_{7/2}$, $^2H_{11/2}$, $^4F_{9/2}$, $^4F_{7/2}$, $^4S_{3/2}$, $^4F_{5/2}$, $^2H_{9/2}$, $^4F_{3/2}$, $^4I_{15/2}$, and $^4I_{13/2}$. At the UV limit, 4 more multiplets were identified as $^2I_{11/2}$, $^2L_{15/2}$, $^2I_{13/2}$, and $^4D_{7/2}$.

A polarized room temperature spectrum $\boldsymbol{E//N}_m$ polarized is added by way of example. However, we were not able to resolve these multiplets because of its low intensity; in addition, the resolution of the spectrophotometer in this range is rather poor.

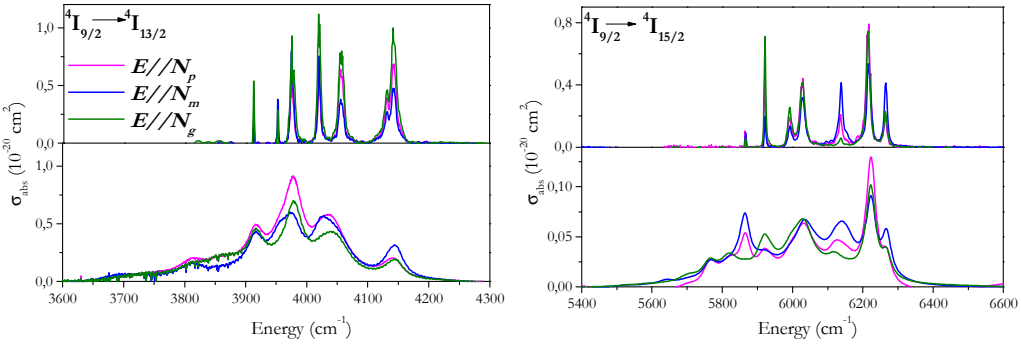

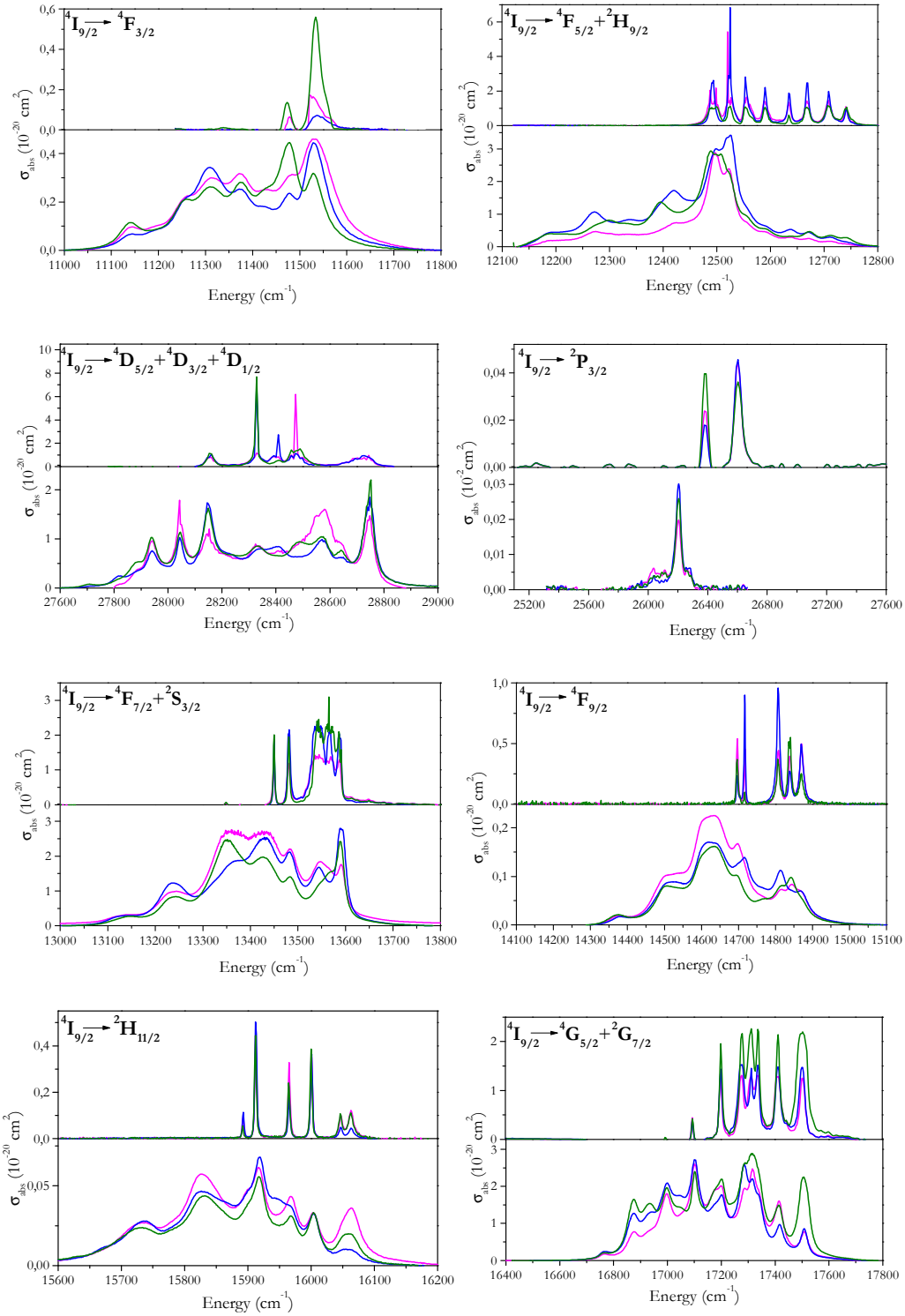
$^4I_{9/2} \rightarrow {}^4F_{3/2}$
$^4I_{9/2} \rightarrow {}^4F_{5/2}+{}^2H_{9/2}$
$^4I_{9/2} \rightarrow {}^4D_{5/2}+{}^4D_{3/2}+{}^4D_{1/2}$
$^4I_{9/2} \rightarrow {}^2P_{3/2}$
$^4I_{9/2} \rightarrow {}^4F_{7/2}+{}^2S_{3/2}$
$^4I_{9/2} \rightarrow {}^4F_{9/2}$
$^4I_{9/2} \rightarrow {}^2H_{11/2}$
$^4I_{9/2} \rightarrow {}^4G_{5/2}+{}^2G_{7/2}$
σ_{abs} (10^{-20} cm^2)
σ_{abs} (10^{-2} cm^2)
Energy (cm^{-1})

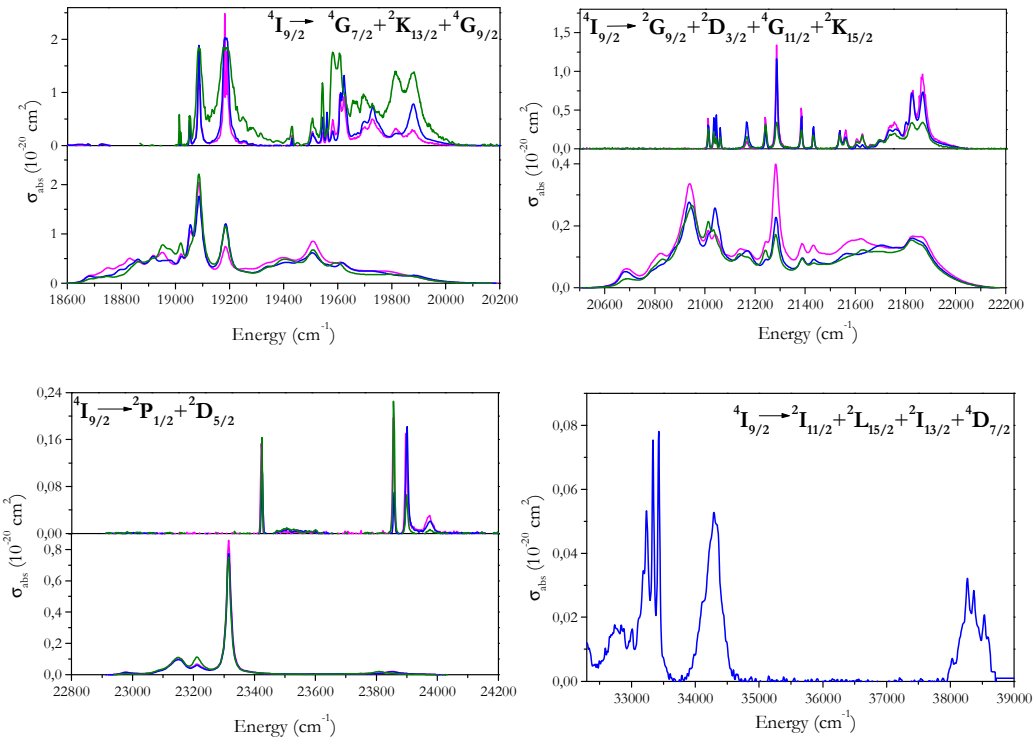

Figure 5.7. Absorption cross sections of Nd^{3+} in the $KGd(PO_3)_4$ at room and low temperatures for the three orthogonal polarizations

Currently, Nd-lasers are directly pumped with AlGaAs diodes at around 800 nm. This wavelength corresponds to the optical absorption from the $^4I_{9/2}$ ground multiplet to the $^4F_{5/2}$ excited multiplet.

The absorption band associated with the Nd^{3+} transition in $KGd(PO_3)_4$ approximately extends from 12100 to 12800 cm^{-1} (826.4-781.3 nm) at room temperature (figure 5.7).

As expected, the anisotropy of the optical absorption was rather low though the absorption cross section was maximized for $\boldsymbol{E//N_m}$. The maximum cross section at 800 nm (12500 cm^{-1}), calculated with Nd^{3+} concentration of 4.050×10^{21} cm^{-3}, amounts to 3.00×10^{-20} cm^2. The corresponding maximum absorption cross

sections at the same wavelength amount to 2.78×10^{-20} and 2.83×10^{-20} cm^2 for $\boldsymbol{E//N_p}$ and $\mathbf{E//}\boldsymbol{N_g}$, respectively.

The absorption spectrum of the excited multiplet $^4F_{5/2}$ at room temperature shows a clear substructure that may be related to phonon-electron coupled transitions. Therefore, the polarized absorption with $\boldsymbol{E//N_m}$ was studied therefore between 6 K and room temperature (Figure 5.8).

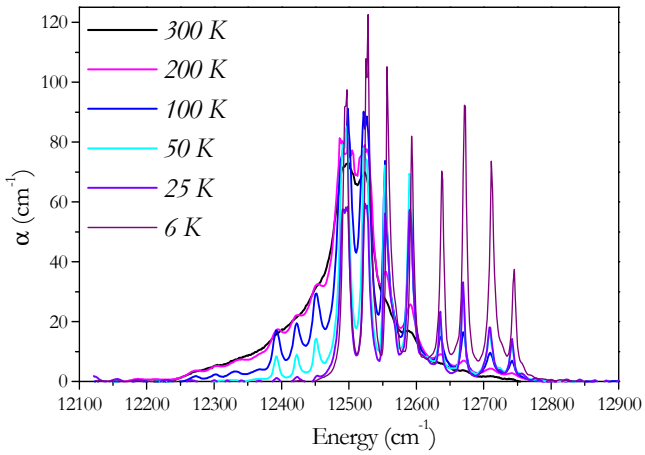

Figure 5.8. Temperature evolution of the optical absorption of Nd:KGP for $\boldsymbol{E//N_m}$

The maximum absorption of the $^4I_{9/2}\rightarrow{}^4F_{5/2}$ transition decreased when the temperature was increased although this effect was masked at higher temperatures because of the population redistribution among the other sublevels of the ground state. When the temperature was increased, additional peaks below 12500 cm^{-1} appeared and progressively increased in intensity. These peaks are probably related to the thermal population of upper sublevels of the ground state multiplet $^4I_{9/2}$. This effect was common to all the multiplets.

The energies of the three Stark sublevels accurately determined from the optical absorption spectra recorded at 6 K are summarized in Table 5.3.

Table 5.3. Energies of the Stark sublevels of the excited energy levels of Nd^{3+} in $KGd(PO_3)_4$

$^{2S+1}L_J$	Energy (cm^{-1})							
$^4D_{1/2}$	28722							
$^4D_{3/2}$ + $^4D_{5/2}$	28474	28458	28409	28328	28157			
$^2P_{3/2}$	26273	26204						
$^2D_{5/2}$	23944	23855	23807					
$^2P_{1/2}$	23313							
$^2G_{9/2}$+$^2D_{3/2}$+	21865	21824	21749	21697	21662	21626	21604	21559
$^4G_{11/2}$+$^2K_{15/2}$	21535	21430	21382	21283	21239	21164	21059	21042
	21033	21010						
$^2K_{13/2}$+$^4G_{9/2}$	19879	19814	19751	19728	19700	19624		
	19609	19580	19559	19544	19507	19431		
$^4G_{7/2}$	19185	19086	19052	19016				
$^4G_{5/2}$+$^2G_{7/2}$	17505	17413	17339	17315	17278	17202	17095	
$^2H_{11/2}$	16064	16048	16000	15965	15912	15893		
$^4F_{9/2}$	14871	14839	14808	14717	14697			
$^4F_{7/2}$+$^2S_{3/2}$	13649	13589	13567	13544	13482	13450		
$^4F_{5/2}$+$^2H_{9/2}$	12742	12709	12668	12635	12590	12555	12524	12492
$^4F_{3/2}$	11533	11472						
$^4I_{15/2}$	6264	6215	6139	6028	5993	5920	5866	-
$^4I_{13/2}$	4142	4139	4056	4020	3976	3952	3913	

5.2.2. Optical emission

The emission spectra of $Nd:KGd(PO_3)_4$ were studied at room and low temperatures to determine the emission channels and the Stark sublevels of the $^4I_{13/2}$ and $^4I_{11/2}$ excited multiplets and the ground state multiplet $^4I_{9/2}$.

In order to totally resolve the peaks, the low Nd-doped sample of $KNd_{0.006}Gd_{0.994}(PO_3)_4$ was used in the experiments, which was pump at λ=0.8 μm. Figure 5.9 shows the polarized emission spectra for the three orthogonal polarizations at room temperature. Again, the anisotropy of the optical emission was rather low though the optical emission intensity was maximized for $\boldsymbol{E//N_m}$. Figure 5.10 shows the emission spectra of at 300 and 10 K of $^4I_{13/2}$, $^4I_{11/2}$, and $^4I_{11/2}$ for $\boldsymbol{E//N_m}$.

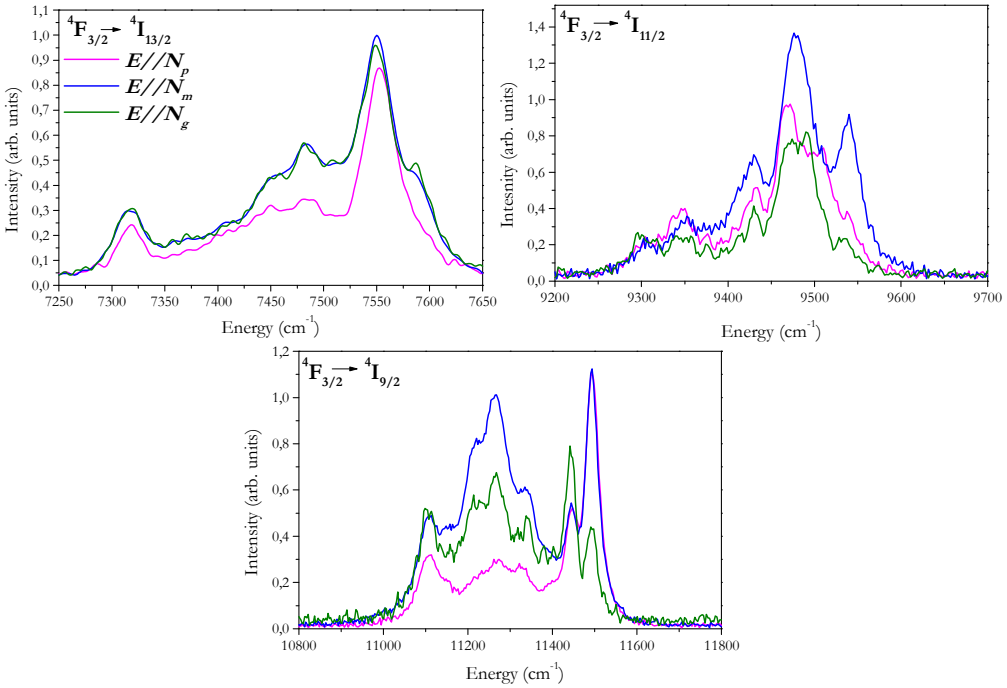

Figure 5.9. Polarized emission spectra of $KNd_{0.006}Gd_{0.994}(PO_3)_4$ for the three orthogonal polarizations at room temperature

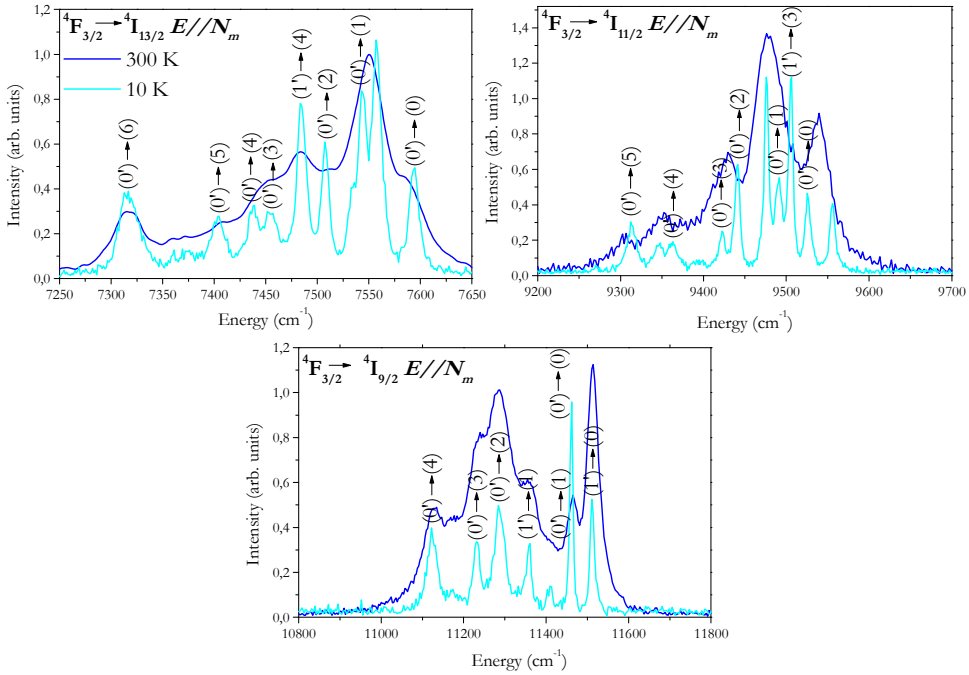

Figure 5.10. Emission spectra of $KNd_{0.006}Gd_{0.994}(PO_3)_4$ at 300 and 10 K for $E//N_m$

Figure 5.11 shows a schematic diagram of the Stark sublevels and the absorption and emission transitions among them of Nd^{3+} in KGP crystals obtained from the low temperature absorption and emission spectra.

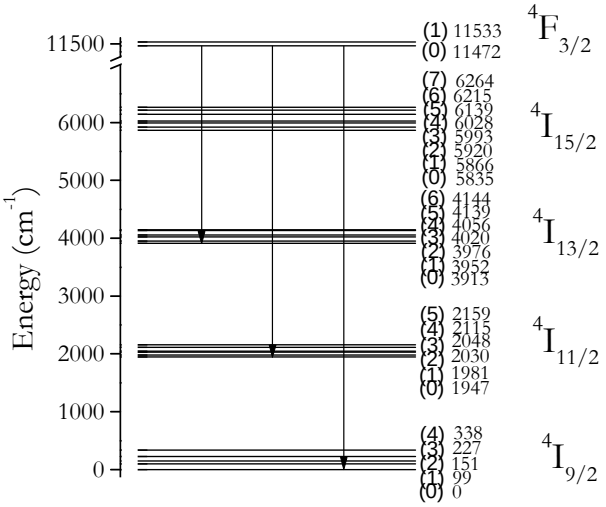

Figure 5.11. Schematic diagram of the Stark sublevels involved in laser operation of Nd^{3+} in KGP

The crystal field splitting is much lower than that of such other well known materials like Nd-doped garnets[152], which indicates again that the crystal field of the KGP host is much weaker.

The emission cross sections of the laser transitions from $^4F_{3/2}$ to $^4I_{11/2}$ and $^4I_{13/2}$ (wavelengths about 1 and 1.3 μm) of $KNd(PO_3)_4$ have been reported in the literature[148,149]. They were determined by the direct absorption method and the conventional spectroscopic method[153]. This latter method consists of two processes: determination of the cross section of a reference transition by an absorption measurement and successive determination of the intensity ratio of the laser transition by fluorescence measurements. The values of cross section values calculated using these two methods were consistent with each other[148].

Table 5.4 shows the effective cross sections values of the $^4F_{3/2} \rightarrow {}^4I_{11/2}$ and $^4F_{3/2} \rightarrow {}^4I_{13/2}$ transitions at 1.052 and 1.322 μm respectively for $\boldsymbol{E//N_p}$, $\boldsymbol{E//N_m}$, $\boldsymbol{E//N_g}$ using the direct method. The experimental uncertainties are estimated to be ± 15%[149].

Table 5.4. Emission cross sections of KNP at λ=1.0520 and 1.3220 mm in KNP for the three orthogonal polarizations

	σ_e (10^{-20} cm^2)	
	$^4F_{3/2} \rightarrow {}^4I_{11/2}$	$^4F_{3/2} \rightarrow {}^4I_{13/2}$
$\boldsymbol{N_p}$	4.7	1.5
$\boldsymbol{N_m}$	6.2	3.0
$\boldsymbol{N_g}$	3.9	1.4

These values are around 10 times lower than those of the Nd-doped garnets[154,155].The σ_e of $KN(PO_3)_4$ was probably reduced by the concentration quenching effects caused by the high concentration of Nd^{3+} in the crystal. Nevertheless, this effect is lower than in other neodymium stoichiometric crystals such as NdP_5O_{14}[85,86,87], $LiNd(PO_3)_4$[88,88,89,90,91] or $NaNd(PO_3)_4$[92] since the interatomic distance between the Nd^{3+} ions in KNP is higher than in the others.

5.2.3. Lifetime measurements

The measured fluorescence decay time of the $^4F_{3/2}$ level of Nd^{3+} in the stoichiometric crystal $KNd(PO_3)_4$ is 110 μs. This value agrees with those reported in the literature[74,93]. The fluorescence decay time increased to 246 μs for $KNd_{0.006}Gd_{0.994}(PO_3)_4$ because of concentration quenching via resonant migration of the excitation energy between the Nd^{3+} ions (Figure 5.12). The probable final transfer to impurities in the crystal lattice resulting in radiative or nonradiative deexcitation is less likely in stoichiometric materials because they are probably purer than doped materials.

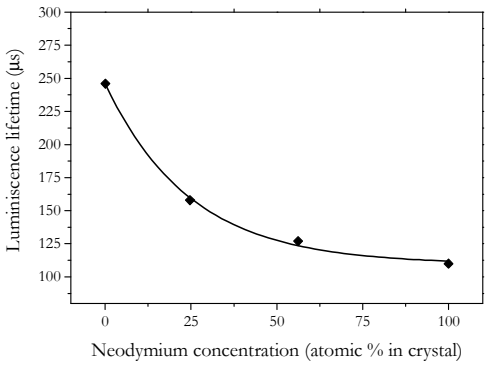

Figure 5.12. Fluorescence lifetime of $KNd_xGd_{1-x}(PO_3)_4$ versus the Nd^{3+} concentration

Figure 5.13 shows the evolution of the fluorescence lifetime as a function of the temperature. τ slightly increases when the temperature decreases.

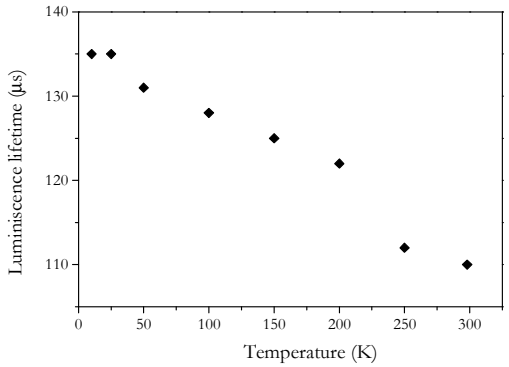

Figure 5.13. Florescence lifetime of $KNd(PO_3)_4$ versus the temperature

Chapter 6: Laser operation of Yb^{3+} in $KGd(PO_3)_4$

This chapter describes to the results of the room temperature laser operation near 1μm of Yb^{3+} in $KGd(PO_3)_4$ in the continuous-wave (cw) regime. As far as we know, this is the first time that laser operation with Yb:$KGd(PO_3)_4$ has been demonstrated for the first time.

6.1. Yb:$KGd(PO_3)_4$, a quasi-three level gain medium

The advantages of Yb^{3+} as a laser-active ion have their origin in its simple two-manifold electronic structure. However, this simple energy level structure corresponds to a quasi-three-level scheme for laser operation. The properties of quasi-three-level lasers are between those of three-level and four-level lasers (Figure 6.1). Inversion can be achieved more easily in four-level lasers than in three-level lasers because in the three-level scheme, the lower laser level coincides with the ground level, which has a significant population at the operating temperature. However, because of the larger difference between the pump and laser wavelengths (larger quantum defect), four-level lasers experience greater thermal load than three-level lasers.

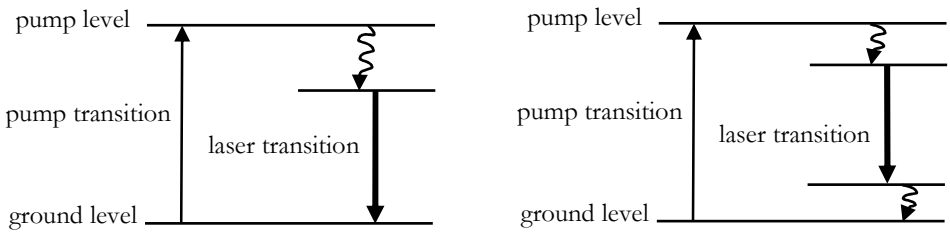

Figure 6.1. Energy level schemes of a three-level laser (left) and a four-level laser (right)

Figure 6.2 shows the quasi-three-level scheme of Yb^{3+} in $KGd(PO_3)_4$ for a pump wavelength corresponding to the maximum absorption at 977 nm (Figure 5.1).

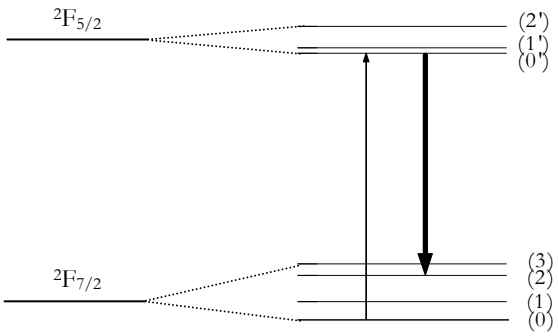

Figure 6.2. Quasi-three-level scheme in Yb^{3+} in $KGd(PO_3)_4$ at λ_p = 977 nm

At room temperature, the lower laser level (normally the $^2F_{7/2}(3)$ or $^2F_{7/2}(2)$ Stark sublevel) has appreciable population, so the Yb^{3+} ion system can be described as a quasi-three-level laser scheme. The gain cross section spectra of $KYb_{0.024}Gd_{0.976}(PO_3)_4$ (Figure 5.6) lead us to expect lasing in this crystal on the $^2F_{5/2}(0') \rightarrow {}^2F_{7/2}(2)$ transition, at a wavelength close to 1010 nm.

A low laser threshold requires high laser gain (σ_g) and low cavity losses. The fundamental origin of the laser threshold is the power loss via fluorescence into a large number of spatial modes. Just below threshold, a laser already emits some power, which is the result of amplified spontaneous emission and has a bandwidth, which is larger than that of the above-threshold laser emission but smaller than the regular fluorescence bandwidth.

In the cw regime, above threshold, the inversion density and the gain of a laser are clamped at their threshold values; the round-trip gain of the cavity is equal to the round-trip loss. When the pumping is increased, the gain remains fixed while the laser output power increases.

Because the output power of a laser varies linearly with the pump rate, the efficiency of a laser is often discussed in terms of slope efficiency (η_s). Slope efficiency is defined as the slope of the curve obtained by plotting the laser output versus the absorbed pump power. In simple situations, the slope efficiency is basically determined by the pump absorption efficiency, the area efficiency, the inversion efficiency, the quantum efficiency of the gain medium, and the output coupling efficiency of the laser cavity. The pump absorption efficiency (η_p) is the ratio of the power absorbed by the active medium to the power of the pump source. In an optically pumped laser, part of the incident pump energy may be reflected or transmitted by the optical elements such as the active medium or the mirrors. The area efficiency (η_a) measures which portion of the pump volume is used in the oscillating mode (i.e. contributes to the gain of the laser system). For a longitudinally pumped laser, the area efficiency can often

be approximated by $\eta_a = 1/\left(\left(r_p^2/r_m^2\right)+1\right)$, where r_p is the radius of the pump beam and r_m is the radius of the oscillating mode. The inversion efficiency (η_i) is the ratio of the energy of a photon at the oscillating frequency to the energy of an absorbed pump photon. The quantum efficiency of the gain medium (η_q) is the fraction of inverted ions that emit a photon into the oscillating mode. The output coupling efficiency of the laser cavity is the ratio of the output coupling to the total round-trip loss of the cavity. Mathematically, the slope efficiency is determined by the product of these five factors:

$$\eta_s = \eta_p \eta_a \eta_i \eta_q \eta_o \qquad \text{eq. 6.1}$$

6.2. Continuous wave (cw) laser operation in Yb:$KGd(PO_3)_4$ crystal

To generate laser radiation from Yb^{3+} in $KGd(PO_3)_4$, we used a sample of composition $KYb_{0.024}Gd_{0.976}(PO_3)_4$ (1.007×10^{20} cm^{-3} Yb^{3+} ions) accurately oriented along the $\boldsymbol{N}_p$, $\boldsymbol{N}_m$ and $\boldsymbol{N}_g$ principal optical axes with dimensions of 2.34, 2.68, and 2.47 mm along these axes, respectively. Using this sample, we were able to check the laser activity for each polarization and propagation configuration although, as stated above, lasing was expected to have lower threshold for $\boldsymbol{E//N}_m$ (see section 5.1.4). The uncoated $KYb_{0.024}Gd_{0.976}(PO_3)_4$ cube was placed under Brewster angle to avoid Fresnel losses in a standard astigmatically compensated Z-shaped cavity (Figure 2.14). At Brewster angle, the cavity losses are zero only for one polarization in the plane of reflection (*p*). The high Fresnel losses for polarization perpendicular to this plane (*s*) do not allow lasing with such polarization. The pump beam can be in principle polarized in either of the two directions, or be unpolarized. In our case, using a polarized pump source, we selected its polarization to be parallel to the laser polarization (*p*), so that no additional losses occurred for the pump.

cw laser operation was obtained at room temperature when the $KYb_{0.024}Gd_{0.976}(PO_3)_4$ sample was orientated for $\boldsymbol{E//N_p}$ and $\boldsymbol{N_m}$ and the propagation was along $\boldsymbol{N_g}$. No generation was possible for $\boldsymbol{E//N_g}$ when propagating along $\boldsymbol{N_p}$ or $\boldsymbol{N_m}$.

The slope efficiency was as high as 55% was obtained for $\boldsymbol{E//N_m}$ with an output power around 100 mW for an output coupler of 1%. For $\boldsymbol{E//N_p}$ both the slope efficiency and the output power were lower: around 30% and 75 mW ($T_{OC} = 1\%$), respectively. The pump threshold was also higher for $\boldsymbol{E//N_p}$ than for $\boldsymbol{E//N_m}$. This is in agreement with the predictions in section 5.1.4 and can be explained by the lower gain cross section for $\boldsymbol{E//N_p}$ (Figure 5.6.).

Paper VI discusses the laser operation of $KYb_{0.024}Gd_{0.976}(PO_3)_4$. Table 3 in the paper shows the relevant laser parameters such as slope efficiency, oscillation wavelength (λ_l) and pump threshold. The experimental oscillation wavelengths for each T_{OC} are slightly different from the calculated wavelengths (Table 6.1). Hence, we can conclude that the cavity losses are basically determined by the output coupling and additional (unwanted) losses are negligible.

Table 6.1. Estimated versus experimental laser wavelengths(λ_l) for $E//N_p$ and N_m corresponding to T_{OC} =1, 3, and 5 %

	λ_l (nm)			
	$\boldsymbol{E//N_p}$		$\boldsymbol{E//N_m}$	
T_{OC} (%)	estimated	experimental	estimated	experimental
1	1016.5	1016.3	1015	1017.1
3	1012	1013.5	1010	1013.8
5	1010	no lasing	1009.5	1012.1

Figure 6 in the paper shows the output power versus the absorbed pump power for output couplers of 1 and 3%. For T_{OC}=5% the slope efficiency for $\boldsymbol{E//N_m}$ could not be reliably estimated. The shorter oscillation wavelength at higher output couplers is typical for Yb-lasers and is related to the maximum of the

inversion dependent gain cross section curve (Figure 5.6). As expected, laser oscillation occurred on the $^2F_{5/2}(0') \rightarrow {}^2F_{7/2}(2)$ transition near 1010 nm.

Conclusions

The most important results from this study are, on the one hand, the successful synthesis of single crystals of undoped type III $KGd(PO_3)_4$ and ytterbium- or neodymium-doped $KGd(PO_3)_4$ and on the other, the optical, spectroscopic and laser characterization of the active ions in the $KGd(PO_3)_4$ host, which shows that Yb:$KGd(PO_3)_4$ is a promising candidate to obtain a new self-frequency doubling crystal.

Despite of the high viscosity of the growth solution, we were able to grow macrodefect-free single crystals of type III $KGd(PO_3)_4$, Yb:$KGd(PO_3)_4$, and Nd:$KGd(PO_3)_4$ from their self-fluxes using the top seeded solution growth-slow cooling technique. The related crystallization regions in the ternary system of the corresponding oxides were also determined. In particular, we accurately analyzed the changes produced by the ytterbium and neodymium active ions in the crystallization region of the undoped $KGd(PO_3)_4$. The changes produced by ytterbium were much more appreciable that those produced by neodymium. This was more related to the stability of the type III ($P2_1$) crystalline phase than to the difference in ionic radii between gadolinium and ytterbium or neodymium, which is very similar. Whereas the stoichiometric crystals of neodymium, $KNd(PO_3)_4$, crystallize as type III, those of ytterbium, $KYb(PO_3)_4$, crystallize as type IV ($P2_1/n$) or type V ($P2_1/n$). Hence, it was possible to grow type III Yb:$KGd(PO_3)_4$ single crystals with a ytterbium concentration in solution as high as 15 at %, which corresponds to about 7.5 at% in the bulk crystal. This ytterbium concentration proved high enough to generate laser radiation. Further investigations in the crystallization region of Yb:$KGd(PO_3)_4$ indicate that type III could be grown from solutions with a ytterbium concentration as high as 50 at %, which corresponds to about 25 at % in the bulk crystal. Thus, the laser efficiency could be improved by optimizing the ytterbium concentration in the crystal. We

also grew Nd:$KGd(PO_3)_4$ single crystals with a neodymium concentration in crystal as high as 100% (i.e. the stoichiometric $KNd(PO_3)_4$ crystal).

The crystal structure of type III $KGd(PO_3)_4$ and $KNd(PO_3)_4$ indicates that although these crystals belong to the monoclinic class ($P2_1$) their cell parameters are so isometric and their β angle so close to 90º that they are close to the rhombic class. This isometric structure required standard methodology to be developed to identify the crystal morphology. When we analyzed the structural, physical, optical and spectroscopic properties of these crystals, the ef isometric structure meant that the anisotropy was low. This led to an almost isotropic thermal expansion of $KGd(PO_3)_4$, which is advantageous for crystal growth, processing of active elements and laser operation.

The $KGd(PO_3)_4$ host has optical properties that make it an excellent solid-state laser or self-frequency doubling crystal. For example, its transmission window is very broad, extending from 180 nm to 4 μm, which covers both the fundamental and the second harmonic ranges. The rather large band-gap of $KGd(PO_3)_4$ should not only lead to high damage resistivity but also make it possible to use this host in the UV range, either as nonlinear crystals or as a host for cerium.

The theoretical simulations of self-frequency doubling showed thaht $KGd(PO_3)_4$ and isostructurals belong to the negative biaxial class. This means that $n_x > n_y > n_z$ and consequently $\boldsymbol{N_p//Z}$, $\boldsymbol{N_m//Y}$, and $\boldsymbol{N_g//X}$. We found that this family of crystals can be phase-matchable for type I second harmonic generation in the $\boldsymbol{YZ}$ plane in a wavelength from 0.918 μm. The wavelength range for which the crystal can be phase-matchable perfectly covers the luminescence ranges of both Yb^{3+} and Nd^{3+} ions in $KGd(PO_3)_4$ (see sections 5.1.2 and 5.2.2). Therefore, Yb:$KGd(PO_3)_4$ and Nd:$KGd(PO_3)_4$ are very promising candidates to be applied as self-frequency doubling crystals.

To our knowledge, ytterbium in the $KGd(PO_3)_4$ host has generated laser luminescence for the first time. Although the maximum output power achieved

(93 mW) was limited by the size and ytterbium doping level of the sample ($KYb_{0.024}Gd_{0.976}(PO_3)_4$) the more than 55% slope efficiency obtained with this first sample is rather promising for the future. As stated above, further investigations indicate that the ytterbium doping level can be increased, so the laser efficiency can be optimized. One feature that distinguishes Yb:KGP from other nonlinear crystals is the short oscillation wavelength near 1014 nm. This wavelength perfectly matches the wavelength range for which these crystals can be phase-matchable. We can conclude, therefore, that Yb:$KGd(PO_3)_4$ is a promising crystal for self-frequency doubling, which should be able to generate blue-green radiation.

These encouraging results suggest that future investigations can focus on the development of a new self-frequency doubling crystal. To reach this objective, the lasing generation of Yb:$KGd(PO_3)_4$ and Nd:$KGd(PO_3)_4$ should be further investigated and optimized by controlling the active ion doping level in the crystal.

References

[1] A. Einstein, "Zur Quantentheorie der Strahlung", *Physikalische Zeitschrift XVIII*, **1917**, 121

[2] J.P. Gordon, H.J. Zeiger, C.H Townes, "Molecular Microwave Oscillator and New Hyperfine Structure in the Microwave Spectrum of NH_3", *Phys. Rev.* **1954**, *95*, 282

[3] A.L. Schallow, C.H. Townes. "Infrared and optical masers", *Phys. Rev.* **1958**, *112*, 1940

[4] T.H. Maiman, "Stimulated optical radiation in ruby", *Nature* **1960**, *187,* 493

[5] P.F. Moulton, "Spectroscopic and laser characteristics of Ti:Al_2O_3", *J. Opt. Soc. Am.* **1986**, *B3*, 125.

[6] S. F. Pereira, Min Xiao, H. J. Kimble, J. L. May, "Generation of squeezed light by intracavity frequency doubling", *Phys. Rew. A* **1988**, *38*, 4931

[7] L. F. Johnson, h. G. Guggenheim, "Infrared-pumped visible laser", *Appl. Phys. Lett.* **1971**, *19*, 44

[8] J. Y Allain, M. Monerie, H .Poignant, "Blue upconversion fluorozirconate fibre laser", *Electron.* Lett. **1990**, *26*, 166

[9] D. Funk, "Glass-fiber lasers in the unltraviolet and visible", *IEEE J. Selct. Topics Quant. Electron.* **1995**, *1*, 784

[10] W. Length, R. M. Macfarlane, W. E. Moerner, F. M. Schellenberg, R. M. Shelby, G. C. Bjorklund, "High-density frequency-domain optical recording", *Proc. SPIE* **1986**, *695*, 261

[11] W. Kozlovsky, "Optical data storage requirements on short wavelength laser sources", *Proc. SPIE* **1995**, *2379*, 186

[12] J. C. Owens, "Compact visible lasers in reprographics", Compact blue-green lasers technical digest, vol. 6, pp 8, Washington: Optical Society of America, **1992**

[13] E. A. Downing, L. Hesselink, R.M. Macfarlane, J. R. Klein, D. Evans, J. Ralson, "A laser-diode-driven, three-color, solid-state-3D display", OSA Technical digest Series, vol. 9, pp. 89, Washington: Optical Society of America, **1996**

[14] L.A. Sklar, "Lasers in flow cytometry and biotechnology", Compact blue-green lasers technical digest, vol. 6, pp 5, Washington: Optical Society of America, **1992**

[15] L.M. Smith, J. Z. Sanders, R. J. Kaiser, O. Hughes, C. Dodd, C. R. Connell, C. Heiner, S. B. H. Kent, L.E. Hood, "Fluorescence detection in automated DNA sequence analysis", *Nature* **1986**, *321*, 674

[16] F. C. Painter, "Submarine laser communications", Defence electronics, June, 82, **1989**

[17] W.P. Risk, T. R. Gosnell, A. V. Nurmikko, *Compact blue-green lasers*, Cambridge University Press, **2003**

[18] L. Goldberg, M. K. Chun, "Efficient generation at 421 nm by resonant enhanced doubling of GaAlAs laser diode array emission", *Appl. Phys. Lett.* **1989**, *55(3)*, 218

[19] P. A. Franklen, A. E. Hill, C. W. Peters, G. Weinreich, "Generation of Optical Harmonics", *Phys. Rev. Lett.* **1961**, *7(4)*, 118

[20] M. Richardson, D. Hammons, J. Eichenholz, B. H. T. Chai, Q. Ye, W. K. Jang, L. Shah, "YCOB lasers", *J. Korean Phys. Soc.* **2000**, *37(5),* 633

[21] L. F. Johnson, A. A. Ballman, "Coherent emission from rare earth ions in electro-optic crystals", *J. Appl. Phys.* **1969**, *40(1)*, 297

[22] V. G. Dmitriev, E. V. Raevskii, N. M. Rubina, L. N. Rashkovich, O. O. Silichev, A. A. Fomichev, "Simultaneous emission at the fundamental frequency and the second harmonic in an active nonlinear medium: neodymium-doped lithium metaniobate" *Sov. Tech. Phys. Lett.* **1979**, 5, 590

[23] A. Brenier, "The self-doubling and summing lasers: overview and modelling", *J. Lumin.* **2000**, *91(3-4),* 121

[24] T. Y. Fan, A. Cordova-Plaza, M. J. F. Digonnet, R. L. Byer, H. J. Shaw, "Nd:MgO:LiNbO3 spectroscopy and laser devices", *J. Opt. Soc. Am. B* **1986**, *3(1)*, 140

[25] I. Schütz, I. Freitag, R. Wallenstein, "Miniature self-frequency-doubling cw Nd:YAB laser pumped by a diode-laser", *Opt. Commun.* **1990**, *77(2-3),* 221
[26] S. C. Wang, R.E. Stone, "Spectroscopy and laser properties of neodymium-doped yttrium aluminium borate crystals", Advanced Solid State Lasers, Topical Meeting of OSA, Hilton Head, SC, March **1991**
[27] S. Amano, T. Mochizuki, "Diode-pumped NYAB green laser" *Nonlinear Opt.* **1991**, *1*, 297
[28] H. Hemmati, "Diode-pumped self-frequency-doubled neodymium yttrium aluminium borate (NYAB) laser", *IEEE. J. Quant. Electron.* **1992**, *28(4),* 1169
[29] M.W. Qui, Y. X. Fan, R. C. Schlecht, Z. D. Luo, A. D. Jiang, C. Huang, "An efficient NYAB self-frequency-doubling green laser with diffraction-limited beam quality", *Nonlinear Opt.* **1993**, *4*, 31
[30] R. Li, C. Xie, J. Wang, X. Liang, K. Peng, G. Xu, "CW Nd:MgO:$LiNbO_3$ self-frequency-doubling laser at room temperature", *IEEE. J. Quant. Electron.* **1993**, *29(9),* 2419
[31] J. K. Yamamoto, A. Sugimoto, K. Yamagishi, "Self-frequency doubling in Nd,Sc_2O_3 $LiNbO_3$ at room temperature", *Opt. Lett.* **1994,** *19,* 1311
[32] S. Ishibashi, H. Itoh, T. Kaino, I. Yokohama, K. Kubodera, "New cavity configurations of Nd:MgO:$LiNbO_3$ self-frequency-doubled lasers", *Opt. Commun.* **1996**, *125(1-3),* 177
[33] J. Bartschke, R. Knappe, K. -J. Boller, R. Wallenstein, "Investigation of efficient self-frequency-doubling Nd:YAB lasers", *IEEE J. Quantum. Electron.* **1997**, *33(12),* 2295
[34] J. Capmany, D. Jaque, J. G. Sole, A. A. Kaminskii, "Continuous wave laser radiation at 524 nm from a self-frequency-doubled laser of $LaBGeO_5$:Nd^{3+}", *Appl. Phys. Lett.* **1998**, *72(5),* 531
[35] P. Dekker, Y. Huo, J. M. Dawes, J. A. Pipper, P. Wang, B. S. Lu, "Continuous wave and Q-switched diode-pumped neodymium, lutetium: yttrium aluminium borate lasers ", *Opt. Commun.* **1998**, *151(4-6)*, 406
[36] J. Capmany, D. Jaque, J. A. Sanz Garcia, J. Garcia Solé, " Continuous wave laser radiation and self-frequency-doubling in ZnO doped $LiNbO_3$:Nd^{3+} ", *Opt. Commun.* **1999**, *161(4-6)*, 253
[37] A. A. Kaminskii, D. Jaque, S. N. Bagaev, K. Ueda, J. G. Sole, J. Capmany, "New nonlinear-laser properties of ferroelectric Nd^{3+}:$Ba_2NaNb_5O_{15}$-cw stimulated emission $^4F_{3/2}$ -> $^4I_{11/2}$ and $^4F_{3/2}$ -> $^4I_{13/2}$, collinear and diffuse self-frequency doubling and summation", *Quant. Electron.* **1999**, *29(2),* 95
[38] J. M. Eichenholz, D. A. Hammons, L. Shah, Q. Ye, R. E. Peale, M. Richardson, B. H. T. Chai, "Diode-pumped self-frequency doubling in Nd^{3+}:$YCa_4O(BO_3)_3$", *Appl. Phys. Lett.* **1999**, *74(14),* 1954
[39] S. Zhang, Z. Cheng, J. Han, G. Zhou, Z. Shao, C. Wang, Y. T. Chow, H. Chen, "Growth and investigation of efficient self-frequency-doubling $Nd_xGd_{1-x}Ca_4O(BO_3)_3$ crystal " *J. Cryst. Growth* **1999**, *206(3)*, 197
[40] F. Augé, S. Auzanneau, G.Lucas-Leclin, F. Balembois, P. Georges, A. Brun, F. Mougel, G. Aka, A. Kahn-Harari, D. Vivien, "Efficient self-frequency-doubling Nd:GdCOB crystal pumped by a high brightness laser diode", Advanced Solid State Lasers, Topical Meeting of OSA, Boston, February **1999**
[41] L. D. DeLoach, S. A. Payne, L. L. Chase, L. K. Smith, W. L. Kway, W. F. Krupke, "Evaluation of absorption and emission properties of Yb^{3+} doped crystals for laser applications", *IEEE J. Quantum. Electron.* **1993**, *29(4),* 1179
[42] W. F. Krupke, "Ytterbium solid-state lasers. The first decade", *IEEE J. Sel. Top. Quantum. Electron.* **2000**, 6(6), 1287
[43] X. Zou, H. Toratani, "Evaluation of spectroscopic properties of Yb^{3+}-doped glasses", *Phys. Rev. B* **1995***, 52(22)* 15889

[44] X. Mateos, V. Petrov, M. Aguiló, R. Solé, J. Gavaldà, J. Massons, F. Díaz, U. Griebner, "Continuous-wave laser oscillation of Yb^{3+} in monoclinic $KLu(WO_4)_2$", *IEEE J. Quantum. Electron.* **2004***, 40(8),* 1056
[45] E. Montoya, J. Capmany, L. E. Bausá, T. Kellner, A. Diening, G. Huber, "Infrared and self-frequency doubled laser action in Yb^{3+}-doped $LiNbO_3$:MgO", *Appl. Phys. Lett.* **1999**, *74(21)*, 3113
[46] A. Brenier, G. Boulon, "New criteria to choose the best-doped laser crystals", *Europhys. Lett.* **2001**, *55 (5)*, 647
[47] A. Brenier, "A new evaluation of Yb^{3+}-doped crystals for laser applications", *J. Lumin.* **2001**, *92(3),* 199
[48] J. M. Dawes, P. Dekker, P. Burns, J. A. Piper, "Self-frequency-doubling ytterbium lasers", *Opt. Rev.* **2005**, *12(2),* 101
[49] P. Wang, J. M. Dawes, P. Dekker, D. S. Knowles, J. A. Piper, B. Lu, "Growth and evaluation of ytterbium-doped yttrium aluminium borate as a potential self-doubling laser crystal", *J. Opt. Soc. Am. B* **1999**, *16(1),* 63
[50] P. Wang, J. M. Dawes, P. Dekker, J. A. Piper, "Spectral properties and infrared laser performance of diode-pumped $Yb:YAl_3(BO_3)_4$", Advanced Solid State Lasers, Topical Meeting of OSA, Boston, February **1999**
[51] F. Auge, F. Balembois, P. Georges, A. Brun, F. Mougel, G. Aka, A. Kahn-Harari, D. Vivien, "High-efficiency cw diode-pumped lasing and tunability of Yb:GdCOB (Yb^{3+}:Ca_4 $GdO(BO_3)$", Advanced Solid State Lasers, Topical Meeting of OSA, Boston, February **1999**
[52] P. Wang, J. M. Dawes, P. Dekker, H. Zhang, X. Meng, "Spectral characterisation and diode-pumped laser performance of Yb:YCOB", Advanced Solid State Lasers, Topical Meeting of OSA, Boston, February **1999**
[53] D. Hammons, L. Shah, J. Eichenholz, Q. Ye, M. Richardson, B. Chai, A. Chin, J. Cary, "980 nm diode pumped laser operation and wavelength tunability performance in Yb^{3+}: YCOB", Advanced Solid State Lasers, Topical Meeting of OSA, Boston, February **1999**
[54] F. Mougel, K. Dardenne, G. Aka, A. Kahn-Harari, D. Vivien, "Ytterbium-doped $Ca_4GdO(BO_3)_3$: an efficient infrared laser and self-frequency doubling material", *J. Opt. Soc. Am. B* **1999**, *16(1),* 164
[55] F. Druon, F. Balembois, P. Georges, A. Brun, A. Courjaud, C. Hönninger, F. Salin, A. Aron, F. Mougel, G. Aka, D. Vivien, "Generation of 90-fs pulses from a mode-locked diode-pumped Yb^{3+} $Ca_4GdO(BO_3)_3$ laser", *Opt. Lett.* **2000**, *25(6)*, 423
[56] F. Auge, F. Balembois, P. Georges, A. Brun, F. Mougel, G. Aka, A. Kahn-Harari, D. Vivien, "Efficient and tunable continuous-wave diode-pumped Yb^{3+}:$Ca_4GdO(BO_3)_3$ laser", *Appl. Opt.* **1999**, *38(6),* 976
[57] P. Wang, J. M. Dawes, P. Dekker, J. A. Piper, "Highly efficient diode-pumped ytterbium-doped yttrium aluminium borate laser", *Opt. Commun.* **2000**, *174(5-6)*, 467
[58] P. Wang, P. Dekker, J. M. Dawes, J. A. Piper, Y. Liu, J. Wang "Efficient continuous-wave self-frequency-doubling green diode-pumped $Yb:YAl_3(BO_3)_4$ lasers", *Opt. Lett.*. **2000**, *25(10)*, 731
[59] E. Montoya, J. A. Sanz-García, J. Capmany, L. E. Bausá, A. Diening, T. Kellner, G. Huber, "Continuous wave infrared laser action self-frequency doubling, and tunability of Yb^{3+}:MgO:$LiNbO_3$, *J. Appl. Phys.* **2000,** *87(9),* 4056
[60] H. D. Jiang, J. Li, J. Y. Wang, X. B. Hu, H. Liu, B. Teng, C. Q. Zhang, P. Dekker, P. Wang, "Growth of Yb : $YAl_3(BO_3)_4$ crystals and their optical and self-frequency-doubling properties", *J. Cryst. Growth* **2001**, *233(1-2)*, 248
[61] P. Dekker, J. M. Dawes, J. A. Piper, Y. Liu, J. W. Wang, "1.1 W CW self-frequency-doubled diode-pumped $Yb:YAl_3(BO_3)_4$ laser ", *Opt. Comun.* **2001**, *195(5-6)*, 431

[62] A. Aron, G. Aka, B. Viana, A. Kahn-Harari, D. Vivien, F. Druon, F. Balembois, P. Georges, A. Brun, N. Lenain, M. Jaquet, "Spectroscopic properties and laser performances of Yb:YCOB and potential of the Yb:LaCOB material ", *Opt. Mat.* **2001**, *16(1-2)*, 181
[63] H. Zhang, X. Meng, P. Wang, L. Zhu, X. S. Liu, X. M. Liu, Y. Yang, R. Wang, J. Dawes, J. A. Pipper, S. Zhang, L. Sun, "Growth of Yb-doped $Ca_4GdO(BO_3)_3$ crystals and their spectra and laser properties ", *J. Cryst. Growth* **2001**, *222(1-2)*, 209
[64] P. A. Burns, J. M. Dawes, P. Dekker, J. A. Piper, J. Li, J. Y. Wang, "Coupled-cavity, single-frequency, tunable cw Yb:YAB yellow microchip laser ", *Opt. Commun.* **2002**, *207(1-6)*, 315
[65] M. J. Lederer, M. Hidelbrandt, V. Z. Kolev, B. Luther-Davies, B. Taylor, J. Dawes, P. Dekker, J. A. Pipper, H. H. Tan, C. Jagadish, "Passive mode locking of a self-frequency-doubling $Yb:YAl_3(BO_3)_4$ laser", *Opt. Lett.* **2002**, *27(6)*, 436
[66] P. Dekker, P. A. Burns, J. M. Dawes, J. A. Piper, "Widely tunable yellow-green lasers based on the self-frequency doubling material Yb:YAB", *J. Opt. Soc. Am. B* **2003**, *20(4),* 706
[67] L. E. Bausá, M. O. Ramírez, E. Montoya, "Optical performance of Yb^{3+} in $LiNbO_3$ laser crystal", *Phys. Stat. Sol (a).* **2004**, 201(2), 289
[68] A. Durif, *Crystal Chemistry of Condensed Phosphates*, Plenum Press, New York, **1995**
[69] D. E. C. Corbridge, *The Structural Chemistry of Phosphorus*, Elsvier, Amsterdam, **1966**
[70] K. K. Palkina, N. N. Chudinova, B. N. Litvin, N. V. Vinogradova, "Classifiaftion of double phosphates of rare earths and alkali metals, $M^{I}M^{III}(PO_3)_4$", *Izv. Akad. Nauk SSSR, Neorg. Mater.* **1981**, *17(8)*, 1501
[71] M. Bagieu-Beucher, J.-C. Guittel, **"**Crystal Structure of the Yttrium-Ammonium Polyphosphate $YNH_4(PO_3)_4$", *Z. Anorg. Allg. Chem.* **1988**, *559(1)*, 123
[72] H. Y.-P. Hong, "Crystal structure of $LiNdP_4O_{12}$", *Mater. Res. Bull.* **1975**, *10(7),* 635
[73] H. Kaizumi, "Sodium neodymium metaphosphate $NaNdP_4O_{12}$" *Acta Crystallogr. B* **1976**, *32*, 2254
[74] H. Y.-P. Hong, "Crystal structure of potassium neodymium metaphosphate, $KNdP_4O_{12}$, a new acentric laser material", *Mater. Res. Bull.* **1975**, *10(10),* 1105
[75] A. M. Dago, D. Yu. Pusharovskii, E. A. Pobedimskaya, N. V. Belov, "The crystal structure of γ-$KEr(PO_3)_4$ – a new modification of the rare earth metaphospahtes $KTR(PO_3)_4$", *Dokl. Akad. Nauk SSSR* **1980**, *251(5),* 1392
[76] K. K. Palkina, S. I. Maksimova, N. N. Chudinova, N. V. Vinogradova, N. T. Chibiskova, "The structure of crystals of $KYb(PO_3)_4$," *Izv. Akad. Nauk SSSR, Neorg. Mater.* **1981**, *17(1),* 110
[77] K. K. Palkina, S. I. Maksimova, V. G. Kuznetsov, "The crystal structure of $CsPr(PO_3)_4$", *Izv. Akad. Nauk SSSR, Neorg. Mater.* **1978**, *14(2),* 284
[78] O. G. Karpov, G. I. Dorokhova, "Crystal structure of a new polymorphic modification of $KErP_4O_{12}$", *Sov. Phys. Crystallogr.* **1989**, *34(4)*, 607
[79] K. K. Palkina, V. G. Kuznetsov, N. N. Chudinova, N. T. Chibiskova, "The crystal structures of double poly- and metaphosphates of the composition $KLn(PO_3)_4$", *Izv. Akad. Nauk SSSR, Neorg. Mater.* **1976**, *12(4),* 730
[80] K. K. Palkina, S. I. Maksimova, N. T. Chibiskova, "The crystal structure of β'-$RbSm(PO_3)_4$", *Izv. Akad. Nauk SSSR, Neorg. Mater.* **1981**, *17(7),* 1248
[81] K. K. Palkina, S. I. Maksimova, N. T. Chibiskova, " Strcuture of crystal of cubic modification of cesium neodymium tetrametaphosphate β-$CsNd(PO_3)_4$ ($CsNdP_4O_{12}$)", *Dokl. Akad. Nauk SSSR* **1981**, *257(2),* 357
[82] H. Ettis, H. Naïli, T. Mhiri, "Synthesis and crystal structure of a new potassium-gadolinium cyclotetraphosphate, $KGdP_4O_{12}$", *Cryst. Growth and Design.* **2003**, *3(4)*, 599
[83] W. Rekik, H. Naïli, T. Mhiri, "Potassium gadolinium phosphate, $KGd(PO_3)_4$", *Acta Crystallogr. C* **2004**, 60, i-50
[84] J. –P. Noblanc, "Fiber optical communications devices", *Appl. Phys.* **1977**, *12(3),* 211

[85] J. –P. Budin, M. Neubauer, M Rondot, "Miniature Nd-pentaphosphate laser with bonded mirrors, side-pumped with low current density LED", *Appl. Phys. Lett.* **1978**, *33(4)*, 309
[86] H.P. Weber, T.C. Damen, H.G. Danielmeyer, B.C. Tofield, "Nd-ultraphosphate laser", *Appl. Phys. Lett.* **1973**, *22(10),* 534
[87] H. G. Danielmeyer, G. Huber, W. W. Krühler, J. P. Jeser, "Properties and laser oscillation of the (Nd, Y) pentaphosphate system", *Appl. Phys. A* **1975**, *2(6)*, 329
[88] M. Saruwatari, T. Kimura, "LED pumped lithium neodymium tetraphosphate lasers", *IEEE J. Quantum Electron.* **1976**,*12(10)*, 584
[89] K. Otsuka and T. Yamada, "Transversely pumped LNP laser performance", *Appl. Phys. Lett.* **1975**, *26(6),* 311
[90] S. R. Chinn, H. Y.-P. Hong, "Low-threshold cw $LiNdP_4O_{12}$ laser", *Appl. Phys. Lett.* **1975**, *26(11),* 649
[91] K. Otsuka, T. Yamada, M. Saruwatari, T. Kimura, "Spectroscopy and laser oscillation properties of lithium neodymium tetraphosphate", *IEEE. J. Quantum Electron.* **1975**, *11(7),* 330
[92] J. Nakano, K. Otsuka, T. Yamada, "Fluorescence and laser emission cross sections in $NaNdP_4O_{12}$", *J. Appl. Phys. A* **1976**, *47(6)*, 2749
[93] S. R. Chin, H. Y.–P. Hong, "CW laser action in acentric $NdAl_3(BO_3)_4$ and $KNdP_4O_{12}$ ", *Opt. Commun.* **1975**, *15(3)*, 345
[94] D. Xue, S. Zhang, "Calculation of nonlinear optical properties of $KNdP_4O_{12}$", *Phys. Stat. Sol. (a)* **1998**, *165(2)*, 509
[95] V. Nikolov, K. Iliev, P. Peshev, "Relationship between the hydrodynamics in the melt and the shape of the crystal/melt interface during Czochralski growth of oxide single crystals. I. Determination of the critical crystal rotation rate from physical simulation on free and forced convections", *J. Cryst. Growth* **1988**, *89(2-3)*, 313
[96] T. M. Bruton, E. A. D. White, "Measurements of solution properties and the growth of single crystals of lead tantalate $PbTa_2O_6$", *J. Cryst. Growth* **1973**, *19(4)*, 341
[97] T.-S. Ke, M Ross, "An apparatus for measurement of extremely high internal friction", *Rev. Sci. Intrum.* **1949**, *20(11),* 795
[98] T. S. Ke, "Experimental evidence of the viscous behaviour of grain boundaries in metals", *Phys. Rev.* **1947**, *71(8)*, 533
[99] D. W. G. White, "Theory and experiment in methods for the precision measurement of surface tension", *Trans. ASME* **1962**, *55*, 757
[100] T. B. King, "The surface tension and structure of silicate slags", *J. Soc. Glass Tech.* **1961**, *23*, 241
[101] L. Shartsis, W. Spinner, W. Smock, "Surface tension of compositions in the systems PbO-B_2O_3 and PbO-SiO_2", *J. Amer. Ceram. Soc.* **1948**, *31(1),* 23
[102] V. Nikolov, K. Iliev, P. Peshev, "Relationship between the hydrodynamics in the melt and the shape of the crystal/melt interface during Czochralski growth of oxide single crystals. II. Determination of the critical crystal rotation rate from physical simulation on free and forced convections; comparison with experimental data on crystal growth", *J. Cryst. Growth* **1988**, *89(2-3)*, 324
[103] W. Tolksdorf, *Handbook of crystal growth*, vol. 2:part A, Elsevier Science publishers, Amsterdam, **1994**
[104] J. L. Pouchou, F. Pichoir, "Un nouveau modèle de calcul par la microananlyse quantitative par spectrómetrie de rayons X. Partie I : application a l'analyse d'échantillons homogènes", *Rech. Aerosp.* **1984**, *3*, 167
[105] W. L. Brag**, "**X-Rays and Crystal Structure*",* *Philosophical Transactions of the Royal Society of London. Series A* **1915**, *215*, 253
[106] J. Pickworth Glusker, K. N. Trueblood, *Crystal structure analysis: A premier*, Oxford University press, New York, **1985**

[107] J. Rodríguez-Carvajal, *Short reference guide for the computer program FULLPROF*, Laboratoire Léon Brillouin, CEA-CNRS, Gif sur Yvette, 1998
[108] R.A. Young "*The Rietveld method*", Internacional union of crystallography, monographs on crystallography 5, Oxford University press, Oxford,**1995**
[109] B. D. Cullity, *Elements of X-ray diffraction*, Addison-Wesley, **1978**
[110] L. G. Schulz, "Determination of preferred orientation in flat transmission samples using a Geiger counter X-ray spectrometer", *J. Apl. Phys.* **1949**, *20(11)*, 1033
[111] B. W. Mott, *Micro-indentation hardness testing*, Butterworths, London, **1956**
[112] G. R. Fowles, *Introduction to modern optics*, Dover publications, New York, **1989**
[113] T. Y. Fan, C. E. Huang, B. Q. Hu, R. C. Eckardt, Y. X. Fan, R. L. Byer, R. S. Feigelson, "Second harmonic generation and accurate index of refraction measurements in flux-grown KTiOPO4", *Appl. Opt.* **1987**, *26(12)*, 2390
[114] F. A. Jenkins, H. E. White, *Fudamentals of Optics*, Auckland, McGraw Hill, **1976**
[115] R. Solé, V. Nikolov, A. Vilalta, J. J. Carvajal, J. Massons, Jna. Gavaldà, M. Aguiló, F. Díaz, "Growth of $KTiOPO_4$ films on $KTi_{1-x}Ge_xOPO_4$ substrates by liquid-phase epitaxy", *J. Mater Res.* **2002,** *17(3),* 563.
[116] S. K. Kurz, T. T. Perry, "A Powder Technique for the Evaluation of Nonlinear Optical Materials", *J. Appl. Phys.* **1968**, *39(8)*, 3798
[117] V. G. Dimitriev, G. G. Gurzadyan, D. N. Nikogosyan, *Handbook of nonlinear optical crystals*, Springer-Verlag, New York, **1991**
[118] B. Boulanger and J. Zyss, "Nonlinear optical properties", *International Tables of Crystallography, volume D: Physical properties of crystals*, Kluwer Academic, **2003**
[119] S. Miyazawa, H. Koizumi, K. Kubodera, H. Iwasaki, "Epitaxial growth of $KNdP_4O_{12}$ laser waveguides", *J. Cryst. Growth* **1979**, *47(2),* 351
[120] B. N. Litvin, G. I. Dorokhova, O. Filipenko, "Synthesis, structure, and properties of single crystals of potassium-neodymium tetraphosphates", *Dokl. Akad. Nauk SSSR* **1981**, *26(8),* 717
[121] Z. Mazurak, B. Jezowska-Trzebiatkowska, D. Schultze, C. Waligora, "Growth, intensity and probabilities of f-f transitions of Nd^{3+} ions in KNd(PO3)4 single crystals", *Cryst. Res. Technol.* **1984**, *19(1)*, 7
[122] D. Elwell, H. J. Scheel, *Crystal growth from high-temperature solution*, Academic Press, New York, **1975**
[123] E. Dowty, *Shape for windows*, version 5.0.1., **1995**
[124] W. K. Burton, N. Cabrera, F. C. Frank, *Phil. Trans. Royal Soc. London* **1951**, *A243*, 299
[125] N. Cabrera, D. Vermilyea, *Growth and Perfection of Crystals,* Wiley, New York, **1958**
[126] K. Sangwal. R. Rodríguez-Clemente, Surface Morphology of Crystalline Solids, Trans. Tech., Brookfield, 1991.
[127] K. Sangwal, "Etching of Crystals, theory, experiment and application", North-Holland, Amsterdam, **1987**
[128] P. Hartman, "Crystal growth - an introduction", North-Holland, Amsterdam, **1973**
[129] M. B. Ives, D. D. McAusland, "On the slope of etch pits", *Surf. Sci.* **1968**, *12(2),* 189
[130] G. M. Spink, M. B. Ives, "Morphology of crystallographic etch pits in iron", *J. Appl. Phys.* **1971**, *42(2),* 511
[131] N. P. Barnes, D. J. Gettemy, R. S. Adhav, "Variation of the refractive index with temperature and the tuning rate for KDP isomorphs", *J. Opt. Soc. Am.* **1982**, *72(7)*, 895
[132] S. Kielich, "", *Optoelectronics* **1970,** *2,* 125
[133] S. Biswal, S. O'Connor, S. Bowman, "thermo-optic parameters measured in ytterbium-doped potassium gadolinium tungstate", *Appl. Opt.* **2005**, *44(15),* 3093

[134] M. Saito, T. Honma, Y. Benino, T. Fujiwara, T. Komatsu, "Formation of nonlinear optical $KSm(PO_3)_4$ crystals in phosphate glasses by YAG laser irradiation ", *Solid State Sciences* 2004, *6(9),* 1013
[135] B. G. Wybourne, *Spectroscopic properties of rare earths*, Wiley, New York, **1965**
[136] C. Görller-Walrand, K. Binnemans, *Handbook on the physics and chemistry of rare earths*, vol. 25, chap. 167, Elsevier Science, Amsterdam, **1998**
[137] V. V. Ovsyankin, A.A. Kaplyanskii, R.M. McFarlane (editors), *Spectroscopy of solids containing rare earth ions*, Elsevier Science, Amsterdam, 1987
[138] N. V. Kuseshov, A. A. Llagatsky, A. V. Podlipensky, V. P. Mikhailov, G. Huber, "Pulsed laser operation of Yb-doped $KY(WO_4)_2$ and $KGd(WO_4)_2$", *Opt. Lett.* **1997**, *22(17)*, 1317
[139] X. Mateos, V. Petrov, M. Aguiló, R. Solé, Jna. Gavaldà, J. Massons, F. Diaz, U. Griebner, "Continues wave laser oscillation of Yb^{3+} in monoclinic $KLu(WO_4)_2$", *IEEE J. Quantum Electron.* **2004**, *40(8),* 1056
[140] J. J. Carvajal, R. Solé, jna. Gavaldà, J. Massons, P. Segonds, B. Boulanger, A. Brenier, G. Boulon, J. Zaccaro, M. Aguiló, F. Diaz, "Spectroscopic and second harmonic generation properties of a new crystal: Yb-doped $RbTiOPO_4$", *Opt. Mat.* **2004,** *26(3),* 313
[141] F. D. Patel, E. C. Honea, J. Speth , S. A. Payne, R. Hutcheson, R. Equall, "Laser demonstration of $Yb_3Al_5O_{12}$ (YbAG) and materials properties of highly doped Yb:YAG", *IEEE J. Quantum Electron.* **2001**, *37(1),* 135
[142] D. S. Sumida, T. Y. Fan, "Effect of radiation trapping on fluorescence lifetime and emission cross section measurements in solid-state laser media", *Opt. Lett.* **1994**, *19(17)*, 1343
[143] N. Uehara, K.K. Ueda, Y. Kubota, "Spectroscopic measurements of a high-concentration Yb^{3+}:LiF_4 crystal" *Jpn. J. Appl. Phys.* **1996**, *35*, L499
[144] M. P. Hehlen, "Effect of radiation trapping on measures excited-state lifetimes in solids" J. Opt. Soc .Am. B 1997, 14, 1312
[145] T. Y. Fan, "Nd^{3+} versus Yb^{3+} solid-state lasers at 1 micron", CMF1, CLEO, Baltimore, Maryland, May **1999**
[146] B. R. Judd, "Optical Absorption Intensities of Rare-Earth Ions**",** *Phys. Rev.* **1962,** *127(3)*, 750
[147] G. S. Ofelt, "Intensities of Crystal Spectra of Rare-Earth Ions", *J. Chem. Phys.* **1962**, *37(3)*, 511
[148] J. Nakano, K. Kubodera, T. Yamada, S. Miyazawa, "Laser-emission cross sections of $MeNd_4O_{12}$ (Me=Li, Na, K) crystals", *J. Appl. Phys.* **1979***, 50(10),* 6492
[149] C. Gueugnon, J. P. Budin, "Determination of the fluorescence quantum efficiency and laser emission cross sections of neodymium crystals: application to $KNdP_4O_{12}$", *IEEE J. Quantum Electron.* **1980**, *QE-16(1),* 94
[150] M. Malinowski, W. Wolinski, "Radiative transition probabilities and energy levels of Nd^{3+} ion in $KNdP_4O_{12}$ crystals", *Acta Phys. Pol.* **1984**, *A65(4),* 303
[151] Z. Mazurac, B. Jezowska-Trzebiatkowska, D. Schultze, C. Waligora, "Growth, intensity probabilities of f-f transitions of Nd^{3+} ions in $KNd(PO_3)_4$ single crystals", *Cryst. Res. Technol.* **1984**, *19(1),* 7
[152] J. B. Gruber, M. E. Hills, T. H. AILLC, C. K. Jayasankar, J. R. Quagliano, F. S. Richardson, "Comparative analysis of Nd^{3+} ($4f^3$) energy levels in tour garnet hosts", *Phys. Rev.* **1999**, *41(12),* 7999
[153] K. Otsuka, T. Yamada, M. Saruwatari, T. Kimura, "Spectroscopy and laser oscillation properties of lithium neodymium tetraphosphate", *IEEE J. Quantum Electron.* **1975**, *QE-11(7)*, 330
[154] T. Cusida, H. M. Marcos, J. E. Geusic, "Laser transition cross section and fluorescence branching ratio for Nd^{3+} in Yttrium Aluminium Garnet", *Phys. Rev*. **1968**, *167(2),* 289
[155] K. Fuhrmann, N. Hogson, F. Holliger, H. Weber, "Effective cross section of the Nd:YAG 1.064 mm-laser transition", *J. Appl. Phys.* **1987**, *62(10),* 4041

Paper I

Crystal growth, structural characterization, and linear thermal evolution of $KGd(PO_3)_4$

I. Parreu, R. Solé, Jna. Gavaldà, J. Massons, F. Díaz, M. Aguiló

Chemistry of Materials **2005**, 17(4), 822

Crystal Growth, Structural Characterization, and Linear Thermal Evolution of $KGd(PO_3)_4$

I. Parreu, R. Solé, Jna. Gavaldà, J. Massons, F. Díaz, and M. Aguiló*

Física i Cristallografia de Materials (FiCMA), Universitat Rovira i Virgili, C. Marcel lí Domingo, 43007, Tarragona, Spain

Received September 9, 2004. Revised Manuscript Received November 5, 2004

We determined the crystallization region of $KGd(PO_3)_4$ (KGP) in the ternary system $Gd_2O_3-K_2O-P_2O_5$, the isotherms of saturation temperature and six neighboring phases: KPO_3, $GdPO_4$, $KGdP_4O_{12}$, $Gd(PO_3)_3$-orthorhombic, $Gd(PO_3)_3$-monoclinic, and GdP_5O_{14}. We successfully grew KGP single crystals by the top-seeded solution growth (TSSG) slow cooling method. To optimize the growth process and obtain high-quality KGP crystals, solution composition and seed orientation were analyzed and a growth device was added. KGP is isostructural to $KNd(PO_3)_4$, crystallizes in the monoclinic system $P2_1$ and the cell parameters determined are $a = 7.2701(11)$, $b = 8.3818(8)$, and $c = 7.9608(10)$ Å, $\beta = 91.776(12)°$, $Z = 2$, and $V = 484.87(11)$ Å^3. We studied how they evolved as the temperature increased from room temperature to 773 K and observed an almost isotropic linear thermal expansion, the tensor of which we also calculated. In the room temperature to 1273 K range analyzed, we found that KGP irreversibly decomposed at 1142 K. The second harmonic efficiency, qualitatively measured by the Kurtz method, was at least similar to that of KH_2PO_4 (KDP).

Introduction

Condensed phosphates have been widely studied because they can be used in several scientific fields, such as catalysis, electricity, and optics. Optics involves the so-called polyphosphates of lanthanides, which are generated from a large number of phosphate ions in either long-chain or cycling geometry. Several of these are reported[1−11] to have good optical properties for the laser technology field. Most are neodymium-stoichiometric polyphosphates designed for use as mini-lasers, such as $KNd(PO_3)_4$ (KNP).[5,8,12] KNP has two important advantages: first, it can be obtained as high-quality single crystal, and second, its almost isotropic thermal expansion prevents it from deforming.

We therefore decided to grow and study $KGd(PO_3)_4$ (KGP). This material should maintain the good properties of KNP because it is reported to be isostructural[13] to it and, in fact, we verified this by comparing both X-ray powder diffraction patterns recorded in the same conditions. KGP was therefore regarded as a promising new laser host that can also be easily doped with any other lanthanide ion since the gadolinium has a high capacity to be substituted.

In this paper we analyze the conditions of the KGP crystal growth process and present its basic structural characterization.

As KGP has never been reported before, we performed a parallel study to our previous one for KNP,[12] for which there is also little information in the literature. We determined the KGP crystallization region in the self-flux. Then, taking into account the results obtained with KNP, we optimized its crystal growth process. The KGP cell parameters and morphology were determined. We also studied how KGP behaved with temperature and determined thermal expansion and phase transitions. Finally, as this structure is not centrosymmetric, we qualitatively analyzed the possibility of second harmonic generation.

Experimental Section

Crystallization Region of $KGd(PO_3)_4$. To determine the region where $KGd(PO_3)_4$ crystallizes as a single phase in its self-flux, we grew small crystals of a large number of compositions in the $Gd_2O_3-K_2O-P_2O_5$ ternary system and determined their saturation temperatures.

A vertical tubular furnace with a Kantal AF heater was used to carry out the experiments. The temperature was measured by an S-type thermocouple and controlled by a Eurotherm 818 P controller/programmer connected to a thyristor.

We mixed the chosen ratios of Gd_2O_3, K_2CO_3, and $NH_4H_2PO_4$ to prepare roughly 20 g of solution in a 25-cm^3 platinum crucible.

* To whom correspondence should be addressed. E-mail: aguilo@quimica.urv.es.

(1) Otsuka, K.; Yamada, T. *Appl. Phys. Lett.* **1975**, *26*, 311.
(2) Chinn, S. R.; Hong, H. Y.-P. *Appl. Phys. Lett.* **1975**, *26*, 649.
(3) Otsuka, K.; Yamada, T.; Saruwatari, M.; Kimura, T. *IEEE J. Quantum Electron.* **1975**, *QE11*, 330.
(4) Nakano, J.; Otsuka, K.; Yamada, T. *J. Appl. Phys.* **1976**, *47*, 2749.
(5) Hong, H. Y.-P. *Mater. Res. Bull.* **1975**, *10*, 1105.
(6) Otsuka, K.; Miyazawa, S.; Yamada, T.; Iwasaki, H.; Nakano, J. *J. Appl. Phys.* **1977**, *48*, 2099.
(7) Chinn, S. R.; Hong, H. Y.-P. *Opt. Commun.* **1975**, *15* (3), 345.
(8) Mazurak, Z.; Jezowska-Trzebiatkowska, B.; Schultze, D.; Waligora, C. *Cryst. Res. Technol.* **1984**, *19*, 7.
(9) Weber, H. P.; Damen, T. C.; Danielmeyer, H. G.; Tofield, B. C. *Appl. Phys. Lett.* **1973**, *22*, 534.
(10) Danielmeyer, H. G.; Huber, G.; Krühler, W. W.; Jeser, J. P. *Appl. Phys.* **1975**, *2*, 335.
(11) Chinn, S. R.; Pierce, J. W.; Heckscher, H. *IEEE J. Quantum Electron.* To be published.
(12) Parreu, I.; Solé, R.; Gavaldà, Jna.; Massons, J.; Díaz, F.; Aguiló, M. *Chem. Mater.* **2003**, *15*, 5059.
(13) Palkina, K. K.; Chudinova, N. N.; Litvin, B. N.; Vinogradova, N. V. *Izv. Akad. Nauk SSSR, Neorg. Mater.* **1981**, *17* (8), 1501.

10.1021/cm048442n CCC: $30.25
Published on Web 01/19/2005

Table 1. Growth Data Associated with KGP Single Crystals

expt	solution composition $Gd_2O_3-K_2O-P_2O_5$	solution wt (g)	seed orientation	seed position	cooling interval (K)	cryst dimens ($a \times b \times c$) (mm^3)	cryst wt (g)
1	4/31/65	20	a^*	centered	15	$1.4 \times 2.4 \times 1.8$	0.01
2	6/34/60	20	a^*	centered	15	$2.3 \times 6.7 \times 3.6$	0.13
3	6/34/60	20	a^*	acentered	15	$3.4 \times 7.1 \times 5.5$	0.29
4	6/34/60	200	a^*	acentered	20	$5.9 \times 15.6 \times 10.3$	1.77
5	6/34/60	200	b	acentered	20	$8.6 \times 4.8 \times 9.7$	1.63
6	6/34/60	200	c^*	acentered	20	$11.0 \times 16.2 \times 5.6$	1.94

These initial reagents were decomposed by heating them until the complete bubbling of NH_3, CO_2, and H_2O was reached. The solution was then homogenized by maintaining the temperature at about 50−100 K above the expected saturation temperature for 3−8 h, depending on the solution composition. The axial temperature gradient in the solution was about 10 K/mm and the surface was the coldest point of the whole volume.

We decreased the temperature of the homogeneous solution by 10 K approximately every 30 min until crystals appeared on a platinum wire immersed in the solution. The saturation temperature was then accurately determined by observing the growth or dissolution of these small crystals over long periods of time. Next, we used a platinum disk placed in contact with the solution surface and rotated it at 45 rpm to grow the crystals. The temperature was decreased to about 25 K below its saturation temperature at a cooling rate of 0.5−1 K/h to obtain the supersaturation of the solution.

We preliminarily identified the crystals by direct observation with an optical microscope and then by X-ray powder diffraction analysis. Some were also observed and photographed in a scanning electron microscope (SEM) JEOL JSM 6400.

X-ray Powder Diffraction. We used the X-ray powder diffraction technique to identify the KGP crystalline phase and some neighboring ones of the KGP crystallization region. The experiments were carried out with a D5000 Siemens X-ray powder diffractometer in a $\theta-\theta$ configuration using the Bragg−Brentano geometry and Cu Kα radiation. The X-ray powder diffraction patterns were recorded using a scintillation counter as detector.

Using this same equipment, we calculated the crystal cell parameters of KGP from the powder diffraction data obtained at 298 K in the 2θ range from 10 to 70°, using a step size of 0.03° and a step time of 5 s. To refine them, we used the structure of KNP previously solved[5,14] by single-crystal X-ray diffraction as the starting model.

We also used X-ray powder diffraction analysis to study how the crystal cell parameters evolved with temperature and to determine the thermal expansion tensor of KGP. We used the same equipment as before but with the addition of an Anton-Paar HTK10 platinum ribbon heating stage. The X-ray powder diffraction patterns were recorded at the same conditions: $2\theta = 10-70°$, step size = 0.03°, step time = 5 s, at temperatures of 298, 323, 373, 473, 573, 673, and 773 K, with a delay time of 300 s before each pattern recording.

We also analyzed the evolution of KGP with temperature in the room temperature to 1273 K range both by heating and cooling the sample. In this case, the X-ray powder diffractometer was equipped with the heating stage and also a Braun position-sensitive detector (PSD). The X-ray powder diffraction patterns were recorded at $2\theta = 10-70°$ and the measuring time per degree was 10 s. During the heating cycle, the sample was heated at a rate of 10 K/s from room temperature to 673 K and from this point to the maximum (1273 K) it was heated at a lower rate of 0.17 K/s. The cooling cycle was designed using the same conditions. Diffraction patterns were registered every 50 K between 673 and 1273 K in both processes.

Differential Thermal Analysis (DTA). We also used DTA measurements to study the evolution of KGP with temperature before analyzing it more accurately by X-ray powder diffraction. This analysis was carried out in a TA Instruments simultaneous differential techniques instrument SDT 2960. We used calcined Al_2O_3 as reference material and Ar, at a flow of 90 cm^3/min, as purge gas. The powdered sample, which weighed around 20 mg, was placed in a platinum pan and heated at a rate of 10 K/min between room temperature and 1273 K. The storage rate of data was 0.5 s/data point.

Top-Seeded Solution Growth (TSSG). We used the top-seeded solution growth (TSSG) slow cooling method without pulling to obtain inclusion-free KGP single crystals of a suitable size for later studies. We performed the growth experiments using a vertical furnace controlled by a Eurotherm 818 P controller/programmer. A conical platinum crucible was used to contain the solution, the homogenization of which was achieved by keeping the temperature about 50 K above the expected saturation temperature for 3−4 h. The solution surface was the coldest point of the whole volume and the temperature gradient in its axial direction was 1.2 K/mm. We accurately determined the saturation temperature by observing the growth or dissolution of a seed in contact with the solution surface. Then, when the solution temperature was decreased at a rate of 0.1 K/h, the crystal began to grow completely submerged in the solution on the seed bottom, which was constantly rotated during the growth process at 75 rpm. We used parallelepipedic oriented seeds of similar size for all experiments. These were around 8 mm along the axial direction (a^*, b, or c^*) of the rotation movement and around 2 mm in the other two radial directions. After the temperature was decreased by the chosen interval (15 or 20 K) the crystal was slowly removed from the solution and then cooled to room temperature at 30 K/h.

To optimize the crystal growth process, we performed several experiments under conditions chosen by taking into account the results of the previous study on KNP.[12] The cooling rate and rotation velocity were thus kept constant at 0.1 K/h and 75 rpm because the viscosities of the two solutions were similar. We analyzed how the solution composition and seed orientation affected the KGP crystal growth (see Table 1 for values and corresponding results). We evaluated these results by taking into account the growth rate and quality of the KGP crystal grown.

First we filled a platinum conical crucible of 25 cm^3 with suitable amounts of reagents to prepare roughly 20 g of solution with the compositions shown in Table 1 (experiments 1 and 2) to study the effect of solution composition. With this lower amount of solution we also checked the suitability of using the previously introduced growth device.[12] In this case it also improved both crystal quality and growth rate (experiment 3). This growth device comprises a platinum turbine centered on the rotation axis and a seed support above it displaced around 11 mm from this axis. The effect of seed orientation was then analyzed using a larger amount of solution (around 200 g) placed in a platinum crucible of 125 cm^3. The seeds used were as described above (experiments 4−6).

(14) Parreu, I.; Solans, X.; Aguiló, M. Unpublished.

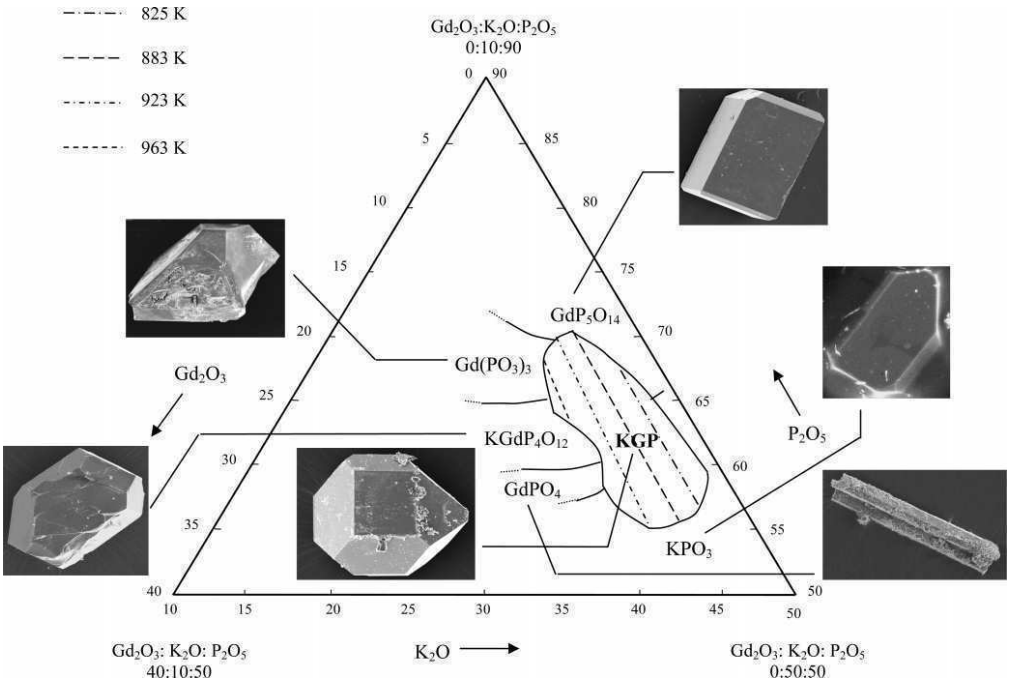

Figure 1. Crystallization Region of KGP and saturation temperatures in the $Gd_2O_3-K_2O-P_2O_5$ system. SEM images of KGP and neighboring phases.

Second Harmonic Generation (SHG) Measurements. We evaluated the second harmonic response of KGP using the Kurtz method.[15] Small KGP crystals were powdered and graded with standard sieves to obtain a uniform particle size between 5 and 20 μm, and then uniformly packed. The sample was then placed in a 2-mm-thick quartz cell and irradiated using a pulsed Nd:YAG laser.

To estimate the incident power, we measured the energy reflected by the sample. We also measured the energy of the double radiation it emitted, the frequency of which was twice that of the incident radiation, using a silicon PIN. We used the ratio between these signals, calculated as an average of over 100 laser shots, to estimate the second harmonic efficiency of the sample and compared this efficiency with that of KDP,[16] which is a well-known nonlinear optical material.

Results and Discussion

KGP Crystallization Region. Figure 1 shows the crystallization region of KGP in the $Gd_2O_3-K_2O-P_2O_5$ ternary system and the saturation temperature isotherms determined after studying about 50 solution compositions. SEM images of KGP and neighboring phases are added.

In general, polyphosphates have many local geometries—long-chains or cycles—and crystalline structures, because when they are formed the phosphate units have a high versatility of condensation. The structure of those of lanthanides is highly dependent on the size of this ion. From this point of view, two groups are defined, one for ions belonging to the first half of lanthanides and one for ions belonging to the second half. Since gadolinium is placed just in the middle, $KGd(PO_3)_4$ can present the phase presented and named by us as KGP (monoclinic, $P2_1$, $a = 7.2701(11)$ Å, $b = 8.3818(8)$ Å, $c = 7.9608(10)$ Å, $\beta = 91.776(12)°$, $Z = 2$, and $V = 484.87(11)$ Å^3) usual for the first half, and the usual for the second half (monoclinic, $P2_1/n$, $a = 10.412(2)$ Å, $b = 8.996(2)$ Å, $c = 10.836(2)$ Å, $\beta = 105.94(1)°$, $Z = 4$, and $V = 975.9(3)$ Å^3).[17] Studying the KGP crystallization region, we found that the neighboring phase $Gd(PO_3)_3$ also presented polymorphism in most of the compositions we studied—a mixture of the orthorhombic phase (first half) and the monoclinic one (second half).

The high versatility would explain the irregularity of the KGP crystallization region and the many neighboring phases around it, among which we also found the polymorph phase of KGP in a cycling geometry, $KGdP_4O_{12}$. In Table 2, therefore, we summarize the composition limits of the KGP crystallization region and the neighboring phases determined. The limit points are defined by the intersection of the Gd_2O_3/K_2O isoconcentrational lines with P_2O_5 molar concentrations. The isoconcentrational lines of this ratio are roughly parallel to the saturation temperature isotherms whcih increase from 825 to 963 K when the Gd_2O_3/K_2O ratio is also increased. KGP crystallizes inside these points (Table 2) and up to a Gd_2O_3/K_2O ratio of 3/97 and P_2O_5 concentration approximately between 58 and 65. The six neighboring phases

(15) Kurtz, S. K.; Perry, T. T. *J. Appl. Phys.* **1968**, *39*, 3798.
(16) Dmitriev, V. G.; Gurzadyan, G. G.; Nikogosyan, D. N. *Handbook of Nonlinear Optical Crystals*; Springer-Verlag: New York, 1991.
(17) Rekik, W.; Naïli, H.; Mhiri, T. *Inorg. Acta Crystallogr.* **2004**, *C60*, i50.

Table 2. Solution Composition Limits of the KGP Crystallization Region and the Neighboring Crystalline Phases Determined

solution composition (mol %)		
molar ratio Gd_2O_3/K_2O	P_2O_5 mol %	neighboring phase
5/95	57	KPO_3
5/95	67	GdP_5O_{14}
10/90	56	KPO_3
10/90	71	GdP_5O_{14}
15/85	55	KPO_3
15/85	70	GdP_5O_{14}
20/80	58	$GdPO_4$
20/80	64	$KGdP_4O_{12}$
20/80	68	$Gd(PO_3)_3$

identified are KPO_3, $GdPO_4$,[18] $KGdP_4O_{12}$,[19] $Gd(PO_3)_3$-orthorhombic,[20] $Gd(PO_3)_3$-monoclinic,[20] and GdP_5O_{14}.[21] While KPO_3 crystallizes below the crystallization region, GdP_5O_{14} crystallizes above it. In the same P_2O_5 concentration range as the crystallization region, but in the highest Gd_2O_3 concentration zone, the other phases—$GdPO_4$, $KGdP_4O_{12}$, and orthorhombic and monoclinic $Gd(PO_3)_3$—crystallize.

The viscosity of the solutions was quite high, though varied, throughout the crystallization region. Crystal growth is very difficult in highly viscous solutions because, due to the low molecular mobility inside them, the growth units find it difficult to reach the crystal surface. The average growth rate and the crystal quality therefore decrease and the average time of homogenization increases. So we qualitatively studied the relationship between the solution composition and the growth rate, which is directly influenced by the viscosity of the solution. When we increased the P_2O_5 concentration and kept the Gd_2O_3/K_2O ratio constant, the viscosity went up. The viscosity also went up when we decreased this Gd_2O_3/K_2O ratio, probably because the saturation temperature also decreased, taking into account the inverse relationship between viscosity and temperature. When the K_2O concentration was above 98 mol %, the increase in solution viscosity hindered crystallization at all P_2O_5 concentrations.

Using these results, we chose an apparently optimal composition zone to initiate the growth experiments of KGP single crystals. This is the zone with a low P_2O_5 concentration and fairly displaced to the left corner, where the saturation temperature is highest and the K_2O concentration is lowest.

Top-Seeded Solution Growth (TSSG) of KGP Single Crystals. We analyzed how solution composition and seed orientation affected the growth rate and quality of KGP single crystals. The conditions and results of the experiments are shown in Table 1. For all of these experiments, the rotation velocity was 75 rpm and the cooling rate was 0.1 K/h.

To check how viscosity affected the crystal growth process, we chose $Gd_2O_3-K_2O-P_2O_5 = 4/31/65$ mol % (experiment 1) that was fairly displaced from the optimal composition zone previously determined because of the high P_2O_5 concentration. The crystals obtained from this solution were too small and too light, despite the long cooling period, and their quality was also very low. The composition of the solution for growing KGP single crystals should therefore be chosen from the optimal zone determined. We used $Gd_2O_3-K_2O-P_2O_5 = 6/34/60$ mol % placed in this zone to grow the crystals, the optimal value for KNP.[12]

We also checked the use of the previously described growth device. Its platinum turbine increased the movement of the growth units inside the solution, which had been hindered by the viscosity. As with KNP,[12] this device increased both the growth rate and the quality of the crystals (experiment 3).

KGP crystal growth was achieved using the three crystallographic directions, a^*, b, and c^*, as axial seed orientation. Although the quality of the crystals was quite similar, there were some differences in growth rate. The lowest growth rate was for the b seed orientation. For the other two orientations (experiments 4−6), the growth rates were similar. Figure 2a shows a KGP single-crystal grown in experiment 4.

Crystal Structure of KGP. We calculated the crystal cell parameters of KGP from the X-ray powder diffraction data using the FULLPROF program[22] and the Rietveld method.[23] The structure of KNP, solved earlier[5,14] by single-crystal X-ray diffraction, was used as the starting model. We selected a Pearson VII function and included in the final Rietveld refinement the following parameters: zero-point, scale factor, background coefficients, the four cell parameters (a, b, c, and β), and one profile shape parameter. We determined the following: $a = 7.2701(11)$ Å, $b = 8.3818(8)$ Å, $c = 7.9608(10)$ Å, $\beta = 91.776(12)°$, $V = 484.87(11)$Å^3, $P2_1$, and $Z = 2$. The cell parameters were slightly smaller than those for KNP because the ionic radius for Gd^{3+} is slightly smaller than that for Nd^{3+} (0.938 Å and 0.995 Å, respectively).

Crystal Morphology of KGP. We observed small KGP single crystals by scanning electron microscopy (SEM) (Figure 1) and large ones using an optical microscope (Figure 2a) to describe its morphology. The habit was made up of the crystalline forms $\{00\bar{1}\}$, $\{100\}$, $\{011\}$, $\{0\bar{1}1\}$, $\{110\}$, $\{\bar{1}10\}$, $\{10\bar{1}\}$, $\{101\}$, $\{\bar{1}\bar{1}1\}$, and $\{111\}$. Figure 2b shows the theoretical model, made with the Shape software,[24] in which most faces are hexagonal or square. Many of these faces are not equivalent by symmetry but are very similar since the β angle of KGP is close to 90° and its cell parameters are quite similar, which recommends using X-ray diffraction techniques in face indexation.

Linear Thermal Expansion Tensor. As some of the pumping light power is converted into heat inside KGP, we determined and located its thermal ellipsoid in order to determine how the temperature affected its structure. We analyzed the X-ray powder diffraction patterns in the 298−773 K temperature range using the FULLPROF program[22] and the Rietveld method[23] to determine how the cell

(18) Mullica, D. F.; Grossie, D. A.; Boatner, L. A. *Inorg. Chim. Acta* **1985**, *109*, 105.
(19) Ettis, H.; Naïli, H.; Mhiri, T. *Cryst. Growth Des.* **2003**, *3* (4), 599.
(20) Mel'nikov, P. P.; Komissarova, L. N.; Butuzova, T. A. *Izv. Akad. Nauk SSSR, Neorg. Mater.* **1981**, *17* (11), 2110.
(21) Bagieu-Beucher, M.; Duc, T. Q. *Bull. Soc. Fr. Mineral Crystallogr.* **1970**, *93*, 505.
(22) Rodríguez-Carvajal, J. *Short Reference Guide of the Computer Program FULLPROF*; Laboratoire León Brillouin, CEA-CNRS: Saclay, France, 1998.
(23) Young, R. A., Ed. *The Rietveld Method*; Oxford Science Publication-;International Union of Crystallography: Chester, U. K., 1995.
(24) Dowty, E. *Shape for Windows*, version 5.0.1; 1995.

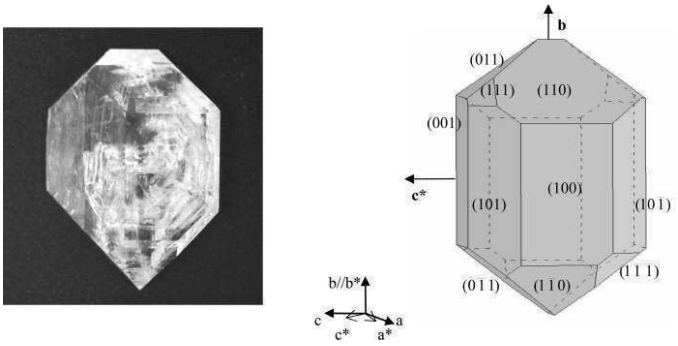

Figure 2. (a) KGP single-crystal grown with a seed in the *a** direction. (b) Scheme of the crystal morphology.

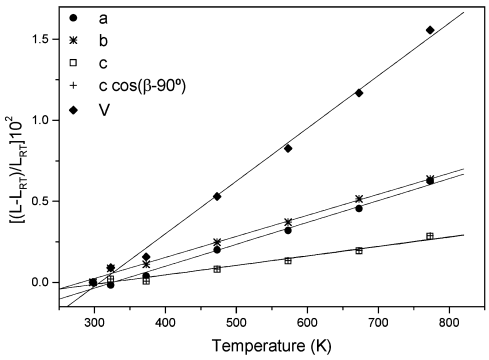

Figure 3. Relative thermal evolution of the cell parameters and unit cell volume of the $KGd(PO_3)_4$.

parameters evolved with temperature. The linear relationship between the average change in each cell parameter ($\Delta L/L$) and temperature is shown in Figure 3. As the temperature increased, KGP dilated slightly. While the β angle remained roughly constant, the cell parameters *a*, *b*, and *c* all increased in a similar way. This almost isotropic thermal expansion is a good property that prevents KGP from deforming when it is working above room temperature.

The linear thermal expansion coefficients can be calculated from the slope of the linear relationship ($\Delta L/L$) and the temperature for each unit cell parameter. The linear thermal expansion tensor at room temperature in the crystallophysical system $X_1||a$, $X_2||b$, $X_3||c^*$ is

$$\alpha_{ij(\mathrm{KGP})} = \begin{pmatrix} 13.50 & 0 & 0.60 \\ 0 & 13.00 & 0 \\ 0.60 & 0 & 5.86 \end{pmatrix} \times 10^{-6}\,\mathrm{K}^{-1}$$

In the principal system X_1',$X_2'||b$, X_3', the diagonalized linear thermal expansion tensor is

$$\alpha_{ij}{}'_{(\mathrm{KGP})} = \begin{pmatrix} 13.55 & 0 & 0 \\ 0 & 13.00 & 0 \\ 0 & 0 & 5.81 \end{pmatrix} \times 10^{-6}\,\mathrm{K}^{-1}$$

The principal axis, X_1', was found 4.76° clockwise from the *a* axis. The axis with a minimum thermal expansion, X_3', was found 2.69° from the *c* axis. The thermal expansion ellipsoid in the principal axes is shown in Figure 4.

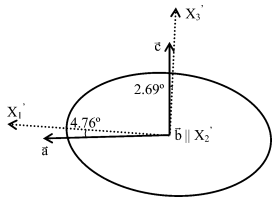

Figure 4. Thermal expansion ellipsoid for KGP in projection parallel to [010].

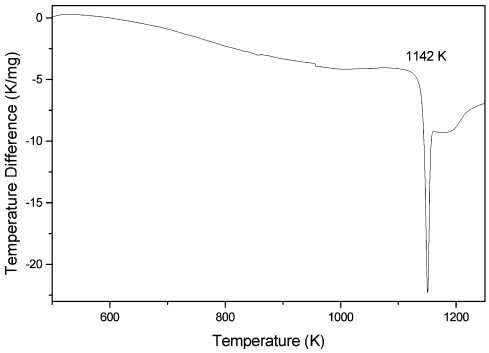

Figure 5. Differential thermal analysis (DTA) thermogram of $KGd(PO_3)_4$ in the 573−1273 K temperature range.

Phase Transitions. We analyzed how KGP evolved with temperature between room temperature and 1273 K using differential thermal analysis (DTA) and X-ray powder diffraction. Using DTA, we determined the exothermic transformation suffered by KGP at 1142 K. Figure 5 shows the thermogram obtained during the heating process in the 500−1250 K range. The change in weight during the experiment was not representative.

We studied this transformation more accurately by X-ray powder diffraction and identified the crystal phases involved. The bottom of Figure 6 shows the X-ray powder diffraction pattern of $KGd(PO_3)_4$ at room temperature and the selected

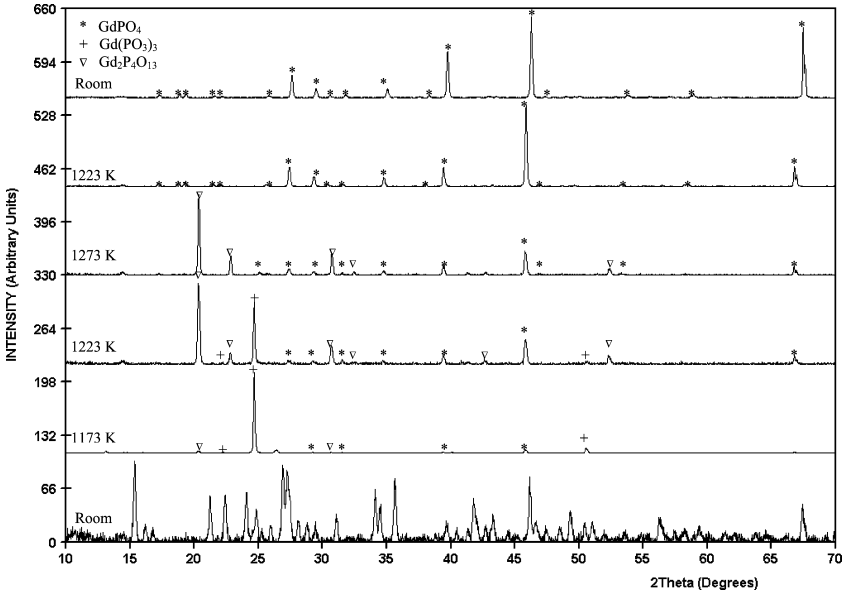

Figure 6. X-ray powder diffraction pattern of $KGd(PO_3)_4$ at room temperature and the selected patterns at several temperatures describing the evolution of $KGd(PO_3)_4$ with temperature in both the heating and cooling processes.

patterns at several temperatures which describes its evolution in both the heating and the cooling processes. The three new crystalline phases were identified as $GdPO_4$ (83-0657 ICDD database[18]), $Gd(PO_3)_3$ (the orthorhombic form, which is isostructural to that of the EuP_3O_9 31-0519 ICDD database[25]), and $Gd_2P_4O_{13}$ (35-0078 ICDD database[26]). Though all appeared in the X-ray diffraction pattern recorded at 1173 K, they behaved differently since only $GdPO_4$ remained until room temperature. $Gd(PO_3)_3$ appeared as the predominant phase at 1173 K but the intensity of its peaks rapidly decreased between this temperature and 1273 K, when it completely disappeared. As the intensity of the $Gd(PO_3)_3$ peaks decreased, the intensity of the peaks for the other two phases increased steadily in the same temperature range. At 1223 K during the cooling process $Gd_2P_4O_{13}$ completely disappeared and $GdPO_4$ became the only phase. From this temperature, the intensity of the $GdPO_4$ peaks remained fairly constant until room temperature. A slight displacement of the peaks was observed in the last X-ray diffractogram at room temperature because of the dilation of the material.

The X-ray powder diffraction study showed that KGP decomposed at 1173 K into GdPO4, $Gd(PO_3)_3$, $Gd_2P_4O_{13}$, and an amorphous phase, which probably contained phosphorus and potassium oxides because the sample weight remained roughly constant. However, between this temperature and 1223 K during the cooling process, a completely crystalline transformation of $Gd(PO_3)_3$ and $Gd_2P_4O_{13}$ into $GdPO_4$ occurred which probably involved a loss of amorphous potassium oxide. The $Gd(PO_3)_3$ transformation was completed first (at 1273 K) and the $Gd_2P_4O_{13}$ transformation was completed at 1223 K cooling process. The exothermic peak observed in the thermogram at 1142 K may be related to this decomposition.

These results therefore suggest that KGP decomposes irreversibly at 1142 K in accordance with this reaction:

$$4KGd(PO_3)_4 \rightarrow Gd(PO_3)_3 + GdPO_4 + Gd_2P_4O_{13} + \text{amorphous phase}$$

Second Harmonic Generation. The SHG efficiency (η) of KNP, calculated as previously described, was compared with the efficiency of KDP, which is widely used for nonlinear optical applications. The value of η/η_{KDP} we obtained was approximately one. The possibility of developing a self-frequency doubling laser increases interest in this material.

Conclusions

We determined the crystallization region of $KGd(PO_3)_4$ in the $Gd_2O_3-K_2O-P_2O_5$ system with its saturation temperature isotherms. We proved that solution compositions chosen from the optimal zone determined were suitable to grow single crystals. This zone is poor in P_2O_5 and rich in Gd_2O_3 and saturation temperatures related are the highest. We successfully grew KGP single crystals by the top-seeded solution growth-slow cooling method (TSSG). To achieve a suitable quality and size of crystals for later studies, several crystal growth conditions were optimized. We conclude that all three seed orientations are suitable for growing KGP by TSSG. Our results were similar when we used a^* or c^* orientations but the growth rate slightly decreased when we

(25) Tsujimoto, Y. *J. Electrochem. Soc.* **1977**, *124*, 553.

(26) Agrawal, D.; Hummel, J. *J. Electrochem. Soc.* **1980**, *127*, 1550.

used the *b* orientation. The suitability of the growth device was also proved.

KGP dilates slightly in any crystallographic direction and in an almost isotropic way. It decomposes irreversibly at 1142 K according to the reaction proposed and between this temperature and 1223 K crystalline transformations occur to finally generate a single product, $GdPO_4$, at room temperature.

Finally, we found that the second harmonic efficiency of KGP was similar to that of KDP.

Acknowledgment. We acknowledge financial support from DURSI 2001SGR317 and 2003FI00770 and CICyT MAT-02-04603-C05-03 and FIT070000-2003-661.

CM048442N

Paper II

Crystal growth and characterization of type III ytterbium-doped $KGd(PO_3)_4$: a new nonlinear laser host

I. Parreu, R. Solé, J. Massons, F. Díaz, M. Aguiló

Chemistry of Materials (submitted)

Crystal Growth and Characterization of type III Ytterbium-doped $KGd(PO_3)_4$: a new non-linear laser host

I. Parreu, R. Solé, J. Massons, F. Díaz , and M. Aguiló *

Física i Cristal·lografia de Materials (FiCMA), Universitat Rovira i Virgili. Campus Sescelades. C/Marcel·lí i Domingo, s/n, 43007. Tarragona. Spain.

Abstract. We determined how evolved the $P2_1$ crystallization region of ytterbium-doped $KGd(PO_3)_4$ (Yb:KGP) as a function of the ytterbium concentration in the compositions region close to the previously determined as optimum to growth single crystals of undoped KGP. In this region, the border between the polymorphs $KYb_xGd_{1-x}(PO_3)_4$ with long-chain geometry and $KYb_xGd_{1-x}P_4O_{12}$ with cyclical geometry, varied depending on the ytterbium concentration. Inclusion-free single crystals of Yb:KGP were successfully grown using the top seeded solution growth technique under similar conditions to those of KGP. Ytterbium doping in KGP was proved to be possible and effective. The effect of the ytterbium doping on structural and optical properties of the KGP host was determined. We found that Yb:KGP decomposed irreversibly at 1130 K. The vibrational structure of both KGP and Yb:KGP was found to be similar to other metaphosphates. The spectroscopic properties of ytterbium in the KGP host were analyzed.

* to whom correspondence should be addressed.
e-mail: magdalena.aguilo@urv.net

Crystal Growth and Characterization of type III Ytterbium-doped $KGd(PO_3)_4$: a new non-linear laser host

I. Parreu, R. Solé, J. Massons, F. Díaz , and M. Aguiló [*]

Física i Cristal·lografia de Materials (FiCMA), Universitat Rovira i Virgili, Campus Sescelades c/ Marcel·lí Domingo, s/n, E-43007-Tarragona, Spain.

Introduction

Currently, a great range of wavelengths from the ultraviolet to the infrared are needed for a huge variety of applications such as high-density optical data storage, color displays, biotechnology, medicine, submarine communications, transparent atmosphere applications, etc. These wavelengths can be managed from frequency conversion of a given laser emission by non-linear optical processes such as frequency doubling. Attractive crystals for frequency conversion are bi-functional laser and optical materials, in which the laser effect and the nonlinear optical process occur simultaneously inside the same host. A self frequency doubling (SFD) laser has lower loses, i.e. reflections, absorption, scattering loses, and leads to a simpler and more compact laser device. This advantage can be added to the others that have the solid-state laser sources such as efficiency, low maintenance and cost and the possibility to be diode pumped. Since the first demonstration of SFD laser action in the green region from Nd-doped $MgO:LiNbO_3$ [1], a great effort was focused on searching new nonlinear laser crystals capable of generating SFD laser radiation in the visible. Up to now, SFD in the visible has been proved in several Nd- and Yb-doped nonlinear crystals [2,3]. The 1 μm-laser emission of these ions can be combined with the second harmonic generation properties of the nonlinear host to produce green laser radiation by SFD. The ytterbium ion is an interesting alternative to neodymium in the same wavelength range near 1 μm because of several important advantages [4,5,6,7]. The ytterbium ion has a longer energy-storage capability because of the longer radiative lifetime of the upper laser manifold, about three or four times longer. The simple two-manifold electronic structure of ytterbium excludes a variety of competitive processes which can depopulate the upper laser level and hence reduce the laser efficiency. The small Stokes shift between absorption and emission, i.e. quantum defect, reduces the thermal load and gives efficient operation at high powers. Finally, ytterbium is totally transparent in the green region, so the inevitable reabsorption losses of neodymium in the wavelength range of the second harmonic can be avoided. For the same reason, the non-linear host should also be transparent at the generated wavelength range. More recently, it has been furthermore reported [2,3,8,9,10,11,12,13] highly efficient laser operation in some non-linear crystals doped with ytterbium. As a rule, a self-frequency doubling crystal must (i) accept fluorescent ion doping and (ii) be phase-matchable for its laser emission. The potentiality of these crystals relies on a strong and wide pump absorption bandwidth as well as on a relative gain cross-section.

We propose in this paper a new candidate to self-frequency doubling laser material Yb-doped $KGd(PO_3)_4$ (Yb:KGP) because it satisfies all of these preliminary essential conditions. The KGP host has a noncentrosymmetric structure; SFD can therefore originate from the second order non-linear polarization. Type III KGP is monoclinic and has $P2_1$ as space group. The crystal cell parameters are [14]: a=7.255(4), b=8.356(5), c=7.934(5) Å, β=91.68(5)º; Z=2; V=480.80(5) $Å^3$. A priori, the gadolinium ion ensures high acceptance of rare-earth dopants in its structural site because of its privileged position in the middle of the lanthanides series, i.e. highly Nd-substituted KGP crystals [14] and even the stoichiometric isostructure of neodymium, $KNd(PO_3)_4$ (KNP) [15,16] have been synthesized. Because of the wide transparency window of KGP, which extends from 180 nm to 4 μm [14], transparency is guaranteed at both the fundamental and the second harmonic range. This really low UV cut-off allows in principle to

use this host also in the UV range (either as a nonlinear crystal or as a host for cerium). The quite large band-gap should increase the damage resistivity of the crystal, so high power diode-pumping should be allowed. KGP presents also some promising properties to be a new candidate to nonlinear solid-state laser host such as an almost isotropic thermal expansion, which protects it from thermal deforming during laser operation [17] and a high chemical stability, which ensures that the useful life of the laser device would not be limited by its chemical degradation [18]. The highly microhardness of KGP [18], around that of quartz in the Moh's scale, facilitates sample preparation and allows polishing the laser surfaces with good optical quality. Yb:KGP has similar absorption and emission cross-sections [19] than those of other nonlinear ytterbium doped crystals in which SFD in the visible has been proved such as Yb:GdCOB [9], Yb:YCOB [10], Yb:YAB [11], Yb:$LiNbO_3$ [12] and Yb:MgO:$LiNbO_3$ [13]. Recently, room temperature laser generation in the 1 μm range has been demonstrated [19] in this new Yb host for the first time. The lasing studies were based on a preliminary single $KYb_{0.024}Gd_{0.976}(PO_3)_4$ sample which was cut and polished as a cube accurately oriented along the N_p, N_m, and N_g principal optical axes with dimensions of 2.34, 2.68, and 2.47 mm along these axes, respectively. Although the size and the doping level of the sample limited the maximum output power achieved, of the order of 100 mW, the more than 55% slope efficiency obtained with this first sample is rather promising for the future. We decided therefore to dedicate many efforts to optimize the synthesis of Yb:KGP crystals with a higher ion doping level.

As KGP inclusion-free single crystals can be successfully grown [17], we studied how evolved the crystallization region and the growth process when introducing ytterbium in solution. The structural effect of ytterbium in the KGP structure was also studied hence the variation of the crystal cell parameters *a*, *b*, *c*, *β*, and *V* as a function of the ytterbium concentration was determined. The thermal behavior of Yb:KGP was also analyzed in terms of phase transition and thermal evolution. A short study of Raman scattering was made to determine the phonon frequencies of the KGP and the Yb:KGP lattice. Because of its potential application as self-frequency doubling laser material, some optical and spectroscopic studies were also performed. We determined the optical transmission of Yb:KGP and compared it to that of the host. The optical absorption and emission of ytterbium in KGP at room temperature were also included.

Experimental section

Crystallization Region of Yb:KGP. To determine the region where ytterbium doped KGP crystallizes as the $P2_1$ single phase (type III) from its self-flux, we grew small single crystals of several ytterbium concentrations from three different solution compositions. All these composition points were placed inside the previously determined KGP crystallization region [17] and were: (Yb_2O_3+Gd_2O_3):K_2O:P_2O_5 = 6:34:60, 4:36:60, and 2:38:60 mol %. The phosphorus oxide percentage was kept constant at 60 mol % because higher concentrations imply too much higher solution viscosities [14,16,17], therefore only the Ln_2O_3/K_2O ratio was varied among 15/85, 10/90, and 5/95. In each of these three solution compositions, ytterbium concentrations of 0.5, 1, 3, 5, 10, 15, 20, 30 and 50 atomic % were used. The desired ratios of the corresponding oxides were mixed to prepare roughly 20 g of solution in a platinum crucible. We used Yb_2O_3, Gd_2O_3, K_2CO_3, and $NH_4H_2PO_4$ as initial reagents. The crucible was kept in a vertical furnace with a Kantal AF heater whose temperature was measured by an S-type thermocouple and controlled by a Eurotherm 818 P controller/programmer connected to a thyristor. The axial gradient in solution was about 5 K/mm, increasing the temperature from the surface to the bottom. We determined the saturation temperature by observing the growth or dissolution of crystals spontaneously nucleated on the solution surface. From the saturation temperature, the

solution was cooled at a rate of 0.1 to about 12 K below. Crystals grown on a platinum disk rotating at 60 rpm placed at the center of the solution surface. To identify the crystalline phase of the small crystals grown, we used X-ray powder diffraction analysis.

X-ray Powder Diffraction. The X-ray powder diffraction technique was used to perform some structural characterizations of the Yb:KGP crystals as well as their simply identification. The experiments were carried out using the Cu Kα radiation in a D5000 Siemens X-ray powder diffractometer in a θ–θ configuration with the Bragg-Brentano geometry and a scintillation counter as detector.

Small crystals grown on a platinum disk from fluxes containing an ytterbium atomic % of 1, 3, 5, 10, 15, 20, 30, and 50 were analyzed to calculate the crystal cell parameters of ytterbium-doped KGP crystals. The composition of the growth solution was changed depending on the ytterbium concentration in order to ensure the crystallization of the $P2_1$ phase. The X-ray diffraction patterns were recorded in the 2θ range from 10 to 70º at a step size of 0.02º and a step time of 16s. The crystal cell parameters were refined using the FULLPROF [20] program and the Rietveld [21] method using the KGP structure, solved previously by single-crystal X-ray diffraction [14], as starting model.

We also used X-ray powder diffraction analysis to check if the evolution of the crystal cell parameters of Yb:KGP and undoped KGP when increasing the temperature was comparable. We analyzed therefore a powdered sample of $KYb_{0.029}Gd_{0.971}(PO_3)_4$ small crystals grown from a solution composition of Yb_2O_3:Gd_2O_3:K_2O:P_2O_5 = 0.3:5.7:34:60 mol %. The diffractometer above described was equipped with an Anton-Paar HTK10 platinum ribbon heating stage. The diffraction patterns were recorded in the same 2θ range at a step size of 0.03º and a step time of 5s at temperatures of 298 and 773 K, with a delay time of 300 s before each pattern recording.

The thermal evolution of Yb:KGP from room temperature to 1273 K, both heating and cooling the sample, was also analyzed. The same powdered sample of $KYb_{0.029}Gd_{0.971}(PO_3)_4$ was used. The diffractometer was equipped therefore also with a Braun position-sensitive detector (PSD). To compare with undoped KGP, the same thermal program was used. The sample was heated at 10 K/s from 298 to 673 K and from this point to the maximum (1273 K) at 0.17 K/s, then it was cooled using the same conditions. Diffraction patterns were registered every 50 K in the slowest heating and cooling ranges (673-1273 K) from a 2θ of 10 to 70º using a measuring time per degree of 10 s.

Differential Thermal Analysis. Before analyzing more accurately the thermal evolution of Yb:KGP crystals by powder XRD, differential thermal analysis (DTA) were made. We used a TA Instruments simultaneous differential techniques instrument SDT 2960. The analyses were made under argon atmosphere using a gas flow of 90 cm^3/min and calcined alumina as reference material. Around 20 mg of powdered samples of $KYb_{0.029}Gd_{0.971}(PO_3)_4$ and $KYb_{0.045}Gd_{0.955}(PO_3)_4$ obtained from solution compositions of Yb_2O_3:Gd_2O_3:K_2O:P_2O_5 = x:6-x:34:60 mol %, with x=0.3 and 0.6, respectively, were placed in a platinum pan and heated at 0.17 K/s from room temperature to 1273 K. The cooling process was not analyzed because of the irreversible transition of type III KLnP materials, with Ln = Gd and Nd [17,16]. To compare with the cyclic polymorph $KYb_xGd_{1-x}P_4O_{12}$ [22] (type A; S.G. *C2/c*), about the same weight of a sample obtained from a solution with 1 atomic % of ytterbium and composition Yb_2O_3:Gd_2O_3:K_2O:P_2O_5 = 0.06:5.94:34:60 was analyzed.

Yb:KGP Crystal Growth. The top-seeded solution growth–slow cooling (TSSG–SC) method without pulling was used to grow Yb:KGP single crystals. The equipment was the same as that used for the crystallization region studies. Around 200 g of solution, prepared the same as

previously, had in this case an axial gradient around 1.2 K/mm. To begin the growth experiments, we used the same growth parameters as those previously optimized for KGP [17] and Nd-doped KGP [14] (see Table 1 for values and corresponding results). Crystals were grown therefore from the optimized solution composition of Yb_2O_3:Gd_2O_3:K_2O:P_2O_5 = x:6-x:34:60 mol % (experiments from 3 to 9) as long as the *$P2_1$*-phase crystallized. To grow crystals with an ytterbium concentration in solution either below 3 or above 10 atomic %, a solution composition of Yb_2O_3:Gd_2O_3:K_2O:P_2O_5 = x:4-x:36:60 mol % (experiments 1 and 10) had to be used to obtain the *$P2_1$* crystalline phase. Crystals were grown on **a***-oriented paralepipedic seeds of Yb:KGP. This orientation ensures a suitable growth rate and avoids the possibility to lose the crystal because of the cleavage plane [18]. The rotation velocity was kept at 75 rpm since the solution viscosity was comparable. Depending on the ytterbium concentration, we used a cooling rate of 0.1, 0.05 or 0.02 K/h. The higher the ytterbium concentration, the greater the number of inclusions appeared in crystals, as in the case of Nd-doped KGP. Furthermore, polycrystallization occurred more frequently as the ytterbium concentration rose. The crystallization of various growth nuclei, probably due to the high viscosity of the solution, was also observed for the previously isostructurals but in this case it was much more usual. To avoid polycrystallization and succeed to grow inclusion-free single crystals, the cooling rate was decreased to 0.05 K/h from an ytterbium content in solution of 3 atomic %. From an ytterbium concentration in solution of 10 atomic % even a slower a cooling program, combining cooling rates of 0.02 and 0.05 K/h, was used (experiments 9, 10, and 11). As previously, seeds were hold on the same growth device equipped with a turbine, which is shown in reference 18.

Ytterbium concentration analysis. Electron probe microanalysis (EPMA) was used to determine the chemical composition of both crystals grown on a platinum disk and crystals grown by TSSG. The measurements were made using a CAMECA SX-50 operating at an accelerating voltage of 20 kV and an electron current of 100 nA. We used KYbW and KGP crystals grown by us as the standards for measuring Yb and K, Gd, P, and O, respectively. K and P were analyzed with the PET (Pentaery thritol, 002) crystal using the line Kα. O Ka was measured with a W/Si multilayer crystal and the Lα line of Yb and Gd were analyzed using the LIF (Lithium Fluoride, 200) crystal. The measurements were integrated for 10s for all ions. From these results and the solution composition used in every case, the distribution coefficient of ytterbium in the structural sites of gadolinium were calculated using the expression $K_{Yb}=([Yb]/[Yb]+[Gd])_{crystal}/([Yb]/[Yb]+[Gd])_{solution}$.

Raman Spectroscopy of Yb:KGP. The lattice vibrations of Yb:KGP and KGP were studied using the Raman technique. As the intermanifold electronic transitions of ytterbium are strongly coupled with lattice vibrations, the knowledge of the phonon frequencies can be useful to interpret the substructure in absorption and emission spectra.
We cut and polish plate samples of about 1mm thick of KGP and $KYb_{0.029}Gd_{0.971}(PO_3)_4$ to do the measurements. The experimental setup comprised a Jobin-Yvon T64000 spectrophotometer with excitation by a CW argon laser (Coherent INNOVA 300, λ=514 nm). Behind the triple monochromator (1800 g/mm) the light was detected by a two-dimensional CCD matrix cooled with liquid nitrogen. A pre-monochromator eliminated the plasma discharge lines of the argon laser. A microscope (Olympus BH2) with high resolution was used to locate the laser spot in the sample. The laser power incident on the sample was about 60 mW. A backward scattering scheme was chose in order to increase the signal to noise ratio.

Optical Transmission of Yb:KGP. The optical transmission Yb:KGP was measured in the wavelength range from 0.175 to 10 μm. We used a Varian Cary 500 Scan spectrophotometer to

do the measurements in the UV-Visible and NIR regions up to 3.3 μm and an FTIR Midac Prospect spectrophotometer in the IR region. 1mm-thick plate sample of $KYb_{0.029}Gd_{0.971}(PO_3)_4$ was cut and polished to do the measurements. The UV and IR cut-off values were calculated as the maximum transmission value divided by the *e* number. The ultraviolet region close to the UV cut-off is interesting from the point of view of the UV emitting sources pumping, such as Xe lamps. These highly energetic pumps cause often optical damage in the illuminated crystals. The susceptibility to optical damage, which is enhanced by the presence of dopants in the crystals, can shift the UV edge to longer wavelengths. As this shifting was clearer when measuring the absorption coefficient (α) rater that the transmission, we measured the optical absorption of $KYb_{0.029}Gd_{0.971}(PO_3)_4$, $KYb_{0.045}Gd_{0.955}(PO_3)_4$, and KGP between 175 and 500 nm.

Ytterbium Optical Absorption and Emission. We studied the optical absorption and emission of the ytterbium ion in the KGP host. A $KYb_{0.024}Gd_{0.976}(PO_3)_4$ crystal was cut and polished as an isometric 2 mm-sided cube accurately oriented along the three principal optical axes N_p, N_m, and N_g. The optical absorption was measured in the 1μm wavelength region using the same spectrophotometer as in the transmission measurements. The splitting of the Yb absorption band was also studied at 6 K equipping the spectrophotometer with a Leybold RDK-6-320 closed-cycle helium cryostat. The measurements were made by polarizing the incident beam parallel to each principal optical axis. The fluorescence spectra were recorded at both 300 K and 10 K in 90º geometry with excitation by a 200 mW diode laser at 940 nm modulated at 1 kHz. The fluorescence was dispersed by a 0.46 m double monochromator (Jobin Yvon-Spex HR 460). We used a cooled Hamamatsu NIR R5509-72 photomultiplier for detection connected to a lock-in amplifier (EG&G, 7265 DSP).). A close-cycle helium cryostat (Oxford CCC1104) was used to cool the sample for low temperature measurements.

Results and Discussion

Crystallization region of Yb:KGP. We determined how the type III Yb:KGP crystallization region evolved as a function of the ytterbium concentration close to the optimum composition zone previously determined. In this zone, the most optimum point to grow KGP single crystals was found to be Gd_2O_3:K_2O:P_2O_5 = 6:34:60 mol %. We have therefore kept the P_2O_5 concentration at 60 mol %. A higher P_2O_5 concentration leads to higher solution viscosity and consequently to lower growth rate and crystal quality. The crystallization region was also limited at a Gd_2O_3/K_2O molar ratio of 3/97 because of the same reason. Above this ratio the viscosity was too high for growing crystals mostly because of the temperature since as the Gd_2O_3/K_2O ratio decreased the saturation temperature also decreased. The boundaries of the crystallization region of Yb:KGP were defined by the intersection of the $(Yb_2O_3+Gd_2O_3)/K_2O$ isoconcentrational lines of 15/85, 10/90, and 5/95 with the P_2O_5 concentration of 60 mol % after studying several solution compositions. These isoconcentrationals lines were, as for the other isostructural crystals, roughly parallel to the saturation temperature isotherms of 950, 880, and 825 K, respectively. Table 2 shows the crystalline phase identified for each ytterbium atomic % and each tested solution molar ratio $(Yb_2O_3+Gd_2O_3)/K_2O$.

In the compositions zone studied, Yb:KGP can crystallize into two different polymorphs, type III $KYb_xGd_{1-x}(PO_3)_4$ (S. G. $P2_1$) with long-chain geometry, and type A $KYb_xGd_{1-x}P_4O_{12}$ (S. G. *C2/c*) with cyclical geometry. Because of the centrosymmetrical structure of type A, second order nonlinear optical processes are not allowed so it can not be used as a self-frequency doubling crystal. The high structural versatility of condensed polyphosphates has been extensively studied [23,24]. KGP crystallizes into these two polymorphs and even into a third one,

type IV [25] (S. G. $P2_1/n$) also with long-chain geometry, which coincides with the structure of the ytterbium stoichiometric material, $KYb(PO_3)_4$ (KYbP) [26]. Depending on the ytterbium concentration, the border between type III and type A varies. Whereas the ytterbium concentration in solution was between 3 and 10 mol %, the $P2_1$ crystallization region border was placed above a $(Yb_2O_3+Gd_2O_3)/K_2O$ molar ratio of 15/85. This limit is similar to that of KGP, which is placed at a Gd_2O_3/K_2O molar ratio of 18/82 at 60 mol % of P_2O_5. However, as the ytterbium concentration is either reduced or increased from this ytterbium concentration range, the border was shifted to a lower $(Yb_2O_3+Gd_2O_3)/K_2O$ molar ratio and the $P2_1$ crystallization region was slightly narrowed (table 2).
Figure 1 shows a SEM photograph and a morphological scheme drawn using the Software Shape utility [27] of both $P2_1$ and $C2/c$ phases. Any important morphologic change was observed when the ytterbium content in solution was increased but the light tendency to twinning (figure 1c) was observed.

Yb:KGP Crystal Growth. We analyzed the Yb:KGP crystal growth process in order to manage to grow suitable sized inclusion-free single crystals. Among the different growth parameters that can affect the crystal quality, we analyzed the influence of the cooling rate. The composition of the growth solution was fixed by the stability of the $P2_1$-phase, taking into account the crystallization region previously determined. For any ytterbium concentration, the solution composition used was the most close to the optimum $(Yb_2O_3+Gd_2O_3):K_2O:P_2O_5$ = 6:34:60 mol %. The high viscosity of this kind of solutions, around 2 Dp for KGP [18], is due to the high polymerization degree of the phosphate compounds in the flux, mostly $Ln(PO_3)_3$, with Ln= Yb, Gd. The greater the viscosity, the slower the crystal growth process. The growth rate is therefore lower for a solution composition of $(Yb_2O_3+Gd_2O_3):K_2O:P_2O_5$ = 4:36:60 mol % (experiments 1 and 10) and even lower for that of $(Yb_2O_3+Gd_2O_3):K_2O:P_2O_5$ = 2:38:60 mol % (experiment 2). For a fixed solution composition, the saturation temperature slightly increases when the ytterbium content also increases. Polycrystallization also get out when the Yb_2O_3 content in solution increases, probably due to an increase of the solution viscosity. This higher tendency to polycrystallization may be related to the increase to twinning already observed on small crystals (figure 1c) and never observed with KGP. Therefore, it was necessary to reduce the cooling rate in the first steps of the cooling program, when polynucleation can occur, for Yb_2O_3 concentrations from 10 atomic % in solution (experiments 9 and 10).

Ytterbium doping in KGP. The chemical composition of crystals grown from solutions containing an ytterbium atomic % of 1, 3, 5, 10, 15, 20, 30 and 50 was determined by EPMA. Table 3 shows the ytterbium distribution coefficients in the structure, defined as K_{Yb} = $([Yb]/[Yb]+[Gd])_{crystal}/([Yb]/[Yb]+[Gd])_{solution}$ and the ytterbium atomic % in solution and in crystal As the ionic radius of ytterbium is only around 6.5 % smaller than that of gadolinium, an ytterbium distribution coefficient close to the unit was expected. However, not only it was lower for all the ytterbium concentrations but also it decreased as the ytterbium content increased until it stabilized around half the unit. The crystal cell parameters *a*, *b*, *c*, and *V* slightly decreased as the concentration of ytterbium increased in crystals because it progressively substituted gadolinium in its structural position. All cell parameters evolved linearly with the concentration. Figure 2 shows the average change in each cell parameter ($\Delta Y/Y$) versus the concentration. In table 3 are listed the cell parameters values the for each ytterbium concentration.

Thermal Stability and Phase Transitions. We analyzed how Yb:KGP evolved with temperature between 298 and 1273 K. By differential thermal analysis (DTA), we determined

that both $KGd_{0.029}Gd_{0.971}(PO_3)_4$ and $KGd_{0.045}Gd_{0.955}(PO_3)_4$ decomposed at 1130 K (Figure 3). The transition temperature was lower than that of KGP, which shows an endothermic peak at 1142 K. The polymorph $KGdP_4O_{12}$ *C2/c* (type A) decomposed at a slightly higher temperature (1138 K). These results agreed with those of the isostructurals $KSm(PO_3)_4$ and $KSmP_4O_{12}$ [28], which decompose at 1133 and 1145 K, respectively. The weight change during the experiments was rather imperceptible.

The decomposition of $KGd_{0.029}Gd_{0.971}(PO_3)_4$ was more accurately studied by X-ray powder diffraction. Figure 4 shows the X-ray pattern at room temperature and the selected patterns at several temperatures which describe the thermal evolution in both the heating and the cooling processes. The crystal phases evolved in the phase transition were identified as $GdPO_4$ (83-0657 ICDD database [29]), orthorhombic $Gd(PO_3)_3$ (isostructural to $Eu(PO_3)_3$ 31-0519 ICDD database [30]), $Gd_2P_4O_{13}$ (35-0078 ICDD database [31]), and GdP_5O_{14} (73-1068 ICDD database [32]). All these crystal phases were also present during the decomposition of KGP [17] except GdP_5O_{14}, which was though identified as the neighboring phase in the richest P_2O_5 zone of the KGP crystallization region. This phase (GdP_5O_{14}) appeared at 1223 K in the heating process and disappeared at 1173 K in the cooling process. $Gd(PO_3)_3$ appeared as the only phase at 1173 K but the intensity of its peaks quickly reduced between this temperature and 1273 K, when it completely disappeared. As the intensity of the peaks of $Gd(PO_3)_3$ decreased, that corresponding to the rest of the phases steadily increased in the same temperature range. $GdPO_4$ and $Gd_2P_4O_{13}$ remained and even slightly increased its intensity from this temperature until room temperature. Because of the dilation of the material, a slight displacement of the peaks was observed in the last pattern at room temperature. The most important difference in the thermal evolution caused by the presence of the ytterbium ion was that $Gd_2P_4O_{13}$ remained until room temperature but it completely transformed into $GdPO_4$ for undoped KGP. The final product of the Yb:KGP thermal decomposition was therefore a mixing of both phases.

From powder XRD analysis and DTA, we determined that Yb:KGP decomposed at 1130 K into $Gd(PO_3)_3$. However, between this temperature and 1273 K it completely transformed into $GdPO_4$, $Gd_2P_4O_{13}$, and GdP_5O_{14}. This last phase completely disappeared at 1173 Kin the cooling process. An amorphous phase composed by potassium and phosphorous oxides was also present because the sample weight remained roughly constant. The endothermic peak observed in the thermogram at 1130 K may be related to this decomposition.

Yb:KGP slightly dilated as the temperature increased. This thermal expansion was comparable to that of KGP [17] and also was almost isotropic.

Raman Spectroscopy. Raman spectroscopic properties of phosphate crystals and glasses have been extensively studied. Mostly, the Raman spectra have been related to the vibrational motions of simple structural units but in the random network approach is necessary to consider the local geometry of the phosphate units. Metaphosphates with a [O]/[P] ratio of 3 have a geometry of chains or cycles [33]. However, the Raman spectra are qualitatively the same. The spectra are neither affected by the number of repetitive units $(PO_3)_x$ that generate the chains or cycles and even either by the lanthanide or alkali ions in the structure. The spectra have therefore the same characteristic peaks for metaphosphates of lanthanide, $Ln^{III}(PO_3)_3$, with Ln= Gd [34] Sm [35], La [36], or poyphosphates, $M^{I}Ln^{III}(PO_3)_4$ such as $KBi(PO_3)_4$ [37], $M^{I}La(PO_3)_4$ with M^{I}=Na, Ag [38], which have a chain geometry and $P2_1/n$ as space group, and $KSm(PO_3)_4$ [39,40], which is isostructural to KGP. All these Raman spectra have two characteristic strong peaks around 1185 and 700 cm^{-1}. The strong peak around 1185 cm^{-1}, which is accompanied with some other weaker peaks in the region from 1000 to 1300 cm^{-1}, is a common feature to materials built up from linked PO_4 tetrahedra. This peak is generally attributed to the symmetric stretching vibration ν_s of the PO_2 group corresponding to the motion of the nonbridging oxygen. The

weaker peaks around it are assigned to symmetric ν_s and antisymmetric ν_a vibrations of the same group. The strong peak around 700 cm^{-1} is attributed to the symmetric stretching vibration ν_s of the P-O-P chain linkage. Very weak peaks attributed to symmetric ν_s and antisymmetric ν_a vibrations of the same group are often observed in the region from 650 to 1000 cm^{-1}. Peaks around this region are a useful indicator of the structure of metaphosphate. Figure 5 shows the Raman spectra of Yb:KGP and KGP. All metaphosphate characteristic peaks above described are present. In the region of 700 cm^{-1} two strong peaks at 728 and 671 cm^{-1} are observed because of the different positions of the lanthanide and alkali ions give different frequencies of the P-O-P ν_s [40]. In the low frequency region below 650 cm^{-1} it is very difficult to distinguish the symmetric and antisymmetric bending modes of PO_2 and P-O-P groups.

Optical Transmission. Figure 6 shows the transparency window of $KYb_{0.029}Gd_{0.971}(PO_3)_4$. The IR cutoff wavelength is around 5.5 μm because of the absorption resonance of the P-O linkage as in the case of KGP. From this wavelength, the transparency window extends to approximately 200 nm. The cut-off wavelength in this region shifted to longer wavelengths with the presence of ytterbium. The absorption coefficient (α) decreased more gently at shorter wavelengths as the ytterbium concentration increased, e.g. at 208 and 205 nm for $KYb_{0.029}Gd_{0.971}(PO_3)_4$ and $KYb_{0.045}Gd_{0.955}(PO_3)_4$, respectively (inset in figure 6). The strong absorption band close to 1 μm is attributed to the ytterbium transition $^2F_{7/2} \rightarrow {}^2F_{5/2}$.

Ytterbium Optical Absorption and Emission. The polarized optical absorption and emission spectra of Yb^{3+} in KGP at room temperature and 6 K are shown in Figure 7. The ytterbium concentration of the $KYb_{0.024}Gd_{0.976}(PO_3)_4$ cube used for measurements was 1.007 x 10^{20} cm^{-1}.
The absorption band associated with the ytterbium transition $^2F_{7/2} \rightarrow {}^2F_{5/2}$ in KGP extends from 1025-925 nm at room temperature and is characterized by three main peaks centered at 945, 970, and 978 nm. As ytterbium has an odd number of electrons in the 4*f* shell, polarization dependent selection rules are not expected but intensity variation of the peaks is still possible**.** The dichroism for Yb:KGP is quite low but the absorption intensity is higher for $E//N_m$.
The peaks in the fluorescence spectra correspond to the emission from the excited state $^2F_{5/2}$ manifold to the four sublevels of the ground state manifold $^2F_{7/2}$. From the low-temperature polarized fluorescence spectra we determined the four sublevels of the ground state $^2F_{7/2}$. Four main lines were found at 976, 988, 1005, and 1014 nm accompanied with phonon added peaks. These correspond to the transitions $^2F_{5/2}(0') \rightarrow {}^2F_{7/2}(0)$, $^2F_{5/2}(0') \rightarrow {}^2F_{7/2}(1)$, $^2F_{5/2}(0') \rightarrow {}^2F_{7/2}(2)$, and $^2F_{5/2}(0') \rightarrow {}^2F_{7/2}(3)$, respectively.

Conclusions. We successfully grew ytterbium-doped KGP single crystals by TSSG-SC in spite of the high solution viscosity, around 2 Dp, and the usual polycrystallization. Crystals can be grown using the same solution composition previously optimized for undoped or Nd-doped KGP as long as the ytterbium concentration is between 3 and 10 atomic % in solution. Either the concentration is lower or higher and up to 50 atomic %; the $P2_1$ crystallization region is slightly narrowed and moved toward a lower $(Yb_2O_3+Gd_2O_3)//K_2O$ molar ratio since it is the neighboring phase *C2/c* which crystallizes. Polymorphism of Yb:KGP between the long-chain and the cyclical structures is not strange since it is a well know feature of this type of condensed polyphosphates. The rotation velocity and seed orientation are the same as those used to grow Nd-doped KGP. However, the cooling rate have to be decreased down to 0.02 K/h in the first steps of the growth process to obtain Yb:KGP crystals free of macroscopic defects because of polycrystallization. Up to now, we have successfully grown inclusion-free single crystals with a maximum ytterbium concentration in solution of 15 atomic %, hence around 7.5 atomic % in

crystal since the actual ytterbium concentration in the crystal was found to be reduced to about half of that in solution. Nevertheless, we found that the $P2_1$-phase of Yb:KGP can crystallize from solutions with an ytterbium concentration up to 50 atomic %. So, taking into account that the ytterbium concentration in crystal would be reduced by about half, an ytterbium doping level around 25-30 atomic % may be reach in single crystals grown by TSSG-SC. The self frequency doubling properties will not be therefore limited by the active ion concentration unlike other well known nonlinear crystals. Too much high ytterbium doping levels can reduce the laser efficiency due to reabsorption, so further spectroscopic and laser investigations are necessary to determine the optimum ytterbium doping level. The slightly decrease of the cell parameters with the introduction of ytterbium in the KGP structure has been determined for any ytterbium concentration from 1 to 50 atomic % in solution. The actual concentration in crystals has been also determined for each of them. Yb:KGP decomposes irreversibly at 1130 K and after crystalline transformations, that occurred between this temperature and 1173 K during cooling, two final products remained at room temperature, $GdPO_4$ and $Gd_2P_4O_{13}$. The ytterbium ions in KGP cause the slightly shifting of the UV cut-off to longer wavelengths though it continues being quite low. Yb:KGP and KGP shows the typical vibrational structure of metaphosphates. The optical absorption and emission of ytterbium in the KGP host have been measured.

Acknowledgments. The authors acknowledge financial support from Fons Social Europeu i del Departament d'Universitats, Recerca i Societat de la Informació de la Generalitat de Catalunya under Project 2005SGR658 and personal support 2006FIC00469 and from MEC (Ministerio de Educación y Ciencia of the Spanish government) of the Spanish government) under Projects MAT-05-06354-C03-02, MAT-04-20471-E and CIT-020400-2005-14.

Table 1. Growth Data Associated with Ytterbium-doped KGP Single Crystals

A	B	C	D	E	F	G	H	I	J	K
1	0.04:3.96:36:60	1	0.5	0.5	889	12/0.1	**a***	4.5x6.1x5.3	0.77	good
2	0.02:1.98:38:60	1	0.3	0.32	823	12/0.1	**a***	3.4x4.9x4.1	0.49	good
3	0.18:5.82:34:60	3	1.5	0.49	943	12/0.1	**a***	5.1x7.7x6.9	0.91	some inclusions
4	0.18:5.82:34:60	3	1.6	0.53	939	12/0.05	**a***	5.1x7.4x6.8	0.89	good
5	0.3:5.7:34:60	5	2.6	0.51	952	12/0.1	**a***	---	0.87	poly-crystalline
6	0.3:5.7:34:60	5	2.4	0.48	958	12/0.05	**a***	4.7x6.2x6.1	0.85	good
7	0.6:5.4:34:60	10	4.0	0.40	981	12/0.1	**a***	---	0.99	poly-crystalline
8	0.6:5.4:34:60	10	4.2	0.42	975	12/0.05	**a***	5.6x8.3x7.6	1.00	some inclusions
9	0.6:5.4:34:60	10	4.0	0.40	971	2/0.02 10/0.05	**a***	5.8x6.8x6.3	0.88	good
10	0.6:3.4:36:60	15	7.7	0.51	995	2/0.02 10/0.05	**a***	4.2x6.5x5.7	0.76	good

A: growth experiment, B: solution composition Yb_2O_3:Gd_2O_3:K_2O:P_2O_5 (mol %), C: Ytterbium atomic % in solution, D: Ytterbium atomic % in crystal, E: distribution coefficient of ytterbium in KGP, F: saturation temperature (K), G: cooling program: decreased temperature interval/ rate of temperature decreasing, H: seed orientation, I: crystal dimensions (a x b x c) (mm^3), J: crystal weight, K: crystal quality.

Table 2. Crystalline Phase for each Ytterbium Concentration and Solution Composition [*]

Yb at.% in solution	molar ratio $(Yb_2O_3+Gd_2O_3)/K_2O$	Phase	molar ratio $(Yb_2O_3+Gd_2O_3)/K_2O$	Phase	molar ratio $(Yb_2O_3+Gd_2O_3)/K_2O$	Phase
0.5	(0.075+14.925)/85	$P2_1$ +$C2/c$	(0.05+9.95)/90	$P2_1$	(0.025+4.975)/95	$P2_1$
1	(0.15+14.85)/85	$P2_1$ +$C2/c$	(0.1+9.9)/90	$P2_1$	(0.05+4.95)/95	$P2_1$
3	(0.45+14.55)/85	$P2_1$	(0.3+9.7)/90	$P2_1$	(0.15+4.85)/95	$P2_1$
5	(0.75+14.25)/85	$P2_1$	(0.5+9.5)/90	$P2_1$	(0.25+4.75)/95	$P2_1$
10	(1.5+13.5)/85	$P2_1$	(1.0+9.0)/90	$P2_1$	(0.5+4.50)/95	$P2_1$
15	(2.25+12.75)/85	$P2_1$ +$C2/c$	(1.5+8.5)/90	$P2_1$	(0.75+4.25)/95	$P2_1$
20	(3.0+12)/85	$P2_1$ +$C2/c$	(2.0+8.0)/90	$P2_1$	(1.0+4.0)/95	$P2_1$
30	(4.5+10.5)/85	$P2_1$ +$C2/c$	(3.0+7.0)/90	$P2_1$	(1.5+3.5)/95	$P2_1$
50	(7.5+7.5)/85	$P2_1$ +$C2/c$	(5+5)/90	$P2_1$	(2.5+2.5)/95	$P2_1$

[*] The solution composition is expressed as a function of the $(Yb_2O_3+Gd_2O_3)/K_2O$ molar ratio with a constant P_2O_5 molar concentration of 60 mol %.

Table 3. Ytterbium and Gadolinium Distribution Coefficients and Cell parameters for each Ytterbium Concentration (at. %)

Solution composition (mol%) Yb_2O_3:Gd_2O_3: K_2O:P_2O_5	Yb at. % in solution	Yb at. % in crystal	K_{Yb}	K_{Gd}	a (Å)	b (Å)	c (Å)	β (º)	V (Å^3)
0.04:3.96:36:60	1	0.8	0.80	1.09	7.252(1)	8.352(1)	7.932(1)	91.67(1)	480.2(1)
0.18:5.82:34:60	3	1.8	0.61	1.01	7.250(1)	8.350(1)	7.930(1)	92.68(1)	479.9(1)
0.3:5.7:34:60	5	2.9	0.57	1.03	7.249(1)	8.347(1)	7.928(1)	91.69(1)	479.5(1)
0.6:5.4:34:60	10	4.5	0.45	1.07	7.247(1)	8.343(1)	7.921(1)	91.71(1)	478.7(1)
0.6:3.4:36:60	15	6.6	0.44	1.02	7.245(1)	8.339(1)	7.916(1)	92.74(1)	478.0(1)
0.8:3.2:36:60	20	11.6	0.58	1.10	7.242(1)	8.334(1)	7.904(1)	92.78(1)	476.8(1)
1.2:2.8:36:60	30	19.9	0.66	1.14	7.237(1)	8.324(1)	7.892(1)	92.82(1)	475.2(1)
2:2:36:60	50	29.8	0.60	1.40	7.231(1)	8.310(1)	7.873(1)	92.90(1)	473.1(1)

Figures

Figure 1. SEM photograph and morphological scheme of a small single crystal of (a) type III Yb:KGP (S.G. $P2_1$) with long-chain geometry and (b) type A Yb:$KGdP_4O_{12}$ (S.G. C2/c) with cycling geometry. (c) twining on a Yb:KGP crystal

Figure 2. Relative evolution of the cell parameters and unit cell volume of $Yb_xGd_{1-x}(PO_3)_4$ as a function of the ytterbium content in KGP.

Figure 3. Differential thermal analysis thermogram of type III $KYb_{0.029}Gd_{0.971}(PO_3)_4$ crystal, type III $KYb_{0.045}Gd_{0.955}(PO_3)_4$ crystal, type A $KYb_{0.006}Gd_{0.994}P_4O_{12}$ crystal.

Figure 4. X-ray powder diffraction pattern at room temperature of $KYb_{0.029}Gd_{0.971}(PO_3)_4$ and selected patterns at several temperatures describing its evolution with temperature in both heating and cooling processes.

Figure 5. Raman spectra of $KYb_{0.029}Gd_{0.971}(PO_3)_4$ and $KGd(PO_3)_4$ at room temperature.

Figure 6. (a) Transparency window of $KYb_{0.029}Gd_{0.971}(PO_3)_4$ at room temperature. Inset: evolution of the UV cutoff wavelength with the concentration of ytterbium.

Figure 7. (a) Polarized optical absorption spectra of $KYb_{0.024}Gd_{0.976}(PO_3)_4$ at room temperature and 6K. (b) Polarized emission spectra of $KYb_{0.024}Gd_{0.976}(PO_3)_4$ at room temperature and 10K.

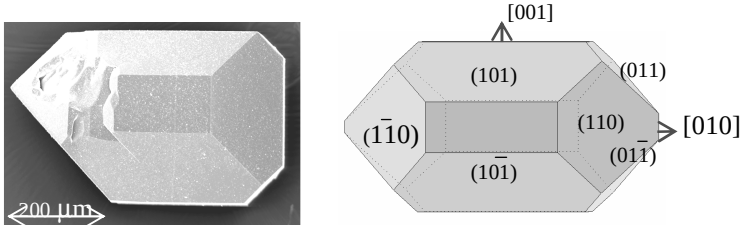
200 µm
[001]
(101)
(011)
(1$\bar{1}$0)
(110)
[010]
(01$\bar{1}$)
(10$\bar{1}$)

(a)

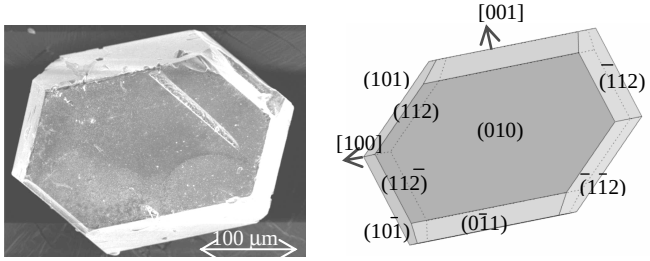
100 µm
[001]
(101)
($\bar{1}$12)
(112)
(010)
[100]
(11$\bar{2}$)
($\bar{1}\bar{1}$2)
(10$\bar{1}$)
(0$\bar{1}$1)

(b)

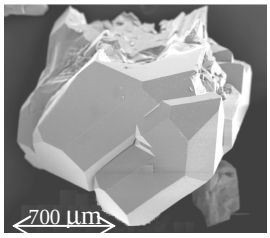
700 µm

(c)

Figure 1.

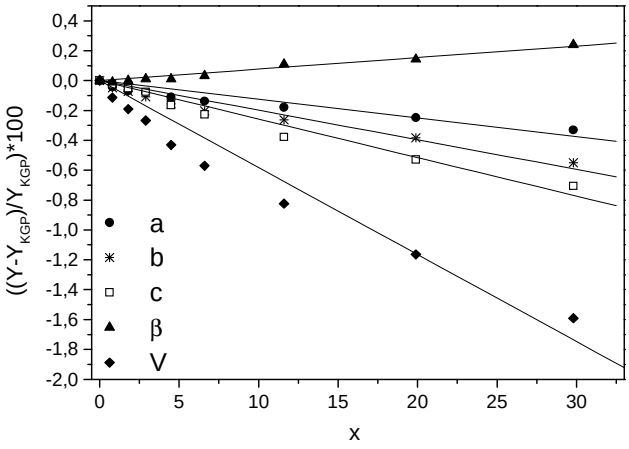
0,4
0,2
0,0
-0,2
-0,4
-0,6
-0,8
-1,0
-1,2
-1,4
-1,6
-1,8
-2,0
0
5
10
15
20
25
30
x
((Y-Y_KGP)/Y_KGP)*100
a
b
c
β
V

Figure 2.

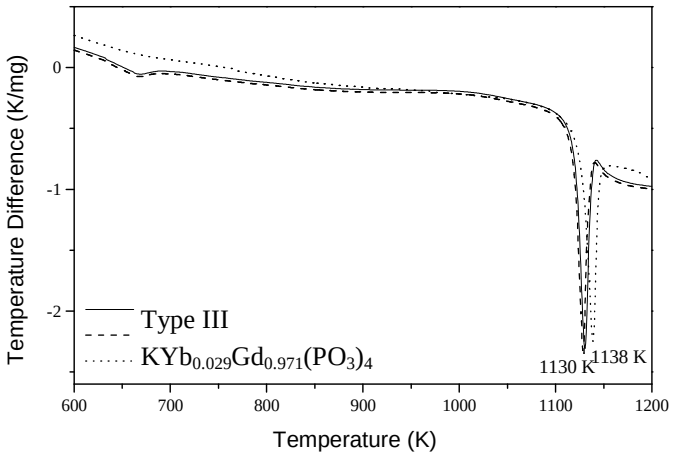
Temperature Difference (K/mg)
0
-1
-2
Type III
KYb0.029Gd0.971(PO3)4
1130 K
1138 K
600
700
800
900
1000
1100
1200
Temperature (K)

Figure 3.

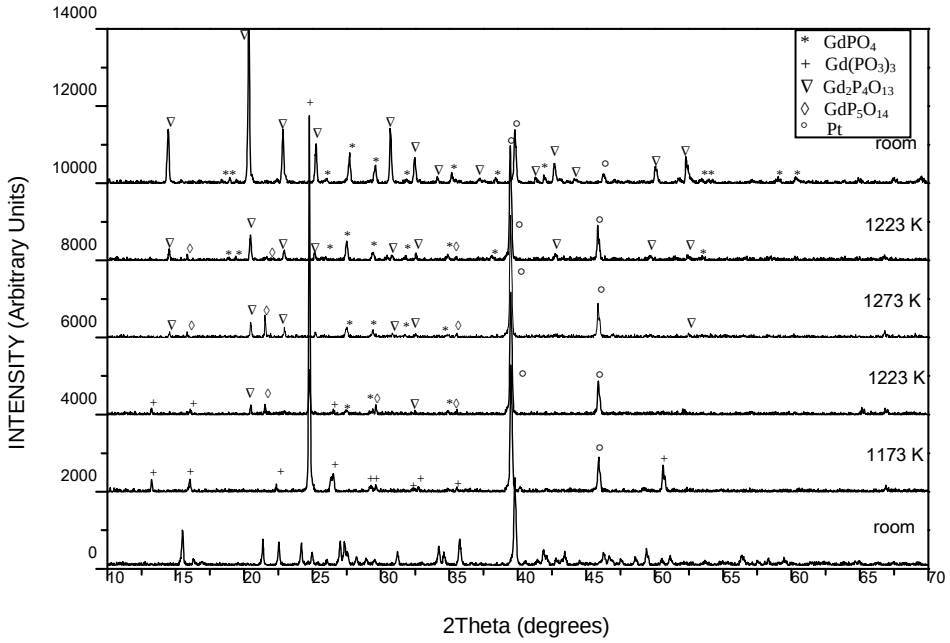
INTENSITY (Arbitrary Units)
2Theta (degrees)
* GdPO4
+ Gd(PO3)3
∇ Gd2P4O13
◊ GdP5O14
° Pt
room
1223 K
1273 K
1223 K
1173 K
room

Figure 4.

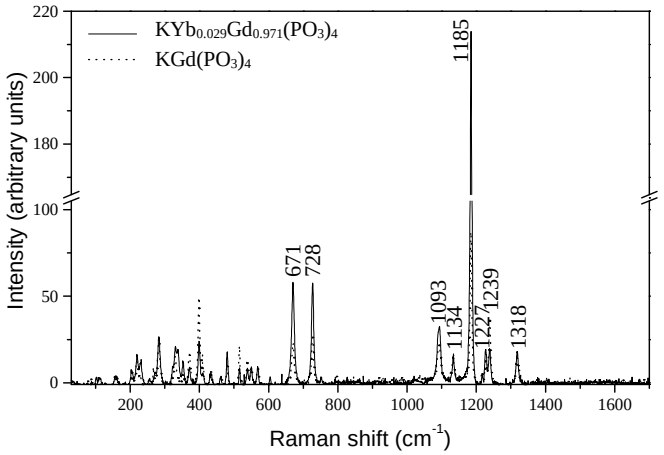
KYb0.029Gd0.971(PO3)4
KGd(PO3)4
Intensity (arbitrary units)
Raman shift (cm-1)
1185
671
728
1093
1134
1227
1239
1318

Figure 5.

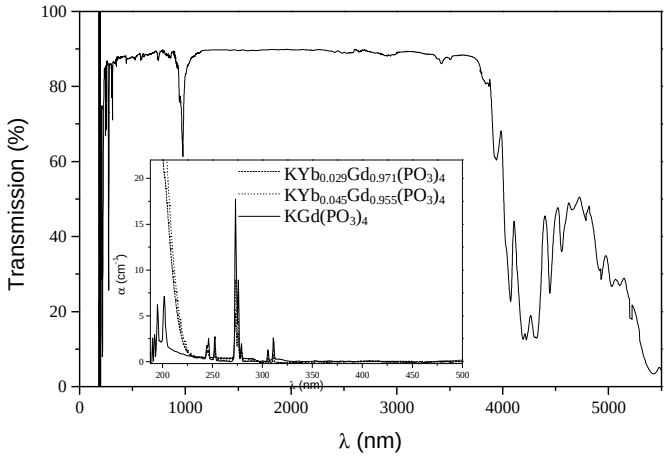
Transmission (%)
λ (nm)
α (cm⁻¹)
λ (nm)
KYb0.029Gd0.971(PO3)4
KYb0.045Gd0.955(PO3)4
KGd(PO3)4

Figure 6.

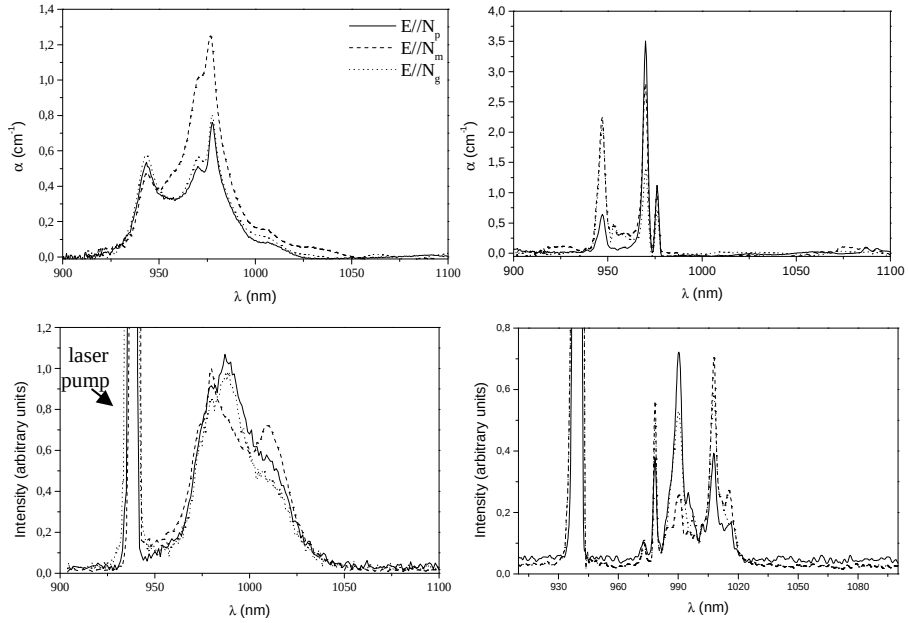

Figure 7.

References

[1] Fan, T. Y.; Cordova-Plaza, A.; Digonnet, M. J. F.; Byer, R. L.; Shaw, H. J. *J. Opt. Soc. Am.* **1986**, *B3(1)*, 140.
[2] Brenier, A. *J. Lumin.* **2000**, *91(3-4)*, 121.
[3] Brenier, A.; Jaque, D.; Majchrowski, A. *Opt. Mat.* **2006**, *28(4)*, 310
[4] DeLoach, L. D.; Payne, S. A.; Chase, L. L.; Smith, L. K.; Kway, W. L.; Krupke, W. F. *IEEE J. Quantum. Electron.* **1993,** *29(4)*, 1179.
[5] Krupke, W. F. *IEEE J. Quantum. Electron*. **2000**, *6(6)*, 1287.
[6] Zou, X. ; Toratani, H. *Phys. Rev. B* **1995**, *52(22)*, 15889.
[7] Mateos, X.; Petrov, V.; Aguiló, M.; Solé, R.; Gavaldà, Jna.; Massons, J.; Díaz, F.; Griebner, U. *IEEE J. Quantum. Electron.* **2004,** *40(8)*, 1056.
[8] Brenier, A. *J. Lumin.* **2000**, *92(3)*, 199.
[9] Mougel, F., Dardenne, K.; Aka, G.; Kahn-Harari, A.; Vivien, D. *J. Opt. Soc. Am. B* **1999**, *16(1)*, 164.
[10] Richardson, M.; Hammons, D.; Eichenholz, J.; Chai, B. H. T.; Ye, Q.; Jang, W. K.; Shah, L. *J. Korean Phys. Soc.* **2000,** *37(5)*, 633.
[11] Dekker, P.; Burns, P. A.; Dawes, j. M.; Piper, J. A. *J. Opt. Soc. Am.* B **2003,** *20(4)*, 706.
[12] Bausá, L.E.; Ramírez, M.O.; Montoya, E. *Phys. Stat. Sol.* **2004,** *201(2)*, 289.
[13] Montoya, E.; Sanz-García, J. A.; Capmany, J.; Bausá, L. E.; Diening, A.; Kellner, T.; Huber, G. *J. Appl. Phys* **2000**, *87(9)*, 4056.
[14] Parreu, I.; Carvajal, J. J.; Solans, X.; Díaz, F.; Aguiló, M. *Chem. Mater*. **2006**, *18(1)*, 221.
[15] Hong, H. Y-P. *Mater. Res. Bull*. **1975,** *10(10)*, 1105.
[16] Parreu, I.; Solé, R.; Gavaldà, Jna.; Massons, J.; Díaz, F.; Aguiló, M. *Chem. Mater*. **2003**, *15(26)*, 5059.
[17] Parreu, I.; Solé, R.; Gavaldà, Jna.; Massons, J.; Díaz, F.; Aguiló, M. *Chem. Mater*. **2005,** *17(4)*, 822.
[18] Parreu, I.; Solé, R.; Massons, J.; Díaz, F.; Aguiló, M. submitted to *Cryst. Growth & Design.*
[19] Parreu, I.; Pujol, M. C.; Aguiló, M.; Díaz, F.; Mateos, X.; Petrov, V. submitted to Opt. Express
[20] Rodríguez-Carvajal, J. *Short Reference Guide for the Computer Program FULLPROF*; Laboratoire León Brillouin, CEA:CNRS: Gif sur Yvette, France, 1998.
[21] Young, R. A. *The Rietveld Method*; International Union of Crystallography Monographs on Crystallography 5; Oxford University Press: Oxford, UK, 1995.
[22] Ettis, H.; Naïli, H.; Mhiri, T. *Cryst. Growth Des.* **2003**, *3*(4), 599.
[23] Palkina, K. K.; Chudinova, N. N.; Litvin, B. N.; Vinogradova, N. V. *Izv. Akad. Nauk, Neorg. Mater*, **1981**, *17* (8), 1501.
[24] Durif, A. *Crystal Chemistry of Condensed Polyphosphates*; Plenum Press: New York, 1995.
[25] Rekik, W.; Naïli, H.; Mhiri, T. *Acta Crystallogr. Sect. C* **2004**, *60(4)*, i-50.
[26] Palkina, K. K.; Maksimova, S. I.; Chudinova, N. N.; Vinogradova, N. V.; Chibisova, N. T. *Izv. Akad. Nauk, Neorg. Mater*, **1981**, *17* (1), 110.
[27] Dowty, E. *Shape for Windows*, version 5.0.1.; **1995**.
[28] Ferid, M.; Ariguib, N. K.; Trabelsi, M. *J. Solid State Chem.* **1987**, *69(1)*, 1.
[29] Mullica, D. F.; Grossie, D. A.; Boatner, L. A. *Inorg. Chem. Acta* **1985**, *109(2)*, 105.
[30] Tsujimoto, Y. *J. Electrochem. Soc*, **1977**, *124*, 533.
[31] Agrawal, D.; Hummel, J. *J. Electrochem. Soc.* **1980**, *127*, 1550.
[32] Bagieu-Beucher, M.; Duc, T. Q. *Bull. Soc. Fr. Mineral Crystallogr*. **1970**, *93*, 505.
[33] Hong, H. Y. G. *Mater. Res. Bull.* **1975**, *10(7)*, 635.
[34] Ileva, D.; Jivov, B.; Kovacheva, D.; Tsacheva, Ts.; Dimitriev, Y.; Bogachev, G.; Petkov, Ch. *J. of Non-Crsyt. Solids* **2001**, *293-295*, 562.
[35] Mierzejewski, A.; Saunders, G. A.; SIDEC, H. A. A. *J. Non-Crsyt. Solids* **1988**, *104(2-3)*, 323.
[36] Hall, D. W.; Brawer, S. A., Weber, M. J. *Phys. Rev.* **1982**, *25(4)*, 2828.
[37] Jaouadi, K.; Naïli, H.; Zouari, N.; Mhiri, T. Daoud, A. *J. Alloys and Comp.* **2003**, *354(1-2)*, 104.
[38] El Masloumi, M.; Imaz, I.; Chaminade, J.-P.; Videau, J.-J.; Couzi, M.; Mesnaoui, M.; Maazaz, M. J. *J. Solid State Chem*., **2005**, *178(11)*, 3581.
[39] Mokhtar, F., Ariguib, N.K. Trabelsi, M. *J. Solid State Chem*., **1987**, *69(1)*, 1.
[40] Saito, M.; Honma, T.; Benino, Y.; Fujiwara, T; Komatsu, T. *Solid State Sciences* **2004**, *6(9)*, 1013.

Paper III

Crystal structure and optical characterization of pure and Nd-substituted type III $KGd(PO_3)_4$

I. Parreu, J. J. Carvajal, X. Solans, F. Díaz, M. Aguiló

Chemistry of Materials **2006**, 18(1), 221

Crystal Structure and Optical Characterization of Pure and Nd-Substituted Type III $KGd(PO_3)_4$

I. Parreu,[†] J. J. Carvajal,[†] X. Solans,[‡] F. Díaz,[†] and M. Aguiló*,[†]

Física i Cristal·lografia de Materials (FiCMA), Universitat Rovira i Virgili, Campus Sescelades, C/Marcel·lí i Domingo, s/n, 43007 Tarragona, Spain, and Departament de Cristal·lografia, Mineralogia i Diposits Minerals, Universitat de Barcelona, C/Martí i Franquès, s/n, 08028 Barcelona, Spain

Received September 20, 2005. Revised Manuscript Received October 28, 2005

The crystal structure of type III $KGd(PO_3)_4$ has been solved, and the related data are presented in this paper. $KGd(PO_3)_4$ (KGP) is monoclinic and has $P2_1$ as space group. Its cell parameters are $a = 7.255(4)$ Å, $b = 8.356(5)$ Å, $c = 7.934(5)$ Å, $\beta = 91.68(5)°$, and $Z = 2$. KGP is characterized by infinite polyphosphate long chains, which run along the [100] direction and are linked through gadolinium polyhedra. We determined the crystallization region of $KGd_{0.47}Nd_{0.53}(PO_3)_4$, and compared it to those of KGP and $KNd(PO_3)_4$ (KNP). The isotherms of the saturation temperature and four neighboring phases were also determined. Small Nd-substituted KGP single crystals free of macroscopic defects were successfully grown under conditions similar to those used to grow KGP and KNP crystals. Nd substitution on the structure was efficient, and its effect was analyzed. We determined the transparency windows of both KGP and KNP crystals, and evaluated the optical tensors at room temperature and 632.5 nm. Finally, we used the Kurtz method to qualitatively measure the second harmonic efficiencies of Nd-substituted KGP crystals. The values obtained for all substitutions were similar to those showed by KGP and KNP and at least to that of H_2PO_4 (KDP).

Introduction

Condensed polyphosphates of lanthanide and alkali ions with the general formula $M^{I}Ln^{III}(PO_3)_4$ crystallize into many structural types. The current nomenclature and classification of this kind of polyphosphates were first proposed by Palkina et al.[1] in 1981. The same author suggested two structural types for the polyphosphate of potassium and gadolinium: type III $KGd(PO_3)_4$ and type A $KGdP_4O_{12}$. Whereas type III was characterized by a PO_4 long-chain geometry, a PO_4 cycling geometry was typical for type A. Type III had a space group $P2_1$, $Z = 2$, $cn(M^{I}) = 8$, and $cn(Ln^{III}) = 8$, and type A had a space group $C2/c$, $Z = 4$, $cn(M^{I}) = 8$, and $cn(Ln^{III}) = 8$. The $M^{I}Ln^{III}(PO_3)_4$ structure seems to be highly dependent on the size of the alkali ion but also on that of the lanthanide when the alkali is kept fixed. From this point of view, two groups could be defined. Because gadolinium is placed in the middle of the lanthanide series, corresponding polyphosphates can crystallize into usual structural types for both the first and second groups. In fact, the type A $KGdP_4O_{12}$ structure, which is usual for the first part of the series, has been recently solved[2] by single-crystal diffraction analysis; structural type IV, which is typical for the second part of the series, has also been solved recently.[3] This structure also has a PO_4 long-chain geometry, space group $P2_1/n$, $Z = 4$, $cn(M^{I}) = 9$, and $cn(Ln^{III}) = 8$. As the type III structure has never been reported before, we solved it by single-crystal diffraction analysis.

Type III has an advantage over the other two polymorphs in that it has a noncentrosymmetrical structure, so nonlinear optical processes, such as second harmonic generation, may be allowed. Type III KGP can be easily doped with other lanthanide ions because gadolinium has a high capacity for substitution. Moreover, it expands almost isotropically with temperature, which prevents it from deforming when working above room temperature. Type III KGP is therefore regarded as a promising self-doubling host that could be used to obtain light all over the UV−vis range to low wavelengths, as the UV cutoff is about 180 nm.

In this paper, we solved for the first time the crystal structure of type III KGP and compared the crystal data with those of the isostructural KNP.[4] We also analyze the effect of substituting gadolinium with neodymium on the synthesis and on some structural and optical properties.

It has been proved that inclusion-free single crystals of both KGP[5] and KNP[6] can be successfully grown. Therefore, we determined the evolution of the crystallization region depending on the neodymium content in the KGP structure. To analyze the structural effect of Nd, we determined the evolution of the crystal cell parameters a, b, c, β, and V as a function of neodymium concentration by studying six compositions that are intermediate to the undoped composi-

* To whom correspondence should be addressed. E-mail: magdalena.aguilo@urv.net.
[†] Universitat Rovira i Virgili.
[‡] Universitat de Barcelona.

(1) Palkina, K. K.; Chudinova, N. N.; Litvin, B. N.; Vinogradova, N. V. *Izv. Akad. Nauk, Neorg. Mater.* **1981**, *17* (8), 1501.
(2) Ettis, H.; Naïli, H.; Mhiri, T. *Cryst. Growth Des.* **2003**, *3* (4), 599.
(3) Rekik, W.; Naïli, H.; Mhiri, T. *Acta Crystallogr., Sect. C* **2004**, *60*, i-50.
(4) Hong, H. Y.-P. *Mater. Res. Bull.* **1975**, *10*, 1105.
(5) Parreu, I.; Solé, R.; Gavaldà, Jna.; Massons, J.; Díaz, F.; Aguiló, M. *Chem. Mater.* **2005**, *17*, 822.
(6) Parreu, I.; Solé, R.; Gavaldà, Jna.; Massons, J.; Díaz, F.; Aguiló, M. *Chem. Mater.* **2003**, *15*, 5059.

10.1021/cm052114l CCC: $33.50
Published on Web 12/09/2005

tions. The transparency windows of KGP and KNP were measured. We also localized the principal optical directions and determined the optical tensors. We analyzed how the second harmonic generation response of powdered Nd-substituted KGP samples behaved as the neodymium concentration changed.

Experimental Section

KGP:Nd Crystal Growth. To determine the evolution of the crystallization region with the Nd^{3+} content in the KGP structure, we grew small crystals of $KGd_{1-x}Nd_x(PO_3)_4$ with solutions of 0.25, 0.50, and 0.75 neodymium at. % on a platinum disk. These crystals were grown from the corresponding self-fluxes containing the desired ratios of neodymium, gadolinium, potassium, and phosphorus oxides. About 25 solution compositions were studied in order to set the limits of the crystallization region for any material. The crystal-growth procedure was similar to that used to determine the crystallization regions of KGP and KNP (see refs 5 and 6 for further details). In this case, the axial temperature increased by about 12 K per millimeter when dipping from the surface to the crucible bottom, which was the coldest point of the volume. The cooling rate was 0.5 K/h, and the temperature dropped to about 15−20 K below the saturation temperature. The crystals grown were identified by X-ray powder diffraction analysis.

The same procedure was used to grow small crystals of KGP by varying the Nd concentration in solution from 0.02 to 75 mol %. Some of these crystals were also analyzed by X-ray powder diffraction analysis to calculate the cell parameters at different Nd atomic contents in the structure.

To obtain inclusion-free Nd-substituted KGP single crystals of suitable size for later characterizations, we used the top-seeded solution growth (TSSG)−slow cooling method. The axial gradient in the solution was 1.5 K/mm. To begin the experiments, we used the growth conditions that had been previously optimized for KGP. The solution composition was therefore Gd_2O_3:Nd_2O_3:K_2O:P_2O_5 = 6−*X*:*X*:34:60 mol %, where *X* is the Nd_2O_3 mol % in the solution; the rotation velocity was 75 rpm, the cooling rate was 0.1 K/h, and the seed orientation was *a** or *c**. A seed holder, equipped with a turbine at the bottom, was used to increase the mass transport in the solution and minimize the macroscopic defects in grown crystals. Though it was used to grow KGP:Nd, in some cases the crystals had some inclusions, especially when the neodymium content increased. To eliminate these inclusions, we discussed how the crystal growth parameters may affect the quality of the doped crystals. We previously found that the seed orientation basically affected the growth rate but not the crystal quality, so we used the same *a**- or *c**-oriented parallelepipedic seeds. The solution composition was not changed, as it has the lowest viscosity allowed in the crystallization region of KGP,[5] and was located very close to the border region. As the viscosity of the solution was similar, we also kept the rotation velocity at 75 rpm for all compositions. We therefore decided to try growing the crystals by lowering the cooling rate to 0.05 K/h. At this lower value, the crystal quality improved, and no inclusions were observed.

Neodymium Concentration Analyses. Small single crystals of Nd-substituted KGP with a Nd molar % in solution from 1 to 75 were grown using the same procedure as that in the crystallization region studies. We determined the Nd content of some of these crystals by electron probe microanalysis (EPMA) in a CAMECA SX-50 operating at a 20 kV accelerating voltage and a 100 nA electron current. We used a KGP crystal grown by us as the standard for measuring K, Gd, P, and O, and a synthetic glass (ree4) containing 4.0 mol % Nd as the standard for Nd. K and P were analyzed with PET (Pentaery thritol, 002) crystal using the line Kα. O Ka was measured with a W/Si multilayer crystal, and the Lα lines of Gd and Nd were analyzed using LIF (lithium fluoride, 200) crystal. The measurements were integrated for 10 s for all ions. The accuracy of the measurements was 1.40% for K, 1.30% for P, 1.10% for O, 1.16% for Gd, and 2.43% for Nd. For a Nd concentration below 1 mol % in solution, the measurement's accuracy decreased drastically.

X-ray Diffraction. To determine how the KGP crystallization region limits evolved with the neodymium content in the structure, we identified the Nd-substituted KGP small crystals grown by the X-ray powder diffraction technique. The patterns were recorded using Cu Kα radiation in a D5000 Siemens X-ray powder diffractometer in a $\theta-\theta$ configuration using the Bragg−Brentano geometry.

Small crystals grown from a solution composition of Gd_2O_3:Nd_2O_3:K_2O:P_2O_5 = 4−*X*:*X*:36:60 mol %, with *X* = 0.04−3, were analyzed to calculate the crystal cell parameters of the Nd-substituted KGP crystals.

The X-ray powder diffraction patterns were recorded in the 2θ range from 10 to 70° at ss = 0.03° and st = 5 s. We refined the cell parameters using the FULLPROF[7] program and the Rietveld[8] method, and the KGP structure was solved by single-crystal diffraction as the starting model.

Grown KGP and KNP crystals were analyzed by single-crystal X-ray diffraction using an Enraf−Nonius CAD-4 diffractometer; their structures were solved by the Patterson synthesis using the SHELXS97 computer program,[9] and were refined by the full-matrix least squares method using the SHELX97 program. Table 1 shows the details of the crystal data, data collection, and refinement.

Transparency Window. We measured the optical transmission of KGP and KNP in the wavelength range 0.15−10 μm. The thickness of the plate samples used was around 800 μm for both materials. The transmission in the UV−visible and NIR regions to 3.3 μm were measured using a Varian Cary 500 Scan spectrophotometer, and measurements in the IR region were made using an FTIR Midac Prospect spectrophotometer. The UV and IR cutoff values were calculated as the maximum transmission value divided by the *e* number.

Optical Tensor. Monoclinic structures show crystallographic anisotropy in all physical properties, including the optical ones. KGP and KNP are biaxial crystals whose optical properties are described by the 2-point group symmetry that arises from the $P2_1$ space group. We therefore oriented the optical frame in relation to the crystallographic one. In the monoclinic structure, one of the principal optical axes is parallel to the *b* direction, and the other two are placed in the *ac* plane. The optical ellipsoid is localized by the angle between one of the optical principal axes and one of the crystallographic axes on this plane, e.g., the *c* direction.

This angle was determined using an *ac*-oriented plate sample of KGP (1030 μm thick) and KNP (800 μm -thick), placed between two crossed glam-Taylor polarizers and illuminated under normal incidence by a He−Ne laser beam. First, we verified the crossed configuration between the polarizers when the light received by the detector was minimal. We then placed and rotated the sample

(7) Rodríguez-Carvajal, J. *Short Reference Guide for the Computer Program FULLPROF*; Laboratoire León Brillouin, CEA-CNRS: Gif sur Yvette, France, 1998.
(8) Young, R. A. *The Rietveld Method*; International Union of Crystallography Monographs on Crystallography 5; Oxford University Press: Oxford, U.K., 1995.
(9) Sheldrick, G. M. *SHELXS97 and SHELX97*; University of Göttingen: Göttingen, Germany, 1997.

Table 1. Crystal Data, Data Collection, and Refinement of KGd(PO$_3$)$_4$ and KNd(PO$_3$)$_4$

	KGd(PO$_3$)$_4$	KNd(PO$_3$)$_4$
	Crystal Data	
fw	512.23	499.22
Mo Kα radiation (λ, Å)	0.71069	0.71069
space group	monoclinic, $P2_1$	monoclinic, $P2_1$
no. of reflns	25	25
θ range (deg)	12−21	12−21
a (Å)	7.255(4)	7.2860(10)
b (Å)	8.356(5)	8.4420(10)
c (Å)	7.934(5)	8.0340(10)
μ (mm^{-1})	8.062	6.391
β (deg)	91.68(5)	92.170(10)
V (Å^3)	480.80(5)	493.80(11)
Z	2	2
color	colorless	purple
dimension	equidimensional	equidimensional
T (K)	293(2)	293(2)
diameter (mm)	0.2	0.2
D_x (Mg m^{-3})	3.538	3.358
D_m	not measured	not measured
	Data Collection	
R_{int}	0.0350	0.0386
$\omega-2\theta$ scan, θ_{max} (deg)	29.92	29.95
Abs corr: spherical	$h = -10 \rightarrow 10$, $k = 0 \rightarrow 11$, $l = 0 \rightarrow 10$	$h = -10 \rightarrow 10$, $k = 0 \rightarrow 11$, $l = 0 \rightarrow 11$
no. of measured reflns	1834	1617
no. of independent reflns	1474	1525
no. of reflections with $I > 2\sigma(I)$	1437	1520
	Refinement	
refinement on F^2R [$F^2 > 2\sigma(F^2)$]	0.0675	0.0386
$wR(F^2)$[a]	0.1560	0.1002
$\Delta\rho_{max}/\Delta\rho_{min}$ (e Å^{-3})	0.334/−0.480	0.583/−0.241
extinction correction method	none	none
S	1.168	1.089
no. of reflns	1474	1525
162 no. of params	162	162
Flack absolute struct param	−0.01(3)	0.00(2)
$(\Delta/\sigma)_{max}$	0.008	0.000

[a] From *International Tables for Crystallography, Vol. C.*: $w = 1/[\sigma^2(F_o^2) + (0.1295P)^2 + 1.1201P]$, with $P = (F_o^2 + 2F_c^2)/3$ for KGd(PO$_3$)$_4$, and $w = 1/[\sigma^2(F_o^2) + (0.0917P)^2 + 0.0000P]$, with $P = (F_o^2 + 2F_c^2)/3$ for KNd(PO$_3$)$_4$.

until the measured transmitted beam again reached a minimum, which requires the principal optical direction and the direction of the laser beam polarization to coincide.

We measured the refractive indices corresponding to the principal optical axes at 632.8 nm and room temperature for both KGP and KNP in order to determine the optical tensor under these conditions. The minimum-deviation method with a slight modification was used for this.[10] Two semiprisms were cut and polished with an angle of about 22.5° between faces, one of which was a principal plane (Np−Ng and Np−Nm). The first face was illuminated by an unpolarized laser beam under normal incidence. The prism was then rotated until a normal incidence on the second face (the principal plane) was reached. In this configuration, the beam partially reflects and returns along the same path as the incident beam. So, the path of the laser beam has a symmetrical configuration and deviates minimally throughout the prism. The anisotropic behavior of the crystals allows two beams with orthogonal polarizations to propagate in the crystal, and allows the refractive indices in these directions to be measured. Because the second face was a principal plane, we measured the refractive indices corresponding to principal axes. Thus, we measured n_p and n_g with one prism and n_p and n_m with the other. Note that as n_p was measured twice, it provides an estimate of the error in the measurements. This error is limited by the encoder accuracy, which is 10^{-3}.

Second Harmonic Generation (SHG) Measurements. We evaluated the second harmonic generation response of the Nd-substituted KGP crystals using the Kurtz method.[11] The powdered samples with a uniform particle size between 5 and 20 μm were uniformly packed, and were placed in a 2 mm thick quartz cell. Samples were irradiated using a laser beam of 1064 nm generated by a pulsed Nd:YAG solid-state laser.

We measured the energy reflected by the sample to estimate the incident power. Using a silicon PIN, we also measured the energy of the radiation it emitted. The frequency of this radiation was twice that of the incident one. We estimated the second harmonic efficiency of the sample from the ratio between these signals, which was calculated from an average of more than 100 laser shots. We compared this efficiency with that of KDP,[12] which is a well-known nonlinear optical material.

Results and Discussion

Crystallization Region of KGd(PO$_3$)$_4$ and KNd(PO$_3$)$_4$. We determined the evolution of the crystallization region limits of the type III phase from KGP to KNP in the ternary system of their corresponding oxide, Ln_2O_3, with Ln = Gd, Nd, K_2O, and P_2O_5. Figure 1 shows the crystallization region of the intermediate $KGd_{0.47}Nd_{0.53}(PO_3)_4$ in relation to those of KGd(PO$_3$)$_4$[5] and KNd(PO$_3$)$_4$.[6] The saturation temperature isotherms and SEM images of the neighboring phases

(10) Solé, R.; Nikolov, V.; Vilalta, A.; Carvajal, J. J.; Massons, J.; Gavaldà, Jna.; Aguiló, M.; Díaz, F. *J. Mater. Res.* **2002**, *17* (3), 563.
(11) Kurtz, S. K.; Perry, T. T. *J. Appl. Phys.* **1968**, *39*, 3798.
(12) Dmitriev, V. G.; Gurzadyan, G. G.; Nikogosyan, D. N. *Handbook of Nonlinear Optical Materials*; Springer-Verlag: Dusseldorf, Germany, 1991.

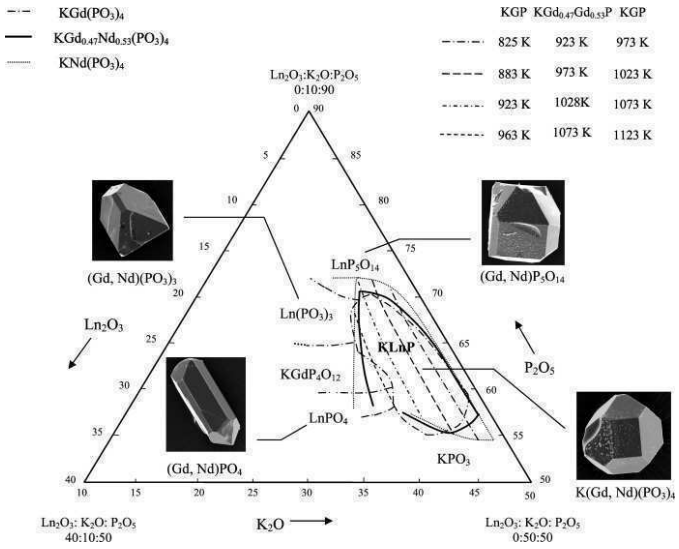

Figure 1. Crystallization region of $KGd_{0.47}Nd_{0.53}(PO_3)_4$ and those corresponding to $KGd(PO_3)_4$ and $KNd(PO_3)_4$ with saturation temperature isotherms in the $Ln_2O_3-K_2O-P_2O_5$ system, Ln = Gd, $Gd_{0.47}Nd_{0.53}$, and Nd. SEM images of $KGd_{0.5}Nd_{0.5}(PO_3)_4$ and neighboring phases.

identified were added. We knew from a previous paper[5] that the gadolinium ion had a high capacity for substitution by any other lanthanide ion because of its position in the lanthanide series, which led to a more irregular crystallization region in comparison with that of KNP. However, the crystallization region of the intermediate $KGd_{0.5}Nd_{0.5}(PO_3)_4$ is more similar to that of KNP than to that of KGP. The region has nearly the same shape, and neither the polymorph phase in the cycling geometry KLn_4O_{12} nor the mixture of orthorhombic/monoclinic $Ln(PO_3)_3$ was found.

When we compared the three crystallization regions, we found that the $P2_1$ phase crystallized in a longer extension when the neodymium concentration in the structure increased. The crystallization region limits of $KGd_{0.47}Nd_{0.53}(PO_3)_4$ were therefore placed between those of KGP and KNP. However, in the K_2O-richer zone of the phase diagram, the $[Gd_{0.47}Nd_{0.53}]O_3/K_2O$ limit coincided for all of them. Above this limit, which has a molar ratio of 3/97, the solution is so viscous that no crystal can grow. Below this limit, and up to a molar ratio of 22/78, the crystallization region is extended. Throughout these limits, $KGd_{0.47}Nd_{0.53}(PO_3)_4$ crystallizes between a P_2O_5 concentration of approximately 55 and 70 mol %. The isoconcentrational lines of $[Gd_{0.47}Nd_{0.53}]_2O_3/K_2O$ are roughly parallel to the saturation temperature isotherms, which increase from 923 to 1073 K. These temperatures are placed between those of KGP and KNP.

The four neighboring phases identified are KPO_3, $LnPO_4$,[13,14] $Ln(PO_3)_3$-orthorombic,[15,16] and $LnPO_5O_{14}$,[16,17] with Ln = Gd, (Gd,Nd), and Nd. KPO_3 crystallizes above the crystallization region and $LnPO_5O_{14}$ further above it. In the Ln_2O_3-richest zone, the other two phases are identified as $LnPO_4$ for low P_2O_5 concentrations and $Ln(PO_3)_3$ for high ones.

Crystal Structure of $KGd(PO_3)_4$ and $KNd(PO_3)_4$. The structure of KGP was solved for the first time in the present paper, and it was compared to that of the isostructural KNP, whose structure we have previously solved and which is in good agreement with that solved by Hong in 1975.[4] Both structures are monoclinic, and have $P2_1$ as its space group. The cell parameters for KGP are $a = 7.255(4)$ Å, $b = 8.356(5)$ Å, $c = 7.934(5)$ Å, $\beta = 91.68(5)°$, and $Z = 2$; those for KNP are $a = 7.2860(10)$ Å, $b = 8.4420(10)$ Å, $c = 8.0340(10)$ Å, $\beta = 92.170(10)°$, and $Z = 2$. All the KNP cell parameters are larger than the KGP ones, as expected, because the ionic radius of Nd^{3+} is slightly larger than the corresponding radius of Gd^{3+} (0.995 and 0.938 Å, respectively). The atomic coordinates, mean atomic lengths, and anisotropic thermal displacement parameters are shown in Tables 2−4.

The crystal cell of KGP and that of the isostructural KNP contain one structural position for gadolinium and potassium, four positions for phosphorus, and twelve inequivalent positions for oxygen. All atomic positions are doubled by the 2-fold screw axis parallel to [010]. The phosphate atoms are four-coordinated with the nearest oxygen atoms to form PO_4 tetrahedra. These tetrahedra are self-linked by sharing two of their vertexes to form chains, which define the type III structure. The basic unit of these chains is made of four PO_4 tetrahedra, and repeats by periodicity to generate the

(13) Mullica, D. F.; Grossie, D. A., Boatner, L. A. *Inorg. Chim. Acta* **1985**, *109*, 105.
(14) Ni, X.-Y.; Hughes, J. M.; Mariano, A. N. *Am. Mineral.* **1995**, *80*, 21.
(15) Melnikov, P. P.; Komissarova, L. N.; Butuzova, T. A. *Izv. Akad. Nauk, Neorg. Mater.* **1981**, *17* (11), 2110.
(16) Hong, H. Y.-P. *Acta Crystallogr., Sect. B* **1974**, *30*, 468.
(17) Bagieu-Beucher, M.; Doc, T. Q. *Bull. Soc. Fr. Mineral. Crystallogr.* **1970**, *93*, 505.

Table 2. Atomic Coordinates and Equivalent Isotropic Displacement Parameters of KGd(PO$_3$)$_4$ and KNd(PO$_3$)$_4$

atom	*x*	*y*	*z*	*U*(eq)	atom	*x*	*y*	*z*	*U*(eq)
Gd	0.2376(1)	0.2500(2)	0.2426(1)	0.016(1)	Nd	0.2349(1)	0.2500(1)	0.2422(1)	0.017(1)
K	0.7360(5)	0.0531(6)	0.2724(4)	0.031(1)	K	0.7268(3)	0.0543(3)	0.2808(2)	0.038(1)
P1	0.1010((5)	0.8295(6)	0.1005(4)	0.027(1)	P1	0.1031(2)	0.8304(3)	0.1037(2)	0.018(1)
P2	0.4396(6)	0.6181(6)	0.0976(5)	0.025(1)	P2	0.4342(3)	0.6280(2)	0.0979(2)	0.018(1)
P3	0.6179(5)	0.4973(6)	0.3980(4)	0.027(1)	P3	0.6220(2)	0.4965(2)	0.3959(2)	0.017(1)
P4	−0.0053(5)	0.1062(5)	0.6177(5)	0.022(1)	P4	0.0006(3)	0.1013(3)	0.6196(2)	0.018(1)
O1	0.0949(16)	0.9888(16)	0.1698(14)	0.038(2)	O1	0.0847(8)	0.9901(7)	0.1734(7)	0.024(1)
O2	0.6923(16)	0.2811(16)	0.8881(13)	0.040(3)	O2	0.6881(8)	0.2808(6)	0.8761(7)	0.025(1)
O3	0.0078(16)	0.2033(13)	0.7842(12)	0.028(2)	O3	0.0105(9)	0.2072(8)	0.7845(8)	0.030(1)
O4	0.8300(20)	−0.0100(20)	0.6154(17)	0.036(3)	O4	0.8294(7)	0.0028(8)	0.6153(7)	0.023(1)
O5	0.6810(20)	0.9870(20)	0.9231(17)	0.034(3)	O5	0.6830(9)	0.9837(8)	0.9297(7)	0.024(1)
O6	0.4320(20)	0.1770(2)	0.0337(18)	0.040(3)	O6	0.4313(9)	0.1527(9)	0.0334(8)	0.032(1)
O7	0.0357(18)	0.1895(18)	0.4675(16)	0.026(2)	O7	0.0266(9)	0.2072(7)	0.4714(8)	0.026(1)
O8	0.1779(16)	−0.0139(15)	0.6581(14)	0.036(2)	O8	0.1687(7)	−0.0119(6)	0.6552(6)	0.020(1)
O9	0.4476(19)	0.1250(19)	0.7221(15)	0.042(3)	O9	0.4608(9)	0.1344(7)	0.7263(7)	0.024(1)
O10	0.5344(15)	0.3315(14)	0.3539(13)	0.029(2)	O10	0.5377(8)	0.3441(7)	0.3448(7)	0.025(1)
O11	0.9620(15)	0.3054(15)	0.0769(13)	0.031(2)	O11	0.9635(7)	0.2975(7)	0.0680(6)	0.023(1)
O12	0.3935(16)	0.0495(15)	0.4235(14)	0.036(2)	O12	0.3858(8)	0.0558(7)	0.4277(6)	0.023(1)

Table 3. Selected Interatomic Distances (Å) in KGd(PO$_3$)$_4$ and KNd(PO$_3$)$_4$

			KGd(PO$_3$)$_4$				
P1−O1	1.441(12)	P3−O12	1.486(11)	Gd−O6	2.292(15)	K−O12	2.790(12)
P1−O11	1.480(11)	P3−O10	1.498(14)	Gd−O4	2.361(16)	K−O1	2.803(12)
P1−O2	1.553(12)	P3−O9	1.548(12)	Gd−O7	2.396(13)	K−O10	2.833(12)
P1−O3	1.617(11)	P3−O8	1.562(11)	Gd−O10	2.402(12)	K−O4	2.834(14)
P2−O5	1.408(16)	P4−O7	1.419(13)	Gd−O11	2.405(11)	K−O5	2.844(13)
P2−O6	1.499(15)	P4−O4	1.538(16)	Gd−O12	2.458(12)	K−O7	2.868(15)
P2−O9	1.628(13)	P4−O3	1.551(10)	Gd−O5	2.461(15)	K−O6	3.044(17)
P2−O2	1.671(13)	P4−O8	1.688(13)	Gd−O1	2.477(13)	K−O11	3.113(11)
			KNd(PO$_3$)$_4$				
P1−O1	1.486(6)	P3−O10	1.477(6)	Nd−O6	2.391(6)	K−O12	2.791(5)
P1−O11	1.471(5)	P3−O12	1.506(5)	Nd−O11	2.413(5)	K−O4	2.796(6)
P1−O2	1.580(6)	P3−O8	1.596(5)	Nd−O12	2.448(6)	K−O1	2.829(6)
P1−O3	1.622(6)	P3−O9	1.624(6)	Nd−O7	2.457 (5)	K−O10	2.864 6)
P2−O6	1.482 6)	P4−O4	1.498 6)	Nd−O10	2.457(6)	K−O5	2.889 6)
P2−O5	1.499 7)	P4−O7	1.506(6)	Nd−O4	2.475(7)	K−O7	2.921(8)
P2−O9	1.581(6)	P4−O8	1.571(5)	Nd−O5	2.494(6)	K−O6	2.992(8)
P2−O2	1.586(5)	P4−O3	1.597(6)	Nd−O1	2.505(6)	K−O11	3.214(6)

zigzag long chains along the *a*-crystallographic direction (Figure 2). The chains are joined by sharing the other two vertexes with the Gd^{3+} and K^+ atoms. The intrachain P−O bond distances are larger than the interchain ones, so the PO_4 tetrahedra are slightly distorted. The distortion parameter, defined as $\Delta d = {}^1/_4\Sigma_{n=1,4}[(d_n - \langle d\rangle)/\langle d\rangle]^2$, where the d_n values are the different P−O distances in the tetrahedra and $\langle d\rangle$ is the mean P−O distance, is relatively high. The values for P_1, P_2, P_3, and P_4 phosphorus tetrahedra (Figure 3), are 1.79×10^{-3}, 4.58×10^{-3}, 4.48×10^{-4}, and 3.71×10^{-3}.

The gadolinium atom is eight-coordinated with oxygen atoms to form a distorted dodecahedra. These GdO_8 polyhedra are isolated from each other because they share O atoms only with the PO_4 tetrahedra to join the chains. They are surrounded by four other GdO_8 polyhedra with large distances of about 7 Å (Figure 3). The potassium ion is also eight-coordinated with the largest distances in the structure, so it is weakly linked to the crystal lattice. It is placed close to the canals defined along the [010] direction in the $[Gd(PO_3)_4]^-$ structure (Figure 3). The Gd^{3+} and K^+ atoms alternate with a zigzag arrangement parallel to the phosphate chains.

Nd^{3+} Substitution in KGd(PO$_3$)$_4$. The chemical compositions of the crystals obtained from solutions of 1, 5, 10, 25, 50, and 75 mol % Nd_2O_3 were analyzed by EPMA. Table 5 shows the neodymium distribution coefficients in the structure, defined as $K_{Nd} = ([Nd]/[Nd]+[Gd])_{crystal}/([Nd]/[Nd]+[Gd])_{solution}$. They are in all cases close to 1, because the ionic radius of Nd^{3+} is only around 6% smaller than that of Gd^{3+}. Figure 4 shows the linear relationship between the average change in each cell parameter ($\Delta Y/Y$) and the neodymium concentration in crystal. Whereas the *a*, *b*, *c*, and *V* parameters increase as the Nd concentration increases, the β angle decreases slightly. The values corresponding to each composition are listed in Table 5.

Transparency Window. Figure 5 shows the transparency windows of KGP (panel a) and KNP (panel b). The IR cutoff wavelength is around 4 μm for both materials because of

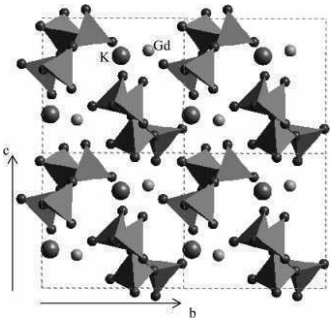

Figure 2. Zigzag arrangement of the PO_4 long chains along [100] in a projection parallel to this direction.

Table 4. Anisotropic Displacement Parameters (Å²) of $KGd(PO_3)_4$ and $KNd(PO_3)_4$

atom	U_{11}	U_{22}	U_{33}	U_{23}	U_{13}	U_{12}
			$KGd(PO_3)_4$			
Gd	0.014(1)	0.021(1)	0.014(1)	0.001(1)	−0.001(1)	−0.001(1)
K	0.028(2)	0.037(2)	0.029(1)	−0.002(2)	−0.004(1)	−0.001(1)
P1	0.023(2)	0.035(2)	0.024(2)	0(1)	−0.003(1)	−0.002(1)
P2	0.0241(2)	0.032(2)	0.017(2)	0.001(1)	0(1)	−0.002(2)
P3	0.023(2)	0.036(1)	0.022(1)	0(1)	−0.002(1)	0.002(1)
P4	0.020(2)	0.030(2)	0.017(1)	0.001(1)	−0.001(1)	−0.002(1)
O1	0.038(6)	0.038(5)	0.036(5)	−0.006(5)	−0.010(5)	0.003(5)
O2	0.030(5)	0.059(7)	0.030(4)	0.002(5)	0(4)	0(6)
O3	0.030(5)	0.033(4)	0.022(4)	−0.003(4)	0.001(4)	0.003(4)
O4	0.032(6)	0.042(6)	0.035(6)	0.002(6)	0(5)	−0.004(6)
O5	0.036(6)	0.038(6)	0.029(6)	−0.006(5)	0(5)	0.006(5)
O6	0.044(8)	0.051(8)	0.025(6)	−0.007(6)	0.006(5)	−0.002(7)
O7	0.028(6)	0.031(5)	0.019(5)	0.003(4)	0(4)	−0.005(5)
O8	0.027(5)	0.041(5)	0.041(6)	0(5)	−0.002(4)	−0.007(5)
O9	0.038(7)	0.057(7)	0.032(5)	−0.005(6)	−0.006(5)	0.010(6)
O10	0.025(5)	0.035(5)	0.026(5)	0(4)	−0.004(4)	0.007(4)
O11	0.026(5)	0.041(5)	0.026(5)	0.0011(4)	0(4)	0.001(4)
O12	0.028(5)	0.044(5)	0.036(6)	0.0015(5)	−0.003(4)	0.001(5)
			$KNd(PO_3)_4$			
Nd	0.017(3)	0.017(1)	0.018(1)	0(1)	0.003(1)	0(1)
K	0.028(1)	0.060(1)	0.027(1)	0.001(1)	0.007(1)	0.008(1)
P1	0.018(1)	0.014(1)	0.020(1)	0.001(1)	0.002(1)	0(1)
P2	0.018(1)	0.015(1)	0.022(1)	−0.001(1)	0.005(1)	0.001(1)
P3	0.015(1)	0.016(1)	0.020(1)	0(1)	0.004(1)	−0.001(1)
P4	0.019(1)	0.016(1)	0.021(1)	−0.001(1)	0.006(1)	0(1)
O1	0.023(3)	0.021(2)	0.030(2)	−0.005(2)	0.011(2)	−0.001(2)
O2	0.020(2)	0.018(2)	0.036(2)	0.002(1)	0(2)	−0.003(2)
O3	0.028(3)	0.031 (3)	0.032(3)	−0.010(2)	0.007(2)	0.003(2)
O4	0.013(2)	0.024 (3)	0.032(3)	−0.007(2)	0.006(2)	−0.003(2)
O5	0.026(3)	0.019 (3)	0.027(3)	−0.003(2)	−0.001(2)	0.001(2)
O6	0.023(3)	0.033 (3)	0.040(3)	0(3)	0.023(2)	−0.004(3)
O7	0.024(3)	0.015 (2)	0.039(3)	0.004(2)	0.020(2)	0.004(2)
O8	0.016(2)	0.016(2)	0.028(2)	0.005(2)	0.002(2)	0.007(2)
O9	0.032(3)	0.012(2)	0.026(2)	−0.002(2)	−0.008(2)	0.004(2)
O10	0.024(2)	0.021(2)	0.030(3)	0.001(2)	0.004(2)	−0.006(2)
O11	0.015(2)	0.033(3)	0.020(2)	−0.005(2)	−0.001(2)	0.007(2)
O12	0.027(3)	0.026(2)	0.016(2)	−0.005(2)	0.005(2)	0.004(2)

the absorption resonance of the P−O linkage. These crystals have a large transparency window that extends from approximately 180 nm to this wavelength. This low UV cutoff wavelength constitutes another important feature of these crystalline materials, especially when combined with their noncentrosymmetrical structures to allow the second and third harmonics of very near-IR beams. The strong absorptive bands in the KNP transmission spectrum are due to the resonance transmissions between manifolds of Nd^{3+}, which has a high concentration in this structure.

Optical Tensor. The optical frames of KGP and KNP crystals were oriented. We found a minimum transmission when the plate sample, with *b* positive toward us, was rotated clockwise 37.3 and 35.4° from the *c* direction for KGP and KNP, respectively. The second principal optical direction in the *ac* plane was therefore placed at 39.1 and 37.6° from the *a* direction for KGP and KNP, respectively.

We measured the refraction indices along the optical principal directions previously determined at 632.5 nm. In this way we were able to identify these directions as N_p, N_m, and N_g and draw the optical ellipsoid, which is shown in Figure 6 for KGP (panel a) and KNP (panel b). We found that the principal optical direction with the highest value of refraction index, N_g, was at 37.3° clockwise from the *c* direction, and the *b* direction corresponded to N_p. We can use these measurements to write the optical tensor at this

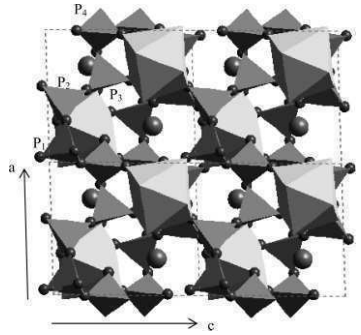

Figure 3. View of the GdO_8 dodecahedra linking the phosphate chains and the potassium atoms near the canals in the $[Gd(PO_3)_4]^-$ frame. Projection parallel to [010].

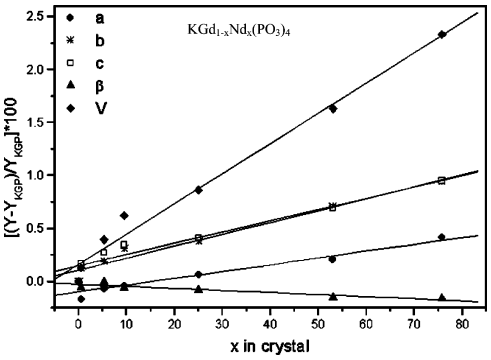

Figure 4. Relative evolution of the cell parameters and unit cell volume of $KGd_{1-x}Nd_x(PO_3)_4$ vs neodymium concentration.

Table 5. Neodymium Distribution Coefficients and Cell Parameter Values for Each Nd Concentration (in atomic %)

at. % Nd in solution	at. % Nd in crystal	K_{Nd}	*a* (Å)	*b* (Å)	*c* (Å)	β (deg)	*V* (Å³)
0.5	0.66	1.33	7.270(1)	8.390(1)	7.968(1)	91.67(1)	485.80
1	1.09	1.09	7.270(1)	8.391(1)	7.969(1)	91.66(1)	485.93
5	5.32	1.06	7.269(1)	8.396(1)	7.977(1)	91.72(1)	486.62
10	9.47	0.95	7.273(1)	8.406(1)	7.982(1)	91.77(1)	487.76
25	24.92	0.99	7.277(1)	8.412(1)	7.988(1)	91.85(1)	488.72
50	52.98	1.06	7.283(1)	8.440(1)	8.010(1)	91.98(1)	492.06
75	75.75	1.01	7.285(1)	8.439(1)	8.030(1)	92.02(1)	493.75

wavelength and at room temperature

$$n_{ij\ (KGP)} = \begin{pmatrix} 1.592 & 0 & 0 \\ 0 & 1.604 & 0 \\ 0 & 0 & 1.609 \end{pmatrix}$$

$$n_{ij\ (KNP)} = \begin{pmatrix} 1.596 & 0 & 0 \\ 0 & 1.586 & 0 \\ 0 & 0 & 1.602 \end{pmatrix}$$

Second Harmonic Generation Efficiency. We measured, as previously described, the SHG efficiency (η) of $KGd(PO_3)_4$, $KGd_{0.75}Nd_{0.25}(PO_3)_4$, $KGd_{0.47}Nd_{0.53}(PO_3)_4$, $KGd_{0.24}Nd_{0.76}(PO_3)_4$, and $KNd(PO_3)_4$, and compared them with that of KDP. For all compositions, the value of η/η_{KDP} was

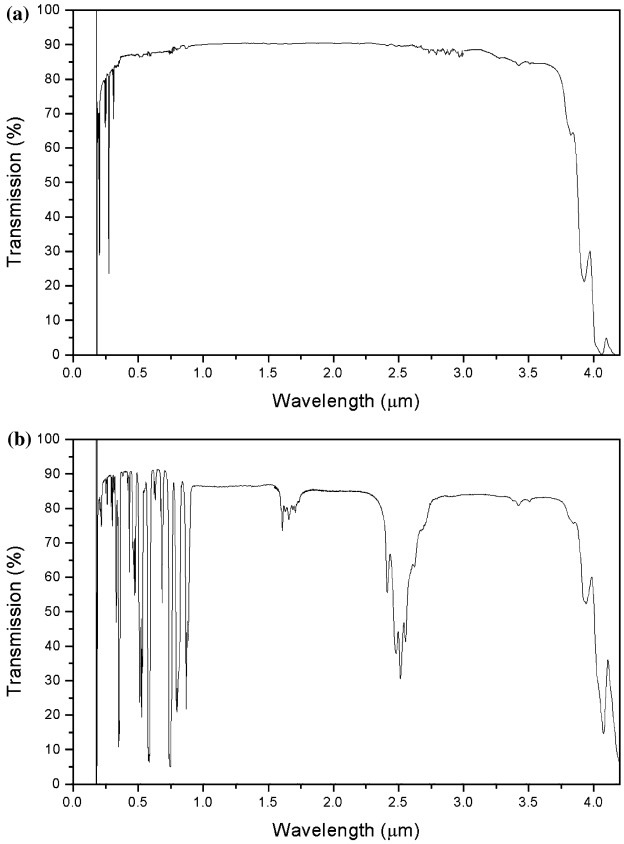

Figure 5. Transparency window of (a) KGP and (b) KNP at room temperature.

approximately 1, so we can confirm that the nonlinearity of KGP does not depend on any percentage substitution of Gd^{3+} by Nd^{3+}.

Conclusions

We determined the crystallization region of intermediate $KGd_{0.47}Nd_{0.53}(PO_3)_4$ and its saturation temperature isotherms, and we identified the neighboring phases found. All our results are consistent with the intermediate situation between KGP and KNP. The saturation temperatures and the number of neighboring phases are between those of KGP and KNP.

The crystal structure of type III KGP has been solved, and has been compared to that of the isostructural KNP. Because of the larger ionic radius of neodymium, when gadolinium was substituted for neodymium, all cell parameters increased except the β angle, which decreased slightly. Because the neodymium distribution coefficient for all compositions was almost 1, the high substitution acceptance of KGP has been proved, and KGP can be regarded as a promising laser host. Because of their noncentrosymmetrical structure, these materials can be used as nonlinear laser hosts

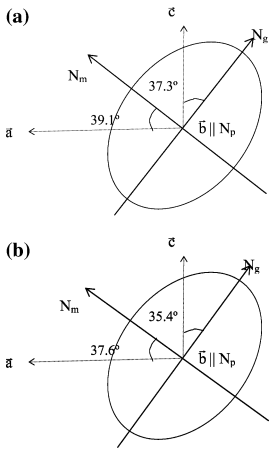

Figure 6. Optical ellipsoid of (a) KGP and (b) KNP in a projection parallel to [010] at $\lambda = 632.5$ nm and room temperature.

whose second harmonic efficiency is similar to that of KDP, and it maintains a constant value with Nd doping. Moreover, this material presents a significant low UV cutoff value (∼180 nm), which allows for the propagation of second and third harmonics of near-IR beams.

As a comparative study between KGP and KNP, we determined the optical tensor and ellipsoid. Few differences were observed between the optical frame orientations because the cell parameters are not very different. The refractive indices were also similar not only between themselves but also among the three principal optical directions.

Acknowledgment. The authors acknowledge financial support from the Generalitat de Catalunya under Projects 2001SGR317 and 2005SGR658 and Project 2003FI00770 (personal support) and from CICyT (Comisión inaterministerial de Ciencia y Tecnologia of the Spanish government) under Projects MAT-02-04603-C05-03 and MAT-05-06354-C03-02.

CM052114L

Paper IV

Crystallization region, crystal growth, and phase transitions of $KNd(PO_3)_4$

I. Parreu, R. Solé, Jna. Gavaldà, J. Massons, F. Díaz, M. Aguiló

Chemistry of Materials **2003**, 15(26), 5059

Crystallization Region, Crystal Growth, and Phase Transitions of $KNd(PO_3)_4$

I. Parreu, R. Solé, Jna. Gavaldà, J. Massons, F. Díaz, and M. Aguiló*

Física i Cristallografia de Materials, Universitat Rovira i Virgili, Imperial Tarraco, 1, 42005 Tarragona, Spain

Received September 2, 2003. Revised Manuscript Received October 24, 2003

We determined the crystallization region of $KNd(PO_3)_4$ (KNP), the isotherms of saturation temperature, and three neighboring phases of this crystallization region, $NdPO_4$, $Nd(PO_3)_3$, and NdP_5O_{14}, in the Nd_2O_3−K_2O−P_2O_5 system. We successfully grew KNP single crystals by the top seeded solution growth slow cooling method (TSSG). To optimize the growth process solution composition, seed orientation and rotation velocity were analyzed. We studied the evolution with the temperature of the KNP cell parameters in the room temperature to 773 K range, and the linear thermal expansion tensor of KNP was studied. We also studied the phase transitions of KNP in the room temperature to 1273 K range and found an irreversible decomposition at 1165 K. The second harmonic efficiency measured was at least similar to that of KH_2PO_4 (KDP).

Introduction

As a Nd stoichiometric laser material, $KNd(PO_3)_4$ (KNP) is potentially useful for miniature laser devices because it strongly absorbs the pumping light in short distances (50−100 μm).[1] This high absorption efficiency is allowed in stoichiometric laser materials by the high active ion concentration. Materials for miniature Nd lasers should have two structural characteristics: first, they should have no local inversion symmetry about the Nd^{3+} ions so as not to decrease the probability of radiative transitions, and second, the Nd−O polyhedrons should be isolated among them so as to decrease the quenching fluorescence process of Nd^{3+} ions. The structure of KNP satisfies both of these crystallographic conditions.[1] When we solved the structure of KNP by single-crystal diffraction analysis,[2] we obtained a similar result that had been reported in 1975. The monoclinic structure of KNP has $P2_1$ as space group, with cell parameters, a = 7.2860(10) Å, b = 8.4420(10) Å, c = 8.0340(10) Å, β = 92.170(10)°; Z = 2; V = 493.80(11) Å^3.

Several Nd-stoichiometric laser materials have so far been reported. Of these, two representative Nd-stoichiometric phosphates are NdP_5O_{14}[3−5] and $LiNd(PO_3)_4$ (LNP);[6−8] both of them satisfied the structural conditions already mentioned. However, KNP has a structural advantage over these other Nd-stoichiometric phosphates: it has an acentric space group ($P2_1$). The fact that the structure of KNP does not have a center of inversion may allow nonlinear optical processes,[9] such as second-harmonic generation.

The aim of this paper is to study and optimize the conditions of the KNP crystal growth process and perform the basic structural characterization of the material.

Therefore, as information in the literature is poor and sometimes confused, we determined the crystallization region of KNP in the self-flux and phase transitions of KNP. Some papers on the growth of KNP single crystals can be found in the literature,[1,10] but they do not contain much information. On the other hand, they reported the incongruent melting of KNP decomposing into $Nd(PO_3)_3$ and KPO_3 at 1155 K,[10] a thermal arrest at 1153 K related to a crystalline-to-amorphous transition and a monoclinic-to-orthorhombic transition at 440 K.[1] However, neither of these transitions is well documented.

We also dedicated so many efforts to determine the morphology of KNP, since it is essential to orient and polish the samples for later physical characterizations.

Finally, we performed some physical characterizations of the material, such as linear thermal expansion tensor and second harmonic generation.

Experimental Section

KNP Crystallization Region. To determine the concentration region and crystallization temperatures of KNP in the Nd_2O_3−K_2O−P_2O_5 system, we studied several solution compositions. The procedure we used for each solution composition study is summarized in the following four steps: solution preparation and homogenization, determination of the saturation temperature, crystal growth, and phase identification.

* To whom correspondence should be addressed. E-mail: aguilo@quimica.urv.es.

(1) Hong, H. Y.-P. *Mater. Res. Bull.* **1975**, *10*, 1105.
(2) Parreu, I.; Solans, X.; Aguiló, M. Unpublished.
(3) Weber, H. P.; Damen, T. C.; Danielmeyer, H. G.; Tofield, B. C. *Appl. Phys. Lett.* **1973**, *22*, 534.
(4) Danielmeyer, H. G.; Huber, G.; Krühler, W. W.; Jeser, J. P. *Appl. Phys.* **1975**, *2*, 335.
(5) Chinn, S. R.; Pierce, J. W.; Heckscher, H. *IEEE J. Quantum Electron.,* to be published.
(6) Otsuka, K.; Yamada, T. *Appl. Phys. Lett.* **1975**, *26*, 311.
(7) Chinn, S. R.; Hong, H. Y.-P. *Appl. Phys. Lett.* **1975**, *26*, 649.
(8) Otsuka, K.; Yamada, T.; Saruwatari, M.; Kimura, T. *IEEE J. Quantum Electron.* **1975**, *QE-11*, 330.
(9) Xue, D.; Zhang, S. *Phys. Status Solidi* **1998**, *165*, 509.
(10) Mazurak, Z.; Jezowska-Trzebiatkowska, B.; Schultze, D.; Waligora, C. *Cryst. Res. Technol.* **1984**, 19.

10.1021/cm034812g CCC: $25.00
Published on Web 12/02/2003

Table 1. Growth Data for KNP Single Crystals

expt	solution composition $Nd_2O_3-K_2O-P_2O_5$	solution wt (g)	seed orientation	rotation velocity (rpm)	cooling interval (K)	cryst dimens ($a \times b \times c$)(mm^3)	cryst wt (g)
1	10/30/60	20	c^*	45	12		
2	10/30/60	20	b	45	16	$7.3 \times 2.6 \times 10.0$	0.37
3	10/30/60	20	a^*	45	17	$3.4 \times 9.5 \times 8.0$	0.30
4	10/30/60	20	a^*	60	17	$4.2 \times 10.6 \times 8.3$	0.33
5	7/31/62	20	a^*	60	17	$3.0 \times 7.9 \times 5.9$	0.34
6	4/31/65	20	a^*	60	24.5	$2.7 \times 9.05 \times 7.3$	0.27
7	6/34/60	20	a^*	60	16	$3.0 \times 9.1 \times 6.8$	0.36
8	6/34/60	20	b	60	15	$8.4 \times 4.4 \times 6.3$	0.41
9	6/34/60	20	a^*	75	15	$3.5 \times 9.3 \times 6.9$	0.47
10	6/34/60	20	b	75	15	$11.8 \times 2.8 \times 7.2$	0.47
11	6/34/60	200	a^*	75	17	$7.8 \times 14.9 \times 9.5$	1.84
12	6/34/60	200	b	75	17	$16.0 \times 6.2 \times 12.7$	1.98

The experiments were carried out in a vertical tubular furnace with a Kantal AF heater. The temperature was measured by an S-type thermocouple and controlled by an EUROTHERM 818 P controller/programmer connected to a thyristor. Platinum crucibles (25 cm^3) were used to prepare roughly 20 g of solution, using Nd_2O_3, K_2CO_3, and $NH_4H_2PO_4$ mixed at the chosen ratios. To prevent the formation of phosphate acids, which can react with platinum at high temperatures, these initial reagents were decomposed by heating them at the minimum temperature required to reach the complete bubbling of NH_3, CO_2, and H_2O. The solution was then homogenized by maintaining the temperature at about 1173−1273 K for 5−12 h, depending on the solution composition.

Small KNP crystals were then added to the solution. Because of the surface tension and natural convection processes, these crystals stayed on the center of the surface, which was the coldest point of the whole solution. Then, the saturation temperature was accurately determined by observing the growth or dissolution of these small crystals over long periods of time. A platinum disk with a rotation of 45 rpm placed into contact with the solution surface was then used to grow the crystals by lowering the solution temperature to about 25 K below its saturation temperature. The cooling rate used to obtain the supersaturation of the solution was 1−2 K/h.

We preliminarily identified the crystals by direct observation with an optical microscope and then by X-ray powder diffraction analysis. Some were also observed and photographed in a scanning electron microscope (SEM) JEOL JSM 6400.

X-ray Powder Diffraction. We used the X-ray powder diffraction technique to analyze several aspects of the KNP structural study, such as identifying the KNP crystalline phase and some neighboring phases in the determination of the KNP crystallization region. The experiments were carried out with a D5000 Siemens X-ray powder diffractometer in a $\theta-\theta$ configuration using the Bragg−Brentano geometry and Cu Kα radiation.

We also used this technique to study the evolution of the crystal cell parameters with temperature and the linear thermal expansion tensor of KNP. The equipment was the same, but with a high-temperature chamber (Anton-Paar HTK10 platinum ribbon heating stage). The X-ray powder diffraction patterns were recorded, with a scintillation detector, at $2\theta = 10-70°$, step size = 0.03°, step time = 5 s, and temperatures of 298, 323, 373, 473, 573, 673, and 773 K, with a delay time of 300 s before each recording.

For the phase transitions of the KNP, performing the heating and cooling of the sample using the same equipment, in this case, a Braun position sensitive detector (PSD) was added. The X-ray powder diffraction patterns were recorded at $2\theta = 10-70°$, and the measuring time per degree was 10 s. We performed two experiments. In the first one, we studied how the material evolved with temperature from room temperature to 1273 K. In the second one, we used a smaller temperature range (from room temperature to 523 K) to specifically study the phase transition reported in the literature.[1] For the first experiment, we first heated the sample at a rate of 10 K/s from room temperature to 673 K, and then we decreased the heating rate to 0.17 K/s and increased the temperature to 1273 K. From this maximum to room temperature, the same rates and temperature intervals were used. Diffraction patterns were registered every 50 K between 673 and 1273 K in both processes. For the second experiment, the sample was heated from room temperature to 373 K also at a rate of 10K/s and between this temperature and 523 K at a rate of 0.017 K/s. We then performed the cooling process from 523 K to room temperature with the same rates and intervals and recorded the diffraction patterns in both processes every 25 K from 373 to 523 K.

Differential Thermal Analysis (DTA) Measurements. We also studied the phase transitions of KNP by DTA measurements before studying them by X-ray powder diffraction. We used a TA Instruments simultaneous differential techniques instrument SDT 2960. The sample, which weighed around 20 mg, was placed in a platinum pan, and calcined Al_2O_3 was used as reference material. We used Ar as purge gas at a flow of 90 cm^3/min. We performed two experiments. In the first one, we used a heating rate of 10 K/min between room temperature and 1273 K, and in the second one, we used a heating rate of 1 K/min between room temperature and 523 K. The storage rate of data was always 0.5 s /data point.

Top Seeded Solution Growth (TSSG). To obtain KNP single crystals of a suitable size and quality for later optical studies, several growth experiments were carried out with the top seeded solution growth (TSSG)-slow cooling method without pulling. We used the same equipment as in the study of the crystallization region. The solution was placed in a platinum conical crucible of 25 cm^3. The temperature was then increased to about 50 K above its saturation temperature and maintained for 3−4 h to homogenize the solution. The axial temperature gradient in the solutions was 0.75−0.92 K/mm, and the surface was colder than any other part of the solution. Crystals were grown with constant rotation using KNP parallelepipedic oriented seeds located at the center of the solution surface. The size of the seeds used was approximately constant for all growth experiences being $10 \times 2 \times 2$ mm^3 along a, b, c with a disposed vertically or $2 \times 10 \times 2$ mm^3 when b is disposed vertically to the solution surface.

We accurately determined the saturation temperature by observing the growth or dissolution of a KNP seed in contact with the surface of the solution. The crystals were grown submerged in the solution with constant rotation by decreasing the solution temperature at a rate of 0.1 K/h.

We studied three parameters of the KNP crystal growth process during the experiments: solution composition, seed orientation, and rotation velocity. These parameters and the results obtained are shown in Table 1 (see expts from 1 to 10).

These results led us to introduce a small change in the growth method in order to increase the mass transport in the solution and improve the quality of the KNP single crystals. We introduced a growth device previously tested in our laboratory.[11] To introduce it, we had to use a platinum conical

(11) Carvajal, J. J.; Nikolov, V.; Solé, R.; Gavaldà, Jna.; Massons, J.; Rico, M.; Zaldo, C.; Aguiló, M.; Díaz, F. *Chem. Mater.* **2000**, *12*, 3171.

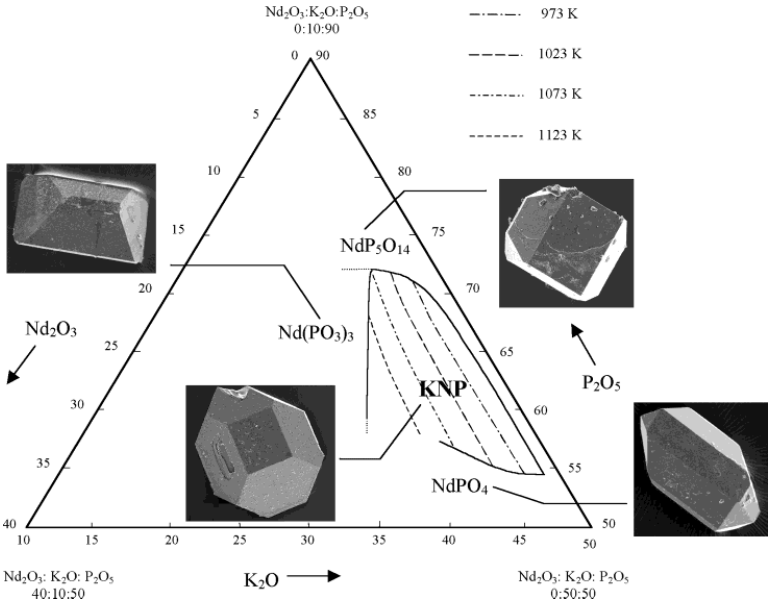

Figure 1. Crystallization Region of KNP and saturation temperatures in the system Nd_2O_3−K_2O−P_2O_5. SEM images of KNP and neighboring phases.

crucible of 125 cm^3. This device comprises a platinum turbine, centered on the rotation axis, and two seed supports above it symmetrically displaced from this axis. With this device, we performed the two last experiments listed in Table 1. The growth parameters used were those that had provided the best results in the first study.

Second Harmonic Generation (SHG) Measurements. We used the Kurtz method[12] to measure the second harmonic response of the KNP. The sample analyzed was powdered and graded with standard sieves to obtain a uniform particle size, between 5 and 20 μm. After being packed uniformly, the sample was placed in a 2 mm-thick quartz cell and irradiated using a pulsed Nd:YAG laser.

We measured the energy reflected by the sample to estimate the incident power. We also measured the energy of the double radiation it emitted, which had double the frequency of the incident radiation, using a silicon PIN. The ratio between these signals was used to estimate the second harmonic efficiency of the sample. This ratio was calculated as an average of over 100 laser shots. This efficiency was compared with that of KDP,[13] which is a well-known nonlinear optical material.

Results and Discussion

KNP Crystallization Region. The crystallization region of KNP in the Nd_2O_3−K_2O−P_2O_5 system and the saturation temperature isotherms could be drawn after studying about 40 compositions of the solution. Figure 1 shows this crystallization region and some neighboring phases. It also shows SEM images of KNP and neighboring phases.

The crystallization region of KNP is placed between a Nd_2O_3/K_2O molar ratio of 25/75 and 3/97 and a P_2O_5 concentration between 55 and 73 mol %. The saturation temperature isotherms are roughly parallel to the border of the crystallization region with the lowest concentration of Nd_2O_3. This is also almost parallel to the isoconcentrational lines of this oxide. The saturation temperature isotherms increase from 973 to 1123 K when the Nd_2O_3 molar ratio is also increased.

The neighboring phases of the crystallization region identified are $NdPO_4$ (ortophosphate),[14] $Nd(PO_3)_3$ (metaphosphate),[15] and NdP_5O_{14} (ultraphosphate).[15] $NdPO_4$ crystallizes below the KNP crystallization region for a P_2O_5 concentration of less than 55 mol %. In the same way, NdP_5O_{14} crystallizes above the KNP crystallization region for a P_2O_5 concentration of more than 73 mol %. In the region between these two P_2O_5 concentrations, and for a Nd_2O_3/K_2O molar ratio below 25/75, the $Nd(PO_3)_3$ phase crystallizes. When the Nd_2O_3/K_2O molar ratio is above 3/97, the increase of the viscosity of the solution hinders the crystallization. Although the viscosity of the solution depends on its composition, it is very high throughout the crystallization region.

Crystal growth is difficult in highly viscous solutions. The molecules inside it have a low mobility so they find it difficult to reach the crystal surface. The average time of homogenization therefore increases, and the average growth rate and crystal quality decrease.

In this paper, we qualitatively studied the relationship between the solution composition and the growth rate, which is directly influenced by the viscosity of the solution. When we increased the P_2O_5 concentration and kept the saturation temperature roughly constant, the viscosity of the solution went up. With this result, and taking into account the inverse relationship between viscosity and temperature, we chose a suitable zone of solution compositions in the crystallization region to initiate the crystal growth experiments and obtain high

(12) Kurtz, S. K.; Perry, T. T. *J. Appl. Phys.* **1968**, *39*, 3798.
(13) Dmitriev, V. G.; Gurzadyan, G. G.; Nikogosyan, D. N. *Handbook of Nonlinear Optical Materials*; Springer-Verlag: New York, 1991.
(14) Ni, X.-Y.; Hughes, J. M.; Mariano, A. N. *Am. Mineral.* **1995**, *80*, 21.
(15) Hong, H. Y.-P. *Acta Crystallogr.* **1974**, *B30*, 468.

quality KNP single crystals. The region that was apparently optimal for crystal growth is the one that has a low concentration of P_2O_5 and the highest saturation temperature and also a high concentration of Nd_2O_3.

Top Seeded Solution Growth (TSSG). The experiments in which we analyzed the three growth parameters aforementioned in order to obtain information about the crystal growth of KNP are summarized in Table 1.

The effect of the seed orientation on the crystal growth was analyzed using $Nd_2O_3-K_2O-P_2O_5$ = 10/30/60 as initial composition and a rotation velocity of 45 rpm (see experiments 1−3). We concluded that the *a** and *b* seed orientations were suitable for growing KNP single crystals. The crystal growth process (growth rate, quality) was similar using both of these orientations. On the other hand, the *c** orientation was unsuitable because when the crystal was heavy, the seed tended to break perpendicular to this direction, which led to a loss of crystal.

Four initial solution compositions were used in the study. Three of these, $Nd_2O_3-K_2O-P_2O_5$ = 10/30/60 (expts 1−4), 7/31/62 (expt 5), and 6/34/60 (expts 7−12), were in the previously described optimum concentrations region and had low concentrations of P_2O_5, but one, 4/31/65 (expt 6), was fairly displaced from it and had a high concentration of P_2O_5. For experiment 6, the high viscosity of the solution due to the high P_2O_5 concentration produced crystals that were too small and too light, despite the long cooling interval. The quality of the KNP single-crystal grown in this experiment was also too low. The growth processes with the other compositions (60 and 62 P_2O_5 mol %) were similar, but for the solution composition of 62 P_2O_5 mol % the growth rate was slightly lower and the average time of homogenization was slightly (about 2 or 3 h) longer.

The rotation velocity was also analyzed. Because the solution was very viscous, a high rotation velocity was needed. In fact, the quality of the crystals was best with the highest of the three rotation velocities we used (45, 60, and 75 rpm), and the growth rate increased slightly.

The quality of the single crystals grown was not sufficient, although it improved considerably when we used the final growth conditions (experiments 9 and 10) with the high rotation rate. We used the previously mentioned growth device. This increased the movement of the growth units inside the solution that had been hindered by its viscosity. The initial growth conditions used with the growth device are shown in Table 1 (experiments 11 and 12). The quality of the single crystals obtained was high. Figure 2a shows a KNP single-crystal grown using the conditions in experiment 11.

Crystal Morphology of $KNd(PO_3)_4$. To describe the morphology of the crystals, we observed KNP small single crystals by scanning electron microscopy (SEM) (Figure 1) and large single crystals using an optical microscope (Figure 2a). The habit was formed by the crystalline forms {001}, {100}, {011}, {0$\bar{1}$1}, {110}, {1$\bar{1}$0}, {10$\bar{1}$}, {101}, {1$\bar{1}$1}, and {111} (Figure 2b). Many of these faces are not equivalent by symmetry, but they are very similar, and it was difficult to identify them. Although KNP crystallizes in the monoclinic system, its β angle is close to 90°, and its cell parameters are quite similar. All these aspects made it difficult to identify the directions and faces of the single crystals by simple observation, so we used X-ray diffraction analysis in face indexation. It is very important to know the morphology of the crystal to be able to made its physical characterization.

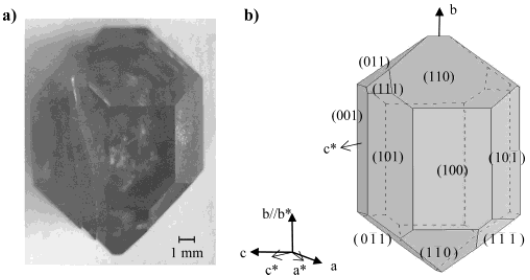

Figure 2. (a) KNP single crystal grown with a seed in the *a* direction. (b) Scheme of the crystal morphology where both direct (*a*, *b*, *c*) and reciprocal (*a**, *b**, *c**) lattices are indicated.

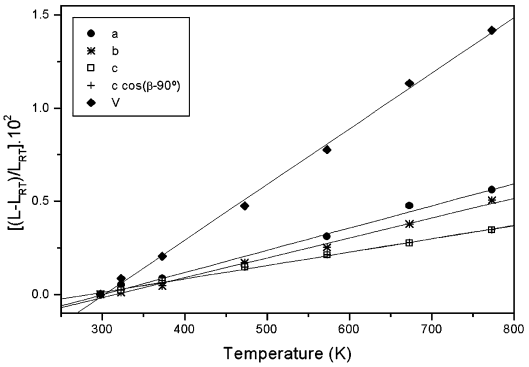

Figure 3. Relative thermal evolution of the cell parameters and unit cell volume of $KNd(PO_3)_4$.

Linear Thermal Expansion Tensor. As a monoclinic material, KNP shows crystallographic anisotropy in all its physical properties, such as its thermal expansion. When studying a laser material, it is very important to determine and locate the thermal ellipsoid because some of the pumping light power is converted into heat inside the crystal. In this paper, we have studied how the temperature affects the structure of the material.

We used X-ray powder diffraction in the 298−773 K temperature range to determine how the cell parameters evolved with temperature and then used the FULLPROFF program[16] and the Rietveld method[17] to refine the cell parameters previously obtained. The linear relationship between the average change in each cell parameter ($\Delta L/L$) and the temperature is shown in Figure 3. Cell parameters *a*, *b*, and *c* increased as the temperature increased, but the β angle remained roughly constant. The increase was greatest in the [100] direction and lowest in the [001] direction. Although this

(16) Rodríguez-Carvajal, J. *Short Reference guide of the computer program FULLPROF*; Laboratoire León Brillouin, CEA-CNRS: Saclay, France, 1998.

(17) Young, R. A. *The Rietveld Method*; Oxford Science Publication, International Union of Crystallography: New York, 1995.

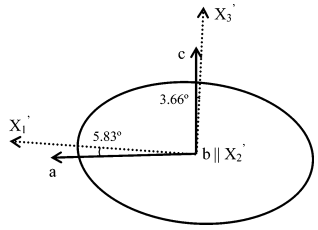

Figure 4. Thermal expansion ellipsoid for KNP in projection parallel to [010].

increase was low, KNP dilated slightly as the temperature increased. This is a good property for laser materials because they have to work at temperatures above room temperature.

The linear thermal expansion coefficients can be calculated from the slope of the linear relationship ($\Delta L/L$) and the temperature for each unit cell parameter. The linear thermal expansion tensor al room temperature in the crystallophysical system $X_1||a$, $X_2||b$, $X_3||c^*$ is

$$\alpha_{ij\ (\mathrm{KNP})} = \begin{pmatrix} 11.90 & 0 & 0.49 \\ 0 & 10.70 & 0 \\ 0.49 & 0 & 7.18 \end{pmatrix} \times 10^{-6}\,\mathrm{K}^{-1}$$

In the principal system, X_1', $X_2'||b$, X_3', the diagonalized linear thermal expansion tensor is

$$\alpha_{ij}'\ _{(\mathrm{KNP})} = \begin{pmatrix} 11.95 & 0 & 0 \\ 0 & 10.70 & 0 \\ 0 & 0 & 7.13 \end{pmatrix} \times 10^{-6}\,\mathrm{K}^{-1}$$

The principal axis with maximum thermal expansion, X_1', was found 5.83° clockwise from the *a* axis. The axis with a minimum thermal expansion, X_3', was found at 3.66° from the *c* axis. The thermal expansion ellipsoid in the principal axes is shown in Figure 4.

Phase Transitions. We used differential thermal analysis (DTA) and X-ray powder diffraction technique to study how the material evolved with temperature. The equipment used to do this analysis has already been described.

The stability of the KNP phase was analyzed between room temperature and 1273 K by differential thermal analysis and X-ray powder diffraction. The thermogram obtained in the 500−1250 K range is shown in Figure 5. An exothermic peak at 1165 K was observed. The change in weight during the experiment was not representative. We did a more detailed study using X-ray powder diffraction by heating and cooling the sample. At this temperature (1165 K), two new phases began to appear, but only one remained until room temperature. Figure 6 shows in the bottom the X-ray powder diffraction pattern of $KNd(PO_3)_4$ at room temperature and the selected patterns at different temperatures describing the evolution of $KNd(PO_3)_4$ with the temperature in both heating and cooling processes.

New peaks in the X-ray diffraction pattern recorded at 1173 K corresponded to these two phases. One was identified as $Nd(PO_3)_3$ (70-0967-JPDS database[18]), and the other was identified as $NdPO_4$ (83-0654-JPDS database[18]). Although both of these phases appeared at this temperature and almost at the same time they behaved differently. The intensity of the peaks for the $Nd(PO_3)_3$ phase decreased steadily between 1173 and 1273 K, until they disappeared completely. On the other hand, the intensity of the peaks for the $NdPO_4$ phase increased steadily in the same temperature range and then remained fairly constant until the last X-ray diffractogram at room temperature in the cooling process. DTA and X-ray powder diffraction analysis showed that, at 1165 K, KNP decomposed irreversibly within weight loss into two new crystalline phases, $Nd(PO_3)_3$ and $NdPO_4$. However, between this temperature and 1273 K, a completely crystalline transformation of $Nd(PO_3)_3$ into $NdPO_4$ occurred. The sample weight remained constant, so any amorphous phase was probably formed. X-ray powder diffraction analysis and DTA results suggested that the exothermic peak at 1165 K in the thermogram may be related to a decomposition of KNP in accordance with this reaction:

$$2KNd(PO_3)_4 \rightarrow Nd(PO_3)_3 + NdPO_4 + \text{amorphous phase}$$

Under the measurement conditions, we used the phase transition at 440 K, reported in the literature[1] as a monoclinic-to-orthorhombic transition, which was not observed. To analyze this, we carried out a DTA study at lower velocity from room temperature to 523 K by heating and cooling the sample. We observed no phase transition at this temperature either in the heating cycle or the cooling cycle, though there was a very small change in weight, either in the heating cycle and the cooling cycle. We also analyzed this temperature range by X-ray powder diffraction and by heating and cooling the sample in the same temperature range and at the same rates. Again, no phase transition was observed.

Second Harmonic Generation (SHG). The SHG efficiency (η) of KNP, calculated as described previously, was compared with the efficiency of KDP, which is widely used for nonlinear optical applications. The value of η/η_{KDP} we obtained was approximately one. The possibility that a self-frequency doubling laser may be developed increases the interest in this material.

Conclusions

We determined the crystallization region of KNP in the Nd_2O_3−K_2O−P_2O_5 system with the saturation temperature isotherms and some neighboring phases. We chose a suitable region of compositions to perform the crystal growth, which is placed in the zone poor in P_2O_5 and with high saturation temperatures, where the Nd_2O_3 concentration is high.

We successfully grew KNP single crystals by the top seeded solution growth slow cooling method (TSSG). Crystal growth was optimized to achieve suitable quality and size of the crystals for later studies to check the applications of this material as miniaturized laser and nonlinear optical device.

KNP growth process have been studied and some growth parameters optimized. We have concluded that

(18) JCPDS-ICDD, Joint Committee for Powder Diffraction Standards-International Center for Diffraction Data: Philadelphia, PA, 2000.

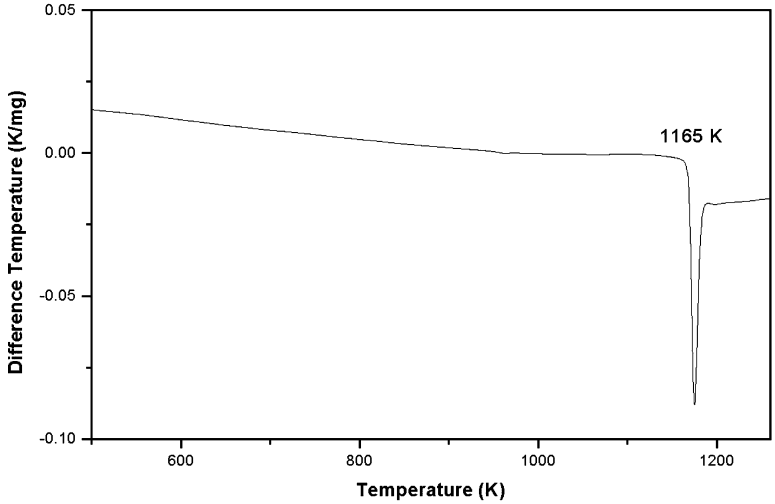

Figure 5. Differential thermal analysis (DTA) thermogram of $KNd(PO_3)_4$ in the 573−1273 K temperature range.

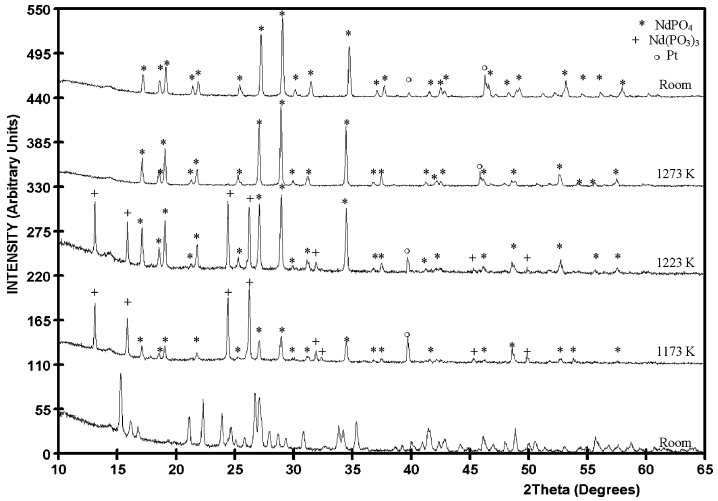

Figure 6. X-ray powder diffraction pattern of $KNd(PO_3)_4$ at room temperature and the selected patterns at different temperatures describing the evolution of $KNd(PO_3)_4$ with the temperature in both heating and cooling processes.

both *a** and *b* seed orientations are suitable for KNP growth by TSSG. For a *c** seed orientation, we have systematically lost the crystal. A low P_2O_5 concentration is suitable for the growth process, which agrees with the conclusion we previously drew from the study of the crystallization region. We have also verified that a high rotation velocity facilitates crystal growth. The growth device we have used improves the quality of the crystals considerably.

We have also studied how the material behaved as the temperature increased. Phase transitions of the material have been determined. KNP decomposes irreversibly at 1165 K, according to the reaction proposed, thus generating two new crystalline phases $NdPO_4$ and $Nd(PO_3)_3$. We have studied how the cell parameters evolved with the temperature and found that the material dilated slightly in any crystallographic direction.

Finally, since it may be used as nonlinear optical material, we measured the second harmonic efficiency of KNP, and this was similar to that of KDP.

Acknowledgment. The authors acknowledge financial support from DURSI 2001SGR317 and 2003FI00770 and CICyT MAT-02-04603-C05-03 and FIT070000-2002-461.

CM034812G

Paper V

Crystal growth, crystal morphology and surface micromorphology of type III $KGd(PO_3)_4$ and $KNd(PO_3)_4$

I. Parreu, R. Solé, J. Massons, F. Díaz, M. Aguiló

Crystal growth and design (in press)

Crystal Growth, Crystal Morphology and Surface Micromorphology of Type III $KGd(PO_3)_4$ and $KNd(PO_3)_4$

I. Parreu, R. Solé, J. Massons, F. Díaz, and M. Aguiló *

Física i Cristal·lografia de Materials (FiCMA), Universitat Rovira i Virgili, Campus Sescelades c/ Marcel·lí Domingo, s/n, E-43007-Tarragona, Spain.

* to whom correspondence should be addressed: magdalena.aguilo@urv.cat

Abstract. Type III $KGd(PO_3)_4$ and $KNd(PO_3)_4$ inclusion-free single crystals can be grown using the top seeded solution growth-slow cooling method (TSSG) without pulling in spite of the high viscosity of the solution, around 2 Dp. Poisoning by impurities in the crystals was minimized using the corresponding self-fluxes as solvent. We determined the main growth process that they follow by analyzing the typical micromorphologies that appeared on the surface of the as-grown faces. The crystal morphologies of KGP and KNP were identified using X-ray diffraction analysis. The external habit appeared more symmetrical than it structurally was because, although KGP and KNP are monoclinic with the space group $P2_1$, they have an almost cubic cell because their cell parameters are similars and the β angle is so close to 90º. We checked the chemical stability of KGP and KNP in basic and acid media. The distribution and geometry of structural defects were studied by analyzing the etch pits that appeared on the {100}, the {010} and the {001} forms. The crystals cleaved parallel to {010} and {001}, so the surface micromorphology of both forms was studied. We determined the orientation, the density and the height of the cleaved planes. We also characterized the local plastic deformation of KGP and KNP by measuring the microhardness on the {100}, {010}, and {001} forms using an indentation method.

Introduction

In the wide family of polyphosphates of potassium and lanthanide, called as $KLn(PO_3)_4$ (long-chain geometry) or $KLnP_4O_{12}$ (cycling geometry), the structural type III $KLn(PO_3)_4$ stands out for being non-centrosymmetrical. Type III structures are monoclinic and have $P2_1$ as space group and Z=2 [1,2]. This structural feature means that type III $KGd(PO_3)_4$ (KGP) can be regarded as a self-doubling host that, because of its doping facilities, can be used to obtain light throughout the UV-Vis region up to 180 nm, when the UV transparency edge of KGP appears. Similarly, the stoichiometric type III $KNd(PO_3)_4$ (KNP) can combine the 1μm infrared laser emission of neodymium with the second harmonic generation properties of the host to produce green laser radiation by self-frequency doubling. Both crystals, can be successfully grown as single crystals of few millimeters without inclusions [3,4]. Moreover, they are protected from deforming when working at high temperatures because of their almost isotropic thermal expansion. This almost isotropic behavior has been repeatedly observed in other properties, such as optical or mechanical properties.

KGP and KNP crystallize in the monoclinic system and have $P2_1$ as space group. The cell parameters for KGP are a=7.255(4) Å, b=8.356(5) Å, c=7.934(5) Å, β=91.68(5)º and Z=2 and those for KNP are a=7.2860(10) Å, b=8.4420(10), c=8.0340(10) Å, β=92.170(10)º and Z=2 [5]. Note that both structures are rather isometric because of the similarity between their cell parameters and the fact that the β angles are close to 90º. These structural parameters describe an almost isometric structure which could explain not only the almost isotropic properties observed but also the indistinguishable crystal morphology of the as-grown crystals by simply observation. In this paper, we describe how we initially determined the crystal morphology of type III $KLn(PO_3)_4$, Ln=Gd and Nd. Using X-ray diffraction analysis, we managed to index the faces that, by symmetry appeared equivalent but in fact were not. It is extremely important to know the morphology of any anisotropic material since all properties are highly dependent on the sample orientation. Crystals must therefore be well orientated when cutting and polishing.

We analyzed the surface morphology of as-grown KGP and KNP single crystals in order to determine their main growth mechanism at the optimized values of growth conditions such as solution composition, rotation velocity, cooling rate and seed orientation [3,4] at constant supersaturation (σ) and without the deliberate presence of impurities in the system.

The surface morphology of the (100), hand-made (010) and (001) etched faces was also analyzed to study the distribution and density of structural defects and to prove the chemical stability of crystals.

When cutting and polishing the type III KGP and KNP crystals, they cleave parallel to {001} and {010}. We analyzed therefore the surface morphology of both planes. To evaluate the local plastic deformation, we also measured the microhardness on the {100}, {010}, and {001} forms.

Experimental Section

Crystal growth. As type III KGP and KNP single crystals melt incongruently at 1142 and 1165 K, respectively, we used a high-temperature solution method to growth them. As solvent we used an excess of potassium and phosphorus oxides in order to avoid foreign ions in solution. The solubilities of KGP and KNP in this system were studied in a composition range within the crystallization region of the $P2_1$-phase-type III for each material [3,4]. Thus, the solubility curve of KGP was determined from 1.5 to 14 solute mol % and that of KNP was

determined from 4 to 20 mol %. Solutions were prepared by mixing the desired ratios of gadolinium or neodymium oxide, respectively, and potassium oxide, and phosphorus oxide, using K_2CO_3 and $NH_4H_2PO_4$ as initial regents. To determine the solubility curves, we decreased the temperature of the homogeneous solution by 25 K approximately every 30 minutes until small crystals appeared on a platinum wire immersed in the solution. The saturation temperature was then accurately determined by observing the growth or dissolution of these small crystals by applying a gradual increase or decrease of 5 K approximately every hour.

Small single crystals were grown on a platinum disk rotating at 60 rpm and in contact with the center of the solution surface. The axial temperature increased by about 12 K per millimeter when dipping from the surface to the bottom of the crucible, which was the coldest point of the volume. The cooling rate was 0.5-2 K/h, depending on the solution composition, and the temperature dropped to about 25 K below saturation temperature. The crystals obtained were analyzed by X-ray powder diffraction in order to ensure that the $P2_1$-phase crystallized.

To obtain inclusion-free KGP and KNP single crystals, we used the top-seeded solution growth (TSSG) - slow cooling method without pulling. The optimized solution composition used was Ln_2O_3:K_2O:P_2O_5=6:34:60, with Ln=Gd or Nd. Crystals were grown on parallelepipedic seeds kept on a seed holder rotating at 75 rpm and equipped with a turbine at the bottom. The seeds were orientated either parallel to the b-direction or normal to the faces (100) or (001), hence parallel to the a*- and c*-directions of the reciprocal lattice, which are placed around 2º from the a- and c-directions of the direct lattice (see figure 6). The cooling rate was 0.1 K/h and the temperature dropped to about 20 K below saturation temperature. Table 1 shows the optimal growth conditions and the results typically obtained when growing both KGP and KNP single crystals (see refs. 3 and 4 for further details).

X-ray Diffraction analysis. In order to identify and orientate the crystalline forms that comprised the morphological habit, we used the X-ray diffraction technique. Analyzes were made using a Siemens D5000 diffractometer (Bragg-Brentano parafocusing geometry, horizontal-2 goniometer with an open Eulerian cradle) fitted with an aperture slit close to the sample (70 mm long) and 0.03º receiving slit. Ni-filtered Cu Kα radiation (30 mA, 40 kV) and a scintillation counter as a detector were used. Intensity was measured with a point focus Cu tube**.** We measured the pole figures (200) or (002). The χ-angle was increased from 0 to 5º with a $\Delta\chi$ of 0.5º and the φ-angle was increased from 0 to 360º with a $\Delta\varphi$ of 3º and 3s of counting time. The pole figure (220) or (022) were measured in order to determine the orientation of the b direction by comparing the theoretical and experimental values of angles between (200) and (220) or between (002) and (022), respectively. Whereas the theoretical value of the angle between (200) and (220) was 40.78º, the theoretical angle between (002) and (022) was 43.56 º. Therefore, the χ-angle was ranged from 30 to 50º for (220) pole figures and from 35 to 55º for (022) pole figures. The other conditions were kept constant. $\Delta\chi$ was 2º and the φ-angle was increased between 0 and 360º with a $\Delta\varphi$ of 3º and 3s of counting time. To confirm each peak observed on the pole figure, with measured χ and φ-angles, a 2θ-scan was recorded from 10º to 50º with a step size of 0.5º and a step time of 3s.

Surface micromorphology analysis. Surface morphology studies were performed using microscopic techniques such as confocal microscopy, scanning electron microscopy (SEM) and atomic force microscopy (AFM).

The as-grown faces of both KGP and KNP single crystals grown on a platinum disk were systematically analyzed using a confocal Sensofar PLμ 2300 microscope under blue light of λ=470 nm in ambient atmosphere. The surface forms identified were more accurately studied

using a scanning electron microscope (SEM) Jeol JSM 6400. The etched faces and indented planes were analyzed by scanning electron microscopy (SEM). We studied the {010} and {001} cleavage forms using the same techniques as above and an atomic force microscope (AFM) Molecular Imaging Pico Plus 2500. The AFM images were recorded in ambient atmosphere at room temperature in the tapping mode. Freshly cleavage internal planes were obtained from well oriented small crystals that were deliberately broken parallel either to {010} or {001} by smartly tapping with a scalpel placed parallel to these planes and along the [100] direction.

Chemical Stability. To check the stability of KGP and KNP against an etchant, a piece of crystal of every material was kept submerged in solution for different periods of time, from 1 minute to 100 hours, at room temperature. Bulk single crystals were cut to prepare samples that contained the (100), (010) and (001) faces in their morphological habit. The (010) face was hand-made by cutting the upper edge of the crystals and taking the edge of meeting of the (100) and (101) faces, thus the [010] direction, as reference. We used a 0.5 M solution of NH_3 (30%) (pH≈11) as basic medium. As acid media we used a 0.012 M solution of HCl (35%) (pH≈2) and a mixture of H_2SO_4 (96%) and HF (40%) at a volume ratio of 75:25 (pH≈1).
The weight of the samples was periodically controlled. Initially, we weight the etching container, which comprised the sample and enough etchant volume to totally cover the sample. The container was carefully closed to avoid etchant evaporation in order to use this initial weight as reference. The crystal faces were also periodically observed using an optical microscope to localize possible etch pits. Once observed, these etch pits were more accurately analyzed by scanning electron microscopy (Jeol JSM 6400).

Microhardness. We measured Vickers microhardness [6,7] in order to evaluate the local plastic deformation of each material. Measurements were taken on the {100}, {010}, and {001} forms to evaluate the microhardness anisotropy. About 1 mm thickness-platelets cut parallel to these planes were used.
The Vickers method is based on a static indentation made by pressing down a standard-sized square-based pyramid [8]. Microhardness can be obtained by applying the expression: $H_v = 1.8544 \cdot g \cdot P/d^2$, where P is the standard load (N) and d is the diagonal of the pyramidal impression (mm) obtained after the load is removed. We applied standard strengths of 1, 0.5, 0.3, and 0.1 N and kept the dwell time constant at 2 s. For each load, several indentations were made and the average diagonal imprints were used in the calculations. To measure the diagonal imprints of the indentation, we used a Jeol JSM 6400 scanning electron microscope (SEM).

Results and discussion

Crystal Growth. The solubility curves of KGP and KNP are shown in Figure 1. From previous investigations [3,4,5], we knew that the crystallization region of KNP is wider than that of KGP. We therefore determined solubility curves between 4 and 20 solute % and between 1.5 and 14 solute %, respectively. The solubility curves are almost parallel in the 8-12 mol % solute/92-88 mol % solvent solution composition range, which corresponds to the optimal zone in the $P2_1$ crystallization region for growing single crystals [3,4]. The change of the lanthanide constitutional element in the structure caused a slight decrease in saturation temperature. KGP is therefore more soluble than KNP in its own flux. In both cases, the saturation temperature sharply rose as the solute concentration in solution increased.

We successfully obtained inclusion-free KGP and KNP single crystals using the top-seeded solution growth method in spite of the high viscosity of this kind of flux, which has been measured with a coaxial viscosimeter to be around 2 Dp. This not only decreased the growth rate and prolonged the growth process but also affected the quality of the crystals. However, we minimized this effect by improving several growth parameters and managed to grow suitably sized inclusion-free crystals that were protected from poisoning by impurities. One of these growth parameters was the solution composition. We found a composition point (Table 1), around the center of the $P2_1$-phase crystallization region, where both crystal phase stability and viscosity were suitable. To improve the solution stirring and hydrodynamics, we designed and developed an accentric growth device equipped with a platinum turbine submerged in the solution. The seed holder was placed around 1.5 cm away from the rotation axis and the platinum turbine around 2 cm under the holder (figure 2). We used a high rotation rate, 75 rpm, not only to improve the homogenization of the volume by the rotation turbine but also to minimize the boundary layer of growth and to improve the mass transfer. Although the solubility of KGP was higher than the solubility of KNP, its viscosity was a little higher. This was observed qualitatively in the growth experiments but it also agreed with the fact that KNP had a higher growth rate (Table 1).

We successfully grew KGP and KNP single crystals along the directions *a**, *b*, and *c**. However, as we mentioned earlier, these crystals are usually grown only from *a** or *b*-oriented seeds so as not to risk losing the crystal when using *c**-oriented seeds. This problem was repeatedly observed with KNP but not with KGP. In fact, not only were KGP crystals of the same size grown with *c**-oriented seeds but also they present the highest growth rate (experiment 3). *c**-oriented KNP seeds were not able to resist such a high crystal weight (experiment 6). Although there is another cleavage plane perpendicular to the *b* crystallographic direction, KGP or KNP crystals were never lost when growing along this direction.

Surface Micromorphology of the As-grown Faces. The surface structures commonly observed on the as-grown faces of both KGP and KNP crystals generally consisted of highly polygonized macrohillocks made up of growth macrolayers. Figures 3a and 3b show SEM images of small KGP single crystals with this kind of structures on the (101) face and either the (100) or (001) face, respectively. As already mentioned, in SEM images, it was impossible to distinguish between the (100) and (001) faces because of the almost isometric structure of KGP. The macrohillocks usually reflected the morphology of the face because the edges of the growth layers become straight to the edges of the crystal. Figure 4 shows an optical microscope image of a highly polygonized macrohillock on a (100) face of a small KGP single crystal grown on a platinum disk. The growth layers repeated the common shape of a (100) plate (figure 4c) formed by the lower-index faces, $(00\bar{1})$ and $(0\bar{1}\bar{1})$ and the angle between them. These macrohillocks are probably formed as a result of unstable growth conditions similar to those responsible for hopper morphology, when both the stability of the surfaces and the instability of the edges participate [9]. The growth lawyers seemed to stars fro the edges of the faces. Their thickness decreased from the edges, where it was about280 nm, 400 times the unit height (a=7.255 Å), to the central region of the faces, where it was about 70 nm, 100 times the unit height. The large depression on the central part of the growing face agreed with this growth mechanism. A topographical analysis on this zone revealed that the central part was about 10 μm deeper than the edges of the faces (figure 4c). Figure 5 shows a large number of isolated macrohillocks on a KNP (001) internal plane that are probably associated with growth dislocations. These were slightly more rounded than those observed on the external faces but they were sparse on the growth layers and rather orientated parallel to them. In fact,

the most of them grew on the kink sites provided by the edges of the macrolayers. Profiles in figure 5 shows that the thickness of the growth layers (left) coincided with that of the macrohillocks (right). It was about 300 nm, which is 375 times the unit height (c=8.0340 Å). The growth layers and the distribution of macrohillocks on them were always orientated parallel to [100]. The isolated macrohillocks were probably formed because the mean interdiffusion distance was smaller than the mean distance between the kinks on this face, according to the interpretation based on the ratio between these two distances [9].

Crystal Morphology. In the first steps of KGP and KNP crystal growth, when the seed orientation could still not be controlled, X-ray diffraction analyses were needed to correctly determine the morphology of the crystals grown, which seemed to be more symmetrical than they really were because of the unique 2-fold axis along the *b* direction.

Taking into account only the crystal cell parameters and the space group, we calculated a theoretical morphological scheme for type III crystals, according to the Donnay-Harker law [10]. Table 2 lists the crystalline forms {hkl}, equivalent faces and corresponding d_{hkl} values for both KGP and KNP. The morphological scheme drawn using the Software Shape utility [11], and the corresponding stereographic projections are shown in Figure 6 in projection parallel to *b* and *c** (normal to the (001) face). The last one is very similar to that parallel to *a** (parallel to the (100) face) (see ref. 3 or 4). The only difference between them are the {111} and $\{\bar{1}\bar{1}1\}$ forms. These faces can therefore be used to distinguish between (100) and (001). However, in the experimental scheme, which does not differ so much from the theoretical, these faces seldom appeared (see ref. 3 and 4). Crystals grown with *a**- or *c**-oriented seeds were therefore not only comparable but they could be easily mistaken.

It was therefore necessary to use X-ray diffraction analysis to discriminate between the (100) and the (001) faces. We measured the (200) and (002) pole figures in a region close to the face perpendicularity. A pole figure (220) or (022), depending on the result of the previous one, was then recorded in order to confirm the *b* orientation by comparing the theoretical and experimental values of the angle between these faces, (200) and (220) or (002) and (022), respectively. Selected three-dimensional (002) and bi-dimensional projection of (022) pole figure and the corresponding 2θ-scans at χ and φ angles fixed by them are show in figure 7. Whereas the theoretical angle between (002) and (022) is 43.56º, the χ angle values obtained were 45.91º and 41.57º. The narrow (002) peak close to a nil χ also revealed the good orientation but also the high crystallinity of the samples.

The next face most likely to appear in the crystalline habit of KGP is (020), according to the Donnay-Harker law [10] (table 2). This face is hardly observed in single crystals grown by top seeded solution growth and is more usual in small crystals grown without seeds. Figure 8 shows a SEM photograph of a KGP small crystal with (figure 8a) and without (figure 8b) the (020) face appearing in the crystalline habit. This face has never observed in the KNP morphology. Probably, the appearance of the (020) face on KGP crystals depended on some crystal growth parameters that are not controlled by us up to date.

Another morphological aspect due to the β angle being close to 90º was the need to distinguish by simply observation between the positive and the negative sense of the *b* direction. This orientation is basic to correctly cutting and polishing monoclinic materials. It is essential to ensure the positive sense of *b* when measuring the ellipsoid that will represent properties such as optical [5] or thermal [3,4]. As a preliminary analysis, we cut a small slice perpendicular to this direction, so one side should be (010) and the other should be $(0\bar{1}0)$. By observing the octagonal contour of the *b*-oriented slice, we were able to distinguish between the positive and negative senses of *b* by analyzing the small turning relation between the direct lattice, *a* or *c* directions, and the reciprocal lattice, *a** or *c** directions (figure 6a). We used an optical

microscope and a milimetrical pattern under the sample as reference. Finally, to verify the positive sense given by observation, we orientated the optical frame with respect to the crystallographic one, as explained in reference 5, using the corresponding optical tensor as reference.

Chemical Stability and Surface Micromorphology of the Etched Surfaces. Both KGP and KNP are nonhygroscopic and highly stable for a long time in normal room conditions. The crystals were also stable in acid (pH≈2) or basic (pH≈11) media since neither weight loss nor surface etch pits were observed even after roughly 100 hours. When the acidity of the medium was increased to pH≈1, etch pits were observed after around 20 hours, when the sample had lost around 0.5% of its initial weight. Figure 8 shows a selection of the rhombohedral, hexagonal, rectangular, and triangular etch pits observed on KGP or KNP samples. These etch pits appeared always well orientated on the faces and their contour walls corresponded to families of low-index planes [12]. Visualizing the crystal morphology of the sample, we could orientate them. Probably, the crystal structure mainly dominated the dissolution process since this type of figures is more controlled by surface-reaction kinetics than by diffusion [13]. As well as these large and deep etch pits, rows of smoother etch pits, which had a more spherical outline (figures 8a, 8b, 8c), appeared in most faces. These rows seemed not to be dominated by the structure since they were distributed along different directions on the surface.

Surface Morphology of Cleavage Planes. As we stated above, KGP and KNP exhibited cleavage along the {010} and {001}. In order to explain the cleavage behavior of KGP and KNP, we analyzed their crystal framework. The most important feature of type III KLnP materials is the long-chain arrangement of the phosphate units PO_4. In both KGP and KNP these long chains run along [100] [5]. They are joined along the other two directions, [010] and [001], through gadolinium or neodymium and potassium ions by sharing oxygen atoms. The frame was formed by intrachain P-O bonds and interchain Gd-O or Nd-O and K-O bonds. Of these bonds, the P-O bonds were the strongest and the K-O bonds were the weakest, according to their covalent character. When we analyzed their bond distance we observed that d(P-O)<d(Nd-O)<d(K-O) [5]. As the P-O bonds generating the long chains ran along [100], we can say that this is the strongest direction of bonds. [010] and [001] are weaker and similar to each other. Therefore, the crystal framework agreed with the cleavage behavior. Not only because of the strength of bonds but also in a more geometrical sense, since cleavage occurred between chains that were on any of the cleavage planes.
On both cleavage planes, {010} and {001}, usually appeared steps of height about the unit height, i. e. monolayer steps, placed between much more thicker steps of heights up to 800 μm, one thousand times the unit height, b= 8.4420 Å and c=8.0340 Å. Both mono and multilayer steps were straight and always parallel to [100]. Most of the monolayer steps were of elementary height, b= 8.4420 Å and c=8.0340 Å, but there were also steps of a height of up to roughly 5 times this height (5b or 5c). The density of these steps was quite regular but higher on {010}. Figure 9 shows 800 mm thick multilayer steps on {010} and 80 nm thick monolayer steps on {001} both oriented parallel to [100].

Microhardness. The measured Vickers microhardness on the {100}, {010}, and {001} planes of KGP and KNP were: H_v=668, 586, 648 HVN and H_v=705, 633, 702 HVN, respectively. These microhardness values were calculated with a reference load of 0.1 N since the impressions on the {010} plane were accompanied by radial cracks emanating from one of both corners when the load exceeded from 0.3N. These cracks were placed along [100], thus probably caused by {001} cleavage planes. As in other properties previously analyzed,

microhardness showed a low anisotropy because of the almost isometric structure of type III crystals. An average microhardness can be defined around 634 and 680 HVN for KGP and KNP, respectively. These values would correspond to about 7 on Moh's scale. So, type III KGP and KNP are as hard as quartz.

Conclusions. Although the viscosity of the solution is really high, type III $KGd(PO_3)_4$ and $KNd(PO_3)_4$ inclusion-free single crystals can be grown using the top seeded solution growth (TSSG) - slow cooling method without pulling. Poisoning by the impurities can be minimized using the corresponding self-fluxes, Ln_2O_3:K_2O:P_2O_5, with Ln=Gd, Nd, as solvent because the working temperature, i.e. the homogenization and growth temperature, was not very high. Though the solubility of KGP was higher than that of KNP, the growth rate of KGP crystals was lower than that of KNP probably because the KGP solutions were more viscous than those of KNP. The micromorphologies that appeared on the surface of the as-grown faces of KGP and KNP crystals revealed typical hopper morphology probably related to unstable growth. We described in this paper the method that we used to determine the isometric morphology of these crystals, which is indistinguishable by direct observation. Both materials proved to be very stable against basic and acid media. The etch pits observed on the {100}, {010} and {001} planes described polygonal outlines that reflected the symmetry of the face. On the {010} and {001} cleavage planes, we found monolayer steps of height about the unit height among much thicker steps. Both were straight and always parallel to [100]. KGP and KNP show hardness similar to that of quartz.

Acknowledgements. The authors acknowledge financial support from the Fons Social Europeu i del Departament d'Universitats, Recerca i Societat de la Informació de la Generalitat de Catalunya under Project 2005SGR658 and personal support 2006FIC00469 and from MEC (Ministerio de Educación y Ciencia of the Spanish government) under Projects MAT-05-06354-C03-02, MAT-04-20471-E and CIT-020400-2005-14.

Table 1. Crystal growth data associated with KGP and KNP crystals

A	B	C	D	E	F	G	H	I	J
KGP	a*	1034	20	18.4	5.9x15.6x10.3	1.77	8.85	colourless	good
KGP	b	1038	20	19.4	8.6x4.8x9.7	1.63	8.15	colourless	good
KGP	c*	1031	20	18.0	11.0x16.2x5.6	1.94	9.70	colourless	good
KNP	a*	1048	17	15.7	7.8x14.9x9.5	1.84	10.82	purple	very good
KNP	b	1045	17	15.0	16.0x6.2x12.7	1.98	11.65	purple	very good
KNP	c*	1046	14	12.7	8.7x12.3x7.1	1.76	12.57	purple	few inclusions

A: single crystal, B: seed crystallographic orientation, C: saturation temperature (K), D: cooling interval (K), E: average supersaturation (%σ), F: crystal dimensions in a, b, and c crystallographic directions, respectively (mm), G: crystal weight (g), H: growth rate x 10^3 (g/h), I: colour, J: crystal quality.

Table 2. {*hkl*}crystalline forms observed in KGP and KNP crystals and corresponding d_{hkl}, ordered in decreasing sense

hkl	KGP d_{hkl} (Å)	KNP d_{hkl} (Å)
{(001)(00$\bar{1}$)}	7.9306	8.0344
{(100)($\bar{1}$00)}	7.2519	7.2863
{(011)(01$\bar{1}$)}	5.7523	5.8122
{(0$\bar{1}$1)(0$\bar{1}\bar{1}$)}	5.7523	5.8122
{(110)($\bar{1}$10)}	5.4769	5.5163
{(1$\bar{1}$0)($\bar{1}\bar{1}$0)}	5.4769	5.5163
{(10$\bar{1}$)($\bar{1}$01)}	5.4316	5.4821
{(101)($\bar{1}$0$\bar{1}$)}	5.2753	5.2998
{(1$\bar{1}\bar{1}$)($\bar{1}\bar{1}$1)}	4.5541	4.5986
{(11$\bar{1}$)($\bar{1}$11)}	4.5541	4.5986
{(111)($\bar{1}$1$\bar{1}$)}	4.4607	4.4894
{(1$\bar{1}$1)($\bar{1}\bar{1}\bar{1}$)}	4.4607	4.4894
{(020)}	4.1780	4.221

Figure 1. Solubility curves of KGP and KNP.
Figure 2. Scheme of the accentric crystal growth device used in growth experiments.
Figure 3. SEM images of hopper morphology on faces (a) (101) and (b) (100) or (001) of KGP small crystals.
Figure 4. High polygonized macrohillock on the (100) face of a KGP small single crystal. (a) optical microscope image, (b) common morphological habit of a (100) plate, (c) three-dimensional topographic image with the profile of the hollow core.
Figure 5. Confocal image of growth layers and macrohillocks on an internal (001) plane of KNP with the corresponding profiles.
Figure 6. Morphological scheme and corresponding stereographic projections of KGP and KNP crystals in projection parallel (a) to *b* and (b) to *c**. Direct (a, b, c) and reciprocal (a*, b*, c*) lattices are indicated.
Figure 7. Selected (a) three-dimensional (002) pole figure and (b) bi-dimensional projection of (022) pole figure. Corresponding 2θ-scan at fixed χ and φ angles of (c) (002) and (d) (022).
Figure 8. Selected SEM images of etch figures observed on KGP or KNP faces. (a) rombohedral etch pits on (100), (b) hexagonal etch pits on (010), (c) rectangular etch pits on (010), and (d) triangular etch pits on (001).
Figure 9. Confocal images of the multilayer steps observed on {010} planes and AFM image of monolayer steps on {001} planes.

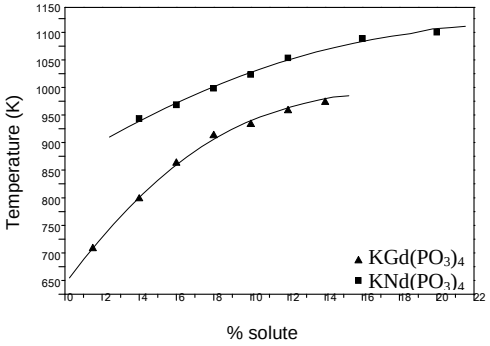

Figure 1.

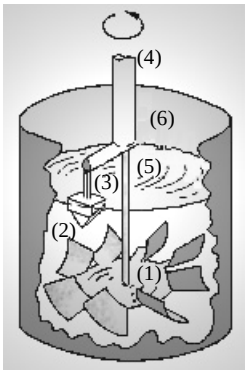

(1) Platinum turbine
(2) KLnP grown crystal
(3) KLnP seed
(4) Alumina rod
(5) Self-flux
(6) Platinum crucible

Figure 2.

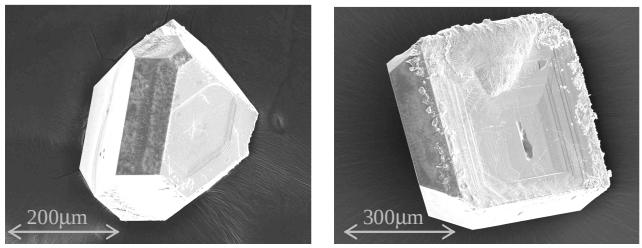

(a) (b)

Figure 3.

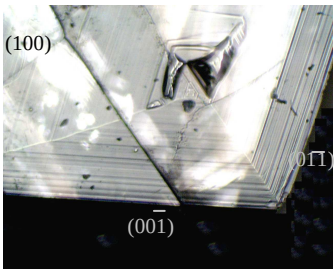
(100)
(011)
(00$\bar{1}$)

(a)

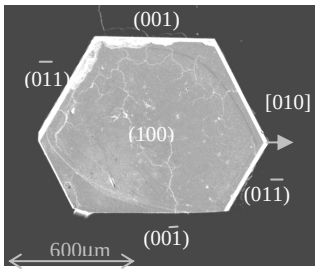
(001)
(011)
[010]
(100)
(011)
(00$\bar{1}$)
600μm

(b)

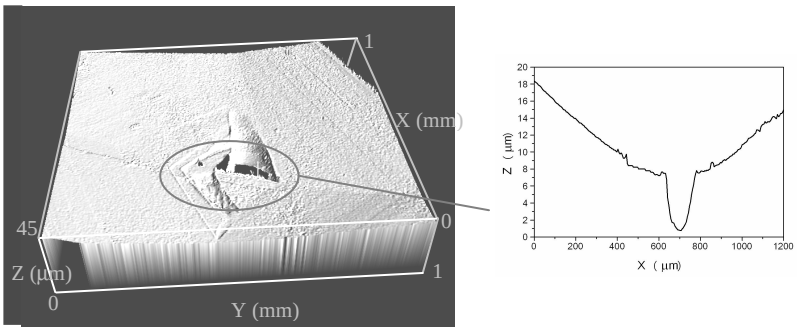
1
X (mm)
0
45
Z (μm)
0
1
Y (mm)
Z (μm)
X (μm)

(c)

Figure 4.

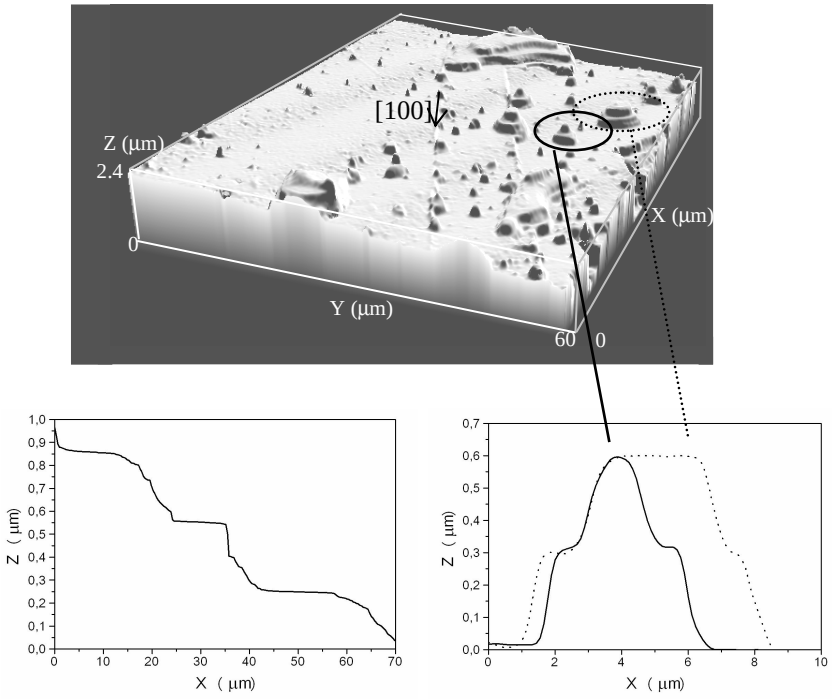

Figure 5.

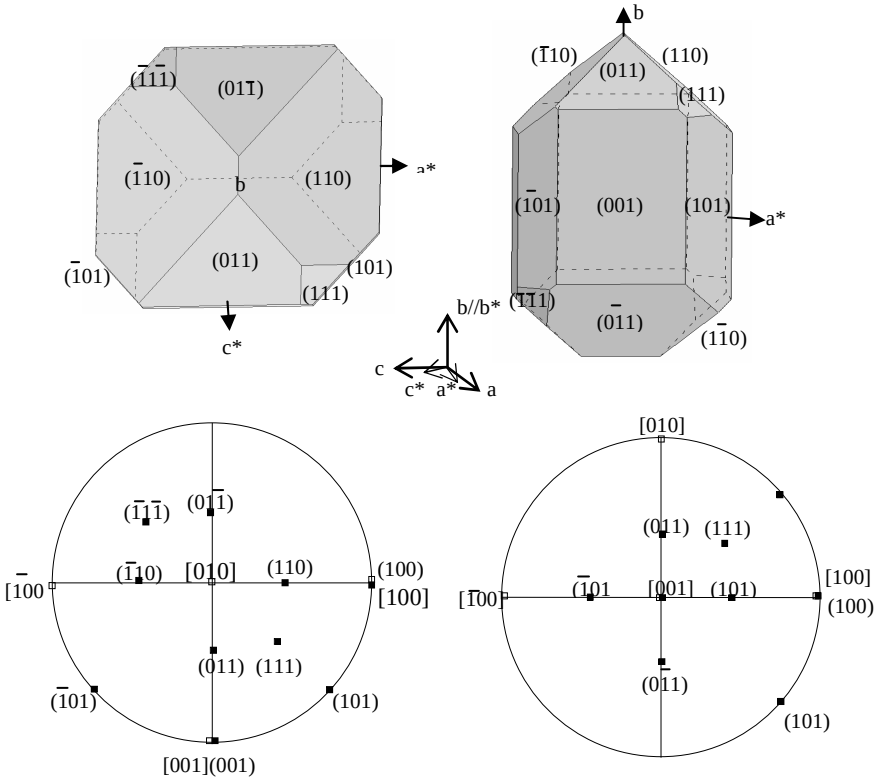
(01$\bar{1}$)
(110)
b
(011)
(101)
(111)
c*
a*
b
(001)
b//b*
c
c*
a*
a
(100)
[100]
[001](001)
[010]
(011)
(111)
(101)
[001]

(a) (b)

Figure 6.

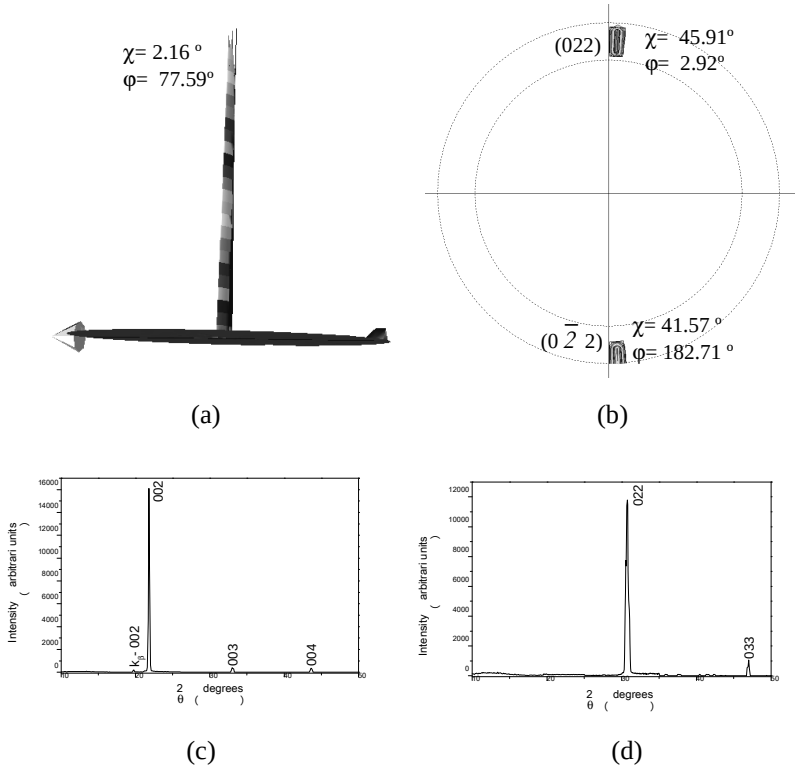
χ= 2.16 º
φ= 77.59º
(022)
χ= 45.91º
φ= 2.92º
(0 $\bar{2}$ 2)
χ= 41.57 º
φ= 182.71 º
(a)
(b)
Intensity (arbitrari units)
002
K_β 002
003
004
2 θ (degrees)
(c)
Intensity (arbitrari units)
022
033
2 θ (degrees)
(d)

Figure 7.

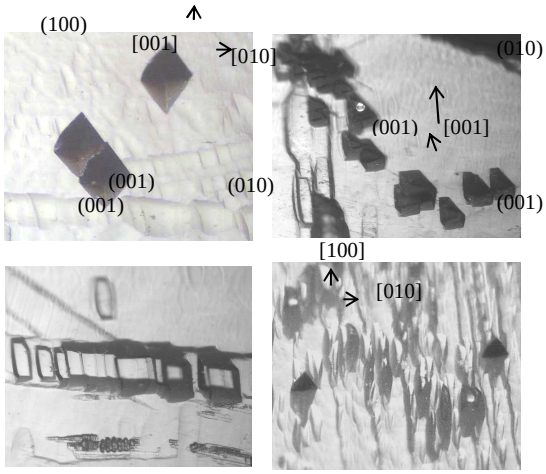

Figure 8.

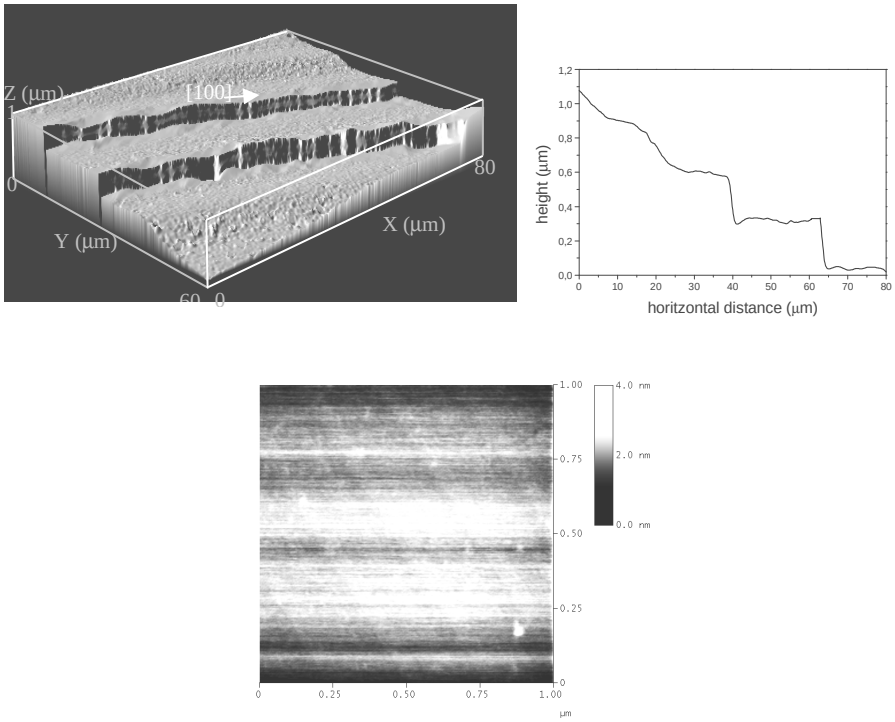
Z (µm)
[100]
0
80
Y (µm)
X (µm)
60 0
height (µm)
horitzontal distance (µm)
4.0 nm
2.0 nm
0.0 nm
µm

Figure 9.

References

(1) Palkina, K.K.; Chudinova, N.N.; Litvin, B.N.; Vinogradova, N. V. *Izv. Akad. Nauk SSSR, Neorg. Mater.* **1981**, *17(8)*, 1501.
(2) Durif, A.; *Crystal Chemistry of Condensed Phosphates*; Plenum Press: New York, 1995.
(3) Parreu, I.; Solé, R.; Gavaldà, Jna.; Massons, J.; Díaz, F.; Aguiló, M. *Chem. Mater*. **2005**, *17*, 822.
(4) Parreu, I.; Solé, R.; Gavaldà, Jna.; Massons, J.; Díaz, F.; Aguiló, M. *Chem. Mater*. **2003**, *15*, 5059.
(5) Parreu. I.; Carvajal, J .J.; Solans, X.; Diaz, F.; Aguiló, M. *Chem. Mater*. **2006**, *18*, 221.
(6) Mott, B.W. *Micro-indentation Hardness Testing*; Butterworths: London, 1956**.**
(7) Quinn, G. D.; Patel, P. J.; Lloyd, I. Res. *Natl. Inst. Stand. Technol.* **2002**, *107*, 299.
(8) Vandert Voort, G. F. *Factors that affect the Precision of Mechanical Tests*; ASTM: Philadelphia, 1989.
(9) Sangwal, K.; Rodriguez-Clemente, R. *Surface Morphology of Crystalline Solids;* Trans Tech: Brookfield, 1991.
(10) Hartman, P. *Acta Crystallographica* **1958**, *11*,459.
(11) Dowty, E. *Shape for Windows*, version 5.0.1.; **1995**.
(12) Hartman, P. *Crystal Growth - an Introduction;* North-Holland: Amsterdam, **1973**.
(13) Sangwal, K. *Etching of Crystals, Theory, Experiment and Application*; North-Holland: Amsterdam, **1987**.

Paper VI

Growth, spectroscopy and laser operation of Yb:$KGd(PO_3)_4$ single crystals

I. Parreu, M. C. Pujol, F. Díaz, M. Aguiló, X. Mateos, V. Petrov

Optics Express (in press)

Growth, spectroscopy and laser operation of Yb:$KGd(PO_3)_4$ single crystals

I. Parreu, M. C. Pujol, M. Aguiló, and F. Díaz

Física i Cristal·lografia de Materials (FiCMA), Universitat Rovira i Virgili.
c/ Marcel·lí Domingo, s/n. E-43007 Tarragona, Spain.
f.diaz@urv.cat

X. Mateos and V. Petrov

Max-Born-Institute for Nonlinear Optics and Ultrafast Spectroscopy, 2A Max-Born Str., D-12489 Berlin, Germany.

Abstract: Macrodefect-free single crystals of Yb-doped $KGd(PO_3)_4$, a noncentrosymmetric laser host which possesses second-order nonlinear susceptibility, were grown using the top seeded solution growth slow-cooling (TSSG-SC) technique, reaching a maximum ytterbium concentration in the crystal of $\approx 3.2\times10^{20}$ at/cm^3. In order to evaluate the potential for self-frequency doubling, the dispersion of the refractive indices of $KGd(PO_3)_4$ was studied and Sellmeier equations were constructed which are valid in the visible and near-infrared. The Stark splitting of the two electronic states of ytterbium was determined from absorption and emission measurements at room and low temperatures, and this allowed to compute the emission cross sections at room temperature. The fluorescence decay time is quite long, 1.22±0.01 ms. Laser generation in the 1 μm range is demonstrated with this new Yb host for the first time. Although the maximum output power achieved, of the order of 100 mW, was limited by the available crystal size and doping level, the more than 55% slope efficiency obtained with this first sample is rather promising for the future.

OCIS codes: (140.3580) Lasers, solid-state; (140.5680) Rare earth and transition metal solid-state lasers; (160.5690) Rare earth doped materials; (190.4400) Nonlinear optics, materials

References and links

1. A. Brenier, "The self-doubling and summing lasers: overview and modeling," J. Lumin. **91**, 121 (2000).
2. A. Aron, G. Aka, B. Viana, A. Kahn-Harari, D. Vivien, F. Druon, F. Balembois, P. Georges, A. Brun, N. Lenain, and M. Jaquet, "Spectroscopic properties and laser performances of Yb:YCOB and potential of the Yb:LaCOB material," Opt. Mater. **16**, 181 (2001).
3. H. Zhang, X. Meng, P. Wang, L. Zhu, X. S. Liu, X. M. Liu, Y. Yang, R. Wang, J. Dawes, J. A. Pipper, S. Zhang, and L. Sun, "Growth of Yb-doped $Ca_4GdO(BO_3)_3$ crystals and their spectra and laser properties," J. Cryst. Growth **222**, 209 (2001).
4. P. Dekker, P. A. Burns, J. M. Dawes, and J. A. Piper, "Widely tunable yellow-green lasers based on the self-frequency-doubling material Yb:YAB," J. Opt. Soc. Am. B **20**, 706 (2003).
5. Z. Zhu, J. Li, B. Alain, G. Jia, Z. You, X. Lu, B. Wu and C. Tu, "Growth, spectroscopic and laser properties of Yb^{3+}-doped $GdAl_3(BO_3)_4$ crystal: a candidate for infrared laser crystal," Appl. Phys. B **86**, 71 (2007).
6. L.E. Bausá, M. O. Ramírez, and E. Montoya, "Optical performance of Yb^{3+} in $LiNbO_3$ laser crystal," Phys. Status Solidi (a) **201**, 289 (2004).
7. I. Parreu, J. J. Carvajal, X. Solans, F. Díaz, and M. Aguiló, "Crystal structure and optical characterization of pure and Nd-substituted type III $KGd(PO_3)_4$," Chem. Mater. **18**, 221 (2006).
8. I. Parreu, R. Solé, Jna. Gavaldà, J. Massons, F. Díaz, and M. Aguiló, "Crystal growth, structural characterization, and linear thermal evolution of $KGd(PO_3)_4$," Chem. Mater. **17,** 822 (2005).
9. I. Parreu, R. Sole, J. Massons, F. Díaz, and M. Aguiló, "Crystal Growth and Characterization of type III ytterbium-doped $KGd(PO_3)_4$: a new non-linear laser host" (submitted to Chem. Mater).
10. H. Ettis, H. Naïli, and T. Mhiri, "Synthesis and crystal structure of a new potassium-gadolinium cyclotetraphosphate, $KGdP_4O_{12}$," Cryst. Growth and Design. **3**, 599 (2003).

11. R. Solé, V. Nikolov, A. Vilalta, J. J. Carvajal, J. Massons, Jna. Gavaldà, M. Aguiló, and F. Díaz, "Growth of $KTiOPO_4$ films on $KTi_{1-x}Ge_xOPO_4$ substrates by liquid-phase epitaxy," J. Mater. Res. **17**, 563 (2002).
12. M. Born and E. Wolf, in *Principles of Optics: Electromagnetic Theory of Propagation, Interference and Diffraction of Light*, 6th.ed. (Pergamon, Oxford 1993).
13. P. Tzankov and V. Petrov, "Effective second-order nonlinearity in acentric optical crystals with low symmetry," Appl. Opt. **44**, 6971 (2005).
14. F. D. Patel, E. C. Honea, J. Speth, S.A. Payne, R. Hutcheson, and R. Equall, "Laser demonstration of $Yb_3Al_5O_{12}$ (YbAG) and materials properties of highly doped Yb:YAG," IEEE J. Quantum Electron. **37**, 135 (2001).

1. Introduction

Solid-state laser sources in the visible play an important role in laser technology because they are potentially interesting for numerous applications like high-density optical data storage or laser displays. Bifunctional crystals, in which the laser effect and a nonlinear optical process, e.g. frequency doubling, occur simultaneously, are very promising for such compact laser designs because diode-pumped solid-state lasers operate mainly in the infrared. So far the noncentrosymmetric hosts used for this purpose were doped mainly with neodymium [1]. More recently highly efficient laser operation in several crystals exhibiting second order nonlinearity, doped with ytterbium, was also reported. These include $YCa_4O(BO_3)_3$ (YCOB) [2], $GdCa_4O(BO_3)_3$ (GdCOB) [3], $YAl_3(BO_3)_4$ (YAB) [4], $GdAl_3(BO_3)_4$ (GAB) [5], and $LiNbO_3$ (LNB) [6]. The ytterbium ion is an interesting alternative to neodymium in the same wavelength range near 1 µm while the second harmonic is also in the green region. This is due to several important advantages. The ytterbium ion possesses higher energy-storage capability because the radiative lifetime of the upper laser manifold is substantially longer. Its simple two-manifold electronic structure excludes a number of competitive processes such as excited-state absorption, upconversion, and cross relaxation which can depopulate the upper laser level and hence reduce the laser efficiency. The small Stokes shift between absorption and emission, i.e. the small quantum defect, reduces the thermal load and facilitates efficient operation at high powers. The development of new Yb-doped laser materials is motivated by the significant advance in diode laser pumps; such lasers can be pumped by the more robust InGaAs diodes delivering high powers in the 0.9-1 µm range. Finally, ytterbium has no bands in the green region, so the inevitable reabsorption losses of neodymium in the wavelength range of the second harmonic can be avoided.

In this paper, we propose a new candidate for self-frequency doubling laser material, Yb-doped $KGd(PO_3)_4$ (KGP). The present work is devoted primarily to spectroscopic investigations, i.e. polarized absorption and fluorescence measurements at room and low temperatures, and lifetime measurements for the upper laser level at room temperature. We report also, for the first time to our knowledge, room temperature laser operation near 1 µm of $KYb_{0.024}Gd_{0.976}(PO_3)_4$, in the continuous-wave regime. In addition, we verify that this crystal is phase-matchable for second harmonic generation in the wavelength range covered by the ytterbium ion.

The host KGP is a monoclinic acentric crystal with the space group $P2_1$ [7]. KGP exhibits a broad transmission window extending from about 180 nm to 4 µm which covers both the fundamental and the second harmonic range. The rather large band-gap, on one hand, should lead to high damage resistivity, on the other hand it allows in principle the use of this host also in the UV range (either as a nonlinear crystal or as a host for cerium). Another advantage of KGP is its almost isotropic thermal expansion [7] which is important for the crystal growth, processing of laser elements, and during laser operation. The high hardness of KGP, close to that of quartz in the Moh's scale, facilitates sample preparation and allows polishing the surfaces with good optical quality. KGP is also chemically stable against moisture as well as against weakly acidic and basic media.

We were able to grow inclusion and macrodefect-free single crystals of Yb:KGP by partial replacement of gadolinium by ytterbium, using the top seeded solution growth-slow cooling (TSSG-SC) technique. Up to now, it was possible to grow single crystals of KGP with ytterbium concentration in the solution as high as 15 at % [9]. This corresponds to ≈7.5 at %

in the bulk crystal since the actual ytterbium concentration in the crystal was found to be reduced to about half of that in the solution (Table 1). The composition of the Yb:KGP crystals was studied by electron probe microanalysis (EPMA) using a Cameca SX 50 equipment operating at an accelerating voltage of 20 kV and electron current of 100 nA.

Table 1. EPMA results for Yb:KGP. K_{Ln} denotes the distribution coefficient of the lanthanide ions in the crystal

Yb at % in solution	K_{Yb}	K_{Gd}	Yb concentration (cm^{-3})	chemical formula
1	0.50	1.01	$2.081x10^{19}$	$KYb_{0.005}Gd_{0.995}(PO_3)_4$
3	0.53	1.01	$6.656x10^{19}$	$KYb_{0.016}Gd_{0.984}(PO_3)_4$
5	0.48	1.03	$1.007x10^{20}$	$KYb_{0.024}Gd_{0.976}(PO_3)_4$
10	0.40	1.07	$1.653x10^{20}$	$KYb_{0.040}Gd_{0.960}(PO_3)_4$
15	0.51	1.02	$3.203x10^{20}$	$KYb_{0.077}Gd_{0.923}(PO_3)_4$

Although the dopant acceptance seemed not to be limited by the ionic radius of ytterbium ion we found it difficult to incorporate high concentrations of ytterbium in the KGP structure. In fact, the problem was related to the crystallization of the monoclinic but centrosymmetric phase *C2/c* [10] instead of the desired structure $P2_1$ [7]. Further investigations on the crystallization region of the $P2_1$-phase of Yb:KGP indicate that this phase could crystallize from solutions with an ytterbium concentration as high as 50 at %. Thus, assuming that the ytterbium concentration in the crystal would be reduced again by about a half, it can be expected that doping levels as high as 25-30 at %, i.e. $\approx 1\times10^{21}$ cm^{-3}, might be reached in single crystals grown by the TSSG-SC method [9]. All results on Yb:KGP reported in this paper are based on a single growth of the composition $KYb_{0.024}Gd_{0.976}(PO_3)_4$ corresponding to an ytterbium concentration of 1.007×10^{20} cm^{-3}. To avoid impurities in the grown crystal, it was obtained from its self-flux and the optimized solution composition was Yb_2O_3:Gd_2O_3:K_2O:P_2O_5=0.3:5.7:34:60 mol %. Because of the high viscosity of the solution, around 2 Dp, the seed holder was equipped with a platinum turbine rotating at the rather high velocity of 75 rpm. The axial temperature gradient was about 1.2 K/mm. The saturation temperature amounted to 958 K. The temperature of the solution was decreased to 12 K below the saturation temperature at a rate of 0.05 K/h. An ***a****-oriented parallelepipedic seed of undoped KGP was used to grow the crystal.

2. Optical Characterization of the KGP host

In a previous publication we characterized the undoped KGP in terms of transmission window and orientation of the optical ellipsoid [8]. The UV transmission edge of Yb-doped KGP is slightly shifted to the visible due to the presence of ytterbium and the cut-off wavelength is 200 nm [9]. The orientation of the three principal optical axes of KGP, denoted as $\boldsymbol{N_p}$, $\boldsymbol{N_m}$, and $\boldsymbol{N_g}$, according to the refractive indices $n_p<n_m<n_g$, was determined with respect to the crystallographic frame (***a***, ***b***, ***c***) at a wavelength of 632.8 nm. For a monoclinic crystal, one of the principal optical axes coincides with the ***b*** crystallographic axis; in the case of KGP this is $\boldsymbol{N_p}$. $\boldsymbol{N_g}$ was found to lie at 37.3° clockwise from the ***c*** crystallographic axis with the positive direction of the ***b*** axis towards the observer.

In order to establish if self-frequency doubling is possible in Yb:KGP we examined as a first step the dispersion of the three refractive indices of undoped KGP (Fig. 1). The refractive indices were measured between 0.45 and 1.2 µm with two semiprisms [11], oriented for measurement of n_p-n_m and n_p-n_g, respectively, using the minimum deviation method. The accuracy of the measurements was 10^{-4}.

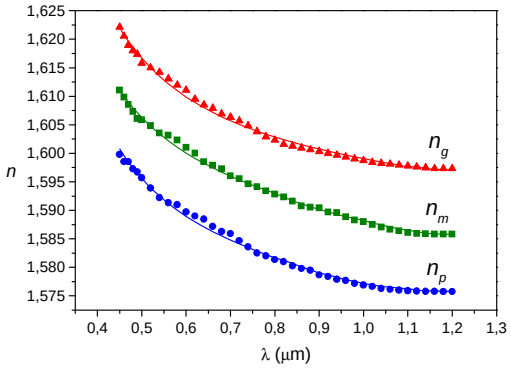

Fig. 1. Dispersion of the principal refractive indices of KGP at room temperature.

As can be seen from Fig. 1 the three refractive indices are nearly equidistant. KGP is an optically negative biaxial crystal since the $2V_g$ angle between the two optic axes [12], lying in the $\boldsymbol{N_p}$-$\boldsymbol{N_g}$ plane, is 94.2° at 632.8 nm. The data points in Fig. 1 were fitted using one UV pole and an IR correction term with the Sellmeier equation,

$$n^2 = A + B/[1-(C/\lambda)^2]-D\lambda^2$$

Table 2 summarizes the Sellmeier coefficients obtained for KGP at room temperature.

Table 2. Sellmeier coefficients of KGP

Principal refractive index	A	B	C (μm)	D (μm^{-2})
n_p	1.7404	0.7479	0.1374	0.0138
n_m	1.7624	0.7667	0.1304	0.0193
n_g	1.7728	0.7782	0.1391	0.0091

Estimations based on these Sellmeier equations indicate that KGP is phase-matchable for type-I second harmonic generation near 1 μm both in the $\boldsymbol{N_p}$-$\boldsymbol{N_m}$ (oo-e type interaction) and in the $\boldsymbol{N_m}$-$\boldsymbol{N_g}$ (ee-o type interaction) principal planes. It should be outlined that biaxial crystals have in general greater potential for self-frequency doubling because they offer greater variety of phase-matching configurations. Considering for instance the preferable type-I interaction, uniaxial crystals allow only one phase-matching configuration (oo-e or ee-o depending on whether they are negative or positive). As can be seen in the case of KGP, both oo-e and ee-o phase-matching are possible and their effective nonlinearity is nonvanishing for point group 2 [13]. Thus one has greater freedom to select the polarization of the fundamental in such a way that the gain is also maximized.

3. Spectroscopic Characterization of Yb:KGP

All further results reported here were based on a single Yb-doped KGP sample which was cut and polished as a cube, accurately oriented along the $\boldsymbol{N_p}$, $\boldsymbol{N_m}$, and $\boldsymbol{N_g}$ principal optical axes, with dimensions of 2.34, 2.68, and 2.47 mm along these axes, respectively.

The polarized optical absorption of $KYb_{0.024}Gd_{0.976}(PO_3)_4$ in the temperature range from 6 to 300 K was measured using a Cary Varian 500 spectrophotometer equipped with a Leybold RDK-6-320 closed-cycle helium cryostat**.** The absorption band associated with the ytterbium transition $^2F_{7/2}\rightarrow{}^2F_{5/2}$ in KGP extends from 9750 to 10800 cm^{-1} (1025-925 nm) at room temperature (Fig. 2). It is characterized by three main peaks centered at 10230, 10305 and 10586 cm^{-1}. As ytterbium has an odd number of electrons in the 4*f* shell, polarization dependent selection rules are not expected but the intensity of the individual peaks may still vary. The anisotropy observed in the absorption spectra of Yb:KGP is rather low and the absorption cross-section is maximized for $\boldsymbol{E}//\boldsymbol{N_m}$. Its maximum value at 977 nm (zero line

transition), calculated with the exact Yb^{3+} concentration of 1.007×10^{20} cm^{-3}, amounts to 1.17×10^{-20} cm^2. For $\boldsymbol{E//N_g}$ and $\boldsymbol{N_p}$, the corresponding maximum absorption cross sections at the same wavelength amount to 0.72×10^{-20} and 0.80×10^{-20} cm^2. Fig. 2 shows the evolution of the absorption coefficient for $\boldsymbol{E//N_m}$ with the temperature from 6 to 300 K. From the lowest temperature spectra we determined the energies of the three Stark sublevels of the exited state multiplet $^2F_{5/2}$. These energies are indicated in the inset of Fig. 2 where the levels are designated as $^2F_{5/2}(0')$, (1'), and (2'). When the temperature is increased, an additional peak emerges at 10140 cm^{-1} which is probably related to the thermal population of the $^2F_{7/2}(1)$ sublevel with transition to $^2F_{5/2}(0')$ but it is smoothed at room temperature.

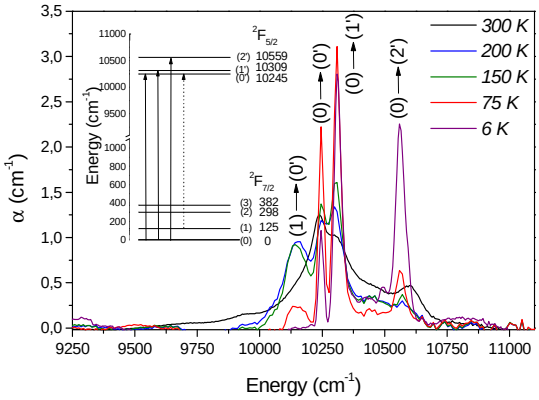

Fig. 2. Temperature evolution of the optical absorption of $KYb_{0.024}Gd_{0.976}(PO_3)_4$ for $E//N_m$. Inset: schematic diagram of the Stark sublevels and absorption transitions.

The fluorescence spectra were recorded at both 300 and 10 K in a 90º geometry. Excitation was provided by a 200 mW InGaAs diode laser emitting at 940 nm which was modulated at 1 kHz. The fluorescence was dispersed by a 0.46 m double monochromator (Jobin Yvon - Spex HR 460). The detector was a cooled Hamamatsu NIR R5509-72 photomultiplier connected to a lock-in amplifier (EG&G, 7265 DSP). A closed-cycle helium cryostat (Oxford CCC1104) was used to cool the sample for the low temperature measurements.

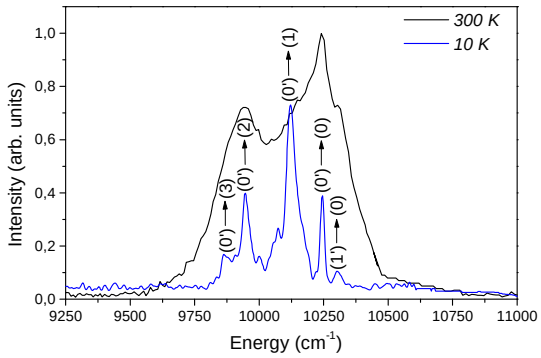

Fig. 3. Emission spectra at 300 K (solid line) and 10 K (dash-dotted line) for $E//N_m$

From the low-temperature polarized fluorescence spectra (Fig. 3) we determined the four sublevels of the ground state $^2F_{7/2}$. Four main lines were found at 10245, 10120, 9947 and 9863 cm^{-1} accompanied by phonon added peaks. These correspond to the transitions $^2F_{5/2}(0')\rightarrow{}^2F_{7/2}(0)$, $^2F_{5/2}(0')\rightarrow{}^2F_{7/2}(1)$, $^2F_{5/2}(0')\rightarrow{}^2F_{7/2}(2)$, and $^2F_{5/2}(0')\rightarrow{}^2F_{7/2}(3)$, respectively.

A dim peak corresponding to the transition from the thermally populated $^2F_{5/2}(1')$ sublevel to $^2F_{7/2}(0)$ is also seen at 10305 cm^{-1}. The reduced intensity of the emission associated with the $^2F_{5/2}(0')\rightarrow{}^2F_{7/2}(0)$ transition is a consequence of the reabsorption at this wavelength. The Stark sublevels of the ground state manifold $^2F_{7/2}$, derived from the 10 K spectrum, are at 0, 125, 298, and 382 cm^{-1}.

The reciprocity method [14] was used to compute the emission cross sections from the absorption cross sections at room temperature and the determined level positions. Fig. 4 shows the calculated emission cross-sections σ_e together with the corresponding absorption cross sections σ_a for the three orthogonal polarizations.

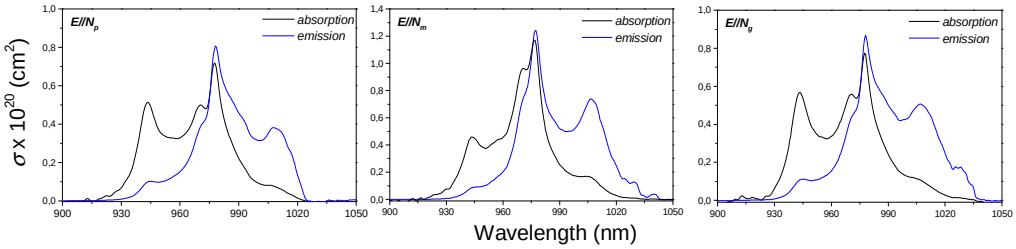

Fig. 4. Measured absorption and calculated emission cross-sections of Yb:KGP at room temperature for the three orthogonal polarizations.

By averaging the calculated $\sigma_e(\nu)$ by the reciprocity method over the three polarizations, a radiative lifetime of τ_{rad}=1.57 ms was obtained at room temperature using the Füchtbauer-Ladenburg equation [14]. The fluorescence decay time was measured by the pinhole method which avoids radiation trapping (Fig. 5). The extrapolated for zero diameter result, at room temperature, was 1.22 (±0.01) ms but the deviation from this value for all the pinhole diameters used, between 0.6 and 2.1 mm, was only ±1%. Thus, reabsorption was negligible in $KYb_{0.024}Gd_{0.976}(PO_3)_4$ probably because of the low ion doping level in the crystal. This leads to an intrinsic quantum efficiency of 78%. Comparing the spectroscopic results with the available data on other acentric Yb-hosts such as Yb:YCOB [2], Yb:GdCOB [3], and Yb:YAB [4], it can be concluded that one feature which distinguishes Yb:KGP is the relatively short oscillation wavelength that can be expected. From Fig. 4, lasing can be expected on the $^2F_{5/2}(0')\rightarrow{}^2F_{7/2}(2)$ transition, at wavelengths near 1010 nm. This was confirmed in the following laser experiments.

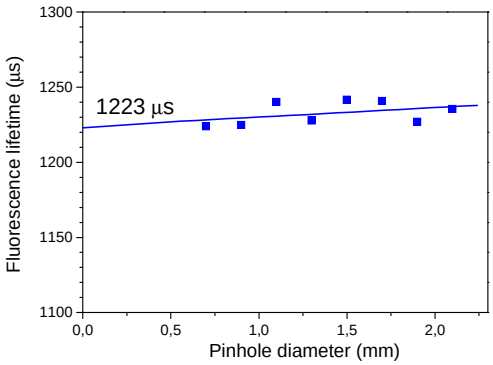

Fig. 5. Dependence of the fluorescence lifetime of $KYb_{0.024}Gd_{0.976}(PO_3)_4$ on the pinhole diameter.

4. Laser operation of Yb:KGP

A standard astigmatically compensated Z-shaped cavity was used as a laser setup. The pump source was a home-made Ti:sapphire laser (960-1025 nm, FWHM<1 nm, max. 3 W). The

estimated pump waist in the focus of the f=6.28 cm anti-reflection coated lens was ≈30 µm. The resonator (depicted in Fig. 6) contained two folding mirrors (M1 and M2), and two plane reflectors (rear mirror M3 and output coupler M4). M2 was highly transmitting at the pump wavelength (977.1 nm). The pumping was in a single-pass. The transmission of the output coupler T_{oc} ranged from 1 to 5%.

The uncoated Yb:KGP sample was attached to a Cu-holder without active cooling and positioned under Brewster angle between the two folding mirrors. We tried to pump this sample with all possible polarizations. Continuous-wave laser operation was obtained for the first time in this monoclinic material at room temperature for pumping with $\boldsymbol{E//N_m}$ (propagation along $\boldsymbol{N_g}$) and with $\boldsymbol{E//N_p}$ (propagation again along $\boldsymbol{N_g}$). The laser always had the same polarization as the pump due to the Brewster orientation. No generation was possible for pumping with $\boldsymbol{E//N_g}$ although we tried this for propagation both along $\boldsymbol{N_m}$ and along $\boldsymbol{N_p}$.

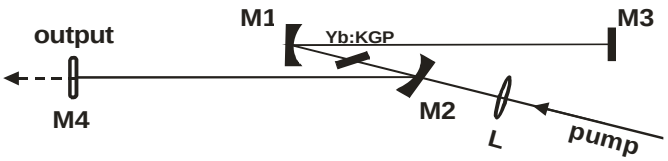

Fig. 6. Laser set-up: Total cavity length, 129 cm; M1 and M2 are curved mirrors with radius of curvature –100 mm, and M3 (rear reflector) and M4 (output coupler with transmission T_{oc}=1, 3, or 5 %) are plane mirrors.

The input-output characteristics obtained for the two polarizations are shown in Fig. 7 against the absorbed pump power for two output couplers (T_{oc}=1 and 3%).

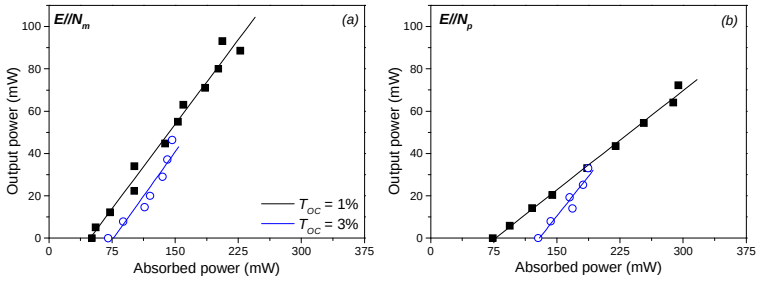

Fig. 7. Room temperature continuous-wave laser performances of Yb:KGP for $E//N_m$ (a) and $E//N_p$ (b). Solid lines are fits to the experimental points for estimation of the slope efficiency.

The relevant laser parameters (slope efficiency η with respect to the absorbed power, oscillation wavelength λ_L and threshold) are summarized in Table 3.

Table 3. Slope efficiency (η), laser wavelength (λ_L), and threshold of the $KYb_{0.024}Gd_{0.976}(PO_3)_4$ laser in dependence on the output coupler (T_{oc}) used

T_{oc} (%)	η (%)		λ_L (nm)		threshold (mW)	
	$\boldsymbol{E//N_m}$	$\boldsymbol{E//N_p}$	$\boldsymbol{E//N_m}$	$\boldsymbol{E//N_p}$	$\boldsymbol{E//N_m}$	$\boldsymbol{E//N_p}$
1	53.2	31.3	1017.1	1016.3	51	73.8
3	55.6	-	1013.8	1013.5	70.5	127.8
5	-	no lasing	1012.1	no lasing	131.8	no lasing

With a maximum incident pump power of roughly 2 W (corresponding to an absorbed power of 206 mW at 977.1 nm), the maximum output power for $\boldsymbol{E//N_m}$ was 93 mW (T_{oc}=1%).

The corresponding slope efficiency was η=53.2%. Pumping with polarization parallel to $\boldsymbol{N_p}$, the maximum output power reached 72 mW for an absorbed power of 294 mW, also with T_{oc}=1%. In this case the slope efficiency was lower, η=31.3%. The laser thresholds for $\boldsymbol{E}//\boldsymbol{N_m}$ and $\boldsymbol{E}//\boldsymbol{N_p}$ were 51 and 74 mW, respectively, both for T_{oc}=1%. The lower slope efficiency and higher threshold for $\boldsymbol{E}//\boldsymbol{N_p}$ can be explained by the lower gain.

For T_{oc}=5% the output power reached 12 mW (only for $\boldsymbol{E}//\boldsymbol{N_m}$) and reliable estimation of the slope efficiency was not possible. The oscillation wavelength was as short as 1012.1 nm in this case. The shorter wavelength at higher output coupler transmission is typical for Yb-lasers and is related to the maximum of the gain curve. In this case we have obviously oscillation on the $^2F_{5/2}(0') \rightarrow {}^2F_{7/2}(2)$ transition.

Under lasing conditions the absorption of the sample was quite low (not more than 15%) but almost constant. This is a consequence of the low Yb-ion density in the crystal and the relatively low absorption cross-sections. Under non-lasing conditions the absorption was completely bleached at the maximum incident power. However, in the lasing state, the intracavity power in the three-level system of ytterbium increases the saturation intensity for the pump and this balances the bleaching effect.

5. Summary

In conclusion, we successfully grew macrodefect-free single crystals of Yb-doped KGP using the TSSG-SC technique. To the best of our knowledge, KGP crystals were doped with ytterbium for the first time. The maximum ytterbium concentration in the bulk crystal achieved until now is around 3.2×10^{20} cm^3. However, there are indications that it can be increased up to about 1×10^{21} cm^3. By measuring the dispersion of the refractive indices of KGP, we confirmed that this host possesses phase-matching properties for self-frequency doubling of the Yb-laser. We determined the Stark splitting of the two electronic states of Yb from absorption and emission measurements, both at room and low temperatures, and calculated the emission cross sections at room temperature. The upper level lifetime of Yb amounts to 1.22 ms at room temperature. Lasing has been demonstrated for the first time with $KYb_{0.024}Gd_{0.976}(PO_3)_4$. Although the maximum output power achieved (93 mW) was limited by the available size and doping level of the crystal, the more than 55% slope efficiency obtained with this first sample is rather promising for the future.

Acknowledgements.

We thank C. Kränkel and K. Petermann (Hamburg University, Germany) for the measurement of the fluorescence decay time.

We acknowledge financial support from the Departament d'Universitats, Recerca i Societat de la Informació de la Generalitat de Catalunya under the Project 2005SGR658 and from MEC (Ministerio de Educación y Ciencia) of the Spanish government, under Projects MAT-05-06354-C03-02, MAT-04-20471-E and CIT-020400-2005-14. This paper is also supported by EU-Commission Project DT-CRYST (STRP-NMP3-CT-2003-505580). I. Parreu acknowledges financial support from Fons Social Europeu i del Departament d'Universitats, Recerca i Societat de la Informació de la Generalitat de Catalunya. X. Mateos knowledges financial support from the Secretaria de Estado de Educación y Universidades of Spain and from the Fondo Social Europeo.